2018

Direct Probing of Neural Stem Cell Interactions on Hydrogel Electrodes using Atomic Force Microscopy

Christina Puckert
University of Wollongong

UNIVERSITY OF WOLLONGONG
Intelligent Polymer Research Institute
Australian Institute for Innovative Materials

Direct Probing of Neural Stem Cell Interactions on Hydrogel Electrodes using Atomic Force Microscopy

This thesis is presented as part of the requirements for the conferral

of the degree:

Doctor of Philosophy

by

Christina Puckert

born 25.03.1986
in Duisburg

Bachelor of Science in Physical Engineering
Master of Science in Biomedical Engineering

2018

Declaration

I, *Christina Puckert*, declare that this thesis is submitted in partial fulfilment of the requirements for the conferral of the degree Doctor of Philosophy, from the University of Wollongong, is wholly my own work unless otherwise referenced or acknowledged. This document has not been submitted for qualifications at any other academic institution.

Christina Puckert

November 2018

Acknowledgements

To Associate Professor Michael Higgins, my principal supervisor, my Doktorvater, thank you for your enthusiasm, calmness, inspiration and eye for detail. Your understanding and help during the very sensitive and at times emotional research environment of a PhD project kept me motivated and is greatly appreciated. Thank you for your willingness to listen and discuss my research even when you have been so busy and for all your support through my doctorate studies and time spent at the University of Wollongong.

To Associate Professor Jeremy Crook and Dr. Eva Tomaskovic-Crook, my co-supervisors, thank you for all your help and support during my work in the PC2-lab. Special thanks for all your continuous, helpful advice and comments, and for always pushing me forward.

To Professor Gordon Wallace thank you for the opportunity to work in a prestigious research environment with advanced laboratory equipment and great IPRI workmates. Thank you for awarding me the great scholarship opportunity from the Australian Research Council Centre of Excellence for Electromaterials Science (ACES). I have grown from the learning opportunities of engaging with fellow researchers and industry, enabling my participation in countless presentations and professional conversations. Thank you for this unforgettable lifetime journey in Australia, where the ocean is so blue and the wildlife and natural environment totally fascinating.

To Dr. Kerry Gilmore, my lab supervisor in the PC2-lab, thank you so much for your help, advice, little chats and suggestions.

Special thanks to Christian Löbbe from Scitech Company (distributor of the JPK AFM) for his fantastic technical support.

To my friends back home who still have me in their mind even when we have lived so far apart, and not seen each other for such a long time. Thank you for believing in me and for giving me hope when I needed it. This has not been taken for granted in this fast spinning world.

Finally, very special thanks to my family; my mum and dad, my sister and brother and my grandma who have always shown great understanding and support of my life choices, even when my journey has taken me to the other end of the world. I know they have missed me, just as I have missed them in my desire to learn.

"Life is too short to wake up with regrets.
So love the people who treat you right.
Forget about those who don't.
Believe that everything happens for a reason.
If you get a chance – take it, if it changes your life – let it.
Nobody said it will be easy, they just promised it would most likely be worth it"

- **Paulo Cohel**

Summary of Thesis

Preface

Implantable electrode devices, such as implantable metal electrodes, are important for treating neural disorders and brain diseases. However, the mechanical compliance between the stiff metal and soft brain tissue causes long-term inflammation associated with glial scar formation, which is detrimental to both the surrounding tissue and performance of the electrode. To address this mechanical mismatch, hydrogels with similar properties to human brain tissue can provide a mechanically compliant, 'biomimetic' interface. Therefore, in this thesis, we incorporated a hydrogel layer on a thin film conducting polymer electrode as a model system to study the properties of the hydrogel and its interactions with living cells, including in the presence of an electrical field. A central theme of the thesis was to improve our understanding of the physical interactions between the hydrogel and human neural stem cells. This question was especially of interest since cell integration and adhesion to an electrode surface, in this case the hydrogel, is very important for many neurotechnologies such as implantable electrodes, microelectrode arrays and electronic cell culture substrates. While studies on cell-hydrogel interactions are rapidly increasing, one aspect that remains unexplored is the direct measurement of the forces that a cell 'experiences' when interacting with the hydrogel, particularly at the molecular level. Hence, the project employed the use of an approach based on Atomic Force Microscopy (AFM), termed Single Cell Force Spectroscopy (SCFS), to enable direct measurement of single cell adhesion on the hydrogel. Lastly and importantly, many of the experiments were designed to consider the dynamic changes of the hydrogel properties in response to electrical stimulation by implementing in-situ electrochemical capabilities.

Chapter Overview

The thesis is comprised of six chapters. **Chapter 1** provides an introduction to the research topic on the need for softer implantable electrodes in neural prosthetics and bionics. The chapter describes the relevant use of hydrogels, e.g. conductive hydrogel electrodes, electro-actuation of hydrogels and hydrogel interactions with human neural stem cells (hNSCs), to address this need. Finally, we outline the significance and aims of the thesis, leading to the characterization of the electrode (hydrogel) – living cell interface of which there is a paucity of information at the molecular level. To address this, we focus on characterization using Atomic Force Microscopy (AFM). Henceforth, **Chapter 2** introduces the operating principles and modes, e.g. force spectroscopy, of AFM. More specifically, the chapter provides background to the technique, SCFS, which is an emerging approach for directly probing the physical, molecular interactions of living cells with biomaterials. The three experimental chapters (**Chapters 3, 4, and 5**), applied AFM in **Chapter 3**, and the SCFS is applied in experimental work in **Chapter 4 and 5. Chapter 6** briefly outlines possibilities for future work.

A summary of the main experimental **Chapters 3, 4 and 5** are as follows:

Chapter 3: Electrical stimulation of hydrogels has been performed to enable micro-actuation or controlled movement of ions and biomolecules such as in drug release applications. Hydrogels are also increasingly used as low modulus, biocompatible coatings on electrode devices and henceforth are exposed to the effects of electrical stimulation. There is growing interest in the latter, especially on the dynamic and nanoscale physical properties of hydrogels. In the chapter, we investigated the electro-mechanical properties of a photocrosslinkable hydrogel, gelatin methacrylate (GelMA), applied as a coating on a conducting polymer polypyrrole-dodecylbenzenesulfonate (PPy-DBSA) electrode. In particular, Electrochemical-AFM (EC-AFM) was used to quantify the nanoscale actuation and dynamic changes in Young's modulus of the GelMA coating during electrical stimulation via the underlying PPy-DBSA electrode. Pulsed electrical stimulation was shown to induce dynamic expansion and contraction, or nanoscale actuation, of the GelMA hydrogel

due to the reversible ingress of electrolyte ions and associated changes in osmotic pressure during oxidation and reduction of the PPy-DBSA film. In addition, dynamic changes in the Young's modulus of up to 59% were observed in the hydrogel and correlated with the actuation process and ion diffusion during oxidation and reduction of the underlying PPy-DBSA film. These dynamic properties were investigated for hydrogels with varying degrees of cross-linking, porosity and modulus, the latter ranging from ≈ 0.2 – 1 kPa. The chapter demonstrated an AFM-based approach to quantify the dynamic physical properties of hydrogels, which are shown to be modulated via electrical stimulation. This enabled a better understanding of the electro-mechanical mechanisms that are important for the controlled release of drugs or controlling cell interactions at the hydrogel-cell interface.

Chapter 4: Studies on the effect of hydrogel stiffness on stem cell differentiation are increasingly revealing the molecular mechanisms by which cells sense and respond to material surfaces. The role of dynamic and time-dependent, viscoelastic properties of polymer networks, i.e. hydrogels, consisting of cell ligands is emerging as an important aspect, and in coventional experimental approaches attempts are often made to correlate such properties to cell morphology or expression of adhesion complexes. During the cell adherens at the cell-hydrogel contact area, the interaction forces and their dynamics responsible for controlling the molecular force-feedback mechanisms of mechanosensing are rarely measured in order to explain the cell interactions on these complex, polymer networks. Furthermore, the bulk properties such as modulus may not adequately describe the nanoscale components and their properties of the polymer network, such as the rheology of crosslinked single polymer chains, which are expected to significantly contribute to the physical, molecular-level interactions with cell surface molecules distributed on equivalent length scales. In this chapter, we applied SCFS to directly measure hNSC de-adhesion forces and energy on the same GelMA hydrogel samples, as prepared and characterized in the previous chapter. Importantly, the SCFS experiments were performed as a function of the GelMA modulus and in the presence of integrin blocking antibodies to elucidate combined

effect of substrate stiffness and integrin receptor recognition/unbinding on the cell de-adhesion. In doing so, the chapter elucidated highly sensitive, modulus-dependent molecular interactions of hydrogel polymer chains, leading to activation of dynamic force regimes and differential binding of integrins.

Chapter 5: Current implantable electrode devices use metal electrodes such as platinum that have poor mechanical compliance with much softer biological tissue, typically causing glial scar formation and reducing electrical performance of the electrode. To address this issue, softer, organic conducting polymers and their composites with hydrogels, e.g. hydrogel coatings on existing metal electrodes, have been developed. Typical bulk properties don't describe all the discrete molecular parameters to understand the interaction between cells and the hydrogel. Conventional methods are limited in measuring individual chain properties that are most likely playing a role in the cell interaction. Hence, in this chapter, we applied SCFS combined with an in-situ electrochemical setup to investigate hNSC de-adhesion on a GelMA hydrogel layer - PPy-DBSA electrode as a function of electrical stimulation. Results in this chapter indicated a clear dependency of the cell de-adhesion to the GelMA moduli. However, the interesting outcome here is that in comparison to the results gained in chapter 4, we show that electrical stimulation induces a reversal effect of cell de-adhesion and dynamic force regimes in relation to the investigated GelMA moduli. Therefore, the chapter presents the effect of an electric field to the GelMA-cell interface at a very narrow modulus range involving hydrogel polymer chains, de-adhesions forces and dynamic loading regimes.

Abbreviations, symbols and units

Abbreviations

AFM	atomic force microscopy
Ag	silver
Au	gold
Biotin-BSA	bovine serum albumin, biotinamidocaproyl-labeled
Biotin-ConA	biotin-concanavalin A
CS/PEG	chitosan/poly (ethylene glycol)
CV	cyclic voltammogram
DBS	deep brain stimulation
DBSA	dodecylbenzenesulphonic acid
DMT	Derjaguin Müller Toporov
DNA	deoxyribonucleic acid
EC-AFM	electrochemical-atomic force microscopy
EC-SCFS	electrochemical-single cell force spectroscopy
ECM	extracellular matrix
F-D	force-distance
FS	force spectroscopy
GelMA	gelatin methacrylate hydrogel
hNSC	human neural stem cell
HUVEC	human umbilical vein endothelial cell
JKR	Johnson Kendall Roberts
Ir	iridium
Irgacure 2959	2-hydroxy-1-[4-(hydroxyethoxy)phenyl]-2-methyl-1-propanone
MSC	mesenchymal stem cell
NaCl	sodium chloride
NPC	neural progenitor cell
NSC	neural stem cell
OCP	organic conducting polymer
PAAm	polyacrylamide
PANI	polyaniline
PBS	phosphate buffered saline
SCN	stem cell niche
PEDOT	poly(3,4-ethylenedioxythiopene)
PGA	polyglycolic acid
PPY	polypyrrole

PSS	poly (styrenesulfonate)
Pt	platinum
PU	polyurethane
SEM	scanning electron microscopy
RGD	arginine-glycine-aspartic acid
SCFS	single cell force spectroscopy
Ti	titanium
TiN	titanium nitrite
USEA	High-Density Utah Slanted Electrode Array
UV	ultra violet
VM	ventral mesencephalon

Symbols

d	detachment length (µm)
E	Young's modulus (Pa)
F_D	detachment force [N]
k_BT	Boltzman constant at room temperature (4.114 pN*nm)
k_{eff}	spring constant
p_f	density of fluid
r	loading rate (pN/s)
Re	Reynolds number
v	pulling speed (µm/s)
v	Poisson ratio
ω_f	resonant frequency
Γ_i	imaginary component

Units

°C	degree Celsius
h	hour
GPa	Gigapascal (10^9 Pa)
Hz	Hertz
K	Kelvin
kPa	Kilopascal (10^3 Pa)
ml	millilitre (10^{-3} l)
m	meter
M	Molar (mol/l)
MPa	megapascal (10^6 Pa)
mS	millisiemens (10^{-3} S)

mW	milliwatts (10^{-3} W)
N	Newton (kg*m/s^2)
nm	nanometer (10^{-9} m)
nN	nanonewton (10^{-9} N)
pN	piconewton (10^{-12} N)
Pa	Pascal [N/m^2]
sec	seconds
V	Voltage
µm	micrometer (10^{-6} m)

List of Figures

Table of Contents

Chapter 1:

Bridging the Electrode – Tissue Interface with Hydrogels

1.1 Bionics

Electrical stimulation of the brain has played a major role in providing remarkable therapeutic benefits for people with a variety of neurological disorders like tremor or Parkinson's disease. As early as in the 1930s, electrical stimulation was used to map cortical function by Penfield and Boldrey et al. (1937) [1]. By the 1960s, treatment of neurological disorders with chronic stimulation began to emerge. Hassler et al. (1960) reported that high frequency 100 Hz stimulation of the ventrolateral thalamus could decrease tremor [2]. Electrical stimulation related to Parkinson's disease was developed by Sem-Jacobsen et al. (1966) who used a method of implanting a bundle of multiple electrode wires deep in the brain and left them in place over weeks [3]. In the early 1970s, chronic stimulation was used as a treatment for pain [4], movement disorders or epilepsy [5]. A major breakthrough came in the 1990s when implantable pacemaker technology was combined with chronically implanted deep brain electrodes [6, 7] for long-term chronic deep brain stimulation (DBS). Since then, DBS has been used for treating a variety of disorders like Epilepsy, Primary Dystonia or Obsessive-Compulsive Disorder [8].

Using electrodes to stimulate biological tissue or living organs has been described as "bionics", the merging of *bio*- and electro-*nics* [9], and is applied in the field of neural prosthetics, i.e. engineering of a biomedical device that rectifies a missing neural function or disorder. The interface between the electrode and biological tissue is critical to the operation of the device. The properties of the electrodes dictate both the function of the device and compatibility with human tissue. Electrode properties such as biocompatibility, capability of injecting high-

density charge to surrounding cells and tissue, low impedance, high flexibility, mechanical fixation and long-term viability [9, 10] are all critical for electrode performance in the physiological environment of the human body. However, long-term inflammation, foreign body responses and mechanical trauma due to insertion of the electrode are commonly associated with implantable electrodes [11]. After implantation, the tissue reaction of wound healing causes glial scar thickening around the electrode, i.e. fibrosis, and inhibits cell survival and increases electrical impedance of the electrode [11]. Tissue injury is often reported by intracortical microelectrodes, involving glial scar tissue growth around the implanted probe and preventing recording or stimulation of neurons (**Figure 1**) [12]. To minimize these tissue responses, the mechanical properties, surface morphology and electrochemistry of the electrodes need to be improved. An understanding of the biological mechanisms and interactions occurring at the electrode surface is necessary to improve design and application of implantable electrodes.

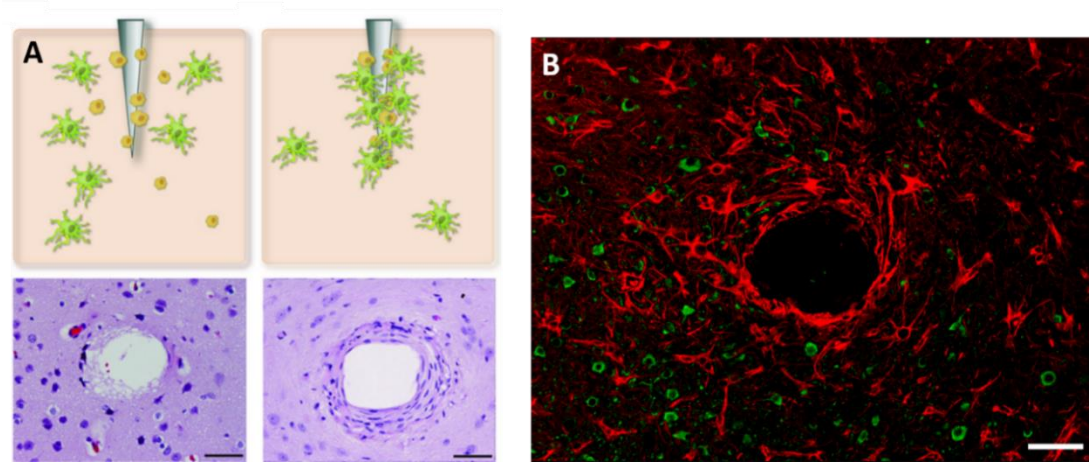

Figure 1: Inflammatory response at the microelectrode-brain tissue interface. Glial scar tissue development on an intracortical microelectrode. (**A**) Inserting a microelectrode into the brain cortex caused an acute neural injury, which activates astrocytes and microglial cells to migrate to the site of injury. (**B**) Photomicrograph showing astrocytes (GFAP staining, red) and neurons (NeuN staining, green) around one microelectrode track in a rabbit occipital cortex (scale bar = 50 µm) [12].

1.1.1 Metal-Based Electrodes

Common materials used for implantable electrodes are inert metals and their alloys, including medical grade stainless steel, titanium (Ti), gold (Au), iridium (Ir), platinum (Pt), alloys of Pt and Ir and titanium nitride (TiN) [13]. These types of metal electrodes have low-reactivity in-vivo, good compatibility, long-term stability, and suitable electrical properties [13, 14]. Most implantable metal electrodes are fabricated as either a single electrode [15], multi-electrode array (**Figure 2**) [16], single wire-based stimulating electrode [17], or wireless implantable microelectrode.

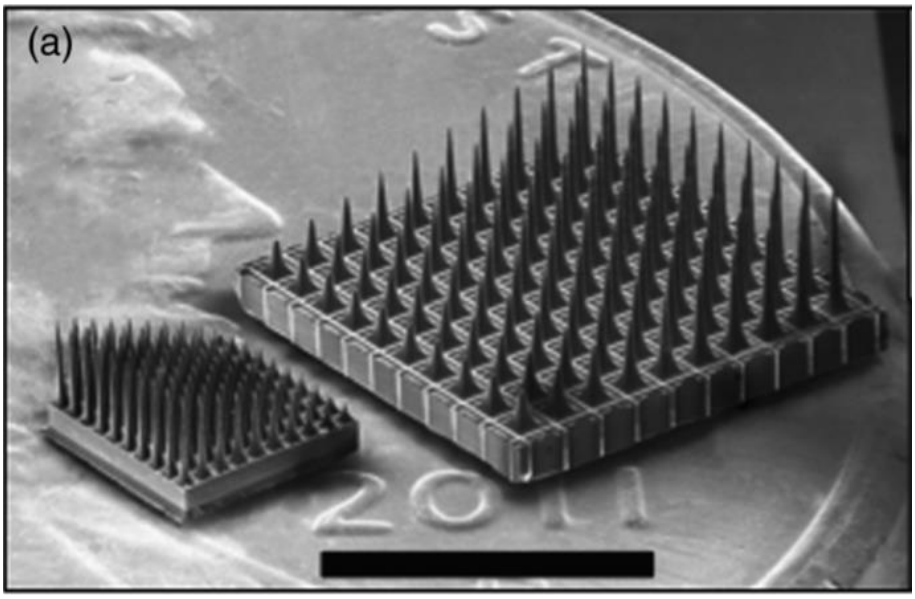

Figure 2: High-Density Utah Slanted Electrode Array (USEA). *A* SEM image of a conventionally spaced USEA (right) and a new HD-USEA (left) located atop a US penny (scale bar = 3 mm) [18].

Electrodes of the cochlear implant [19], bionic eye [20], cardiac pacemaker [21] and early DBS [22] are typically made of Pt. However, the use of these metals is still limited by corrosion, leading to potential release of toxic ions [23, 24]. They are also significantly harder than soft brain tissue [25, 26], which has a modulus of approximately 0.5 kPa to 1 kPa [27]. In comparison, gold, platinum or silicon [25] have

moduli of 69 GPa (Au), 139 GPa (Pt) [28], 1000 GPa (graphene) and 200 GPa (stainless steel) [http://www.engineeringtoolbox.com/young-modulus-d_417.html]. Inevitably, the incompatibility of the moduli at the interface of the metal electrode and brain tissue is the leading cause of the aforementioned inflammatory response, which is an ongoing major challenge in this field [29, 30]. Over the past two decades, the development of electrode materials for bionics and neural prosthetics has therefore looked toward softer, conductive materials such as organic conducting polymers (OCP), hydrogels and their composites.

1.1.2 Organic Conducting Polymers

In 2000, the chemists MacDiarmid, Shirkawa and Heeger were awarded the Nobel Prize in chemistry for their discovery and development of OCPs [31]. These OCPs have good conductivity yet are similar to other plastics in their weight, cost, moldability and mechanical properties, e.g. a modulus of 1.3 GPa (Polyaniline) [32] and 0.3 GPa (Polypyrrole-Chondroitin Sulfate) [33]. In addition, their conductive and optical properties are similar to those of metals and inorganic semiconductors [34]. Due to their diverse properties, OCPs are studied in a wide range of biomedical applications, including drug-delivery devices [35], bio-actuators [36], regenerative medicine [37], neural prostheses [38] and electrochemical biosensors [39].

Polypyrrole (PPy) is one of the most studied OCP because of its biocompatibility [40, 41], ease of synthesis [42], electrical properties [43] and flexibility in modifying chemical surface properties [41]. It is generally synthesized by chemical or electrochemical polymerization. Chemical polymerization uses a strong oxidizing agent (typically $FeCl_3$) with a monomer solution, enabling synthesis of large quantities of material [44, 45]. Electrochemical polymerization is mostly preferred due to the good control over material properties, including thickness, roughness and geometry. A dopant must be incorporated into the OCP to enable conductivity, a process that can either follow chemical or electrochemical ‘p-doping’ (oxidation) or ‘n-doping’ (reduction) [46]. Potential dopants include biopolymers or biomolecules

that enable synthesis of OCP with functionalized biointerfaces [47]. In this thesis, we use the dopant, Dodecylbenzenesulphonic Acid (DBSA), which is a large amphiphilic surfactant molecule. It has been shown that reorientation of the DBSA groups causes switching between a hydrophilic and hydrophobic surface, as the polymer undergoes electrochemical oxidation and reduction [48, 49]. In addition, due to its large size the DBSA remains entrapped within the polymer, allowing movement of ions from the electrolyte in and out of the polymer [49]. Importantly, doping using DBSA provides good electrical conductivity and electrochemical stability, making it an attractive dopant for PPy [50].

1.1.3 Electrical Stimulation of Living Cells using OCP

Earlier studies using conducting polymers as substrates in cell culture were done by Wong et al. (1994) [51]. They showed that seeded bovine aortic endothelial cells spread and adhered to fibronectin-coated oxidized PPy. However, when PPy was electrically switched to its neutral state the cell extension was inhibited but not cell viability [51]. Further studies of oxidized PPy also showed enhanced neurite outgrowth of rat PC12 cells [52]. Stewart et al. (2015) showed differentiation of hNSCs seeded on PPy-DBSA films [53], while Puckert et al. (2016) found that PPy-DBSA films had good biocompatibility and cell viability for cardiac progenitor cells [54]. In general, OCPs have been promising for electrical stimulation of excitable cells like muscle or nerve [55] and most *in vitro* studies present encouraging results for use of OCP as an electrode material in bionic devices. However, the performance of OCP electrodes implanted *in-vivo* appears to have been less efficacious compared to those tested *in vitro* [56]. For example, poly (3,4-ethylenedioxythio-phene) (PEDOT) polymer coated electrodes implanted in rat motor cortex showed an initial improvement of signal-to-noise ratio of neural recordings. However, over a 6-week period, a large increase in impedance was observed for both PEDOT coated and bare electrode (**Figure 3A**) perhaps due to the physical motion of the electrode, reactive tissue response or sustained immune response [57].

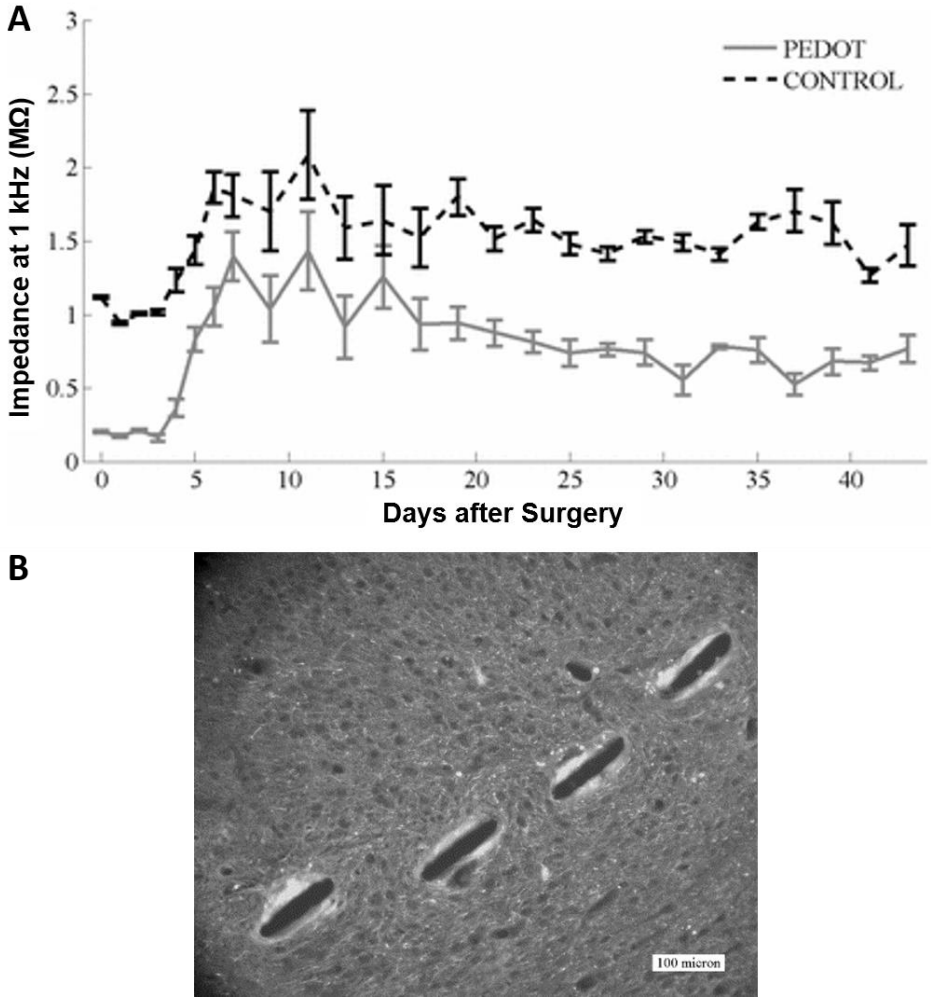

Figure 3: ***In-vivo*** **studies of implanted OCP electrodes.** The 1 kHz average site impedance for both PEDOT and control probes sites increased an average of 70 kΩ immediately upon implantation. Impedances increased dramatically following the third day after implantation, up to a maximum value at the one-week mark. The bars denote standard error of the data set on a given day (n = 64) [57]. (**B**) A 4-shank probe coated with PPy/DCDPGYIGSR was implanted guinea pig brain and pulled out after 3 weeks. Image of neurofilament immunostained tissue sections with the presence of reactive astrocytes, which migrated to the probe and surrounded it [58].

A further *in-vivo* study of an implanted gold electrode coated with PPy/DCDPGYIGSR, the latter a laminin fragment peptide, showed that glial scar tissue growth was reduced but could not be prevented after 3 weeks of implantation in a guinea pig brain (**Figure 3B**) [58]. Even with the use of "softer" OCP, their higher modulus (~0.5

- 1.5 GPa) range relative to soft biological tissue may still not meet the compatibility requirements to overcome the chronic issue of inflammation and associated scar tissue formation around the implanted electrode. Hence, studies have focused on the use of hydrogels, either as a coating or a constituent material (e.g. in composites), to produce electrodes with mechanical properties equivalent to the nerve or muscle tissue [50, 59, 60]. Reducing the modulus of the electrodes to conform to biological tissue is expected to lead to next generation electrodes in bionics [61].

1.2 Composite Hydrogel – OCP Electrodes

1.2.1 Hydrogels

Hydrogels are important in tissue engineering and commonly used in biomedical applications, such as wound healing and drug release [62, 63], due to their low modulus, porosity and water content [64, 65]. They are special types of water-swollen polymer networks, which are mainly cross-linked hydrophilic polymers [66, 67]. Hydrogels have a high water content, which can be more than 90%, due to their hydrophilic nature [68] and thus resemble natural, soft tissue more than any other type of polymeric biomaterial [66] [68]. The appropriate design of their swelling properties allows diffusion of nutrients and cellular waste through the elastic hydrogel network [66], and to and from cells [69]. Potential applications of hydrogels include tissue engineering, implantable devices, biosensors, separation systems, porous membranes, smart microfluidics, energy conversion systems and synthetic extracellular matrix (ECM) [70-72]. For tissue engineering, developing hydrogel systems that mimic complex ECM is difficult to implement [73]. There are many structural and mechanical requirements that need to be fulfilled, including strength, stiffness, mesh size, and porosity [68]. Related to implantable electrodes, studies have shown that the charge transfer properties of a platinum electrode can be improved by adding a hydrogel coating [61]. Therefore, hydrogel-based electrodes not only improve the mechanical compatibility but also enhance electrical properties

[61]. Different types of hydrogel electrode constructs with OCP have been developed over the past two decades. They can be generally divided into three types; 1.) hydrogel layer on top of an OCP film electrode, 2.) conductive hydrogel electrode, and 3.) concept of “living” hydrogel electrode.

1.2.2 Hydrogel Layer - OCP Electrodes

Kim et al. (2010) used an alginate hydrogel layer on a PEDOT film as an electrode to record neural signals in the auditory cortex (**Figure 4**) [60]. It was found that the PEDOT/alginate coating improved long-term performance of the neural electrode by increasing biocompatibility and efficient signal transmission. Furthermore, the PEDOT/alginate electrode showed approximately the same percentage of clearly detectable units (SNR) as compared to the bare electrode without the hydrogel [60]. Lundin et al. (2011) coated a gel layer composed of a reduced growth factor basement membrane matrix (Geltrex^{TM}) on a PPy-DBSA film and obtained good NSC survival compared to the bare PPy-DBSA surface [50]. Viability of the NSCs was maintained after applying a reduction potential of -0.9 V for two minutes due to the hydrogel layer with thickness of hundreds of nanometers, whereas the bare PPy-DBSA film showed loss of survival for NSCs during the reduction process [50].

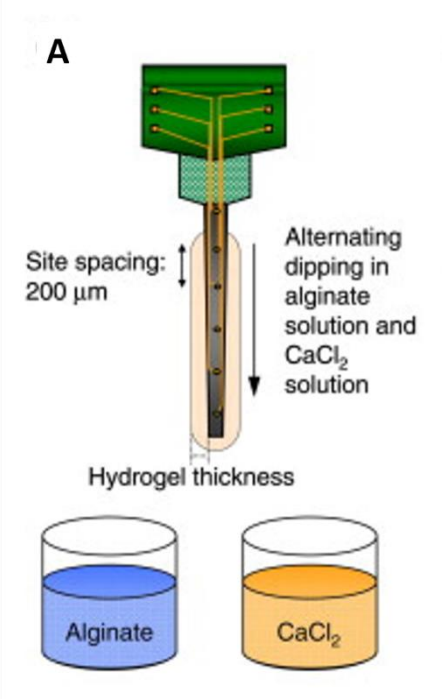

Figure 4: Alginate neural electrode. Alginate coated neural electrode to record from the auditory cortex [60]**.**

1.2.3 Conductive Hydrogel Electrodes

Gilmore et al. (1994) first produced composite conductive hydrogels by electropolymerizing PPy directly within a polyacrylamide hydrogel (**Figure 5A**), opening up new possibilities for development of conductive hydrogels [74]. Various types of graphene-oxide/OCP (GO/OCP) composite hydrogels, made from polyacrylamide gels, have also been developed from either PPy, PEDOT and polyaniline (PANI) (**Figure 5B**). The GO/CP composite hydrogels had low critical hydrogel concentrations (<1%), good electrical conductivity and electrochemical activity [59]. Highly conductive hydrogel-based devices with stretchable/flexible properties have been fabricated using a simple technique involving a combination of chemical polymerization and electropolymerization of PEDOT to achieve tight bonding between PEDOT and a polyurethane (PU) elastic double-network hydrogel (**Figure 5C**) [75]. Further modification of the hydrogel-based device enabled formation of a 3D PEDOT/PU–hydrogel hybrid [75]. Moreover, conductive hydrogel composites have been produced

by addition of conductive nanoparticles. Pardo-Yissar et al. (2001) immobilized gold nanoparticles (Au-NPs) in a polyacrylamide (PAAm) hydrogel by swelling the dehydrated gel in the presence of an Au-NP solution of which the latter was uniformly distributed in the gel matrix [76]. A detailed review on nanoparticle-hydrogel composites is described by Pardo-Yissar (2001) and Thoniyot (2015) [76, 77]. Lastly, a conductive GelMA-PEDOT:poly (styrenesulfonate) (PSS) composite hydrogel was developed by incorporating PEDOT:PSS nanoparticles (**Figure 5D**) [78]. The properties of the composite hydrogels, such as mechanical, degradation, and swelling, could be tuned by changing the concentration of PEDOT:PSS nanoparticles. Further *in vitro* studies showed that composite hydrogels containing 0.1% (w/v) PEDOT:PSS supported the viability and spreading of encapsulated C2C12 myoblasts, which was comparable to GelMA hydrogel without PEDOT:PSS nanoparticles [78].

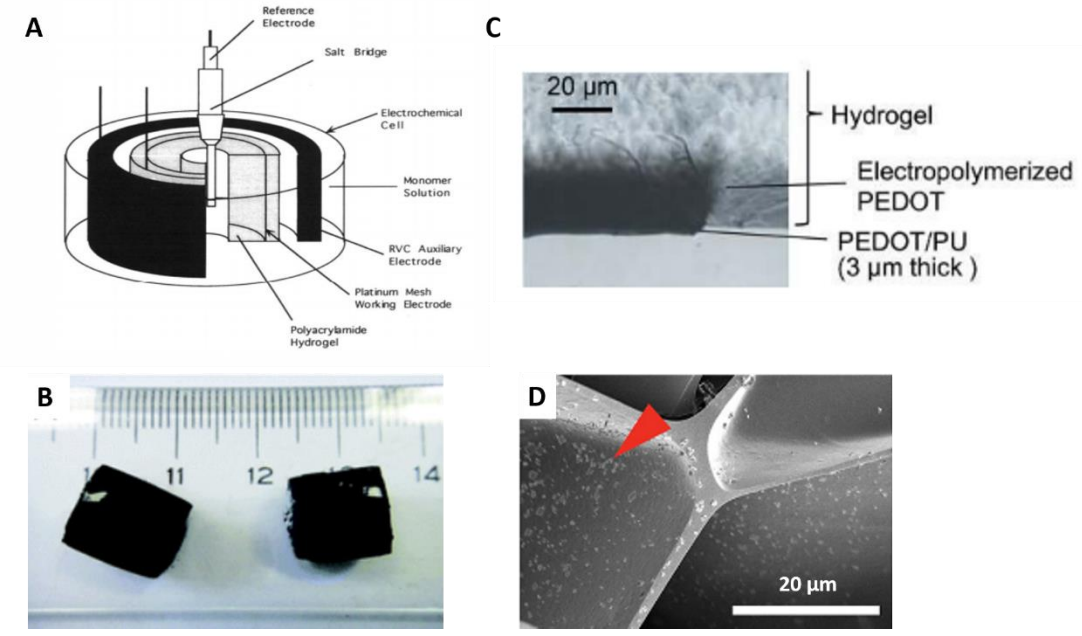

Figure 5: Hydrogel – OCP Composite Electrodes (**A**) Composite Hydrogel Electrode made of polyacrylamide hydrogel with electropolymerized PPy [74]. (**B**) Graphene oxide/conducting polymer (GO/CP) composite made of GO/PANI hydrogel [59]. (**C**) Conductive composite of PEDOT and PU polymerized to an elastic double-network hydrogel [75]. (**D**) SEM image of electroconductive GelMA-PEDOT:PSS composite hydrogel containing loaded PEDOT:PSS nanoparticles (red arrowheads) with a concentration 0.1% PEDOT:PSS [78].

1.2.4 'Living' Hydrogel Electrodes

As an extension of the aforementioned conductive hydrogel composites, the further incorporation of living cells has led to the concept of having a 'living' electrode. For example, Green et al. (2013) fabricated a PVA hydrogel containing PC12 neural cells on PEDOT-hydrogel layer, which was then layered on a Pt electrode, as shown in **Figure 6**. The electrode provides biochemical and mechanical support for the cells and at the same time allows for space to enable the cells to proliferate and differentiate. The concept explains that by the time the hydrogel degrades, the cells will have generated their own supporting matrix to better integrate the electrode with the surrounding tissue. The construct was shown to provide a scaffold for supporting PC12 survival and differentiation without compromising the electrical performance of the electrode [61].

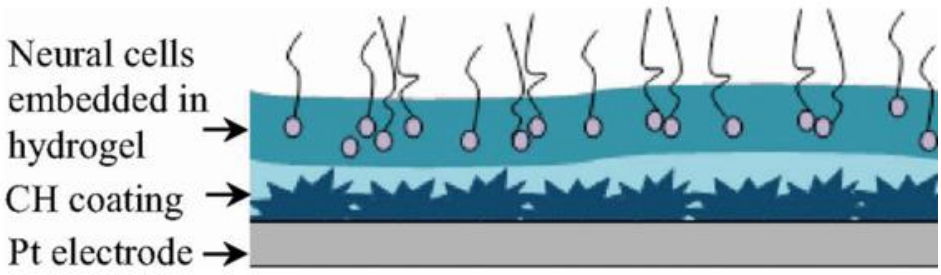

Figure 6: 'Living' electrode. Concept of 'living' electrode with layered conductive hydrogels on a Pt electrode and embedded neural cells [61]**.**

In summary, composite hydrogel-OCP electrodes mimic biological tissue and therefore improve the interface between soft tissue and the hard electrode [60, 61]. Studies by Green et al. (2013), Lundin et al. (2011), Kim et al. (2010) and Spencer et al. (2018) have demonstrated that layering hydrogels on a conductive polymer can enhance the signal transmission, as well as increase the cell survival (**Table *1***) [50, 60,

61, 78]. Therefore, hydrogel – OCP composite electrodes will be of significant interest to enable softer, implantable electrodes in future.

Table 1: Comparison of hydrogel-OCP composite electrodes with their properties.

Gel-Electrode	Hydrogel	Modulus	OCP / Metal	Conductivity	Cell Studies
Hydrogel layer – OCP by Kim et al. (2010)	Alginate	~20 - 24 kPa [79, 80]	PEDOT	SNR = 4,17 detectable units: 50 %	Supports differentiation of encapsulated NSC [79]
Composite Hydrogel electrode by Bai et al. (2011)	Polyaniline hydrogel	~1.x10^4 Pa [81]	PEDOT	~1.7 kΩ	Supports NSC attachment [82]
Living electrode by Green et al. (2013)	poly(vinyl alcohol)	~1.4x10^6 Pa	Pt electrode + PEDOT	50 ± 8.71 mC/cm^2	High viability of P12 cells
Hydrogel Layer – OCP by Lundin et al. (2011)	Geltrex^{TM} BMM	-	PPy-DBSA	-	Enhanced NSC viability
Composite Hydrogel electrode by Spencer et al. (2018)	GelMA	~7.6 - 10.3 kPa	PEDOT:PSS	~281.2 kΩ - 261 kΩ	Supports viability and spreading of encapsulated C2C12 myoblasts

1.3 Electrical Stimulation of Hydrogels

Hydrogels have the ability to change volume and shape reversibly in response to external stimuli in environmental conditions (**Figure 7A**), such as changes of pH, temperature, ionic strength, solvent composition, and magnetic and electric fields. [83, 84]. Early studies on electrical stimulation of hydrogels by Kuhn, Kachalsky and co-workers (1950) found that electrical stimulation of water-swollen gels caused reversible swelling and contraction by successive addition of alkali and acid [85]. This effect due to the shape of polyacids and polybases depends on the number of charges distributed over the molecular chain. Charging the molecule induces

electrostatic repulsion along the coiled molecular chain and subsequently contributes to chain extension. To reverse this effect, a suitable addition of acid or neutral salt induces reversible contraction of the stretched chains [85]. Water-swollen gels are particularly sensitive to an electrical field, generating a large amount of mechanical energy (i.e. swelling and contraction) [86]. Electrically-induced bending of hydrogels is mainly studied for development of mechanical devices like valves, artificial limbs such as fingers or hands, also known as soft actuators. Other studies have focused on the de-swelling, which can affect the movement of solutes out of the gel, especially for drug release applications [87].

1.3.1 Electrically-Induced Bending of Hydrogels

The bending behaviour of gelatin under a non-contact electric field depends on the mobility of ions in solution. Under an electric field at pH $\approx$ 4, the gelatin becomes polyanionic above its isoelectric point and bends toward the cathode. This is mainly due to the osmotic pressure difference between the anode and cathode, which also occurs within the hydrogel and provides the driving force for bending the gel towards the anode electrode [83]. The rate of bending deformation under a non-contact electric field increases with increasing voltage [83, 84, 88]. Furthermore, the speed of gel contraction is dependent only on the amount of charge being transported through the gel. The latter was confirmed by Osada and Gong (1999) who positioned a poly(2-acrylamido-2-methyl-1-propanesulfonicacid) gel between a pair of planar electrodes with an applied DC voltage of 15 V for 10 h [89]. They observed that electrically-induced contraction of the gel was dominated by electrokinetic processes of hydrated ions and water. The process was also reversible and indicated that mechanical deformation of the gel can produce an electrical potential within a gel [89].

Several other studies have demonstrated actuation of hydrogels when electrically stimulated [83, 90, 91]. The electro-responsive behaviour of a 1.5 cm thick PAAm hydrogel showed bending could be induced when positioned between a pair of parallel aluminium plate electrodes with an applied electric field of 10 V for 2 min.

The gel actuation was explained by water electrolysis, causing a change in the local pH gradient [92]. Similar actuation was shown by Sun et al. (2001) with chitosan/poly (ethylene glycol) (CS/PEG) hydrogel fibers when different electric fields (10 – 20 V for 0 – 30 s) were applied between two parallel platinum plates [93]. The extent of actuation was dependent on the applied electric potential, as well as the concentration of the crosslinking agent during material preparation, the diameter of the specimen, and the pH and ionic strength of the aqueous medium [93].

1.3.2 Mechanisms of Hydrogel Bending

Mechanisms of electrically-induced mechanical actuation, attributed to a volume change or swelling behavior, of the hydrogel have been shown by Tanaka et al. (1979), and also by Shiga and Kurauchi (1990) (**Figure 7B**) [90]. The volume change was described as a phase transition mainly due to three forces; 1.) the negative pressure due to the polymer-polymer affinity, 2.) the rubber elasticity of the polymer network, and 3.) the counterion pressure acting on the gel [94, 95]. The counter ion pressure can be explained by Flory's theory of the osmotic pressure [96]. Osmotic pressure occurs when the ion concentration in the gel changes and mobile ions in the gel move toward their respective counter electrode within an electric field. With increasing time, the osmotic pressure increases and the gel swells and bends (**Figure 7A**, **iv**) [90]. Glazer et al. (2012) considered several gel actuation mechanisms such as coulombic mechanisms whereby the electrical field exerts a net force on mobile ions and charged groups of the polymer (**Figure 7A**, **iii**) [91]. A further mechanism is explained by electro-osmosis (**Figure 7A**, **iv**) whereby water transport associated with migration of the gel's counterions induces the gel to locally swell or contract. An electrochemical mechanism (**Figure 7A**, **v**) involves changes in the pH and lastly the dynamic depletion or enrichment mechanism involving the accumulation or depletion of ions on both sides of the gel at the solution interface is said to cause a shift in local ionic strength that induces bending (**Figure 7A**, **vi**) [91]. In summary it is clearly well-established that hydrogels can undergo significant changes in response to an electrical field. Therefore, it is reasonable to suggest that hydrogels

incorporated as part of electrode will be subject to significant effects and undergo changes in properties.

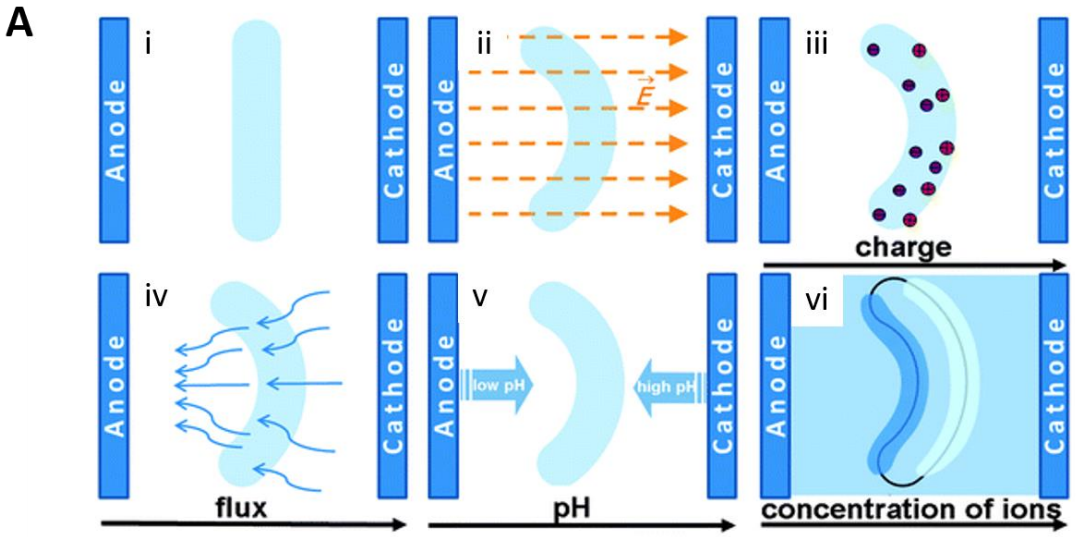

Figure 7: Principle of Gel Actuation during electrical stimulation. (**A**) Actuation principle of electroresponsive polyelectrolyte gel placed in salt solution before (i) and after (ii) electrical stimulation, (iii) coloumb mechanism, (iv) electro-osmosis mechanism, (v) electrochemical mechanism, and (vi) dynamic enrichment/depletion mechanism [91]. (**B**) Electrokinetic processes described by bending motion of an acrylak-acrylamide copolymer gel during electric field application (10 V/ cm) with 10 mm deflection of gel bending. The deflection of gel bending is expressed in terms of the distance between the two ends of a gel before and after bending. When a gel bends to the cathode side, the sign of the deflection is defined positive [90].

1.4 Neural Stem Cell Interactions with Hydrogels

In this thesis, we specifically focus on NSCs as the hydrogel-electrode is envisaged to have several neural-related applications. One possibility is an implantable electrode that interfaces with NSC in the implanted region to improve integration of the electrode. Furthermore, incorporating cells into the electrode prior to implantation, much like a 'living electrode' described in section 1.2.4, provides another approach to bridging the electrode – nerve interface. Finally, the use of NSC will be important for several *in-vitro* electrode applications such as multi electrode arrays, e.g. consisting of hydrogels coatings, or 'electronic' cell culture substrates for controlling stem cell interactions.

1.4.1 Neural Stem Cells

NSCs have the capacity to proliferate and differentiate into more than one neural cell type. They therefore produce progeny cells which terminally differentiate into neurons, astrocytes and oligodendrocytes [97].

NSCs reside in the human brain at two primary locations, including the walls of the lateral ventricles and hippocampal dentate gyrus, each consisting of a complex micro-milieu referred to as the stem cell niche (SCN) [98]. Through a series of well-orchestrated, homeostatic processes, involving cell-cell interactions, ECM interactions and soluble cues, the SCN maintains a supply of self-renewing and differentiated NSCs [99]. Upon injury or disease, a portion of cells are instructed to exit the niche, proliferate extensively and finally differentiate to regenerate tissue.

1.4.2 Importance of Neural Stem Cell Adhesion

As mentioned above, NSCs are subject to various physical contacts (e.g. cell-cell and cell-ECM) that are believed to be primarily responsible for SCN homeostasis, not necessarily soluble cues as first thought. This is emphasized in recent publications

titled "Holding tight onto the niche" and ''Adhesion molecules in the stem cell niche - more than just staying in shape" [100, 101]. For example, integrin α6β1 expression is low in quiescent NSCs but is increased following NSC activation. Disruption of integrin β1 results in proliferation, SCN disorganization and aberrant NSC migration, highlighting that niche adhesion controls the balance between homing and niche exit of NSCs [102]. Furthermore, SCN adhesion involving integrins directs the process of symmetric and asymmetric cell division whereby NSCs will either self-renew or generate a daughter cell committed to a specific lineage [103]. More recently, a major finding is that inhibitor of deoxyribonucleic acid (DNA) binding (Id) transcription factor also promoted integrin mediated adhesion to the SCN [104]. Importantly, this demonstrates that adhesion to the niche and intrinsic programs that instruct the SCN are not disparate but likely to be linked in a larger connected network [104]. Moreover, the interaction of stem cells with their surrounding microenvironment is fundamental to multiple processes such as cell migration, proliferation, lineage specificity, and tissue morphogenesis [105].

Consequently, the picture emerging is that bioengineering a material that temporally elicits effects on cell adhesion to homeostatically maintain the NSC population, whilst still permitting the response to endogenous cues (e.g. soluble cytokines and growth factors) is an optimal strategy. Here, the properties of a biomaterial play a crucial role. For example, the substrate stiffness combined with cell adhesion ligands is an essential property by which cells recognize and sense the external forces, and respond to the environment via mechanotransduction [106, 107]. For this reason, hydrogels of different stiffness have commonly been used to control NSC differentiation or migration [79, 108]. These cell interactions with materials are designed by virtue of stem cell adhesion in their niche, as the latter provides a basis for engineering biomaterials and surfaces to control stem cell function.

1.4.3 Effect of Hydrogel Properties on Neural Stem Cells

A detailed review on designing cell-compatible hydrogels for biomedical applications has been provided by Seliktar et al. (2012), emphasizing the need for understanding hydrogel-stem cell interactions and the role of various sub-cellular and material properties, such as those shown in **Figure 8** [109]. From the review, several studies have shown the effect of hydrogels properties, such as stiffness, porosity and crosslinking effects, on stem cell interactions for both encapsulated cells and seeded cells on hydrogels.

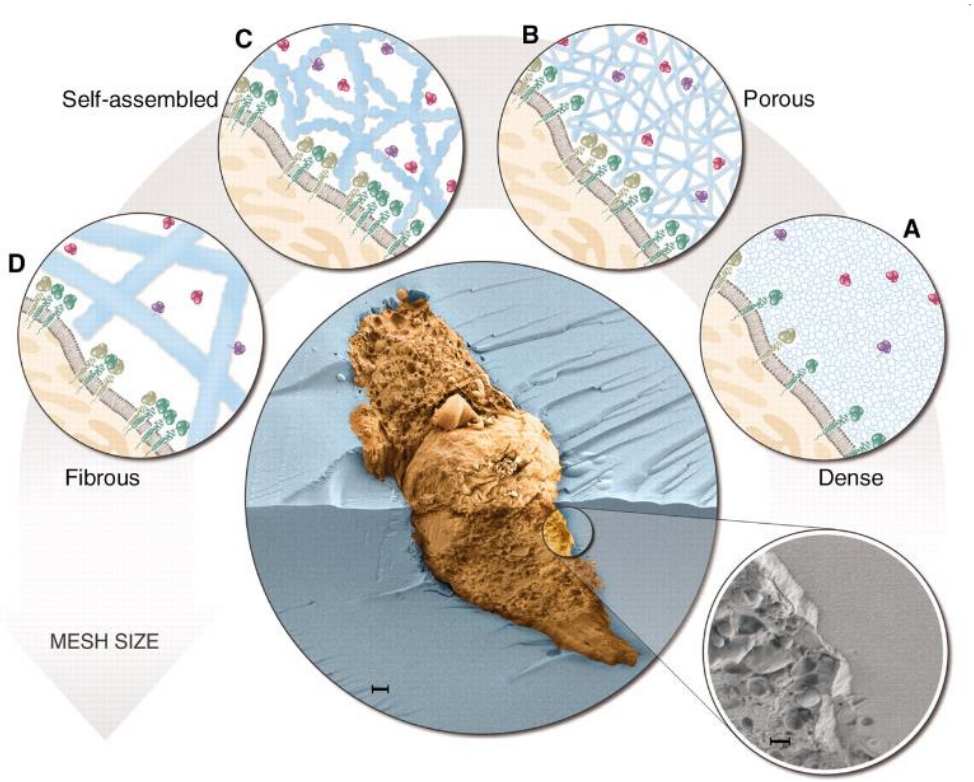

Figure 8: Interface between cell and hydrogel. A SEM image showing an encapsulated cell in a fully hydrated hydrogel (scale bar = 300 nm). A to D present the cell membrane-hydrogel interfaces in different types of hydrogel structures and properties. Those properties can influence the receptor-ligand interactions differently. For example, porous structures support receptor-ligand clustering, whereas in the dense hydrogel these interactions are far less favoured. Cell receptors (green) lie on the cell membrane (grey), whereas bioactive molecules (red) and tethered bioactive factors (purple) lie within the hydrogel mesh [109].

In work related to NSCs, alginate hydrogels with encapsulated cells showed increased proliferation into neurons when the modulus decreased from 19.7 kPa down to 183 Pa [110]. Seidlits et al. (2010) showed that ventral midbrain-derived NPCs photoencapsulated into HA hydrogels remained viable [108]. When the hydrogel had mechanical properties (1.5 ± 0.003 kPa) comparable to those of neonatal brain, the majority of NPCs had differentiated into neurons (ß-III tubulin-positive), many of which had extended long, branched processes, indicative of a relatively mature phenotype occurring after three weeks. In contrast, NPCs within stiffer HA hydrogels (2.6 ± 0.02 kPa), comparable to mechanical properties of adult brain had differentiated into mostly astrocytes (glial fibrillary acidic protein (GFAP)-positive), indicating that NPCs feel the rigidity of their environment, which influences their differentiation [108]. Early work by Banerjee et al. (2009) showed that NSCs encapsulated in 3D alginate hydrogel scaffolds had a decreased rate of proliferation with increasing hydrogel modulus [79]. Modulus dependence of cell differentiation when adult NSCs were seeded on acrylamide hydrogels has been demonstrated by Saha et al. (2008) [111]. In this case, differentiation of the adult NSCs showed neuronal lineages on softer gels (100 – 500 Pa) whereas on stiffer gels (1,000 – 10,000 Pa) glial cell differentiation was promoted [111]. More recently, Gu et al. (2016) biofabricated 3D neural mini-tissue constructs by microextrusion printing of frontal cortical hNSCs within a supporting bioink made of alginate, agarose and carboxymethyl-chitosan, demonstrating in situ differentiation to functional neurons and supporting neuroglia [112]. The same authors (2017) further incorporated human induced pluripotent stem cells (iPSCs) in the same bioink and were able to induce cell differentiation toward multiple lineages [113].

1.4.4 *In Vivo* Studies using Hydrogels

Beyond the above *in vitro* studies where cells are typically grown on gel substrates or encapsulated within the hydrogel, researchers have pursued *in vivo* applications using NSCs combined with hydrogels, with promising results on controlling the spatial and temporal progression of regenerative processes initiated by NSC transplantation.

For example, Park et al. (2000) used Polyglycolic acid (PGA), a degradable hydrogel, as a scaffold in the transplantation of the neural stem – like cell, C17.2, into an infarction cavity formed by the ligation of the carotid artery, promoting neuronal differentiation, enhancing the elaboration of neural processes, fostering the re-formation of cortical tissue, and promoting connectivity [114]. Alginate hydrogel fibers have been seeded with adult spinal cord NSCs and implanted into spinal cord lesions of adult female Fischer 344 rats, resulting in NSCs elongating along the alginate fibers [115]. Cheng et al. (2013) have shown that RADA16 (AcN-RADARADARADARADA-CONH2) and RADA16-IKVAV (AcN-RADARADARADARADAIKVAV-CONH2) SAP self-assembling peptide hydrogels can support transplanted NSC survival, growth and distribution in the rat brain [116]. Further studies have examined the survival and efficacy of adult brain-derived neural stem/progenitor cells (NSPCs) injected within a hydrogel blend of hyaluronan and methyl cellulose (HAMC) [117]. The hydrogel was modified with recombinant rat platelet-derived growth factor-A (rPDGF-A) to promote oligodendrocytic differentiation into a subacute, a clinically relevant model of rat SCI. It was shown that rats with NSPC/HAMC-rPDGF-A transplants had a significant reduction in cavitation, improved graft survival and increased oligodendrocytic differentiation [117].

1.4.5 Electrical Stimulation of Stem Cells on Hydrogel Substrates

There have also been studies investigating the effect of electrical stimulation on stem cell viability, proliferation and differentiation, interestingly where a hydrogel was used as the culture substrate. To date, few such studies have been done on NSCs though more so collectively on a number of other stem cell types. For example, conductive PEG/CS hydrogels showed that exposure to a continuous electric field over five days promoted hMSC proliferation, survival, chondrogenesis and differentiation [118]. Sun et al. (2006) applied a non-invasive electrical field of 7 V/cm

for 30 min to regulate cell adhesion and orientation of bone marrow-derived rat mesenchymal stem cells (MSCs) and fibroblasts in a reconstituted 3D collagen-based scaffold [119]. Rat MSCs showed slight reorientation whereas fibroblasts reoriented perpendicular to the electric field [119]. Further studies by Xu et al. (2016) described a conductive high-strength PANI Coated-P(VDT-VI) hydrogel that supported the attachment and proliferation of NSCs and efficiently induced neuronal differentiation by weak electrical stimulation consisting of a 75 mV DC bias for 7 days, as shown in **Figure 9** [82]. In addition, the external field induced adhesion, proliferation and differentiation of NSCs into neurons [82]. Applying a reduction potential of -0.9 V for two minutes on a PPy-DBSA film coated with a gel layer composed of a reduced growth factor basement membrane matrix (Geltrex^{TM}) revealed that viability of NSCs was maintained, whereas the bare PPy-DBSA film showed loss of survival for NSCs during the reduction process [50].

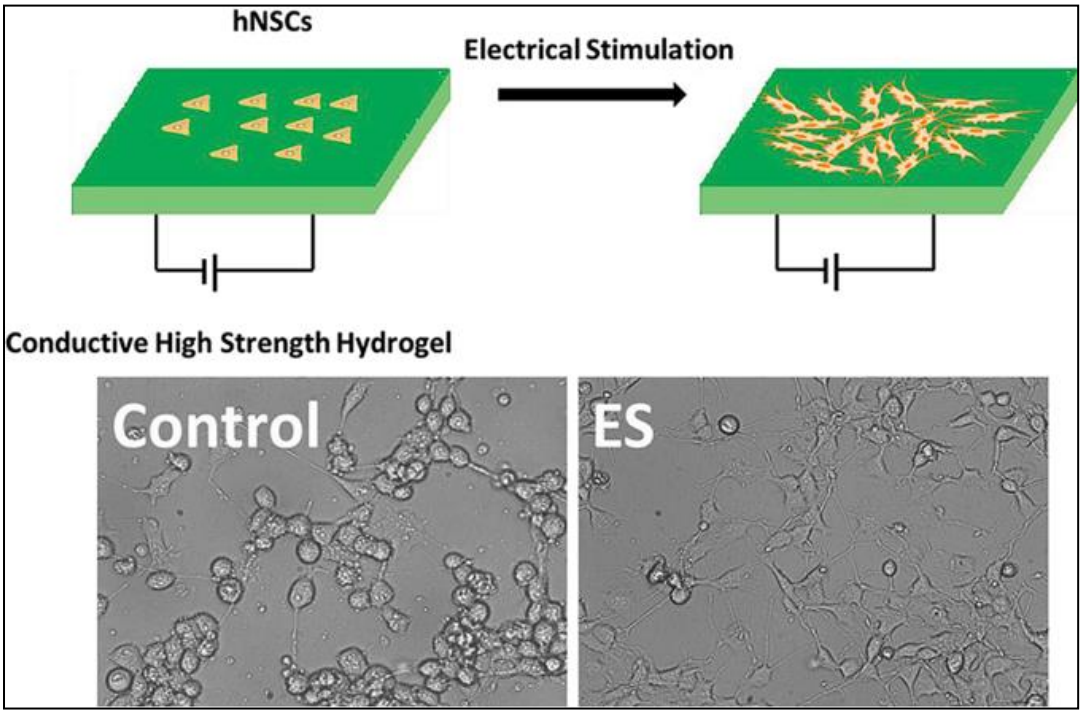

Figure 9: NSCs seeded on high-strength hydrogel. Weak electrical stimulation (75 mV for 7 days) of NSCs proliferates and induces neuronal differentiation [82].

1.4.6 Gelatin Methacrylate Hydrogels

Synthesis and Properties

In the present project, the experimental work was undertaken using GelMA, a photopolymerizable hydrogel composed of modified natural ECM components such as arginine-glycine-aspartic acid (RGD) proteins [120] (**Figure 10A**). GelMA is composed of multiple methacrylic groups on a gelatin molecule, making it light polymerizable via a radical [121, 122] (**Figure 10B**). The modification of gelatin with photocrosslinkable methacrylamide groups creates a hydrogel that maintains the unique property of gelatin and endows a stable hydrogel at higher temperatures [123]. This makes it an attractive material for biomedical applications in tissue engineering and several studies have successfully demonstrated tissue engineering scaffolds formed using GelMA [121, 124-126]. Compared to other polymerization techniques (e.g. thermal), photocrosslinking provides a number of advantages like rapid cure reaction, low energy requirements, use of room temperature, and low costs [127]. To crosslink GelMA hydrogels, one has to generate free radicals to induce a free radical chain polymerization of monomers through the absorption of light by the photoinitiator [128, 129]. The efficiency of the polymerization reaction is dependent on the monomers, photoinitiator and beam wavelength [128].

1.4.7 Photoinitiators

There are two basics types of photoinitiators [130]: Type I photoinitiators undergo a direct photo-fragmentation process based on absorption of light and formation of initiating radicals capable of inducing polymerization. Type II photoinitiators require the presence of molecules in the system. These molecules suffer a primary process of hydrogen abstraction and are often referred to as co-initiators. For biomedical applications, the biocompatibility of the photoinitiator is a critical issue of concern. Williams (2005) and co-workers have shown that different cell types react differently to the same concentration of the same photoinitiator. They also demonstrated that the photoinitiator 2-hydroxy-1-[4-(hydroxyethoxy)phenyl]-2-methyl-1-propanone (Irgacure 2959) was well-tolerated by many cell types [131]. Irgacure 2959 is

commonly used for crosslinking GelMA and was the photoinitiator used in this thesis. The mechanical properties of GelMA can be controlled by varying the methacrylamide degree [121, 132], GelMA concentration [121, 126, 132], curing time [133, 134], photoinitiator concentration [135], and intensity of the UV light [134].

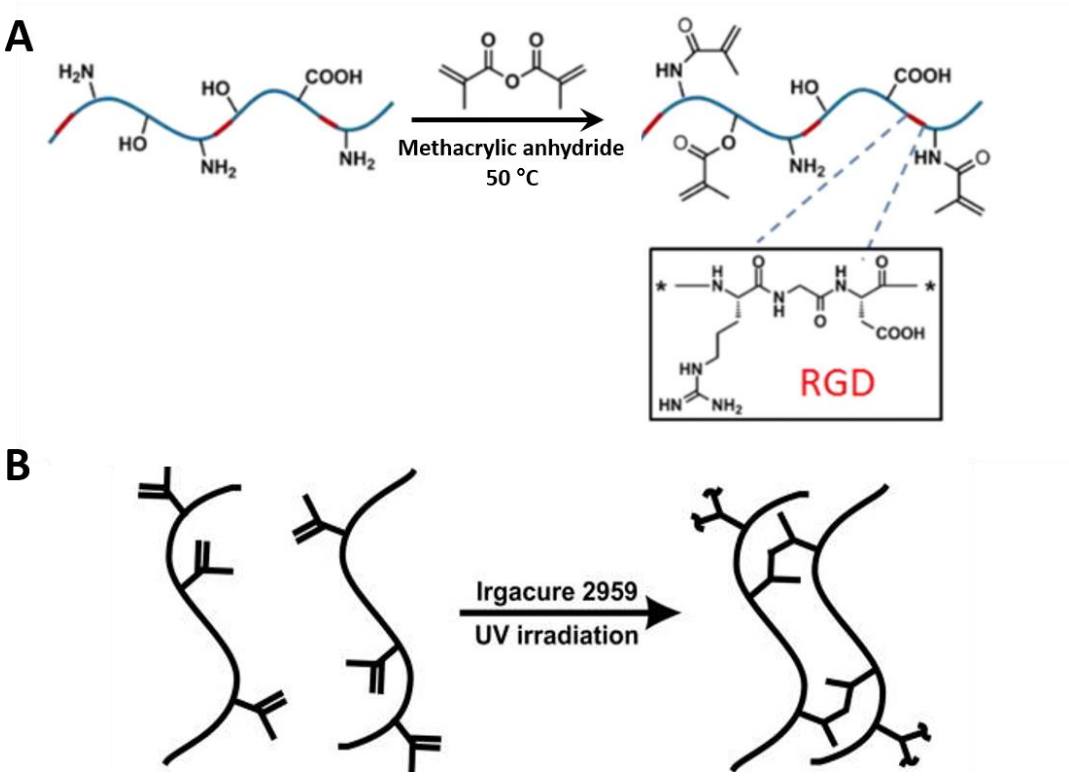

Figure 10: Synthesis of GelMA. (**A**) Primary amino groups located in gelatin macromeres reacting with methacrylic anhydride to add methacrylate pendant groups. The RGD domains are illustrated as red segments along the GelMA chains, and their chemical structure is depicted within the inset [136]. (**B**) GelMA is crosslinked with UV irradiation in the presence of a photoinitiator to create a hydrogel network [121].

1.4.8 Cell Studies using GelMA Hydrogels

Increasing GelMA modulus has been shown to correlate with a significant increase in attachment and proliferation of immortalized human keratinocyte (HaCaT) cells [123]. In the same study, human umbilical vein endothelial cell (HUVEC) density and

confluence showed an increase on the same GelMA samples [121]. Patterning of cell-laden 5% GelMA hydrogels induced the alignment and elongation on HUVEC, C2C12 and cardiac side population (CSP) cells [137]. Micropatterned GelMA scaffolds seeded with human avascular zone meniscus cells showed non-toxicity, produced organized cellular alignment and promoted meniscus-like tissue formation [138]. Benton et al. (2009) showed GelMA hydrogels possessed unique properties such as pore size and modulus that promote aortic valvular interstitial cell survival and differentiation in 3D [139]. Nikkhah et al. (2012) demonstrated a dependence of endothelial cells proliferation, alignment and cord formation on geometrical dimensions of patterned GelMA constructs [140]. Studies on GelMA composites comprising nanomaterials have also emerged. For example, Cha et al. (2013) described a graphene oxide – GelMA hydrogel, which supported viability and proliferation of encapsulated fibroblasts [141]. Jaiswal et al. (2016) investigated mechanically stiff nanocomposite hydrogels made from PEG-dopamine-MNPs with GelMA [142]. The modulus of the nanoengineered hydrogel was tailored between 0.2 and 200 kPa by manipulating the size of the nanoparticles. They showed that human MSCs encapsulated within the GelMA hydrogel (~3.2 kPa) showed circular morphology, however, human MSCs became more elongated and spread out with an increase in modulus due to presence of the nanoparticles (~7.8 kPa and ~26.7 kPa, respectively) (**Figure 11**) [142]. Lastly, GelMA-based hydrogels were used as a semi-synthetic 3D platform for spheroid growth of ovarian cancer cells *in vitro* and *in vivo*. The study shows that in medium stiff hydrogels (3.7 ± 0.5 kPa) round-shaped spheroids of distinctive size were formed, resembling those present in the tumor fluid (ascites) within the abdominal cavity of patients with this disease. Therefore, GelMA represented an alternative reproducible matrix, closer to nature's 3D structure, to improve our understanding of disease progression on a cellular level [143].

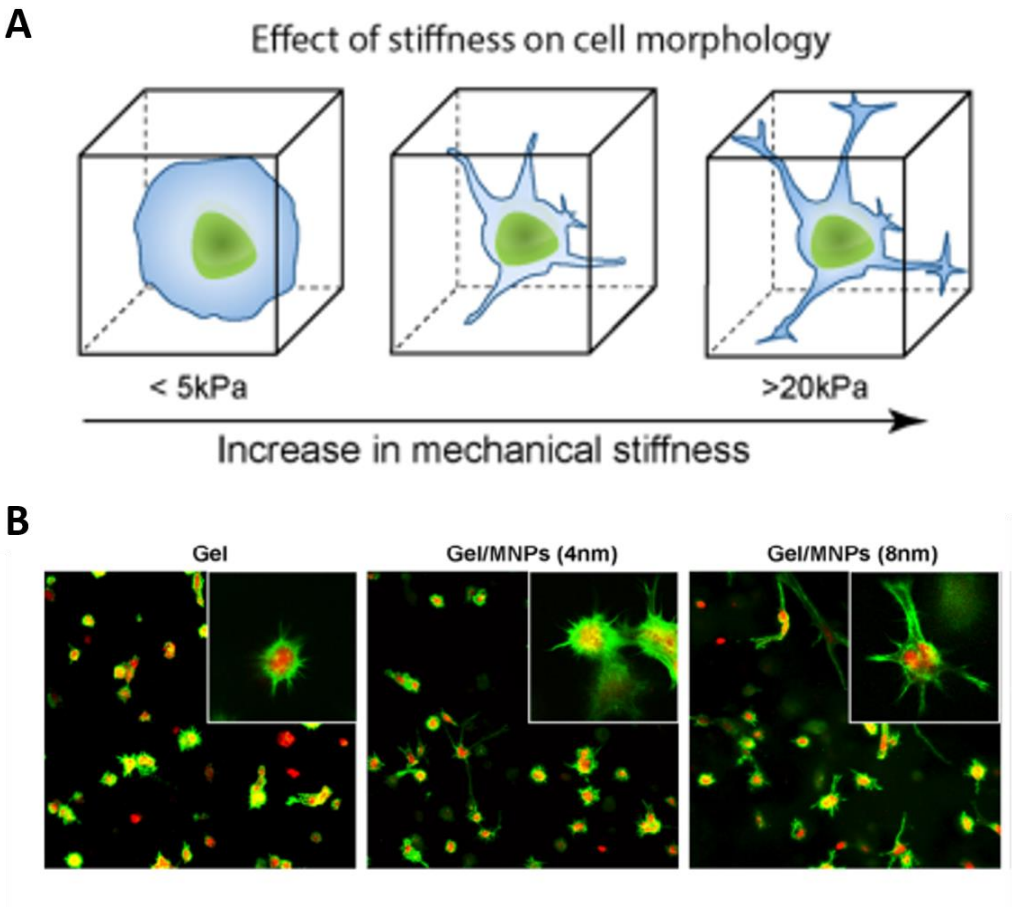

Figure 11: Effect of stiffness on cell morphology. The addition of nanoparticles results in significant increase in mechanical stiffness of hydrogel matrix and it is expected to influence cell morphology. (**B**) Morphology behavior of encapsulated hMSC in GelMA hydrogel (left) and nanocomposite GelMA hydrogel (middle and right) with different nanoparticles size (nm). In soft GelMA hydrogel (~3.2 kPa) encapsulated hMSCs showed circular morphology and encapsulated in stiffer GelMA nanocomposite hydrogels (~7.8 kPa and ~26.7 kPa) hMSCs became more elongated and spread out [142].

1.5 Significance of this Thesis

The advantage of hNSCs is their capacity for self – renewal and ability to differentiate in neurons under the control of stimuli such as mechanical and electrical stimulation. However, the cells need to be surrounded with an environment similar to the ECM stem cell niche to enable cell signalling and communication [144]. That said, the

complex ECM is not well understood making it difficult to fully mimic this environment for the design of effective biomaterials and scaffolds, or to implement cell-based therapies. In particular, the molecular structure and chemistry of the ECM offers a very complex construct consisting of many different factors that are necessary for instructing cell migration, proliferation and differentiation. The cell interactions occur at the nano-(molecular) scale. Therefore, an understanding at this scale is very important. Cells communicate and interact extracellularly via adhesion, involving the formation of adhesive bonds, e.g. slip and catch bonds [145, 146], and tensile forces between cells and other ECM components. The latter is critical for transmitting the instructions of the SCN and part of the cell signalling mechanism termed mechanotransduction [106].

It is evident from the above literature that mechanical properties of hydrogels are important for controlling stem cell growth and differentiation, such as softer gels that "push" the cell lineage toward neural type cells [111, 147]. What is less well-known is the role of the nanoscale components, i.e. single polymer chains, and their properties that may not be adequately described by bulk properties. For instance, the bulk properties are effectively governed by molecular properties such as density of crosslinking groups on chains, viscoelasticity of individual chains and Van der Waals interactions between chains; subsequently single chains become an important entity. Within the hydrogel network, single polymer chains are also expected to participate in physical interactions and binding of cell adhesion molecules occurring on equivalent length scales. That said, there is a paucity of information on the dynamic, physical interactions and forces at the nanoscale level such as integrin receptor binding to peptide groups, e.g. RGD, along the hydrogel polymer chains, as given in **Figure 10A**. It is these molecular forces that the cell "experiences" that are the extracellular 'controls' that determine outside-to-inside signalling via mechanotransduction. Questions to be answered include, what are the unbinding forces between the cell receptors and single polymer chains of a hydrogel and how does the single polymer chain properties such as elasticity and crosslinking affect the interaction forces? At present, studies in the biomaterial field typically make correlations between bulk material properties and the differentiation of stem cells

grown on those materials in cell culture. The desire to control cell differentiation has resulted in using optical or molecular biology techniques to determine expression of cell markers. These approaches are often referred to as studies of “Cell-Material Interactions”, though the actual interactions between cell and hydrogel, or biomaterials in general, are rarely known.

The most common way to investigate the physical interactions and adhesion forces at the cell - material interface is by using aspiration, centrifugation, fluid flow, and enzymatic procedures to probe the detachment of cell populations. The strength of the cell de-adhesion of a cell to a substrate has commonly been studied using simple washing assays [148]. Cells are washed from a surface by running a solute, such as culture medium, over them. The strength of adhesion is quantified by the ratio of the number of bound cells to the number of cells that were originally present on the surface. Different assays based on the regulated flow of media have been implemented to quantify the strength of cell adhesion, including spinning disk [149] and flow chamber assays [150]. However, all of the described assays lack information on the cell de-adhesion at the molecular level. They are also limited in quantifying the shear force, which is strongly influenced by the cell size and shape, and usually can only be applied just once (i.e. once the cell is detached, the experiments end with not possible repeat measurements). Finally, these assays generally only provide pseudo quantitative data [151].

Lastly, the development of conductive hydrogel electrodes is expected to rapidly increase in the future. In applications specific to bionics and neural prosthetics, the ability to improve the cell adhesion or integration with the electrode will remain a priority and require knowledge of interactions at the cell – hydrogel interface. In particular, the idea of a ‘living electrode’, involving the incorporation of living cells in the hydrogel, will greatly depend on understanding fundamental cell interactions with hydrogels. In addition to these applications, we emphasize that such conductive hydrogel electrodes will become more broadly important for a range of applications such as advanced culture substrates, microelectrode arrays and 3D tissue models,

where the hydrogel will be critical for interfacing the cells or tissues. As a focus of this thesis, electrical stimulation will play a role in these applications and be of significant interest for controlling the cell interactions. The combined effects on electrical stimulation and hydrogel properties are not known, but clearly hydrogel properties can be modified via electrical fields which we propose could be an interesting strategy for controlling cell interactions

Therefore, the thesis aims to:

1. Investigate the effect of electrical stimulation on the nanomechanical properties (such as Young's modulus and actuation) of GelMA, using in-situ Electrochemical-AFM (EC-AFM).

2. Elucidate the dynamic and physical, molecular-level forces and interactions between hNSCs and GelMA as a function of hydrogel properties using the AFM-based technique, Single Cell Force Spectroscopy (SCFS).

3. Elucidate the combined effect of GelMA modulus and electrical stimulation on the single hNSC de-adhesion using SCFS combined with in-situ EC-AFM.

To gain insight at the molecular level, the thesis focuses on single cell interactions, particularly quantifying the de-adhesion forces, including those at the molecular level. Several single cell characterization techniques are suitable for this approach such as Micropipette Aspiration [152], Optical Tweezers [153] and the AFM-based approach, SCFS [154]. In this thesis, we employ the latter SCFS and provide an introduction to this approach in the following Chapter 2.

Chapter 2:

Atomic Force Microscopy for Studying Cell – Material Interactions

2.1 Atomic Force Microscopy

2.1.1 Operating Principles

Atomic Force Microscopy (AFM) is part of the broad family of Scanning Probe Microscopy (SPM) [155] invented by Binning and Rohrer in the early eighties for which they received the Nobel Prize for Physics in 1986 [156]. AFM enables high-resolution, nanoscale imaging of native samples in physiological-like conditions such as liquid [157, 158]. The range of biological samples imaged by AFM include the smallest biomolecules such as single proteins, DNA, RNA and subcellular structures (e.g. membranes) through to living cells and tissues [155]. It also opens up the possibility of viewing dynamic processes to gain insights into conformational changes and molecular interactions in real time [159]. In addition to imaging, AFM uniquely is a tool that combines imaging with the ability to quantify intermolecular forces between a probe and a sample [160], which is described further below under 'force spectroscopy'.

The AFM set-up is usually compromised of six main elements; photodetector, laser diode, piezoelectric scanner, cantilever, controller and the feedback loop (**Figure 12**). The AFM uses a flexible cantilever mounted with a sharp tip, which touches the surface of the sample, and a piezoelectric actuator controls the x-y-z position of the cantilever relative the surface (**Figure 12**). A laser beam that is focused on the back of the cantilever monitors the vertical deflection of the cantilever, as it interacts with the surface. The principle of the AFM is to scan the tip over the surface with a constant force by using a feedback mechanism. During the scan, the tip deflects as it encounters changes in the surface topography. The changes in the

cantilever deflection are recorded as changes in the position of the laser as it is reflected into a photodiode detector, thus recording changes in voltage. A feedback loop adjusts the z-position of the piezoelectric scanner to maintain the photodiode voltage at a constant value or setpoint voltage, enabling scanning of the tip with constant force. In doing so, changes in the z-position of the piezoelectric scanner correspond to changes in the sample height. Thus X, Y and Z information is obtained, which represents the three-dimensional topography of the sample surface.

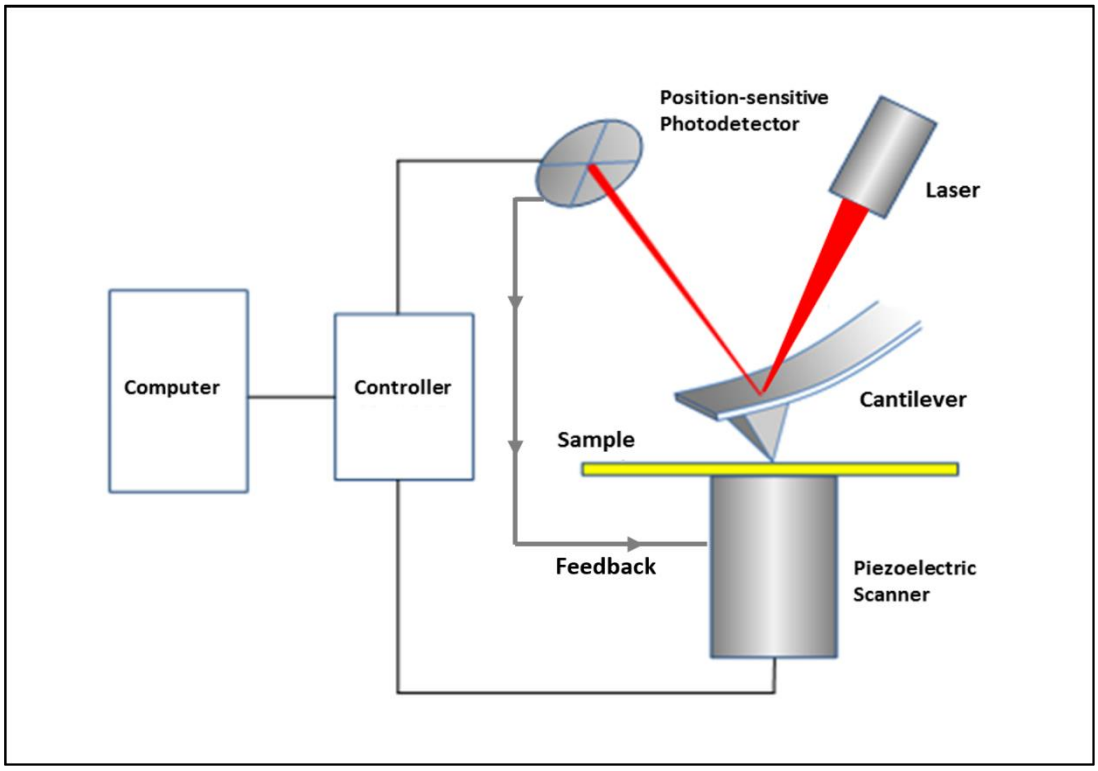

Figure 12: Schematic of AFM operation.

2.1.2 Cantilever

The cantilever with a sharp tip is fabricated using batch chemical etching. The tip is the main tool for imaging the sample surface and commonly available as a conical (**Figure 13B**) or pyramidal shape (**Figure 13C**). Tips can be made of different materials like diamond synthetic, or silicon, depending on the type of measurement that is

required. For example, in conductive AFM, the tip may be coated with Titanium Alloy or Gold. As an alternative to silicon, cantilever tips are commonly fabricated from silicon nitride due to its greater strength and resistance to wear. A plethora of cantilevers fabricated with different geometries can be purchased commercially. Generally, they have either a "diving board" design or V-shape with varying plan view dimensions such as length, width and thickness (**Figure 13A**) that determine their stiffness or spring constant value. The spring constant is one of the most important parameters of the cantilever, as it dictates the force applied by the tip to the sample. Usually the spring constant varies between a very soft cantilever of < 0.1 N/m to typically the stiffest cantilevers of ~ 40 N/m. Soft cantilevers are used for soft samples like hydrogels or operation in fluid, as the stiffer cantilevers are likely to cause damage due to their high lateral and deformation forces.

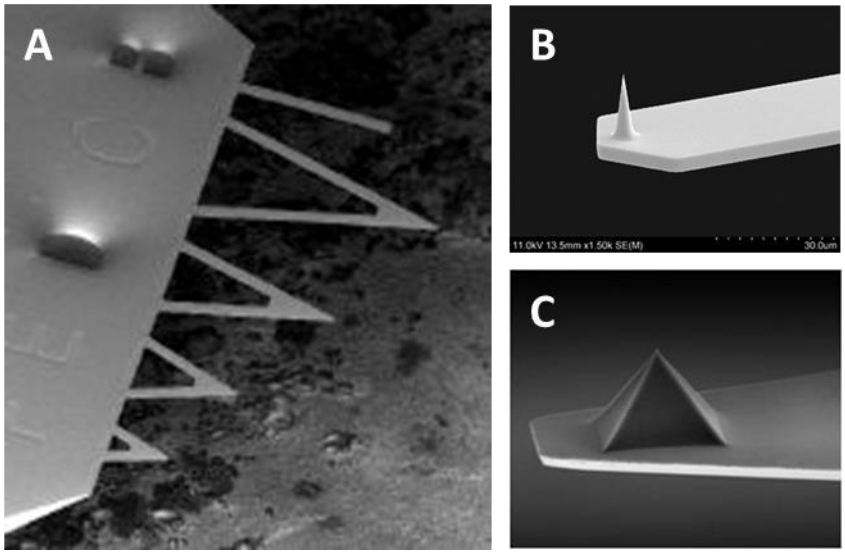

Figure 13: SEM images of AFM tip and cantilever geometries. (**A**) V-shaped and diving board cantilever geometries [adapted from https://www.brukerafmprobes.com]. (**B**) Conical tip [adapted from https://store.nanoscience.com]. (**C**) pyramidal tip [adapted from http://www.nanoworld.com].

2.2 Force Spectroscopy

2.2.1 Force-Distance Curve

In contrast to AFM imaging, where the cantilever tip scans across the sample surface in XY directions, force measurements involve the movement of the cantilever tip in the Z direction at fixed XY position on the sample. During the measurement, the force acting on the tip is recorded as function of the distance, giving a force-distance (F-D) curve. The F-D curve is comprised of several main regions (**Figure 14**), which demonstrate the general types of tip-sample interactions. Firstly, the cantilever tip approaches the sample surface and no deflection of the cantilever is recorded because there is no tip sample interaction (**Figure 14(i)**). At point (ii) the cantilever tip continues approaching (red curve) and can detect fundamental forces such as electrostatic and Van der Waals forces, causing deflection of the cantilever, prior to making contact with the sample surface. When the tip makes contact with the sample surface it continues pushing into the surface, causing an upward deflection of the cantilever (**Figure 14(iii)**). This region of the curve (linear slope in contact region) can provide information on the mechanical properties of a sample (see section 2.2.3). Once the cantilever deflection has reached a pre-defined setpoint, the cantilever tip is retracted from the surface (blue curve) and an opposite downward de-flection of the cantilever is recorded. If de-adhesion occurs between the tip and sample surface, the cantilever deflection will continue to decrease below the zero baseline (**Figure 14(iv)**) until the tip 'pulls-off' from the surface (**Figure 14(v)**), giving a quantitative measure of the de-adhesion force. The deflection then returns to the zero baseline and the cantilever is retracted from the surface (**Figure 14(vi)**).

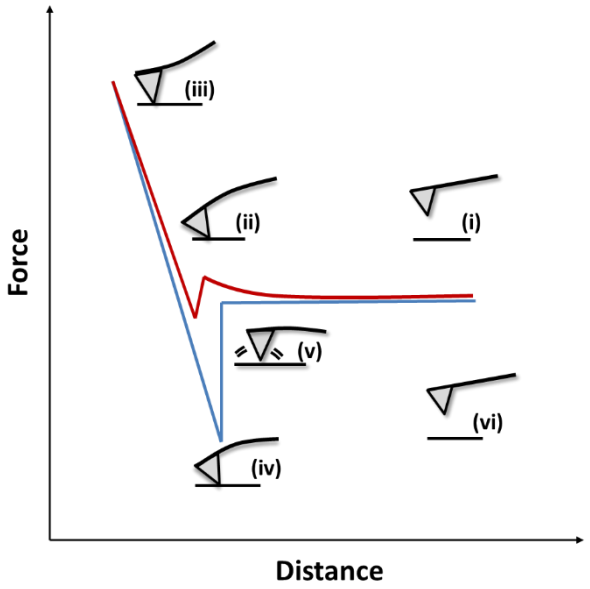

Figure 14: Cantilever deflection/force vs. tip-sample separation. Approaching curve is red, retraction curve is blue. Force spectroscopy (FS) enables a direct measurement of the tip-surface interaction forces such as physicochemical and biological forces in air or in liquid [161].

2.2.2 Sensitivity and Cantilever Calibration

To accurately quantify the force, the cantilever needs to be calibrated prior to each experiment. For example, the manufacturer normally provides a nominal spring constant value for each cantilever. However, due to variation in cantilever fabrication across a wafer, the cantilever thickness may vary and cause significant discrepancy between the nominal value provided by the manufacturer and the actual spring constant. In addition to knowing the spring constant, the other important step in measuring the force is conversion of the cantilever deflection (measured in volts by the photodiode) into a deflection (typically given in nanometers) (**Figure 15A**). To perform this conversion, an F-D curve is measured on an infinitely hard surface, e.g. glass slide, and in the contact region the amount of cantilever deflection in volts is proportional to the distance travelled by the z-piezo scanner (i.e. height of the cantilever tip) in nanometers (**Figure 15A**). Therefore, the inverse of the slope is given as units of nm/V and can be used to convert the deflection voltage into a distance (**Figure 15B**). The inverse slope, also referred to as the sensitivity value, is typically

dependent on the type of cantilever and laser position on the cantilever, as well as other variations in the experimental setup, e.g. position of the cantilever in the holder. Hence, the sensitivity value must be measured before each experiment.

The next step is to convert the cantilever deflection from nanometers (**Figure 15C**) into a force (typically in nanonewtons), which requires knowing the spring constant of the cantilever [162]. Two methods commonly implemented on commercial AFM systems include the thermal method [161] and Sader method [163]. It is recommended that more than one method is used to verify the spring constant value. For the thermal method, the cantilever fluctuates in response to thermal noise, effectively acting as a harmonic oscillator [164]. Therefore, the thermal spectrum of the cantilever deflection is measured to isolate the thermal oscillations from ambient noise. The area below the resonant frequency peak is a measure of the power spectrum *P* of the cantilever thermal fluctuations. Consequently, the spring constant *k* can be calculated from

$$k = \frac{k_B T}{P} \tag{1}$$

where k_B is the Boltzman constant, *T* is the absolute temperature [164]. This method is now implemented on most commercially available AFM's and a more detailed description is given in the original work by Hutter and Bechhoefer [164].

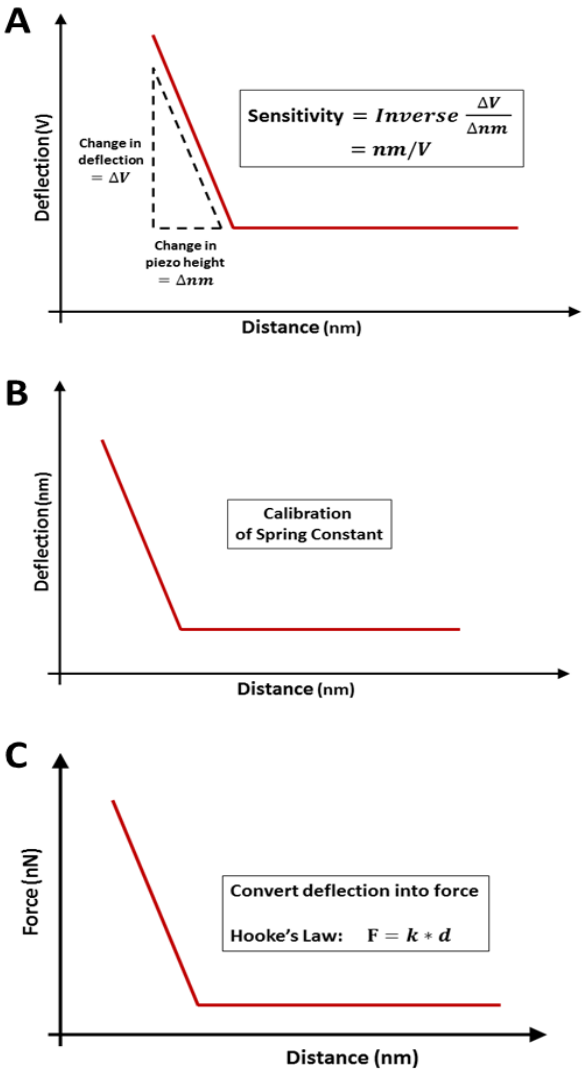

Figure 15: Cantilever calibration. Flow chart of converting the deflection signal (V) of the cantilever into force (nN).

The Sader method calculates the spring constant using the geometry of the cantilever and unloaded resonant frequency and quality factor, where for a rectangular cantilever the spring constant is given by:

$$k = 0.1906 p_f w^2 L Q_f \Gamma_i'(\omega_f) \omega_o^2 \quad (2)$$

where w and L are width and length of the cantilever, p_f is the density of the fluid, Q is the quality factor of the fluid, ω_o^2 is the resonant frequenzy, and Γ_i' is the

imaginary component of the hydrodynamic function $\Gamma'(\omega)$ as a function of the Reynolds number

$$Re = p_f \omega_o w^2/(4_\eta) \quad (3)$$

where η is the viscosity of the surrounding fluid. Once both the sensitivity and the spring constant k is known, the force *F* can be calculated using simple Hooke's law

$$F = k * d \quad (4)$$

where d is the deflection of the cantilever. The data can be converted into a true F-D curve, as shown in Figure. 14C. Further detailed reviews on F-D curves and cantilever calibration is provided by Butt et al. [165].

2.2.3 Nanomechanical Measurements using AFM

The Young's modulus of a material can be quantified by undertaking force measurements whereby the cantilever tip deforms the sample under a given force. For soft materials, the F-D curve gives a non-linear increase in force in the tip-sample contact region. In contrast, hard materials give a linear increase in force. For example, **Figure 16** shows an F-D curve on a stiff sample (blue curve) (e.g. glass slide) compared to a soft sample (red curve) (e.g. hydrogel). For both samples, the tip approaches (1) until it makes initial contact with the sample surface (2). However, the soft sample is deformed as the z-scanner (tip position) is lowered further toward the sample (3). For the same amount of cantilever deflection (or same applied force), the distance moved by the z-scanner is greater on the soft sample compared to the stiff sample, indicating that the former undergoes deformation. In the contact region, the difference in the z-scanner distance between the hard and soft samples at each force value give a measurement of indentation. Force versus indentation curves can then

be obtained and analyzed using mechanical models, which are described below to determine the Young's modulus (see **Figure 19**).

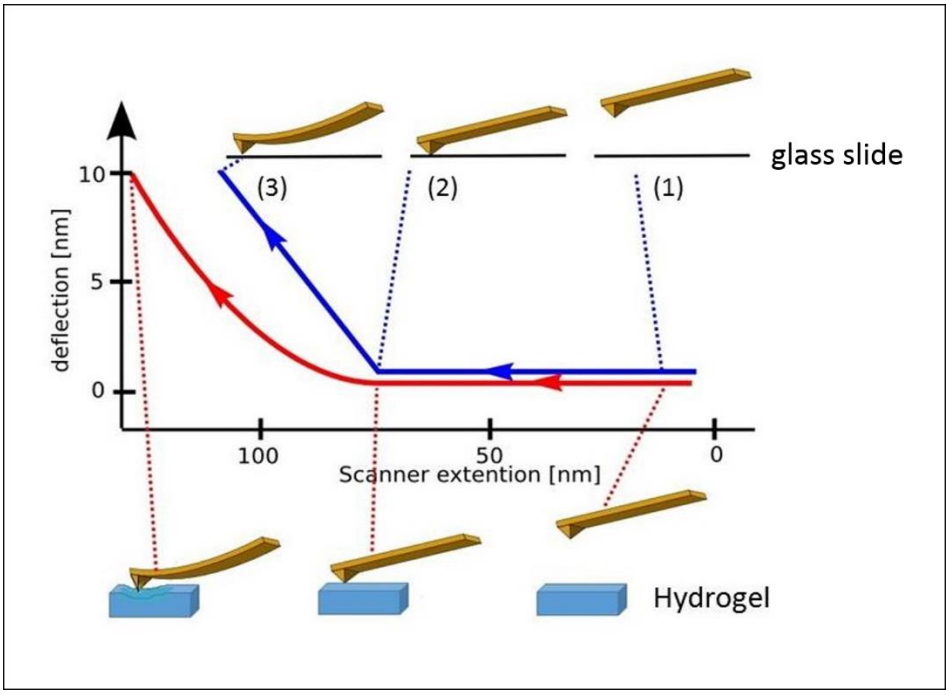

Figure 16: F-D curves on hard (blue) and soft (red) sample surfaces. Both curves are approaching the surface. The difference in the scanner extension between the curves (arrow) at each force value can be used to calculate the amount of indentation.

2.2.4 Analysis of Mechanical Properties (Young's modulus)

Several models can be applied to force versus indentation data to calculate the Young's modulus. The most common models are the Hertz, Johnson, Kendall, Roberts (JKR), and the Derjaguin, Muller and Toporov (DMT) models, assuming a spherical shape of the indenter (**Figure 17**). Geometrical effects on local elastic deformation have been considered by Hertzian theory [166, 167]. The theory describes the relationship between the interaction of a sphere and plane surface, or between two spheres, to the elastic deformation properties of the material. This theory does not consider any surface contact such as Van der Waals interactions or adhesive contacts. As an extension to the Hertzian theory, the JKR theory was provided in 1970 and also

considers the sample adhesion inside the contact area. Due to the restricted elastic sphere-sphere contacts for the Herztian and JKR theory, the DMT theory involves Van der Waals interactions outside the elastic contact regime. The theory simplifies to Bradley's Van der Waals model if the surfaces are separated at significant distances apart.

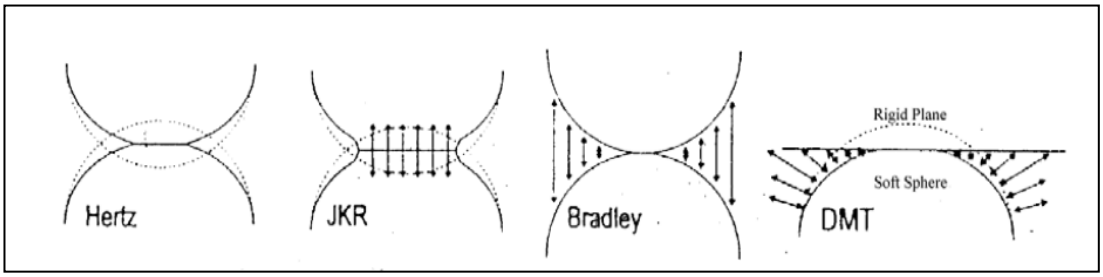

Figure 17: Variation of elastic contact models. Hertz: fully elastic model; JKR: fully elastic model considering de-adhesion in the contact zone; Bradley: purely Van der Waals model with rigid spheres; DMT: fully elastic, adhesive and Van der Waals model [167].

The Hertzian model is described by

$$F = \frac{4E\sqrt{R}}{3(1-v)} I^{\frac{3}{2}} \tag{5}$$

where F is the Force applied by the tip to cause an elastic indentation depth I. E is the complex Young's modulus, R is the radius of the sphere and v is the Poisson's ratio [168], which is sample dependent and typically between 0.2 and 0.5. For a spherical model, the interaction between the tip and the sample is assumed to endure a spherical tip geometry due to the contact forces. Punch and sphere geometries can also be applied for Hertzian model, where punch geometry has an exponent of 1 and the cone geometry has an exponent of 3/2.

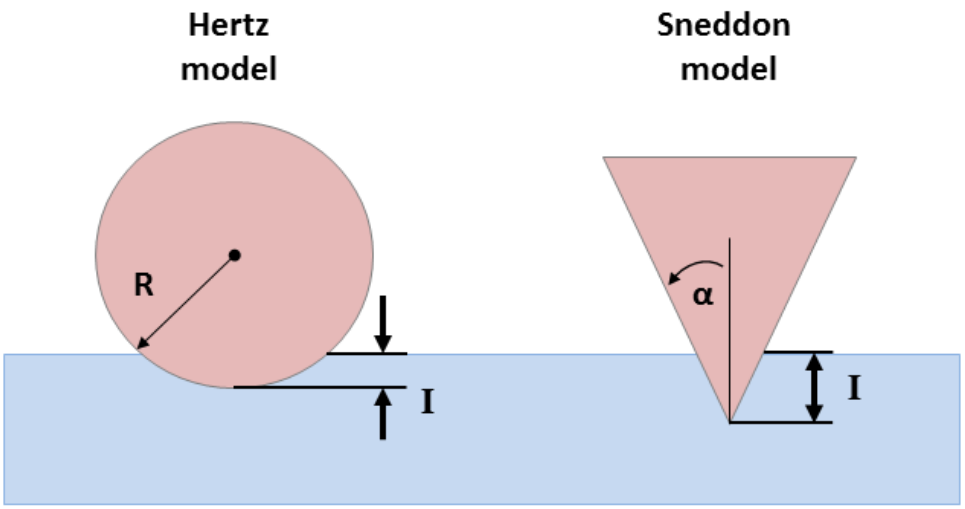

Figure 18: Schematic of Hertz model (sphere) and Sneddon model (cone) with different indentation length I.

Another common model derived by Sneddon [169] assumes a rigid conical shape indenting a soft flat surface. Like the Hertz model, this model does not consider de-adhesion and viscoelastic effects. **Figure 18** shows a comparison of the two models. Namely, the Hertzian model describes an indentation that is significantly smaller than the sphere radius, whereas in the Sneddon model the indentation is much larger than the cone apex, which can be considered infinitely sharp. The Sneddon model can be applied to extract the Young's modulus by:

$$F = \frac{2E}{\pi(1-\nu^2)} \tan\alpha \, I^2 \qquad (6)$$

where F is the Force applied by the tip to cause an elastic indentation depth, I. E is the complex Young's modulus and ν is the Poisson's ratio [168]. The Sneddon model works with the half angle α of the conical tip shape and thus the known radius of the tip is not required (as with the Hertz model) (**Figure 18**). The geometry of the conical tip has a power law slope of 2, which is the exponent in equation (6).

The complex Young's modulus is an equation considering both the mechanical properties of tip and the sample, which is given as:

$$\frac{1}{E} = \frac{3}{4}\left(\frac{1-v_{sample}^2}{E_{sample}} + \frac{1-v_{tip}^2}{E_{tip}}\right) \quad (7)$$

where v_{sample} is the Poisson ratio of the sample, E_{sample} is the Young's modulus of the sample, v_{tip} is the Poisson ratio of the sample and E_{tip} is the Young's modulus of the tip [168]. Silicon Nitride (Si_3N_4 tip) has a Young's modulus of 290 GPa, with approximations of 0.25 and 0.5 for the Poisson ratio of the silicon nitride and hydrogel, respectively. By calculating *E* from a Sneddon model fit to the force versus indentation curve (**Figure 19**), the sample modulus, E_{sample} , can then be calculated from the complex modulus equation in equation. 7. For example, Figure 18 shows the Sneddon model fitted (black trace) to a F-D curve (red line) performed in liquid on a 10% GelMA hydrogel sample cured at a UV-intensity of 12.6 mW/cm^2 for 30 min and with a thickness of 1.0 mm. The fitting gives a Young's modulus of 2.25 kPa and the total indentation of the hydrogel is 580 nm (zero-point indicated as dotted line). Furthermore, it is noted that this analysis was used in the thesis for measurement of Young's modulus of different GelMA samples. In fact, these types of AFM nanomechanical measurements have been extensively applied and well-established, following much earlier work notably by Domke et al. (1998) who calculated the elasticity of thin gelatin films using the Hertzian model [170].

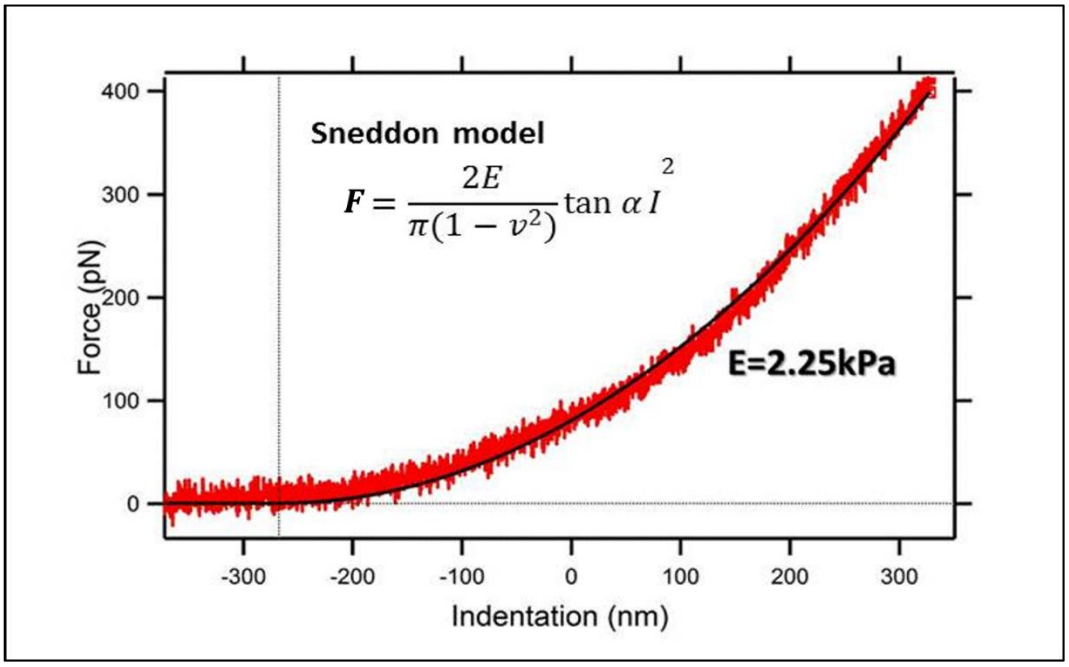

Figure 19: Sneddon fit to force versus indentation curve on GelMA hydrogel sample. The Sneddon model is applied as plotted black line to the F-D curve (red) of a 10% GelMA sample in liquid with 1.0 mm thickness. By applying the Sneddon model to the approached F-D curve, the Young's modulus E can be calculated.

2.3 Application of AFM to Probing of Living Cells

2.3.1 Single Cell Force Spectroscopy

AFM-based SCFS enables the measurement of the de-adhesion forces of living cells, with sensitivity on the order of 10 pN to 1000 pN [151], and provides an opportunity to investigate the effect of various substrates using different sample configurations (**Figure 20**). One approach is to use the substrate as the AFM probe, such as the functionalized with proteins or a material coating, which interacts with a single cell on a substrate (e.g. in a petri dish) (**Figure 20B**) [171]. However, this method is not straightforward due to specialized procedures and chemistries required to functionalize the cantilever. Furthermore, the probe may get contaminated by the cell, affecting subsequent measurements. Alternatively, a single living cell can be attached to the cantilever and brought into contact with a material of interest (**Figure 20A**), with measurements performed at different X-Y locations. This also opens up the possibility of studying cell-cell interactions (**Figure 20C**) [172, 173]. In summary,

due to the ability to quantify cell de-adhesion with sub-nanometer resolution and piconewton (pN) force accuracy [174], SCFS allows unrivalled insights into cell-material interactions [151].

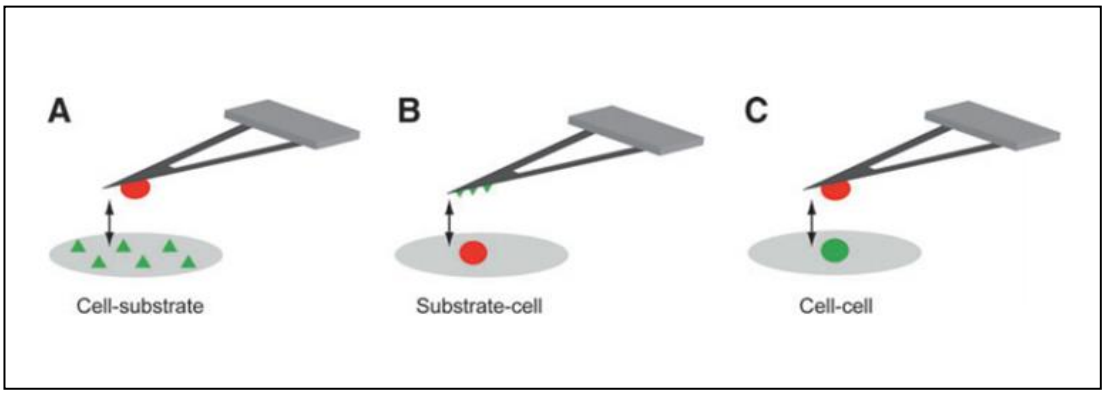

Figure 20: **AFM-SCFS setups.** (**A**) Characterization of a single cell-substrate de-adhesion. A living cell is attached to the functionalized cantilever and is probed to the substrate. (**B**) Characterization of material-single cell de-adhesion. The (bio)material is attached to the cantilever and is probed to a single cell. (**C**) Characterization of cell-cell de-adhesion. A single cell is attached to the functionalized cantilever and probes a single cell attached to a substrate [173].

2.3.2 Converting a Single Living Cell into a Probe

Several methods have been developed to attach a single cell to the AFM cantilever, which generally requires an initial step of functionalizing a tipless cantilever with molecules that will facilitate adhesion of the cell to the cantilever. A common method is to apply the lectin, concanavalin A (ConA) [151, 175], which binds carbohydrate groups on cell surfaces [175]. To functionalize the cantilever with ConA, a streptavidin-biotin linker can be used (**Figure 21A**) [176]. Further details of this cell attachment procedure to a tipless cantilever is given in Chapters 4 and 5 (Methods Section). An alternative method is to grow cells directly on the cantilever [177], while it is also possible to pick up a cell with the cantilever and then remove it after the measurements by using a coating that reverses the cell adhesion [178]. More recently, Potthoff et al. (2012) developed a protein-free technique using a specially

designed cantilever with integrated microfluidic channel connected to an external fluid circuit (**Figure 21B**) [179]. Through defined suction pressure of the fluid circuit system, the cell becomes immobilized as soon as the cell gets in contact with the fluidic cantilever [179]. This method requires additional equipment including an expensive, specialized cantilever and a fluid control system. The microfluidic channel in the cantilever also has the propensity to get blocked. Despite this, the fluidic cantilever approach enables easy pickup and removal of single cells for higher-throughput experiments [173]. Pros and cons of the different approaches are summarized in **Table *2***.

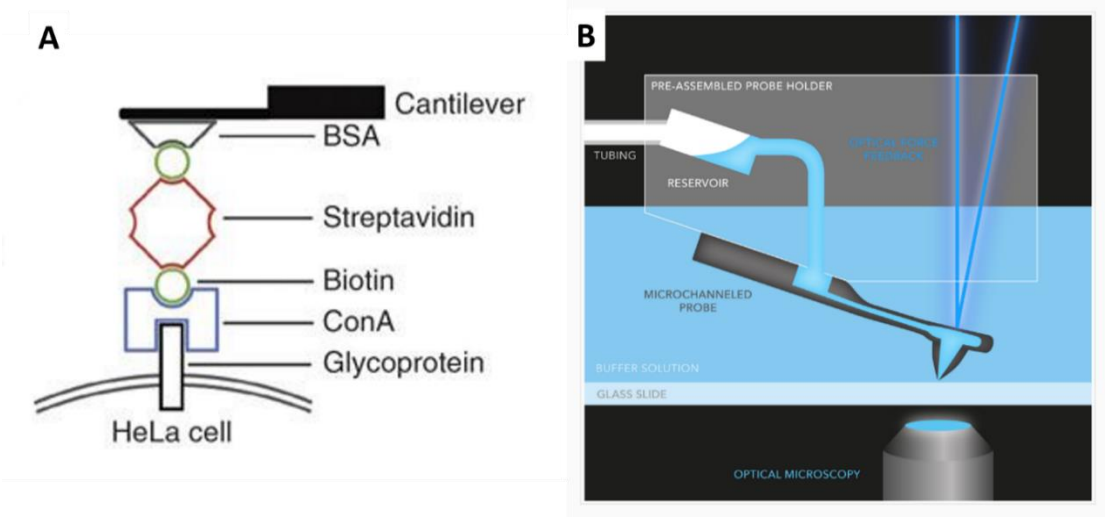

Figure 21: ConA functionalized cantilever and microfluidic cantilever. (**A**) Illustration of functionalizing the cantilever with different components [180]. (**B**) FluidFM scheme based on [181]. AFM probe with closed micro channels based on FluidFM. This technology allows to gently manipulate microscopic objects while grasping them with suction pressure in air or liquid.

Table 2: Comparison of different cantilever approaches [173].

Functionalization Method	Theory	Pros/Contras
Lectin (Concanavalin A)	Binds carbohydrate groups on the cell surface	-causes changes in the cell stiffness
Streptavidin-Biotin	Adsorbs Concanavalin A	-/-
ECM proteins	Binds to cell adhesion receptors on the cell surface	-ECM receptors can modify the adhesive properties of the cell
Microfluidic cantilever	Cells become attached to the cantilever via underpressure	+Attaches cell to the cantilever without functionalization -requires additional equipment

2.3.3 Typical F-D Profiles of Single Cell De-Adhesion

For SCFS experiments, the tipless cantilever with the attached single cell is positioned above the substrate (**Figure 22A**, **(1)**). The cell probe is then brought in contact with the substrate and pushes into the surface with a pre-defined force (setpoint or trigger force) (**Figure 22A**, **(2)**). The cell is usually kept in contact with the substrate for a defined time period, referred to as dwell time, to enable the cell-substrate adhesion (**Figure 22A**, **(3)**). The cantilever with the cell is subsequently pulled away from the substrate surface, causing shrinkage of the de-adhesion area between cell and substrate (**Figure 22A**, **(4)**), until the cell is finally detached (**Figure 22A**, **(5)**). During this process, the corresponding interactions and forces acting on the cell probe as a function of the distance are recorded in SCFS curves (**Figure 22B**). Within the retraction F-D curve, the maximal de-adhesion force, (F_D), required to detach the cell from the substrate can be obtained. Subsequent multiple unbinding events of cell surface molecules from the substrate surface also occur, presenting a characteristic "saw-tooth" and step-like profile (**Figure 22B**) (plateaus are not shown). Typical ruptures undergo a non-linear force over a shorter distance, while plateaus show a constant force over a longer distance. The entire integrated area under the curve (striped region) gives the total energy of de-adhesion. In general, the range of forces that can be measured varies between 10 pN and 100 nN, thus enabling detection of

single molecule unbinding (e.g. cell receptors) through to higher forces, e.g. several nanonewtons, of the bulk single cell de-adhesion [182].

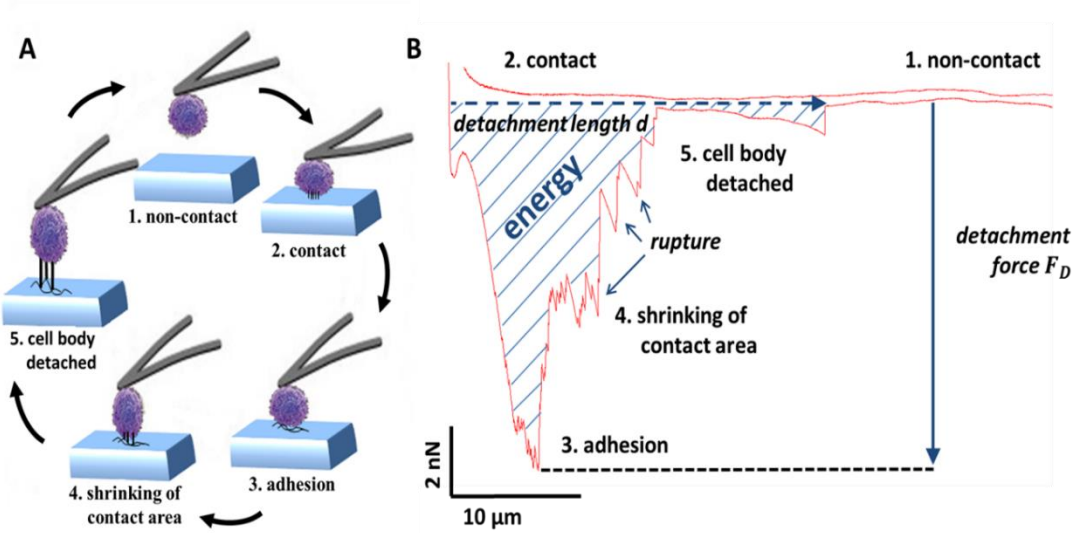

Figure 22: Schematic illustration of a SFCS experiment in relation to detected de-adhesion events. Analysed by typical F-D curve approach (grey) and retraction curve (black) to GelMA. (**A**) A single cell is attached to an AFM cantilever and no force is detected (1). The cell approached GelMA by moving the cantilever towards GelMA (1-2) until it makes contact (2). During the contact time the de-adhesion strength increases between cell and GelMA (3). After the predefined dwell time the cantilever is withdrawn from GelMA and the contact area between GelMA and cell shrinks (4). Bonds that have been formed brake sequentially (5) until the cell is completely separated from GelMA (1). (**B**) The F-D curve represents the five described steps. The retraction force is represented by the maximum detachment force ($\boldsymbol{F_D}$).

2.3.4 Types of SCFS Interactions

De-Adhesion Force, Energy and Detachment Length

In the thesis, the de-adhesion force F_D is defined as the maximum force that is required to fully detach the cell from the ECM or underlying substrate (**Figure 22B**). It strongly depends on the cell interaction, dwell time and on the underlying substrate softness. The de-adhesion energy is the striped area of the F-D curve (**Figure 22B**). The detachment length *d* is the distance required to fully unbind all linkages between the cell from the ECM or underlying substrate. This length is highly

influenced by membrane nanotubes [183] and softness of the underlying substrate, which is described further below.

Rupture and Plateau Unbinding Events

The ruptures in **Figure 22B** have been interpreted as the unbinding of a single receptor, or a few receptor bonds, from ligands on the substrate [184] and believed to involve interactions with cell adhesion receptors that are anchored to the internal cytoskeleton (**Figure 23**). During cell de-adhesion, the bound receptor along with the associated membrane and cytoskeleton linkage are subject to a tensile stress, causing an increase in force acting on the cantilever [185, 186]. Eventually, the receptor-ligand bond breaks, resulting in a non-linear rupture peak that occurs over a short distance (**Figure 23A**). In contrast, plateaus are explained by those cell receptors that are not tightly associated with the internal cytoskeleton, causing the extraction of the receptor along with a membrane tether or nanotube from the cell membrane (**Figure 23B**). Here, the force remains constant during the tether extraction until the receptor-ligand bond fails. The constant force over distances of up to microns is not due to the receptor unbinding but relate to those involved with formation of the membrane tether, including the membrane rigidity and size of the tether. These plateaus give a characteristic staircase-like profile, depending of the number of tethers (**Figure 23B**).

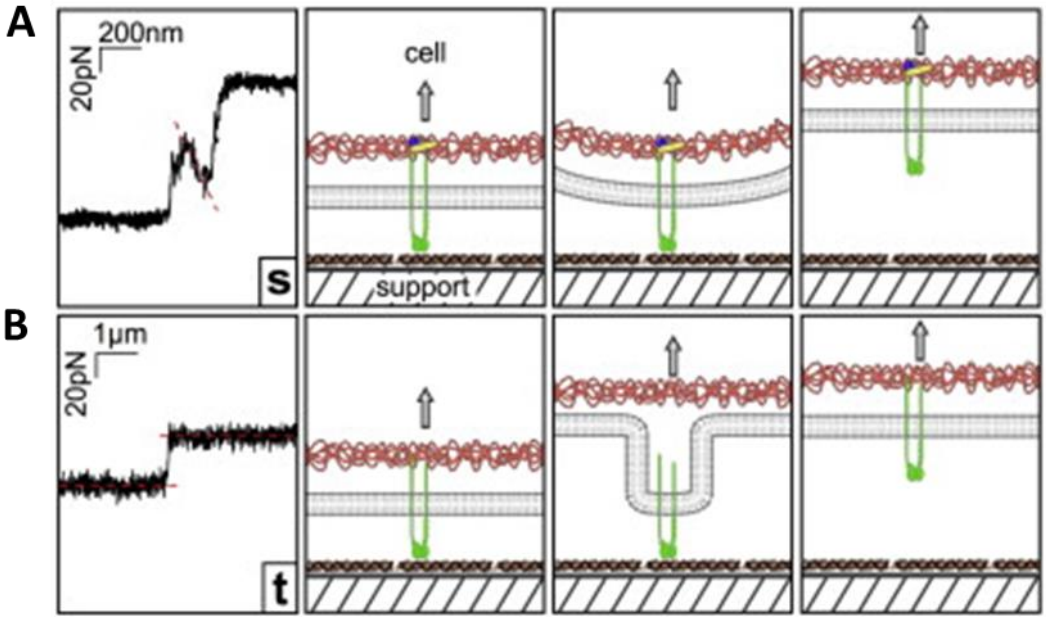

Figure 23: Illustration about the process of causing rupture (s) and plateau (t) events. (**A**) Rupture events (left). By pulling the cantilever with the attached cell from the ECM or underlying substrate, the cell de-adhesion receptor-membrane-cytoskeleton linker is stretched and the force on the cantilever increases. (**B**) Plateau events (left). A receptor is not anchored to the cytoskeleton is extracted with a membrane nanotube from the cell body [184].

2.3.5 Important Control Parameters of SCFS

During SCFS experiments, several parameters can be applied to control the interaction between the living cell and substrate. **Figure 24** depicts the different cell-substrate interactions affected by these different parameters, including contact force, contact time, cantilever retraction speed, cell elastic properties and surface roughness. These are outline further below.

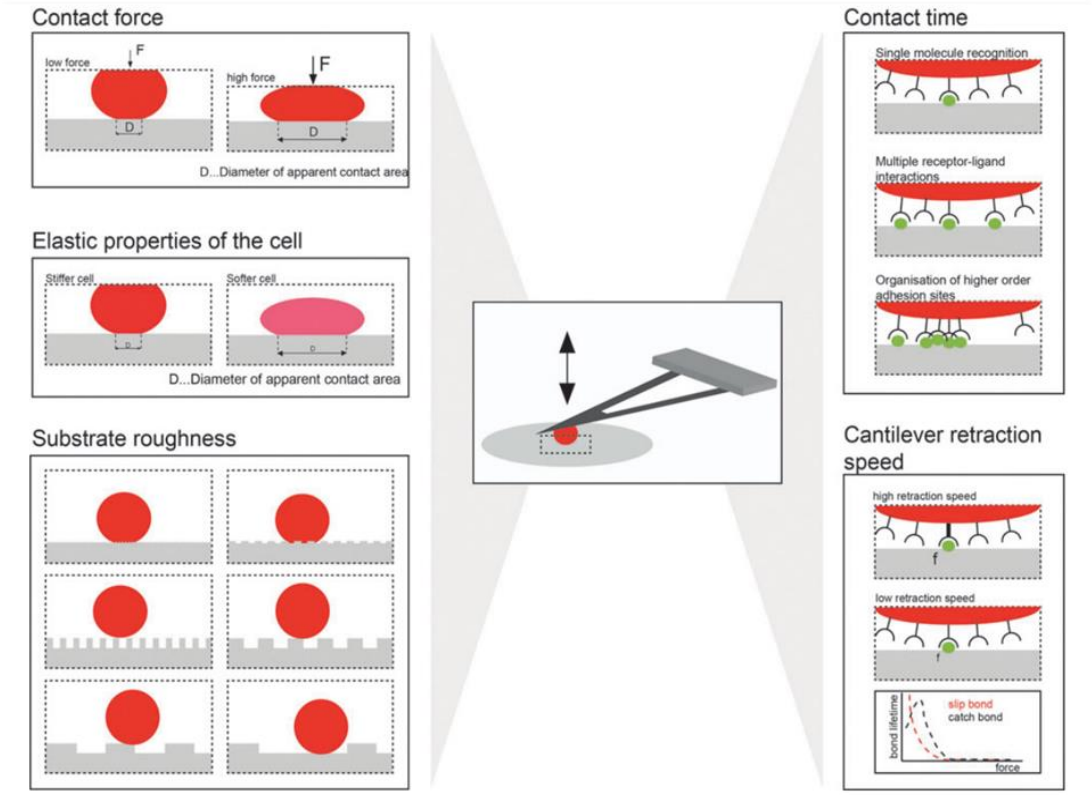

Figure 24: Illustration of the de-adhesion effects influenced by experimental parameters. Different properties of the substrate and the cell influence the outcome of the SCFS experiment. The elasticity of the cell increased the contact area of the cell, depending on the contact force pressing on the cell. Additionally, the de-adhesion is depending on the roughness of the substrate. Depending on the structure, adhesive ligands become available [173].

Contact force

The contact force is the maximum force that the cell probe applies to the substrate and effectively controlled by the setpoint value (or sometimes referred to as trigger force in F-D curves). It has typical values between 100 pN to 500 pN [187, 188] and can significantly influence the interaction. This is because when the contact force increases, there is an increase in deformation of the elastic cell body (depending on the cell elasticity) and corresponding increase in the contact area formed between cell and underlying substrate. Elter et al. (2011) has evidently shown an increase in de-adhesion force with increasing contact force, presumably due to an increase in

the number of ligand-receptors interactions that occur during cell contact with the surface [173, 188, 189].

Contact time

Contact time, or dwell time, defines the time the cell spends in contact with the surface, commencing once the contact force has been reached and until the cell is retracted from the surface. Dwell times are typically kept short, on the order of seconds, to minimize de-adhesion and increase the probability of observing the unbinding of single receptor complexes [190]. Shorter dwell times provide the possibility of studying the very, early and initial stages of cell adhesion, and their use in SCFS has interestingly shown that integrin receptors can undergo binding on very short timescales, i.e. < 1 sec [190]. Longer dwell times expectedly results in greater de-adhesion forces due to increasing formation of de-adhesion complexes such as multiple receptor-ligand interactions and their global de-adhesion forces. SCFS experiments on the effect of varying dwell times from secs to tens of minutes (max 30 mins) has revealed the initial processes of cell de-adhesion, including the de-adhesion forces involved in the recruitment of integrins and formation of their focal adhesions [173]. Friedrichs et al. (2013) showed that for a longer contact time and higher contact force the likelihood of parallel de-adhesion of multiple bonds increased [184]. **Figure 25** shows that the de-adhesion of CHO-A2 cells on substrates covered with collagen type I had an s-shaped response for contact times between 5 and 600 s. Therefore, a three phase of adhesion formation is distinguished where cells seemed to switch progressively from a low to a high adhesion state with increasing contact time [190]. This effect has been associated with an increase of cell–substrate area including new bond formation, receptor linkage to the cytoskeleton and receptor clustering [173, 191].

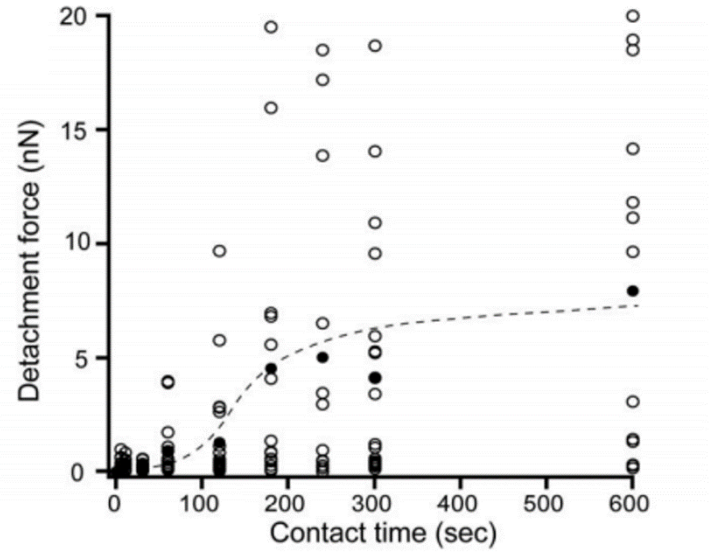

Figure 25: Dependence of cellular de-adhesion on substrate contact time. CHO-A2 cell detachment forces were determined for contact times between 5 and 600 s. Open circles in the diagram represent the detachment forces of individual cells for a given contact time, whereas the closed circles denote the corresponding mean detachment forces of all cells tested. The S-shaped hand-drawn trend line (dashed) indicates a nonlinear increase of cellular de-adhesion with contact time [190].

Cantilever retraction speed and loading rate

The retraction speed is the speed (typically µm/sec) at which the z-piezo is moved away from the substrate after the cell has been in contact with the surface (**Figure 24**). Importantly, it is well established that increasing the retraction speed causes an increase in de-adhesion force [192], thus this parameter must be must considered (i.e. kept consistent) when making comparison of forces between different SCFS experiments. This is because retraction speed determines the loading rate parameter, which is given by the tip or probe velocity (µm/sec) multiplied by the de-adhesion force. Loading rate effectively describes the rate at which the force is loaded onto cell – substrate bonds prior to breaking. AFM studies on the effect of loading rate is referred to as Dynamic Force Spectroscopy and has been important in elcudating different types of bonds, such as catch or slip bonds, that either increase or decrease the de-adhesion force depending on the loading rate. [173, 185, 186, 193].

Elastic properties of the cell

As mentioned above, the elasticity of the cell has an influence on the contact area between the cell and substrate (**Figure 24**). Therefore, comparing the de-adhesion of different cell types may be problematic if their elastic properties are dissimilar. Though as described in section 1.5.3, the approaching part of the F-D curves where the cell contacts the substrate provides information on the cell deformation and can be analysed mechanical models, e.g. Hertzian theory, to quantify the Young's modulus of the cells [194]. These effects of cell elasticity and deformation emphasizes the importance of having combined AFM-Optical Microscopy that enables visualization of the increasing cell area as the AFM probe with attached single cell is pushed into the surface during SCFS [173].

Substrate roughness

The substrate roughness (**Figure 24**) can have a significant effect on the de-adhesion force, as demonstrated in previous studies [188, 195]. Elter et al. (2011) studied SCFS de-adhesion of L929 fibroblasts on a microstructured titanium surface (height ~6 µm, groove width 20 µm) to directly compare the de-adhesion strength of the same cell at different positions [188]. They showed that the cell de-adhesion strength significantly decreased by an increase of the contact area (cell contact near the flanks)) (**Figure 27A-B**) [188]. The relationship between cell de-adhesion and surface roughness was studied by Weder et al. (2010) [195] using quartz microstructured surfaces. After fibroblasts were grown for 24 h on the quartz surface, they were brought into contact with an FN-coated cantilever, allowed to adhere more strongly to the cantilever, and then pulled away from the surface. The cell de-adhesion on the microstructured surface was significantly lower compared to smooth surfaces, suggesting the former resulted in a decrease in cell contact area [173, 195].

2.3.6 Cell De-Adhesion to Extracellular Matrix Proteins

Early SCFS studies focused on cell de-adhesion to ECM proteins such as collagen, fibronectin or laminin, typically coated onto a glass slide or petri dish [180, 190, 196, 197]. For example, partially-denatured collagen exposed RGD-motifs were shown to trigger binding of α5β1- and αv-integrins of murine calvaria pre-osteoblasts [197], while α2β1 integrin mediated de-adhesion of HeLa cells to collagen type I [180]. Friedrichs et al. (2008) measured MDCK cell de-adhesion to collagen IV, laminin-332 and fibronectin coated glass coverslips with a contact time of 20 and 90 sec [196]. The adhesion phenotype of galectin-3-depleted cells was mimicked in a galactoside-deficient MDCK cell line. They showed that depletion of galectin-3 in MDCK cells led to a greater de-adhesion state when measurements were done on collagen IV. This effect was specific to integrin α2β1-mediated de-adhesion and not observed when de-adhesion was mediated by other integrins [196]. Dao et al. (2013) quantified differential matrix de-adhesion of single chinese hamster ovary cells to laminin and adhesion-passivated control surfaces made of PEG and showed that cell de-adhesion on laminin was greatly increased compare to cell de-adhesion on PEG passivated surfaces (**Figure 26**) [198]. They extended their approach by including additional ECM substrates such as bifunctional collagen I and collagen IV surfaces [198]. Furthermore, SCFS experiments using protein covered glass coverslips enabled investigation of de-adhesion processes involving receptor crosstalk where the binding of one type of cell de-adhesion molecule can activate another type [190, 199, 200]. Friedrichs et al. (2010) identified crosstalk between collagen-binding integrin α1β1 and fibronectin-binding integrin α5β1 in HeLa cells [200]. A detailed SCFS study on receptor crosstalk is further described by Bharadwaj et al. (2017) [199]. In particular, they characterized immediate phases of cell de-adhesion and revealed that αV-class integrins outcompete α5β1 integrins [199]. Once engaged, αV-class integrins signalled to α5β1 integrins to establish additional binding to fibronectin, reveals that αV-class integrins outcompete α5β1 integrins [199].

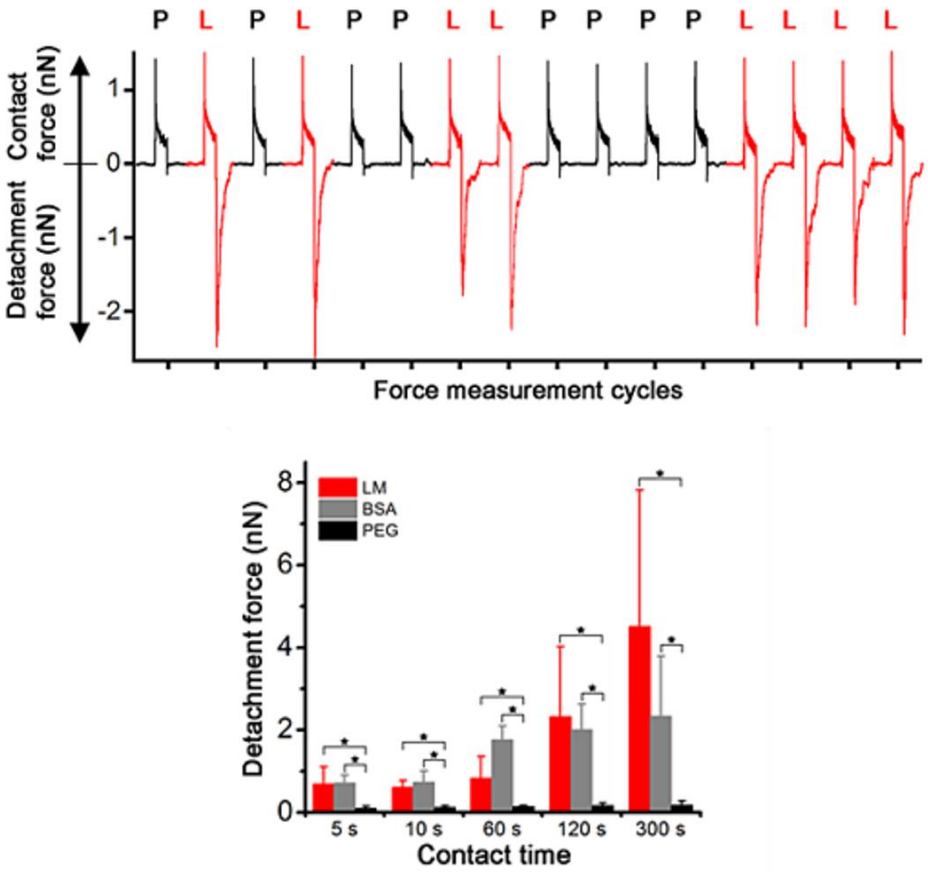

Figure 26: Cell de-adhesion to extracellular matrix proteins. Sequence of 16 force curves generated in a preprogrammed sequence of force cycles alternating between PEG-passivated ("P", black) and laminin-coated ("L", red) areas (top). Contact-time dependent formation of cell adhesion forces on laminin (LM), bovine serum albumin (BSA), and PEG-functionalized surfaces (mean ± median absolute deviation [MAD]) (bottom) [198].

2.3.7 Cell De-Adhesion on Materials

In recent years SCFS has gained interest in quantifying cell de-adhesion to various materials such as CPs, polymer brushes, modified layers or hydrogels. Whilst not mammalian cells, SCFS has been used to quantify bacteria de-adhesion on hydrophilic and hydrophobic layers [201, 202]. SCFS studies by Thewes et al. (2014) have shown that a bacterial functionalized AFM probe gives strong de-adhesion on hydrophobic wafers (up to about 3000 pN) compared to low de-adhesion (about 30–

50 pN) on hydrophilic wafers [202]. Bacterial de-adhesion strength on seven types of polymer brushes (Poly(HOEGMA), Poly(HEMA), Poly(MeOEGMA), Poly(HPMA), Poly(PCMA), Poly(SBMA), Poly(CBAA)) showed that cell de-adhesion forces differ between the polymer brushes. The maximum force and energy required to detach the bacterium was greatly reduced and therefore confirmed the known excellent resistance of polymer brushes to protein adsorption. Highest de-adhesion force was obtained for MeOEGMA and HOEGMA (110 -135 pN), whereas the lowest de-adhesion force was shown for (25–65 pN) [203]. For mammalian cells, single L929 fibroblast cell de-adhesion was measured on topographic titanium microstructures (height ~6 µm, groove width 20 µm) by Elter et al. (2011), revealing that L929 fibroblast cells adhered stronger to planar regions compared to adhesion near the groove flanks of the microstructures (**Figure 27A-B**) [188].

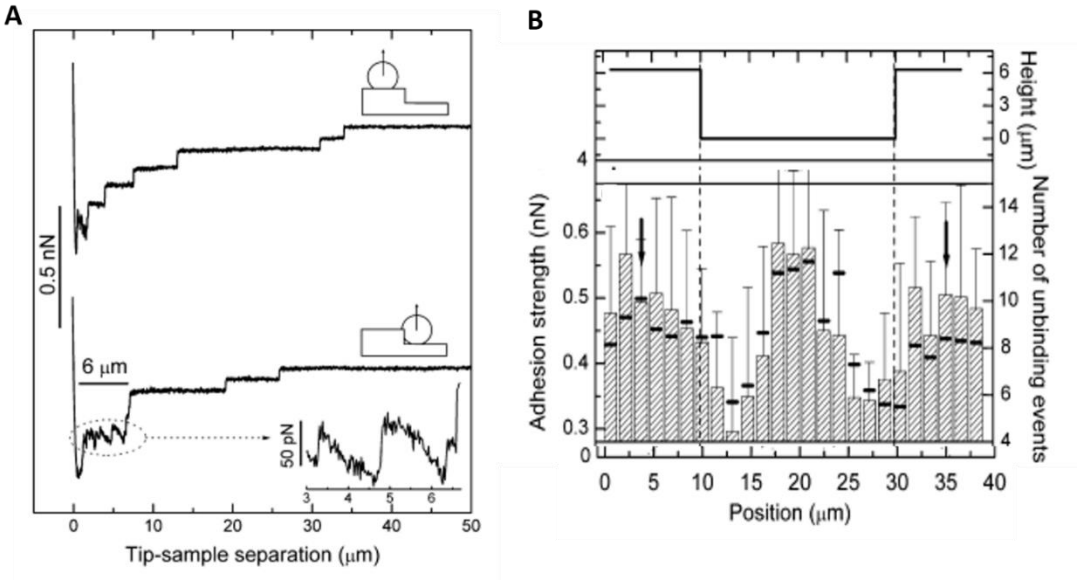

Figure 27: L929 cell de-adhesion on topographic microstructure. (**A**) Curve measured on top with primarily horizontal contact area (top) and curve measured near the flanks with maximal vertical contact area (bottom). (**B**) Schematic profile of the grooved substrate (top) related to measured cell de-adhesion at different positions (bottom) [188].

Recently Zhang et al. (2015) extended the conventional SCFS by combining EC-AFM to quantify the L929 fibroblast interactions with conducting polymer films without adsorbed protein under electrical stimulation [48]. When using PPy-DBSA films, the strength of cell de-adhesion was greatest on electrochemically reduced films and least on oxidised films [48]. In a recent study from the same authors (2018), when electrical stimulation was applied during protein adsorption the de-adhesion decreased for both oxidized and reduced states (compared to the control without stimulation). However, if the electrical stimulation was applied after protein adsorption was established, then interestingly the cell de-adhesion was enhanced on the oxidized films [204]. Related to hydrogels, Martin et al. (2016) functionalized the cantilever with a hyaluronic acid hydrogel and measured the interaction with CD44 cells, revealing that the cell de-adhesion was faster compared to observed adhesion and spreading of cells seeded on the hydrogel surfaces [205]. Yu et al. (2015) quantified PC3 cell and HeLa cell de-adhesion on polydimethylsiloxane (PDMS) and BSA-coated PDMS to address non-specific cell de-adhesion, with the de-adhesion force enhanced on plane PDMS (**Figure 28A**) [206]. Furthermore, Jalali et al. (2015) determined the cell de-adhesion to PAAm hydrogel coating in a Young's modulus range of 65 Pa to 1032 Pa increased with increasing the PAAm modulus, indicating that cells sense their environment within a very low modulus range (**Figure 28B**) [207]. Polymer brushes used as antifouling materials in the food industry and biomedical devices have recently been studied via SCFS (2015) [203].

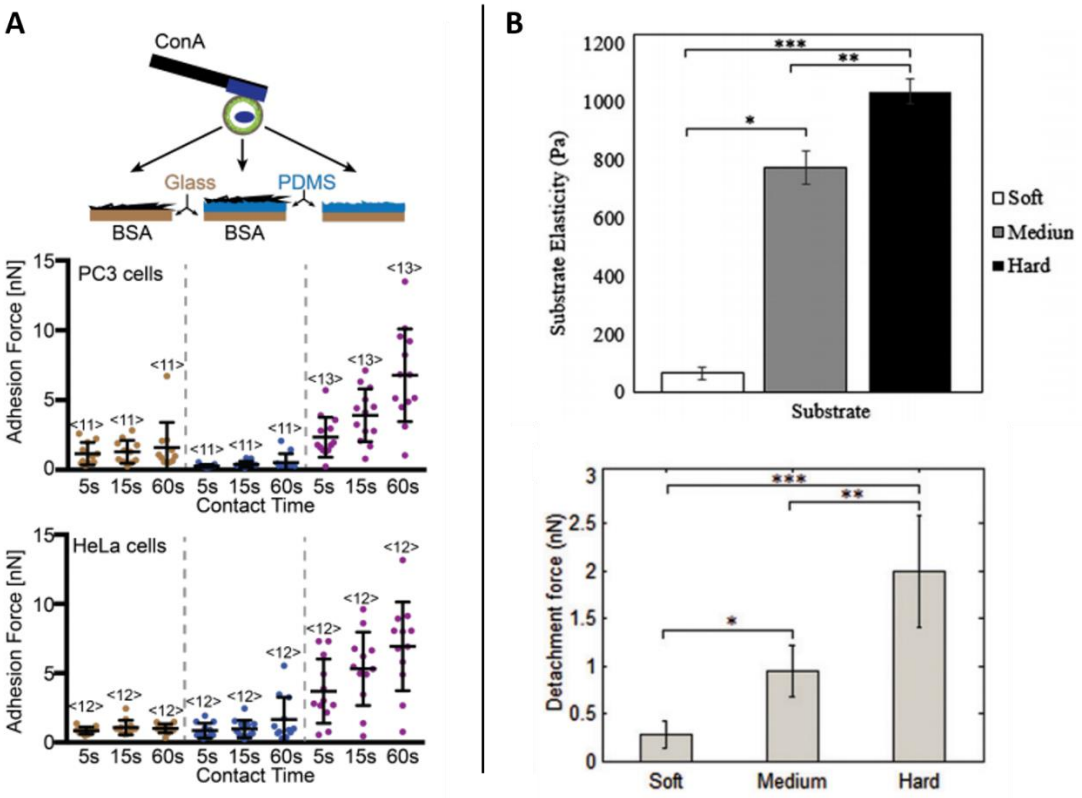

Figure 28: SCFS cell de-adhesion on soft materials. (**A**) SCFS assay used to quantify de-adhesion of PC3 and HeLa cells. Single cells were bound to ConA-coated cantilevers and approached BSA-coated glass or PDMS and a clean PDMS surface [206]. (**B**) Elastic modulus of soft, medium and hard PAAm hydrogel substrates (top) and detachment force values corresponding to the soft, medium, and hard PAAm hydrogel substrates (bottom) [207].

Chapter 3:

Electro-Mechano Responsive Properties of Gelatin Methacrylate (GelMA) Hydrogel on Conducting Polymer Electrodes Quantified using Atomic Force Microscopy

3.1 Introduction

Current implantable electrodes or neural prosthetic devices (e.g. cochlear implant) are manufactured with metals such as platinum or platinum iridium, or other materials based on silicon or carbon [25, 208]. The materials are extremely hard (e.g. 139 GPa for platinum) [28] compared to soft biological tissues that have moduli ranging from 0.5 – 10 kPa [27, 209, 210]. In addition, the low surface roughness and lack of porosity of metal-based electrodes are not inherently compatible with delicate cell processes of nerve cells and neural tissues [25, 26]. Furthermore, unwanted interactions between a metal electrode and soft tissue can lead to general thickening of surrounding tissue such as fibrosis, inhibiting cell survival and growth and reducing the quality of the electrical signal [12, 211]. This effect can, however, be moderated by applying a coating of softer material onto the electrode [60, 61].

OCPs have been extensively investigated as a coating material due to their biocompatibility, high conductivity-to-weight ratio, porosity and ability to electrically stimulate to control cell behavior [53, 55, 212-216]. OCPs can be functionalized through doping with biomolecules or biopolymers [33], and importantly they are significantly softer than metals. Cui et al. (2003) have demonstrated that electrodes coated with the OCP PPy form stronger connections with neuronal structures *in vivo* compared to metallic materials without coating [211]. An ongoing premise for the use of OCPs is their improved mechanical compatibility with soft tissues. However, their moduli measured in liquid are still relatively high, ranging from 30 MPa to 1000

MPa [33], compared to brain tissue that has a modulus ranging from 0.5 to 1 kPa [27] and skeletal muscle being ~10 kPa [217]. Therefore, optimizing the design of OCPs requires consideration of the mechanical, electrical, chemical and other bioactive properties, with neither able to be addressed independently of the others [218].

To overcome this issue, a combination of hydrogels with metal and conducting polymer electrodes has been employed [60, 219]. The hydrogels, commonly used in tissue engineering, wound healing and drug release applications [62, 63] are of significant interest because they have similar moduli and porosities to biological tissues [64, 65]. Lundin et al. (2011) have shown that coating a polypyrrole doped with dodecylbenzenesulfonate (PPy-DBSA) with a gel layer efficiently supported rat fetal neural stem cells during electrical reduction [50]. Green et al. (2013) have shown that a conductive hydrogel layer on a PEDOT electrode provides a scaffold for supporting encapsulated PC12 cell survival and differentiation without affecting the electrical performance of the electrode [61]. It is thought that the charge transfer is due to the ionic partitioning properties of hydrogels as they actuate in the electrolyte [220]. Kim et al. (2009) investigated the effect of alginate-coated neural electrodes on the quality of neural signals, demonstrating that coating the PEDOT electrode with a 30 µm alginate layer had no influence on the signal transmission. Furthermore, the alginate layer creates a softer tissue interface without losing functionality [60]. Therefore, an electrode with a soft hydrogel coating decreases the mechanical mismatch and has potential to improve the electrode-tissue interface.

GelMA is a hydrogel of increasing interest in tissue engineering, particularly as a common reagent in bioprinting and three-dimensional (3D) cell culture [221]. GelMA is a photopolymerizable hydrogel composed of modified natural ECM components [120] and currently used in several applications, including wound healing and 3D printed scaffolds for tissue regeneration [121, 126, 222, 223]. GelMA is composed of multiple methacrylate groups on a gelatin molecule and a photoinitiator is added to the GelMA, making it light polymerizable via a radical [224]. The modification of gelatin with photocrosslinkable methacrylate groups creates a hydrogel that maintains the unique property of gelatin, resulting in a stable hydrogel

at higher temperatures [121]. Gelatin is a derivative of collagen and contains a mixture of proteins obtained by acid or alkaline hydrolysis of collagen. Due to its excellent properties including biocompatibility, biodegradability, and non-immunogenicity, gelatin is used as a biomaterial for both hard and soft tissue engineering, drug delivery and biological glues [225]. This makes GelMA an attractive material for biomedical applications in tissue engineering, which has been successfully demonstrated in several studies [121, 124-126].

Whilst the advantages of having a lower modulus hydrogel layer on an existing electrode are evident to support cell growth and maintain electroactivity [61], the effect of the hydrogel on the electrical properties and conversely the effect of electrical stimulation on the hydrogel properties are less well-understood. For instance, ionic current generated at the electrode surface needs to pass through a micron thick hydrogel layer, consisting of charged polymer groups, proteins and amino acid residues (e.g. such as in GelMA), while the hydrogel itself can also be subject to changes in osmotic pressure or ionic gradients. With this in mind, the effect of electrical fields on hydrogels has previously been studied, including the possible mechanisms underlying the observed bending or actuation of gels [90, 91, 226, 227] and particularly for their use as electro-responsive hydrogels for drug release applications [228].

In this chapter, we investigate the electro-responsive properties of a GelMA/PPy-DBSA electrode using AFM with *in situ* electrochemical measurements. Specifically, EC-AFM was used to quantify the GelMA modulus and actuation, as a function of the applied electrical field and oxidation-reduction of underlying PPy-DBSA film. GelMA samples of varying modulus and porosity determined by UV crosslinking were firstly investigated and then subject to different electrical stimulation parameters. The study reveals a significant effect of the electrical stimulation, as the PPy-DBSA film is oxidized and reduced, causing dynamic changes in the nanomechanical properties of the overlying GelMA. These findings highlight a potential approach for elucidating the electro-mechano responsive properties of hydrogels, as well as for understanding the dynamic hydrogel properties at the electrode-tissue interface.

3.2 Materials and methods

3.2.1 Reagents

The pyrrole (Py) monomer was obtained from Sigma Aldrich and distilled prior to use. DBSA was used as the dopant and was obtained from Sigma Aldrich. GelMA monomer was synthesized following the protocol described by O'Connell et al. (2016) as a freeze dried material with methacrylate degree of 72% [229]. GelMA solutions were prepared using phosphate buffer saline (PBS) and a photoinitiator, Irgacure 2959 in 100% ethanol, which were both obtained from Sigma Aldrich.

3.2.2 Preparation of Polypyrrole Films

The PPy film doped with DBSA (PPy-DBSA film) was grown by electrodeposition at constant current on gold coated mylar. The gold coated mylar was firstly prepared by cutting it into 2.5cm x 5cm area and cleaned with Milli-Q water (18.2 MΩ*cm) and UV exposure. An aqueous solution of 0.2 M Py and 6 mM of the counter-ion dopant DBSA was degassed for 2 min prior to polymerization of the monomer. The PPy-DBSA film was electrodeposited on gold mylar with a current density of 0.25 mA/cm² for 10 min using an eDAQ EA161 potentiostat in a 3-electrode electrochemical cell with the gold mylar as working electrode, a platinum mesh as counter electrode and a Ag/AgCl NaCl 3 M as the reference electrode. After, the films were washed with Milli-Q water, cut into 0.83 cm x 2 cm strips with a use of a scissors and were gently dried with N_2 gas.

3.2.3 Preparation of GelMA/PPy-DBSA electrodes

PBS was prepared at pH 7.4 in Milli-Q water (18.2 MΩ*cm). Freeze dried GelMA (1 g) was dissolved in 5 ml PBS in a water bath at 37 °C. Aliquots of 500 µl GelMA solution were prepared in Eppendorf tubes, each sealed with parafilm and stored at 4 °C until

use. GelMA samples were prepared by warming the GelMA solution in a water bath at 37 °C for 5 min, followed by dissolution in PBS to 10% GelMA with 0.5% Irgacure 2959. The mixture was then cast onto the PPy-DBSA film within a 0.5 cm x 1.0 cm acrylic frame with a height of 1 mm that was fabricated using laser cutting with a PLS6MW laser engraver from Universal Laser Systems (ULS) (see **Figure 31A**). More specifically, the PPy-DBSA film was held within the acrylic frame using a clamp and then GelMA solution cast to completely cover the film and fill the entire volume of frame area, giving a GelMA sample thickness of 1 mm. GelMA was crosslinked using UV Curing Spot Light Device "Blue Wave 50" from DYMAX (USA) by UV-light exposure with a wavelength of 365 nm. Different intensities and exposure times were applied to crosslink GelMA as shown in **Table *3***. After curing the GelMA on the top of the PPy-DBSA film, the GelMA/PPy-DBSA composite electrode was immersed in a small petri dish filled with PBS and stored at 4 °C overnight to ensure a fully hydrated hydrogel.

Table 3: Investigated GelMA samples and their irradiation conditions used to induce cross-linking.

Sample	Intensity (mW/cm^2)	Curing time (min)	Energy (J/cm^2)
1.	3	1	0.18
2.	3	10	1.8
3.	3	30	5.40
4.	12.6	1	0.75
5.	12.6	10	7.56
6.	12.6	30	22.68
7.	89	1	5.34

3.2.4 Scanning Electron Microscopy

The prepared GelMA solution was cast within a 0.5 cm x 1.0 cm acrylic frame with height of 1 mm on a glass slide and crosslinked in situ. Different intensities and curing times were applied to crosslink GelMA as shown in **Table *3***. After the cross-linking

process, GelMA was removed from the glass slide and immersed in a small petri dish filled with PBS and stored at 4 °C overnight to ensure a fully hydrated hydrogel. The surface structure of each sample was investigated with a JEOL 6490LV Scanning Electron Microscopy (SEM) produced by JEOL in Tokyo (Japan). Samples were removed from the PBS solution and residual PBS on the GelMA surface was carefully absorbed with Kimwipes. The GelMA samples were directly snap frozen for 45 sec in liquid nitrogen, sectioned with a blade and mounted in a brass block. SEM images were performed under a low vacuum SEM with an accelerating potential of 15 kV and captured at x1000 magnification.

3.2.5 Cyclic Voltammetry

Cyclic Voltammetry of the GelMA/PPy-DBSA electrodes was performed on an eDAQ EA161 potentiostat in an electrochemical cell specially designed to enable AFM measurements during electrical stimulation. The electrochemical cell was made of two parts in acrylic, shown in **Figure 31A**. The working, counter and reference electrodes were located at the base of the cell and surrounded by silicon to seal it with the upper part of the electrochemical cell. The upper part creates a well to allow all three electrodes to be immersed in electrolyte (PBS). The GelMA/PPy-DBSA electrode functioned as the working electrode, platinum mesh as the counter electrode and a Ag/AgCl wire as the reference electrode positioned alongside the working electrode. The electrochemical voltage was cycled between 0 mV to -1000 mV, at a scan rate of 50 mV/s for 15 cycles in pH 7.4 PBS as the electrolyte.

3.2.6 Electrochemical-AFM Measurements

AFM was undertaken using an MFP-3D AFM (Asylum Research, Santa Barbara, USA) and DNP-S10 silicon nitride cantilevers (Bruker, USA). The thermal calibration method was used to calibrate the spring constant of the cantilever, which was ~0.06

N/m, and the deflection sensitivity was determined by taking a force curve on a glass slide in liquid prior to the measurements on the GelMA/PPy-DBSA electrodes samples. Force curves were firstly measured at four different XY positions on each of the different GelMA/PPy-DBSA electrodes without electrical stimulation. At each XY position, a minimum of 10 force curves were performed using a scan rate of 0.04 Hz, maximum load of 500 pN and z-distance of 5 µm. Measurements were repeated on three replicate samples (n = 3). For electrical stimulation, the force curves were restricted to three samples (samples 1, 5, 7 from **Table *3***) and undertaken using the specially designed electrochemical cell positioned on the AFM sample stage. Prior to the force measurements, cyclic voltammetry of each film was performed and cycled between 0 mV to -1000 mV at a scan rate of 50 mV/s for 15 cycles in pH 7.4 PBS as the electrolyte to ensure complete oxidation and reduction of the GelMA/PPy-DBSA electrode and full uptake of electrolyte. The potentials were converted to the Ag/AgCl NaCl 3 M reference electrode by placing both the Ag/AgCl wire and commercial electrode inside the PBS solution to check the potential difference. The AFM force curves were then triggered manually, and fifteen continuous force curves performed simultaneously during the cyclic voltammetry from 0 mV to -1000 mV with scan rate of 100 mV/s. Each force curve took 25 seconds to complete while a single cyclic voltammogram (CV) cycle took 20 seconds. This was done such that the contact region of the force curve (i.e. when the tip indents the GelMA) occurred at different voltage-ranges over time and allowed for continuous sampling in both the reduced and oxidized states. Due to the manual triggering and differences in the CV response of the different GelMA/PPy-DBSA electrodes, the specific voltage-ranges over which the force curves were collected slightly varied between the different samples though were constant within the one type of sample. Using the Asylum Research software (Igor Pro, Wavemetrics), the force curves were converted to force versus indentation curves and the Sneddon model was fitted to the data to quantify the Young's modulus of the GelMA-PPy composite samples:

$$F = \frac{2E}{\pi(1-\nu^2)} \tan \alpha \, I^2 \qquad (8)$$

where F is the Force applied by the tip to cause the elastic indentation depth I, E is the complex Young's modulus, v vis the Poisson's ratio and α is the half-angle of the conical tip. For the Sneddon model, the interaction between the tip and the sample is assumed to be dependent on a conical tip geometry, which has a power law slope of 2 and indicated by the exponent in equation (8). Instead of the radius of the tip, the Sneddon model considers only the half angle of the conical tip shape, which was given as 35°. The Poisson's ratio for gels is reported as 0.5 [230, 231]. Depending on the hydrogel, the Poisson's ration decreases during relaxation in water, for example, the Poisson's ratio of PAAm hydrogel decreases up to 0.26 [232]. Here, the Poisson's ratio was assumed to be 0.33 [233] in liquid due to changes in the gel during electrical stimulation as well different pore sizes and crosslinking densities. The indentation of the 1 mm thick GelMA samples was kept to 0.2 % (≈ a few microns) to exclude any influence of the underlying conducting PPy-DBSA film on the Young's modulus. The fitting parameters considered the indentation and force offset of each curve individually.

To measure the mechanical actuation of the GelMA/PPy-DBSA electrodes, the AFM tip was lowered and placed in contact with the sample with an applied load of 500 pN and the feedback switched on. Pulse potentials from 0 mV to -1000 mV at different frequencies of 0.05 Hz (20 s), 0.1 Hz (10 s) and 1 Hz (1 s) were then applied to the sample using the eDAQ recorder and EA161 potentiostat and electrochemical cell described above. A minimum of 10 pulses were performed for each frequency and the measurements were repeated at four different XY positions on 3 different GelMA/PPy-DBSA electrodes with 3 replicates for each sample (samples 1, 5, 7 from **Table 3**). The actuation of the hydrogel was measured by recording changes in the z-piezo output voltage. This piezo output voltage was converted to an actuation height in nanometers using the calibrated sensitivity (~60 nm/V) of the z-piezo, and correlated with the monophasic potential and current signals which were all recorded simultaneously using a eDAQ EA161 recorder.

3.3 Results/Discussion

3.3.1 Surface Morphology of GelMA

SEM imaging of different GelMA samples showed that the morphology, including porosity and surface roughness, were dependent on the UV cross-linking conditions (**Figure 29**). Both the pore size and surface roughness decreased with increasing UV intensity and exposure time. GelMA samples cured at low UV intensity and exposure times generally showed a reticulate, porous surface structure that became progressively smoother and less porous with both increasing UV intensity and exposure time (**Figure 29A-G**). The diameter of pore sizes of the different samples was quantified and summarized in **Figure 29H**. For 1 min of exposure time, GelMA samples cured at the lowest UV intensity of 3 mW/cm^2 (**Figure 29A**) had significantly larger average pore size of 8.54 ± 0.36 µm compared to those cured at 12.6 mW/cm^2 (**Figure 29D**) and 89 mW/cm^2 (**Figure 29G**), which had pore sizes of 4.34 ± 0.3 µm and 1.16 ± 0.05 µm, respectively. The same trend was observed for increasing exposure time at a constant UV intensity of 3 mW/cm^2 (**Figure 29A-C**), with decreasing pore sizes of 8.54 ± 0.36 µm (**Figure 29A**, 3 min exposure), 4.33 ± 0.19 µm (**Figure 29B**, 10 min exposure) and 2.36 ± 0.14 µm (**Figure 29C**, 30 min exposure). Similarly, for samples cured at 12.6 mW/cm^2, decreasing pore sizes were observed with increasing exposure time, giving values of 4.34 ± 0.3 µm (**Figure 29D**, 3 min exposure), 3.39 ± 0.22 µm (**Figure 29E**, 10 min exposure) and 1.99 ± 0.09 µm (**Figure 29F**, 30 min exposure). **Figure 29H** provides a summary of the above data, which shows that the change in pores size as a function of either UV intensity or exposure appears to follow a linear relationship.

The magnitude of the applied UV intensity and the exposure time can influence the energy transmitted to the sample, which plays a role in cross-linking and can influence the hydrogel structure and porosity. Changes in the pore size of GelMA with different degrees of methacrylate [132] and percentage of the photoinitiator I2959 from 0.05 wt%, 0.25 wt% and 0.5 wt % [139] have previously been quantified by analysis of cross-sections using SEM. Chen et al. (2012)

investigated three GelMA hydrogels with varying methacrylation degree of 49.8%, 63.8% and 73.2% and photoinitiator I2959 of 0.5 w/v % after exposure of 6.7 mW/cm² for 20 sec [132]. A higher degree of methacrylation gave decreasing pore sizes from 49.7 ± 11.8 µm, 30.13 ± 6.12 µm and 23.6 ± 5.85 µm, respectively. Benton et al. (2009) showed that larger pore sizes (~1800 µm², projected area) of sectioned samples correlated with the lowest amount of photoinitiator Irgacure 2959 (0.05 wt%) compared to the smallest pores (~400 µm², projected area) at 0.5 wt% of the photoinitiator when using the same UV intensity of 8 mW/cm² for 10 min exposure time [139]. In this study a methacrylate degree of 73% and photoinitiator concentration of 0.5% was kept constant while the UV intensity and exposure time were gradually increased [139]. In comparison with the above studies the pore sizes are up to 10-fold smaller, indicating that the UV intensity and exposure time have a significant effect on porosity. The surface morphology of GelMA sample was specifically investigated so as to be consistent with the AFM measurements that directly probe only the surface and not the internal structure. With the exception of the highest applied UV intensity of 89 mW/cm^2, all samples showed a degree of porosity directly at the surface. Further cross-sectional analysis (data not shown) of the samples showed all films also had an internal porous structure, including the highest UV intensity sample (**Figure 29G**) that displayed a smooth, non-porous surface or 'skin-like' layer around the hydrogel.

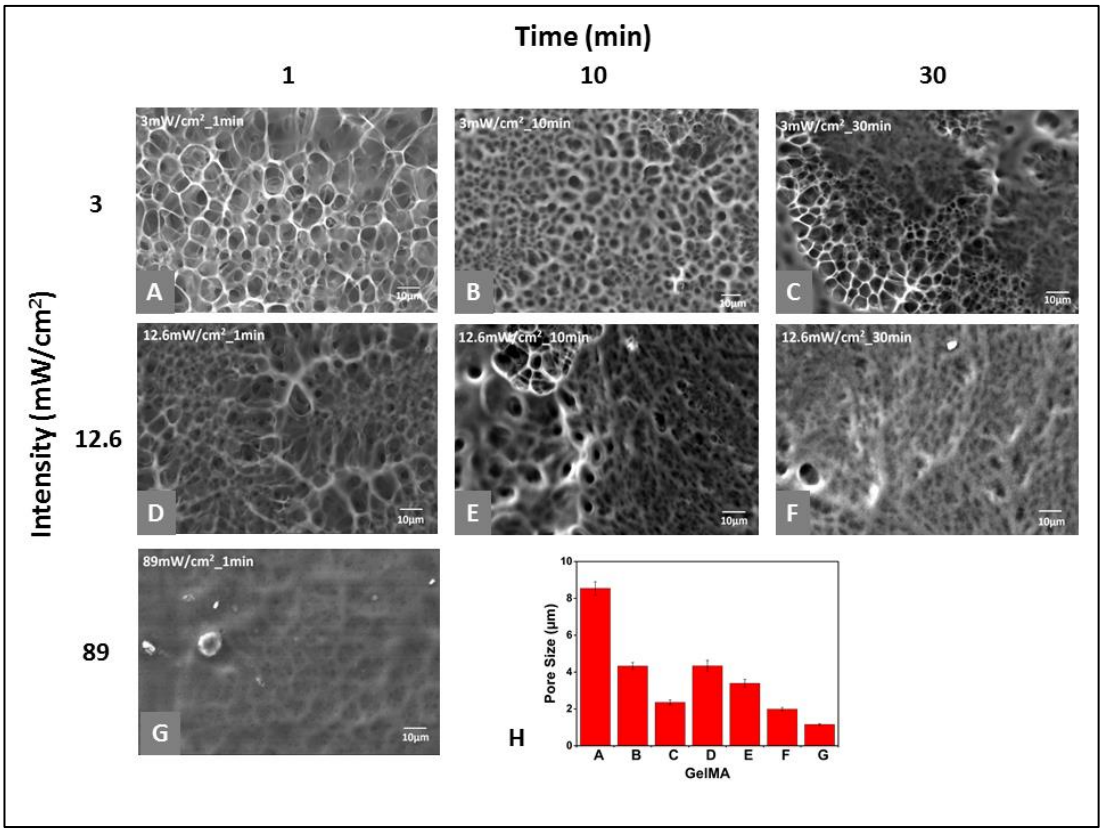

Figure 29: Surface structure of GelMA. (**A-G**) SEM images of GelMA samples prepared using different UV cross-linking intensities and exposure times. (**H**) Average pore size (measured from the SEM images) versus the UV crosslinking intensity and exposure time. Measured pore size for A = 8.54 ± 0.36 µm, B = 4.33 ± 0.19 µm, C = 2.36 ± 0.14 µm, D = 4.34 ± 0.3 µm, E = 3.39 ± 0.22 µm, F = 1.99 ± 0.09 µm and G = 1.16 ± 0.05 µm. Error bars represent standard error (n=3).

3.3.2 Young's Modulus of GelMA in Liquid

Representative AFM force versus indentation curves of each GelMA sample were overlaid for comparison (**Figure 30A**). The amount of indentation ranged between approximately ~0.9 µm for samples cured at the highest intensity of 89 mW/cm^2 (1 min exposure, red curve), indicating the stiffest hydrogel, and up to ~2 µm for the lowest intensity of 3 mW/cm^2 and same exposure time (1 min exposure, grey curve), indicating the softest hydrogel. In addition, there was a clear trend of increasing indentation, or effective decrease in hydrogel stiffness, with both decreasing exposure time and UV intensity. Each force curve was fitted by the Sneddon model to quantify the Young's modulus according to equation (8) and estimated modulus

values are given in **Figure 30B**. The modulus of the GelMA sample ranged from 0.16 ± 0.04 kPa at the lowest UV intensity of 3 mW/cm^2 (1 min exposure) up to 0.9 ± 0.1 kPa at the highest UV intensity of 89 mW/cm^2 (1 min exposure). Similar to the effective stiffness ascertained from the indentation, the modulus of the GelMA sample decreased linearly with both decreasing UV intensity and exposure time. Error bars for the Young's modulus in **Figure 30B** are due to variations in the modulus observed across the different XY positions within each sample, which was expected given the surface morphology of the hydrogels (**Figure 30A-G**) combined with the ability of the nanoscale AFM tip to probe highly localized changes in stiffness. We note that error in measured modulus values, typically in the order of ≈ 10-15%, may be due in part to systematic errors with the AFM measurements such as those associated with the spring constant calibration [234] and sensitivity measurement, as well as due to error in determination of the contact point and assumptions used in the Sneddon model. In previous work, the effect of total UV exposure on the compressive modulus of 20% GelMA and a photoinitiator concentration 0.05% Irgacure 2959 with an applied intensity of 2.7 mW/cm² was demonstrated in PBS and with different crosslinking parameters [126]. It was shown that the stiffness of GelMA samples was influenced by the UV exposure conditions, evidenced by a six-fold longer UV exposure time (from 5 min to 30 min) causing a tenfold increase in compressive modulus (~17 kPa to ~170 kPa) of 20 w/v% GelMA samples submerged in PBS.

Pore size values from **Figure 30H** and calculated energy (applied UV intensity x time) are also plotted in Figure 2B to enable correlation with the Young's modulus. The modulus showed a linear relationship with energy for a given UV intensity value. At 3 mW/cm^2, the modulus linearly increased with energy due to increasing exposure time from 1 to 30 min. A similar trend was observed for the UV intensity of 12.6 mW/cm^2. However, there was no absolute correlation with energy when comparing across the different UV intensities. For instance, despite having a lower or similar applied energy, the samples cured at 12.6 mW/cm^2 and exposure time of 1 min showed a significantly higher modulus than those samples cured at 3 mW/cm^2 for 10 and 1 min. Similarly, curing samples at 89 mW/cm^2 for 1 min, correspond to a

significantly lower or similar applied energy of 5.4 J/cm^2, resulted in the highest modulus of 0.9 ± 0.12 kPa. Conversely, the sample with the highest applied energy of 22.68 J/cm^2 (12.6 mW/cm^2 and 30 min exposure) corresponded to a slightly smaller Young's modulus of 0.72 ± 0.01 kPa (**Figure 30B**). These findings indicate that the applied energy cannot necessarily be used to determine the Young's modulus and that the effects of both UV intensity and exposure time on the cross-linking process need to be considered separately. In particular, high UV intensities may have disproportionate effects on hydrogel modulus and porosity compared to that expected based solely on the applied energy. A comparison of the GelMA pore size with the Young's modulus reveals that they are inversely correlated (Figure 2B). Young's modulus increased with increasing UV intensity and exposure time, whereas the pore size decreased. Therefore, GelMA/PPy-DBSA electrodes with larger pores are softer, while lower porosity leads to stiffer hydrogels.

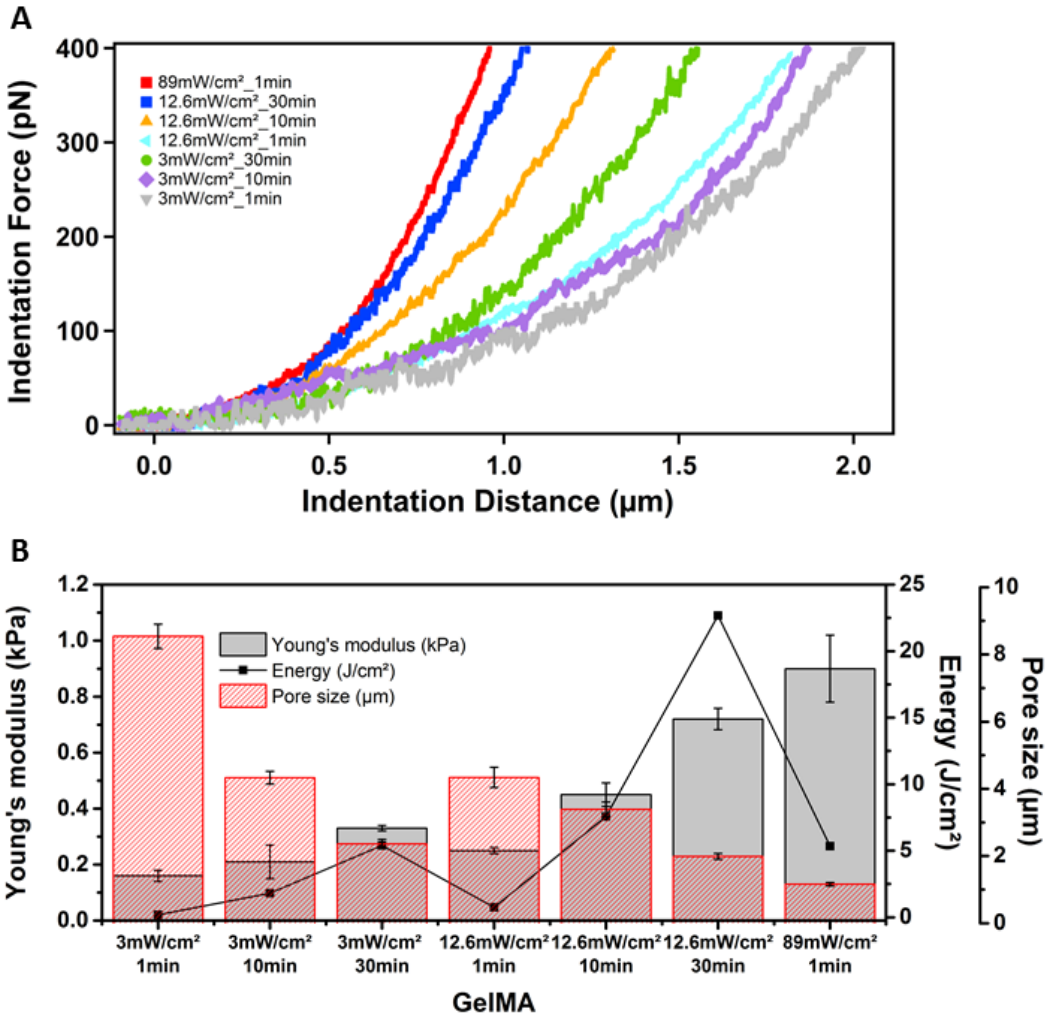

Figure 30: F-D curves of GelMA and its nanomechanical properties. (**A**) Representative F-D curves for each GelMA sample. Listed GelMA samples correspond to those in **Table *3***. (**B**) Plot of mean Young's modulus versus applied energy and versus pore size. Error bars represent standard error (n = 3).

3.3.3 Cyclic Voltammetry of GelMA/PPy-DBSA Electrodes

CV was performed in the same in-situ EC-AFM cell used for measuring the Young's modulus and actuation of the GelMA/PPy-DBSA electrodes, as described above in the method section. The configuration of the EC-AFM cell, consisting of the GelMA/PPy-DBSA electrode as working electrode, platinum mesh counter electrode and Ag/AgCl reference electrode, is also illustrated in **Figure 31A**. In the CV measurements, the bare PPy-DBSA film (solid black line) shows clear oxidation and reduction peaks at -

0.4 V and -0.6 V, respectively (**Figure 31B**). CVs of three GelMA/PPy-DBSA electrodes with increasing Young's modulus of 0.16 ± 0.04 kPa (3 mW/cm^2_1 min), 0.45 ± 0.04 kPa (12.6 mW/cm^2_10 min) and 0.9 ± 0.12 kPa (89 mW/cm^2_1 min) were also measured (**Figure 31B**). Despite the differences in their surface morphology (**Figure 31A**, **E**, **G**), porosity (**Figure 31B**) and indentation/modulus values (**Figure 31B**), all three GelMA-PPy-DBSA electrodes showed a similar electrochemical response. With the hydrogel layer, the oxidation and reduction peaks were slightly broader and more separated, with peak values of -0.45 V and -0.78 V, respectively (Fig. 3B). The peak current values also decreased slightly, collectively indicating an increase in the resistance due to the GelMA layer. Similar results were observed for GelMA samples coated on a pencil graphene electrode [235]. In this study, the reduction peaks clearly dropped with the addition of the GelMA coating, suggesting that the electron transfer was hindered [235]. The ionic conductivity of the different GelMA/PPy-DBSA electrodes, calculated from the resistance values obtained by Electrochemical Impedance Spectroscopy (EIS), showed that the transport of ions was not affected by the different curing conditions (data not shown). Therefore, despite the change in porosity, and even the presence of a skin layer for high UV intensity and exposure times, the ions can still freely diffuse in the gel. This indicates that the pores sizes are significantly greater than the threshold size for limiting ion diffusion, therefore enabling electroactivity throughout the thick GelMA samples.

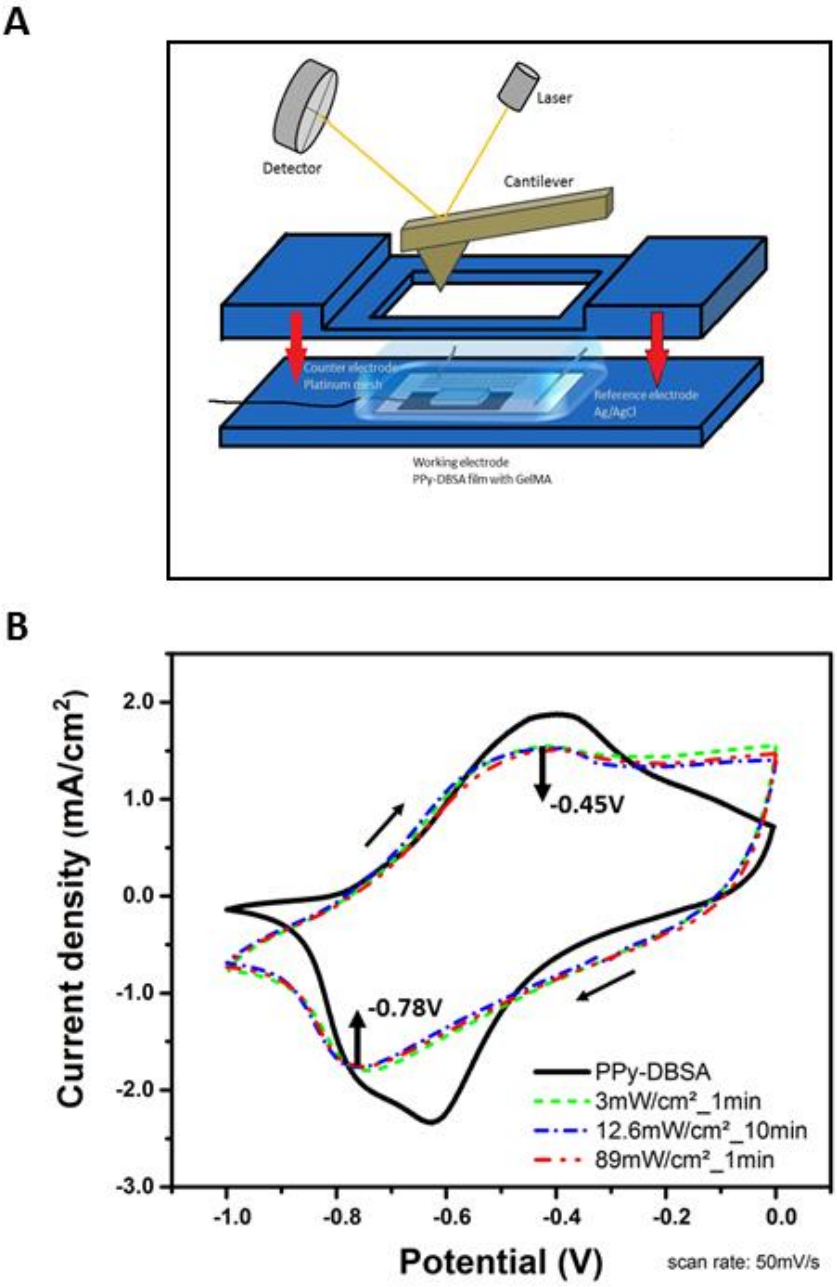

Figure 31: AFM Electrochemical cell and cyclic voltammograms. (**A**) Illustration of AFM electrochemical cell with GelMA/PPy-DBSA electrode as working electrode, platinum mesh as counter electrode and Ag/AgCl wire as reference electrode immersed in PBS. (**B**) Cyclic voltammogram of the plain PPy-DBSA film (black line) in a PBS aqueous solution. Cyclic voltammograms of three GelMA/PPy-DBSA electrodes using different irradiation conditions in PBS aqueous solution. GelMA cured with an UV intensity of 3 mW/cm² and an exposure time of 1 min (dotted green line). GelMA cured with an UV intensity of 12.6 mW/cm² and an exposure time of 10 min (dotted blue line). GelMA cured with an UV intensity of 89 mW/cm² and an exposure time of 1 min (dotted red line).

3.3.4 Mechanical Actuation

AFM was used to measure the displacement of the hydrogel in the z-direction (mechanical actuation) as the underlying PPy-DBSA film underwent expansion and contraction due to diffusion of electrolyte ions in and out the conducting polymer during an applied monophasic pulse (0 mV to -1000 mV). The AFM tip was placed in contact with the GelMA sample with an applied force of 500 pN and the feedback switched on. To maintain a constant applied force, the feedback adjusted the z-piezo height in response to the z-displacement in the GelMA sample. Hence, the z-piezo signal provided a measure of the actuation height, which was recorded simultaneously with the applied current and voltage. A representative measurement of the GelMA/PPy-DBSA electrode (12.6 mW/cm^2_10 min) is shown in **Figure 32A**, including the z-height, voltage and current signals during pulsed stimulation for 20 sec. Immediately after the pulsed stimulation from 0 mV to -1000 mV, there is an abrupt increase of ≈ 12 nm in the z-piezo signal within a few seconds and then the signal plateaus for the remainder of the pulsed period at -1000 mV (**Figure 32A**). Subsequently, during pulsed stimulation from -1000 mV to 0 mV or oxidation of the underlying PPy-DBSA film, the z-height signal again abruptly decreases and appears to show a non-linear component as it approaches the original surface height of the GelMA (**Figure 32A**). The above z-height changes occur for every pulsed cycle and therefore the measurements indicate the GelMA/PPy-DBSA electrode undergoes a reversible increase (reduction) and decrease (oxidation) in height, or actuation process, during the pulsed electrical stimulation.

To further understand the actuation process, a comparison of the actuation between a GelMA/PPy-DBSA electrode (89 mW/cm^2_1 min) and PPy-DBSA film only is given in **Figure 32B**. During actuation, the height of the GelMA/PPy-DBSA electrode abruptly increases and then plateaus, after which a slight linear decrease is observed during the plateau region, followed by a decrease with a non-linear component (**Figure 32B**). For the PPy-DBSA film only, the actuation height is significantly greater and similarly increases over < 1-2 seconds. During the plateau region there is an opposite linear increase in height, followed by a similar abrupt decrease in height

with a non-linear component at the end of the actuation process (**Figure 32B**). Therefore, once the steady-state current is reached, the GelMA/PPy-DBSA electrode effectively decreases in height, or contracts, while the PPy-DBSA film continues to expand. For the GelMA, it may be that the significantly reduced ingress of ions during steady-state is not sufficient to cause further actuation of the already expanded hydrogel that, having been placed under strain, elastically deforms (contracts) to a lower equilibrium strain state. Importantly, this difference in the actuation response of the GelMA/PPy-DBSA electrode versus the PPy-DBSA film implies that the GelMA actuation is influenced by mechanisms of ion diffusion and associated changes in its mechanical properties and is not entirely due to mechanical coupling with the underlying PPy-DBSA film (i.e. whereby the hydrogel is 'lifted up' by the PPy-DBSA film).

Overlaid current signals of the PPy-DBSA film and GelMA/PPy-DBSA electrode (89 mW/cm^2_1 min) (**Figure 32C**) show the peak current signal of the GelMA/PPy-DBSA electrode is approximately ± 15 mA compared to a value of ± 20 mA for the PPy-DBSA film (**Figure 32C**), indicating that the addition of the GelMA causes an ≈ 25% decrease in the current. In contrast, the actuation height of the GelMA/PPy-DBSA electrode drops significantly more by ≈ 60 %. Given that this % decrease in the GelMA actuation is significantly greater than that expected if the process was purely based on the current signal, then this comparative difference between the current and actuation signal may assist in understanding the actuation originating from the GelMA versus the PPy-DBSA film. In this case, one could imply that there is a separate actuation mechanism process of the GelMA (i.e. not purely coupled to the underlying PPy-DBSA film as mentioned above) that contributes to a smaller actuation height in the GelMA/PPy-DBSA electrodes.

Differences between the GelMA/PPy-DBSA electrode and PPy-DBSA film were also observed for the extent of actuation in response to different stimulation frequencies (**Figure 32D**). At longer pulse durations of 10 and 20 sec, the actuation height of the PPy-DBSA films (≈ 30 nm) was significantly greater than the GelMA/PPy-DBSA electrodes (≈ 10-15 nm). However, there was no significant difference in the

actuation height between the PPy-DBSA film (≈ 5 nm) and GelMA/PPy-DBSA electrode (≈ 5-7 nm) when the pulse duration was shortened to 1 sec (**Figure 32D**). Similarly, for the different GelMA/PPy-DBSA electrodes, the actuation height was greater at longer pulse duration times and significantly decreased at the shortest time of 1 sec. The decrease in actuation is due to time-limited diffusion processes where the extent of actuation is limited by the rate (e.g. 20, 10 and 1 sec) and distance of ion transport in and out of the polymer [236]. Comparatively, however, this effect of pulse frequency was more pronounced for the PPy-DBSA film compared to the GelMA/PPy-DBSA electrode. For example, the PPy-DBSA film actuation decreased by ≈ 80 % compared to ≈ 50% when the frequency was increased from 0.1 Hz (1 sec) up to 1 Hz (10 sec), as indicated by the difference in their red and blue bars, respectively in **Figure 32D**. While the absolute magnitude of the GelMA/PPy-DBSA electrode actuation is lower, the reduced sensitivity of the GelMA/PPy-DBSA electrode to the time-limited ion diffusion process may correlate to improved accessibility of ions due to bigger pores sizes of the GelMA/PPy-DBSA electrode and/or the presence of ions already existing within the hydrated gel. Moreover, the ionic conductivity for all GelMA samples was measured at ± 15 mS/cm, which supports their similar actuation heights at the different stimulation frequencies. Using a GelMA/Gold electrode (89 mw/cm^2_1 min) instead of a GelMA/PPy-DBSA electrode resulted in no actuation, indicating that the expansion and contraction is due to the ionic current and redox processes generated by the PPy-DBSA film.

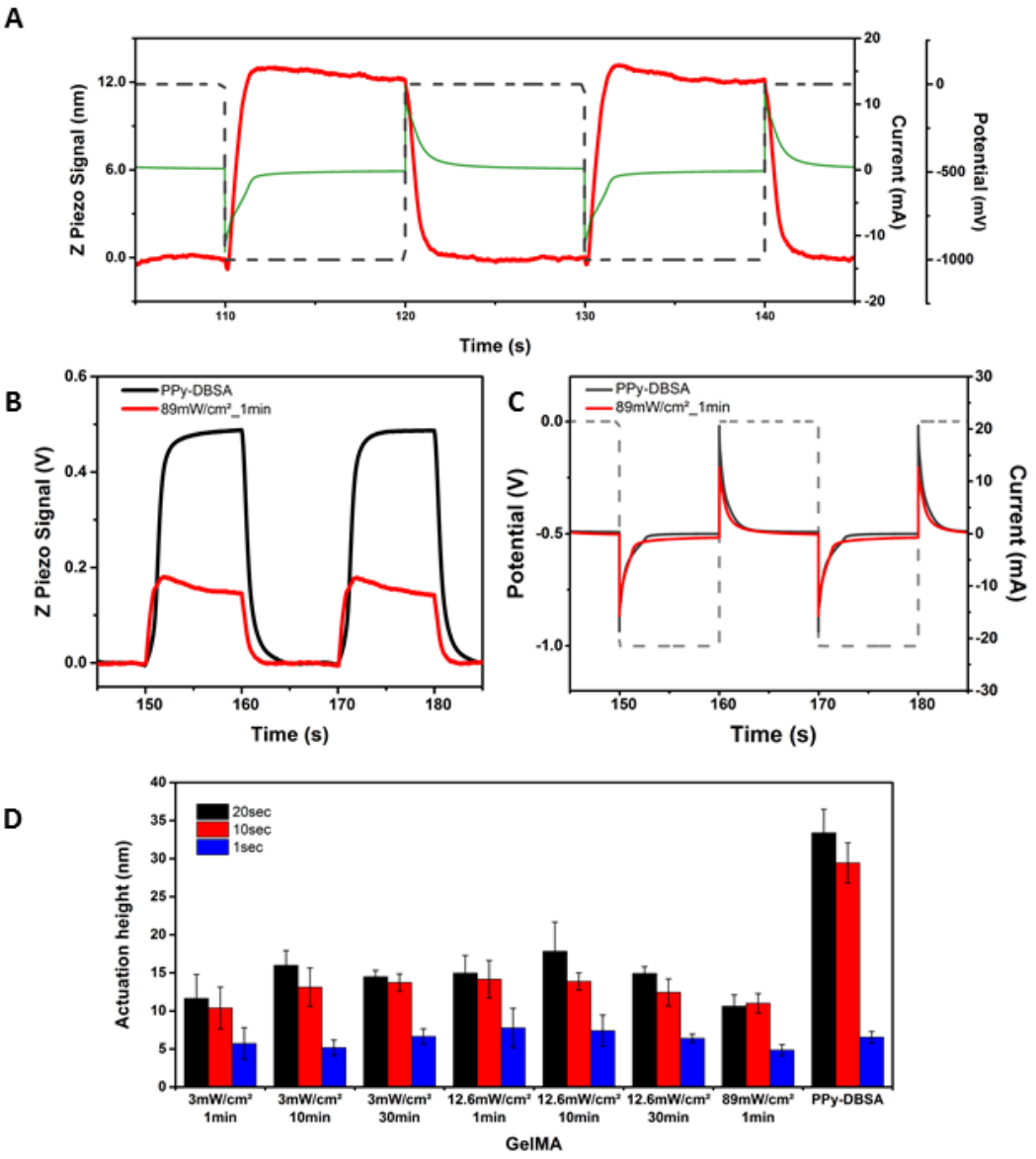

Figure 32: Representative data for actuation of GelMA/PPy-DBSA electrodes. (**A**) Prepared using irradiation conditions of 89 mW/cm^2_1 min for monophasic stimulation with a frequency of 20 sec. Thick red line represents the Z piezo signal (actuation height), green line represents the current signal and black dashed line represents voltage signal. (**B**) Comparison of actuation PPy-DBSA film (black trace) versus 89mW/cm^2_1min GelMA/PPy-DBSA electrode (red trace) for pulse frequency of 20 sec. (**C**) Comparison of the current signal for PPy-DBSA (black trace) versus 89mW/cm^2_1min GelMA/PPy-DBSA electrode (red trace) with a pulse frequency of 20 sec. (**D**) Bar graphs of mean actuation height of each GelMA/PPy-DBSA electrode compared to PPy-DBSA for different pulse frequencies of 20 sec, 10 sec and 1 sec. Error bars represent standard error, (n = 3).

While the actuation of the GelMA versus the PPy-DBSA film cannot be unequivocally decoupled due to the need of having a GelMA top layer with an underlying conducting polymer to enable this type of study, the observations above indicate that the GelMA/PPy-DBSA electrodes and PPY-DBSA films show different responses in their actuation. The comparative difference in the change of the current signal relative to the actuation height, the differing effect of frequency, and their opposing expansion/contraction during the stead-state current, collectively suggest that separate actuation of mechanisms of the GelMA are likely to be occurring.

The driving force for actuation of the GelMA/PPy-DBSA electrodes can be explained by redox processes specific to the underlying PPy-DBSA film. The actuation mechanism of PPy-DBSA films has previously been described and measured by Wu et al. (2007) and additionally with the use of AFM by Higgins et al. (2009) and Smela et al. (2001) [236-238]. In the oxidized polymer state, immobile $DBSA^-$ balances positive charges of the PPy^+ chain, while during reduction the PPy becomes neutral, causing excess negative charge due to immobile $DBSA^-$ in the polymer. The latter is charged compensated by the influx of cations (and associated solvent) from the electrolyte, thereby causing expansion of the polymer. This cation-driven actuation process is reversible and contraction of the polymer is then caused by ejection of ions during oxidation [239, 240]. As a result, volume, strain and osmotic changes occur within the polymer and expansion or bending of the polymer can clearly be observed [239-241]. When correlating this process with the change in actuation of the GelMA/PPy-DBSA electrode (**Figure 32A**), it is confirmed that expansion of the hydrogel occurs during reduction, or the ingress of cations, and contraction occurs during the ejection of the cations, indicating that volume changes likely play a major role in the actuation process.

When an electric field is applied to other hydrogel systems such changes have previously been attributed to volume changes [242]. The volume change is described as a phase transition of the hydrogel, which is divided into three parts: the charged polymer network, counterions and the electrolyte. Furthermore, the phase transition is mainly due to three forces (collectively recognised as osmotic pressure)

acting on the gel, including the negative pressure due to the polymer-polymer affinity, the rubber elasticity of the polymer network, and the counterions pressure [94, 95]. More recently, Glazer et al. (2012) have summarzied the main mechanisms attributed the bending of gels within an electric field, including 1.) the coulombic mechanism where the electrical field exerts a net force on mobile ions and charged groups of the polymer, 2.) the electroosmosis mechanism where water transport associated with migration of the gel's counterions induces the gel to local swell/contract, 3.) the electrochemical mechanisms involving changes in pH and 4.) the dynamic depletion/enrichment mechanism involving the accumulation (depletion) of ions on both sides of the gel at the solution interface, causing a shift in local ionic strength that induces bending [91]. In their work on polyacrylamide gels, they attribute gel bending to the latter mechanims though the effect of pH may also play a role when the gel is close to the electrode [91]. Theoretical studies describing the shrinking and swelling of gels in contact with an electrode.

3.3.5 Effect of Electrical Stimulation on Young's Modulus

CV measurements were cycled between 0 mV and -1000 mV with a scan rate of 100 mV/s while simultaneously collecting continuous force curves at four different XY positions. Three different GelMA samples with increasing Young's modulus from 0.16 ± 0.04 kPa (3 mW/cm^2_1 min), 0.45 ± 0.04 kPa (12.6 mW/cm^2_10 min) up to 0.9 ± 0.1 kPa (89 mW/cm^2_1 min) were used and measurements repeated on 3 replicate samples. **Figure 33A** shows representative current, potential and cantilever deflection signals acquired over time during five CV cycles from 0 mV to -1000 mV for the sample cured at 3 mW/cm^2 and 1 min exposure. The deflection signal is representative of 4 force curve measurements, including the approaching and retracting portions, as a function of time. A single force curve occurs between 175 sec and 200 sec with the observed positive (slope) increase in the deflection signal, or indentation of the GelMA/PPy-DBSA electrode occurring between 180 – 190 sec

(**Figure 33B**). The subsequent decrease in the cantilever deflection signal corresponds to retraction of the tip and unloading of the force from the surface.

As mentioned, the positive increase in the deflection signal, or tip-sample contact region of the force curve, represents the indentation of the polymer and is fitted with the Sneddon model to quantify the modulus. This part of the force curve occurs over a period of ≈ 10 secs, thus the modulus is effectively calculated over a voltage-range in the CV. Four different voltage-ranges in the CV were sampled and this can be understood in **Figure 33A** that shows the tip-sample contact region of the 4 force curves occurring over different time-periods, or voltage-ranges, in the CV. Two of the voltage-ranges encompassed either the oxidation and reduction potentials of the polymer, while the other two voltage-ranges occurred during either the anodic and cathodic sweeps of the CV.

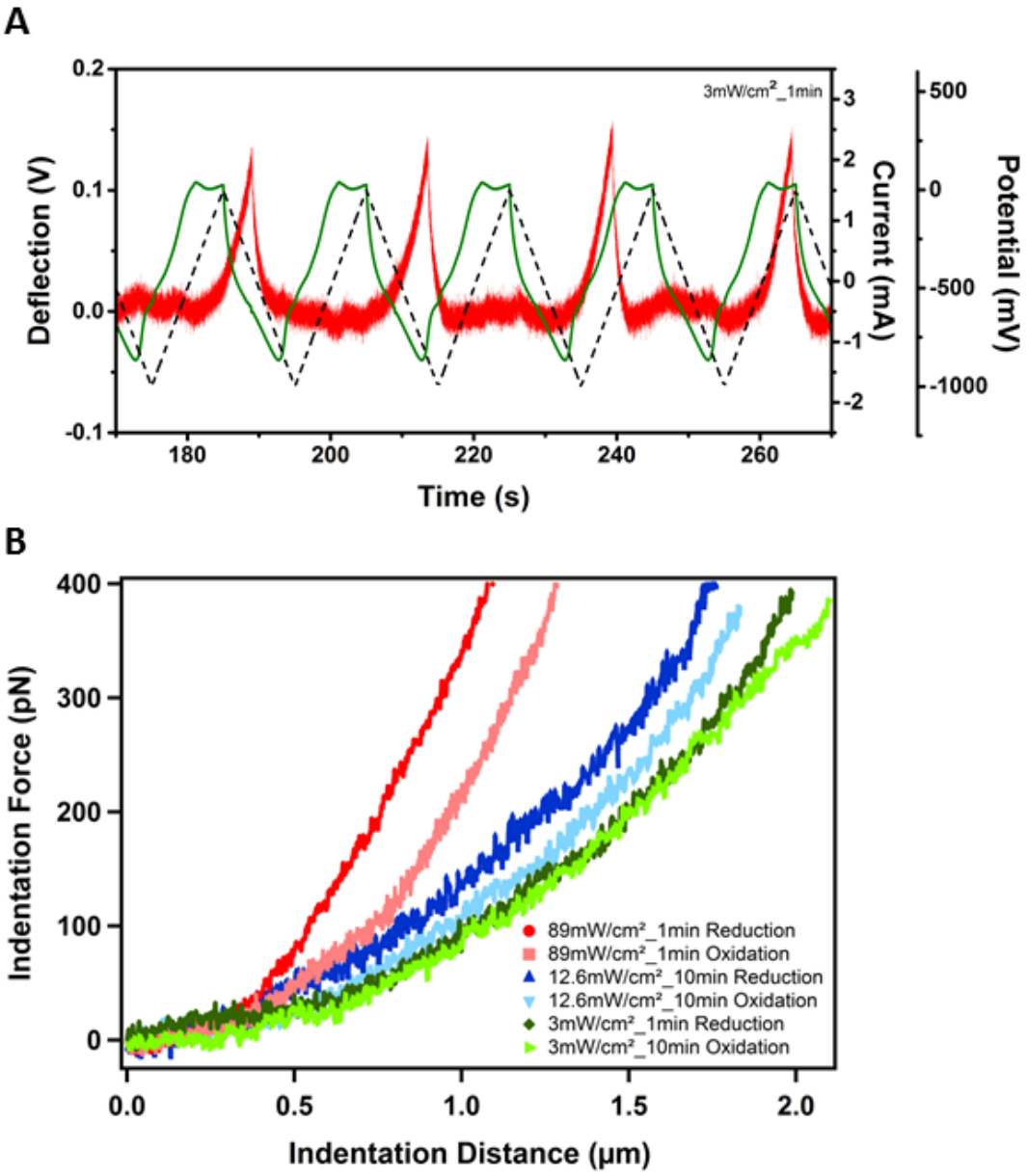

Figure 33: F-D curves of GelMA as function of electrical stimulation. (**A**) Example data for GelMA obtained using irradiation condition of 3 mW/cm^2_1 min as function of triangle waveform voltage stimulation and four continuous force curves. Thick red line represents the deflection of the cantilever, green line represents the current signal and dashed black line represents the voltage signal. (**B**) Representative force versus indentation curves as a function of electrical stimulation for three chosen GelMA/PPy-DBSA electrode samples during reduction and oxidation.

Force versus indentation curves taken on the three differently UV cross-linked GelMA/PPy-DBSA electrodes showed that the total indentation distance was greater during oxidation compared to reduction (**Figure 33B**), with the effect more pronounced for the higher modulus GelMA samples cross-linked at 12.6 mW/cm^2_10 min and 89 mW/cm^2_1 min and indicating that the GelMA becomes softer during oxidation and stiffer during reduction. The effect of electrical stimulation on Young's modulus is further presented in **Figure 34A** that shows the CV measurements with overlaid color traces representing the different voltage ranges, or segments in the CV, over which the modulus was calculated from fitting the tip-sample contact region of the force curves. For the higher modulus GelMA (89 mW/cm^2_1 min) (Figure 6C), a modulus of 811 ± 21 Pa was obtained during the anodic sweep (dark red), which decreased to the lowest modulus of 640 ± 85 Pa at the oxidation potential (light red). The modulus then increased slightly to 695 ± 118 Pa during the reverse cathodic sweep (dark blue) until reaching the highest modulus of 966 ± 123 Pa at the reduction potential (light blue). Both of the other GelMA/PPy-DBSA electrodes showed a similar pattern in the modulus change over the different segments in the CV (**Figure 34B-C**) and **Figure 34D** shows a quantitative comparison of all modulus values. In particular, the greatest change in the dynamic modulus occurred when switching between the segments associated with the oxidation (light blue bar) and reduction (light red bar) potentials (**Figure 34D**), with the anodic (dark red) and cathodic (dark blue) sweeps giving intermediate values. Interestingly, this dynamic change in modulus showed a dependence on the stiffness of the GelMA samples and was most significant for the highest modulus GelMA sample compared to the softer GelMA samples (**Figure 34D**).

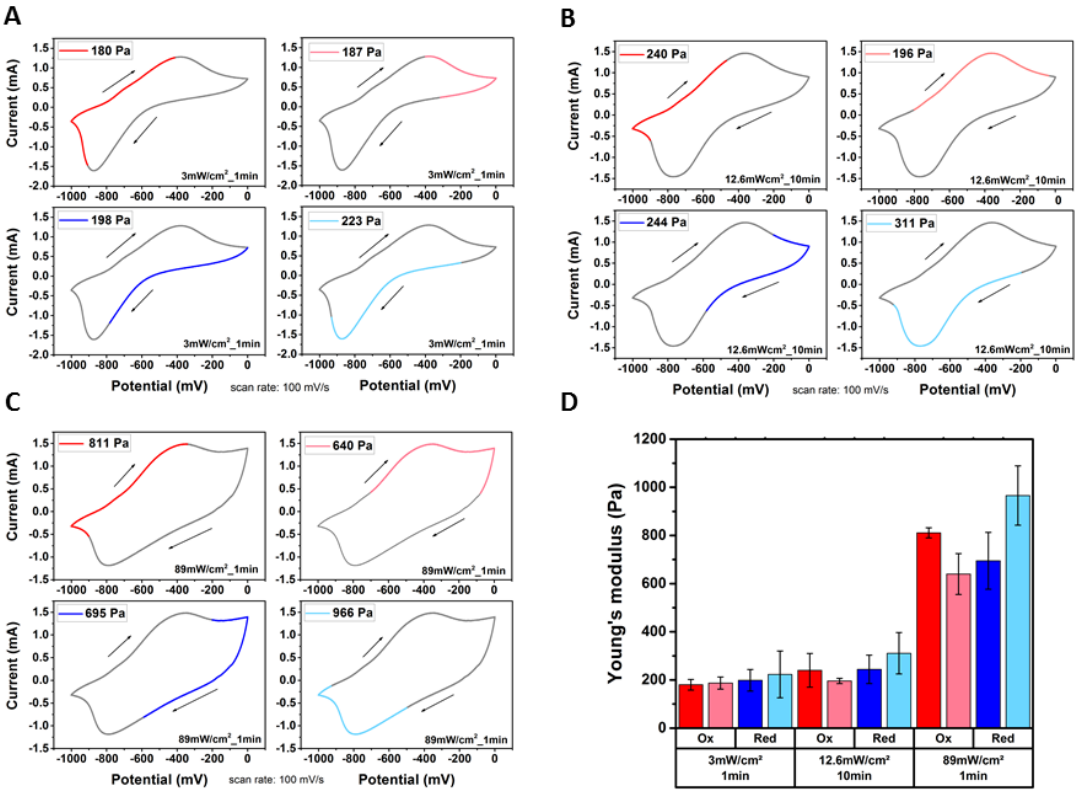

Figure 34: Cyclic voltammograms of three GelMA/PPy-DBSA electrodes. (**A-C**) CVs are obtained using irradiation condition of 3mW/cm2_1min, 12.6mW/cm²_10min and 89mW/cm²_1min. The average Young's modulus value given in each CV correlates to the measured value obtained over the voltage range indicated by the color trace overlaid on the CV. The voltage ranges encompass the anodic sweep (dark red), oxidation potential (light red), cathodic sweep (dark blue) and reduction potential (light blue). (**D**) Chart of mean Young's modulus for the different voltage ranges correlating to the color traces in the CV's. Error bars represent standard error (n = 3).

3.4 Conclusion

Here we show that the expansion of the GelMA/PPy-DBSA electrode occurs during reduction, or when ions move into the gel and towards the PPy-DBSA film (**Figure 32A**). Subsequently, the gel contracts during the oxidation process or when the ions move out of the PPy-DBSA film through the GelMA (**Figure 34A**). Thus, this dynamic change in the gel, or more specifically during reduction, correlates with an increase in the Young's modulus and is likely due to an associated increase in the volume change and osmotic pressure produced by counterions as the gel expands [95]. The process is reversible and therefore a decrease in the modulus occurs upon oxidation, as the ions move out of the gel (osmotic pressure decreases) causing contraction (**Figure 34A-C**).

This dynamic change in the modulus during oxidation and reduction of the GelMA/PPy-DBSA electrodes is likely related to the crosslinking density and strength, and/or the degree of porosity. Sun et al. (2001) investigated the modulus dependence of CS/PEG fiber gels on their crosslinking density, with more highly crosslinked gels having lower chain mobility, decreased rubber elasticity and a higher modulus [93]. Higher Young's modulus, or more highly crosslinked GelMA/PPy-DBSA electrodes, with lower chain mobility and decreased pore size, may result in a higher osmotic pressure within the hydrogel and hence greater dynamic modulus change during oxidation and reduction [93]. In addition, Sun et al. (2001) showed for CS/PES fiber gels that ions diffuse easier through larger pores and causes a decrease in modulus due to the higher water content, which may also be a contributing factor [93].

In conclusion, we present novel insights on the electro-mechano responses of GelMA/PPy-DBSA electrodes that is increasingly being used in tissue engineering and biofabrication applications. By applying EC-AFM, we have demonstrated the ability to probe the dynamic changes in the hydrogel physical properties, including actuation and Young's modulus, which are reversibly controlled via electrical stimulation. We propose that the enabling nanoscale characterization and electrical modulation of the hydrogel coatings can be further investigated to better understand

the electro-induced actuation mechanisms of hydrogels, as well as the dynamic physical properties and interactions of hydrogel-electrode systems.

Chapter 4:

Effect of Modulus and Altered Peptide Binding Motifs on Single Human Neural Stem Cell Interactions with Gelatin Methacrylate Hydrogels as Revealed by SCFS

4.1 Introduction

Hydrogels have the potential to mimic native ECM via their mechanical, physical or viscoelastic properties, to support *in-vitro* and *in-vivo* cell development [243]. They are widely used in tissue engineering [64] and biomedical applications [244, 245], including tissue replacement, wound healing [62, 63], drug release [246, 247] and contact lenses [248]. Due to their tunable stiffness via different cross-linking strategies, they are extensively used to study the effect of mechanical properties on cell differentiation (for reviews see [79, 108, 243, 249]).

GelMA is a hydrogel that has undergone rapid development in tissue engineering and regeneration, including cartilage repair, wound healing and neural *in-vitro* models [121, 126, 132, 222]. GelMA is emerging as a common reagent or 'bioink' in 3D bioprinting due to its thixotropic and cell encapsulation properties [221]. It is composed of collagen-derived gelatin modified with methacrylate groups, and through addition of a photoinitiator, enables a photopolymerizable, patternable hydrogel that maintains the properties of gelatin [120, 122]. As a derivative of collagen, GelMA contains ECM peptides, including the well-known RGD tri-amino acid sequence for recognition and binding of cell adhesion molecules. Liu et al. (2008) found that increasing the density of RGD domains in cross-linked, artificial ECM films caused increased HUVECs adhesion and spreading [250]. Further studies have shown that HUVECs spread more rapidly on artificial ECM containing RGD compared to

those with fibronectin [251]. Fibroblast cell adhesion and spreading was significantly promoted on PEG substrates crosslinked with GelMA [252]. Moreover, Nichol et al. (2010) investigated HUVECs seeded on micropatterned GelMA substrates that enabled cells to readily adhere, proliferate, elongate and migrate [121]. More recently, bovine articular chondrocytes encapsulated in GelMA showed that the stiffest hydrogel produced rounder morphology, highest expression of Collagen II, and highest capacity of maintaining the chondrocyte phenotype [253]. This work was achieved by altering the degree of methacryloyl functionalization whilst maintaining the same concentration of GelMA and RGD density to give hydrogels with different modulus in the range of ~ 5 - 30 kPa.

Mechanisms of stem cell recognition and de-adhesion, i.e. the forces required to detach a cell, on hydrogels are poorly understood yet such information is critical in different feedback mechanisms enabling cells to sense and respond to material surfaces [107, 254-256]. With the increasing demand for GelMA in the aforementioned applications, it is important to gain an understanding of hydrogel-cell interactions, especially those governed by inherent cell-binding peptides in combination with tuneable stiffness of the polymer network. From a materials design perspective, one consideration is that typically measured bulk properties, e.g. compressive modulus of the hydrogel scaffold, may not adequately describe the nanoscale components and their properties, e.g. the rheology of single polymer chains [257], which are expected to participate in physical interactions and binding of cell adhesion molecules occurring on equivalent length scales [258]. Megone et al. (2018) compared mechanical properties of gels at different length scales using rheology, indentation and atomic force microscopy, revealing a discrepancy between the local and bulk mechanical properties [259]. Furthermore, to understand why mesenchymal stem cell morphology and differentiation was unaffected by different cross-linking densities of polydimethylsiloxane (PDMS), Chen et al. (2013) used AFM nanoindentation to characterize the viscoelastic and adhesion surface properties. They showed that the lowest crosslinked PDMS exhibited the highest surface adhesion, indicating coupling effects of nanoscale properties that are not easily ascertained from bulk properties and which could

potentially affect cell adhesion [260]. Similarly, the natural, polymer network of GelMA is likely to exhibit significant nanoscale heterogeneity, with variations in single GelMA polymer chain properties such as viscoelasticity, density of crosslinks, and RGD groups [261-263]. Therefore, further investigation of the physical, molecular interactions involved in cell recognition and adhesion will aid in understanding rational materials design of hydrogels.

Optical techniques are typically used to observe the live cell adhesion, including processes such as cell spreading or detachment. Alternatively, observations can be made by fluorescent labeling of cell adhesion molecules and focal adhesion complexes. Conventional adhesion assays such as washing and shear-force assays enable quantification of cell adhesion forces [173], however, they do not provide the molecular-level details. Therefore, amongst the single cell adhesion techniques, e.g. optical tweezers, biomembrane force probe, micropipette aspiration and AFM, this chapter uses the AFM-based approach, SCFS.

SCFS is an established technique increasingly used to measure single cell and receptor interactions with extracellular matrix proteins [180, 184, 190], cell–cell interactions [264] and cell interactions with chemically functionalized surfaces and materials [48, 173, 197, 265]. SCFS has made a significant impact by elucidating molecular mechanisms of integrin-ECM adhesion (e.g. collagen) [197], including the early stages of adhesion, receptor crosstalk [200] and effect of culturing agents. A detailed practical guide on SCFS and its advantages-disadvantages as a single cell measurement technique have recently been described [184]. More recently, SCFS studies have been used to study cell adhesion on conducting polymers [48, 266] and polyacrylamide hydrogels [207]. In contrast to conventional cell adhesion measurements that are typically conducted on cells that have established adhesion over longer time periods, e.g. in cell culture for > 30min and up to hours or days, the SCFS enables control of cell–substrate contact times on the order of seconds up to several tens of minutes. On second timescales, single integrin bond complexes can form and their unbinding is detected to understand initial cell recognition and de-adhesion, i.e. unbinding of integrin complexes, with a material surface [190, 267].

Furthermore, the ability to repeatedly probe molecular interactions of the same cell on a material surface is important for gaining access to temporal and dynamic processes occurring at the molecular level [48].

In this chapter, the SCFS experiments involve attaching a single living fibroblast (L929) or hNSC onto a tipless AFM cantilever, which is brought into contact with the GelMA surface and force measurements are undertaken to elucidate the interactions involved in initial stages of cell de-adhesion. To investigate the effect of hydrogel modulus on the single cell adhesion, we prepared the GelMA with three different moduli (900 Pa, 450 Pa and 160 Pa) in the range of neural tissue (~ < 1 kPa). During the SCFS experiments, anti-integrin antibodies are also introduced to determine the involvement of principal hNSC integrins and their subunits in cell recognition and de-adhesion on the GelMA. The findings reveal significant effects of hydrogel modulus on cell de-adhesion, including the underlying mechanisms of elastic interactions of GelMA polymer chains and occurrence of dynamic force regimes. Furthermore, we observe a combined effect of modulus and activation of integrin-mediated adhesion mechanisms, which may instruct the molecular design of hydrogels to exert effects on stem cells.

4.2 Materials and methods

4.2.1 Reagents

The pyrrole (Py) monomer was obtained from Sigma Aldrich and distilled prior to use. Dodecylbenzenesulfonate (DBSA) was used as the dopant and was obtained from Sigma Aldrich. GelMA monomer was synthesized following the protocol described by O'Connell et al. (2016) as a freeze-dried material with methacrylate degree of 72% [229]. GelMA solutions were prepared using PBS and a photoinitiator, Irgacure 2959 in 100% ethanol, which were both obtained from Sigma Aldrich.

4.2.2 Preparation of PPy-DBSA Films

The PPy film doped with DBSA (PPy-DBSA film) was grown by electrodeposition at constant current on gold coated Mylar (gold-mylar) electrode. The gold-mylar was firstly prepared by cutting it into 2.2 cm x 2.2 cm area and cleaned with Milli-Q water (18.2 MΩ*cm) and UV exposure. An aqueous solution of 0.2 M Py and 6 mM of the counter-ion dopant DBSA was degassed for 2 min prior to polymerization of the monomer. The PPy-DBSA film was electrodeposited on gold-mylar with a current density of 0.25 mA/cm² for 3 min using an eDAQ EA161 potentiostat in a JPK Electrochemical Cell (ECCell^{TM}) to have PPy-films compatible to the JPK AFM-setup. The gold-mylar was used as working electrode, a platinum mesh as counter electrode and a Ag/AgCl NaCl 3M as the reference electrode (DRIREF-2SH, World Precision Instruments). Afterwards, the films were washed with Milli-Q water, gently dried with N2 gas and stored in a petri dish until use [53].

4.2.3 Preparation of PPy-DBSA films coated with GelMA hydrogel

GelMA hydrogel coatings on PPy-DBSA films were prepared according to our previous study [134]. PBS was prepared at pH 7.4 in Milli-Q water (18.2 MΩ*cm). Freeze dried GelMA (1 g) was dissolved in 5 ml PBS in a water bath at 37 °C. Aliquots of 500 µl GelMA solution were prepared in Eppendorf tubes, each sealed with parafilm and stored at 4 °C until use. GelMA hydrogels were prepared by warming the GelMA solution in a water bath at 37 °C for 5 min, followed by dissolution in PBS to 10% GelMA with 0.5% Irgacure 2959. The mixture was then cast onto the PPy-DBSA film within a 0.5 cm x 1.0 cm acrylic frame with a height of 1 mm that was fabricated using laser cutting with a PLS6MW laser engraver from Universal Laser Systems (ULS). More specifically, the PPy-DBSA film was held within the acrylic frame using a clamp and then the GelMA solution cast to completely cover the film and fill the entire volume of frame area, giving a GelMA thickness of ~ 1 mm. The GelMA hydrogel was crosslinked using a UV Curing Spot Light Device “Blue Wave 50” from DYMAX (USA)

by UV-light exposure with a wavelength of 365 nm. Different intensities and exposure times (**Table *4***) were applied for the crosslinking of GelMA to prepare samples with different moduli and porosity, as characterized in our previous study [134]. **Table *4*** shows three GelMA hydrogels of different modulus that were used in experiments. The PPy-DBSA film was used as underlying support substrate, as it enabled good adhesion to immobilize the top GelMA layer and also intended to be used in future studies whereby electrical stimulation can be applied through the GelMA, as demonstrated in previous work [134]. Therefore, despite the underlying PPy electrode, no electrical stimulation was applied in this work. After curing the GelMA on top of the PPy-DBSA film, the GelMA hydrogel was immersed in a small petri dish filled with PBS and stored at 4 °C overnight to ensure a fully hydrated hydrogel. Afterwards, it was sterilized in 70% ethanol for 15 min, washed 3 times in PBS and stored at 4 °C until use.

Table 4: Crosslinking conditions and nanomechanical properties of GelMA. Asterisks * values measured from previous study [134].

Sample	GelMA (w/v %)	I2959 (w/v %)	Intensity (mW/cm^2)	Curing time (min)	Energy (J/cm^2)	Young's modulus* (Pa)	Pore size* (µm)
Soft	10	0.5	3	1	0.18	160	8.54
Medium	10	0.5	12.6	10	7.56	450	3.39
Stiff	10	0.5	89	1	5.34	900	1.16

4.2.4 Cell culture

Mouse Fibroblast (L929) cell lines

L929 cell lines were originally sourced from ATCC (CCL-1TM). L929 cells were cultured in Dulbecco's Modified Eagle's Medium (DMEM) (12800017, Life Technology) supplemented with 10% Fetal Bovine Serum (FBS) (10099141, Life technology). Cells were cultured at 37 °C in a humidified 5% CO_2 atmosphere (HERA cell 150, Thermo)

and were subcultured every second to third day by splitting 1 in 10 after trypsinizing with 0.25% trypsin to achieve the desired cell density. Before the experiments, L929 cells were cultured to 90%–100% confluency of the cell culture flask. More specifically, old medium was removed from the cell culture flask and then rinsed with 5 ml PBS. To remove cells, trypsin (0.25%, 0.5 ml) was added, and the cell culture flask was stored in a humidified 37 °C incubator for 1–2 min. Five ml of fresh cell culture medium was then added to the flask, the cell suspension was transferred to a 15 ml centrifuge tube and centrifuged at 1500 rpm for 5 min, and the supernatant was removed. Cells were then resuspended in 1 ml CO_2 independent cell culture medium (18045-088, Life Technology) that is capable of maintaining long-term pH stability under atmospheric CO2 (0.04%) without proteins. One ml of CO_2-independent medium containing cells with a concentration of approximately 80,000/ml cells was then transferred into a 5 ml centrifuge tube and 300 µl injected into the JPK electrochemical cell for single cell attachment onto AFM probes described in section 4.2.6 below.

Human Neural Stem Cells (hNSCs)

ReNcell VM hNSC (SCC008, Millipore; approved for use by the University of Wollongong's Human Research Ethics Committee; HE14/049) culture was performed and cells were provided by co-supervisor Dr. Eva Tomaskovic-Crook for subsequent SCFS experiments according to previous methods [268]. Briefly, cells were retained in 6-well culture plates (Corning, Mulgrave, Australia) coated with 10 µg/ml laminin (Invitrogen). Cells were initially seeded at a density of 96 x 10^3 cells in 2 ml Complete NeuroCult Proliferation Medium (human); STEMCELL Technologies) and maintained in a humidified incubator at 37 °C with 5% CO_2. Cells were monitored daily and a half-volume media change performed every 3-4 days. Cell passaging was performed every 7 days by digesting in 0.5 ml pre-warmed TrypLE (Gibco BRL) for 3 min at 37 °C. Following digestion, TrypLE was neutralized by adding 1 ml Complete NeuroCult Proliferation Medium and cells were gently resuspended in solution followed by

centrifugation at 190 x g for 3 min. After removal of supernatant, cells were resuspended in fresh pre-warmed Complete NeuroCult Proliferation Medium and reseeded as described above for further subculture and/or experimentation. One ml of CO_2-independent medium containing cells with a concentration of approximately 80,000 cells/ml was then transferred into a 5 ml centrifuge tube and 300 µl injected into the electrochemical cell for single cell attachment onto AFM probes described in section 4.2.6 below.

4.2.5 AFM Probe Functionalization

AFM probe functionalization to enable attachment of live single cells was done based on previous work [184] and following our recent studies [48, 204]. Firstly, tipless probes (NP-O10) obtained from Bruker were calibrated for their spring constant (~0.06 N/m) using the thermal noise method [269] (nb: the subsequent chemical functionalization did not affect the spring constant values). The probes were incubated at 37 °C in 0.5 mg/ml biotin-BSA (Sigma A6043) solution obtained from Sigma overnight, followed by washing in PBS three times. The probes were then incubated in 0.5 mg/ml streptavidin (Sigma S4762) solution for 30 min at room temperature, followed by further rinsing with PBS three times. Finally, the probes were incubated in 0.4 mg/ml Concanavalin-A-biotin (Sigma C2272) solution for 30 min at room temperature and washed with PBS three times. The probes were stored up to one week immersed in PBS at 4 °C. After usage the cantilevers were cleaned in sulfuric acid for 2 hrs and rinsed with Milli-Q water. Cleaned cantilevers could be reused and were calibrated again prior to each functionalization.

4.2.6 Single Cell Force Spectroscopy

Attachment of Single Cell onto AFM Probes

SCFS was performed using a JPK Biowizard II Atomic Force Microscope (JPK, Germany) mounted on a fully automated Nikon inverted optical microscope. The AFM-inverted optical microscope was fully enclosed in a cell incubation system for temperature and humidity control. The GelMA-PPy film was placed in a JPK 3-electrode electrochemical cell of the AFM and 600 µl of CO_2-independent medium was injected into the electrochemical cell. The Concanavalin functionalized tipless cantilever was then lowered to be approximately 50 µm above the GelMA hydrogel surface while heating was applied to enable the CO_2-independent media to reach thermal equilibration at 37 °C. A further 300 µl of CO_2-independent medium containing cells with a concentration of approximately 80,000/ml cells was then injected into the electrochemical cell and the cells allowed to settle onto the GelMA hydrogel surface for a period of 5-10 min. Rounded up cells that were yet to adhere to the GelMA hydrogel surface were located with the optical microscope and the functionalized AFM probe was positioned over a single cell. The cell was attached manually to the apex of the cantilever by lowering the stepper motor in 1 µm steps and making contact with the cell until an applied force of 0.5 nN had been reached. After attaching the cell, the cantilever was retracted 50 µm and the optical microscope was used to confirm that the cell was positioned correctly at the end of the cantilever. Afterwards the single cell was allowed to adhere for 10-15 min to ensure the strength of cell attachment to the cantilever was greater than to the GelMA hydrogel surface during the SCFS. This procedure combined with only short cell contact times (e.g. seconds) is previously described as an important procedure for ensuring that cell adhesion to the cantilever is greater than adhesion to the opposing surface [175].

4.2.7 Force Measurements

Force measurements were performed according to modified previous methods [48, 204]. After attachment of the cell, the live single cell probe was repositioned over a cell-free region of the hydrogel surface and force-distance (F-D) curves were performed with a loading force of 500 pN, contact-time of 1 sec and retraction speed of 20 µm/sec for all experiments. In this study, a 100 µm z-extended travel stage (provided by the JPK Company) was employed to accommodate the longer-range interactions (~ 10-80 µm) between the cells and hydrogel, which could be significantly greater than the standard z-travel stage (max 15 µm). At least 10 different cells were measured on each GelMA hydrogels with different modulus (**Table *4***) and up to 20 F-D curves collected for each cell (from 4 different positions on the sample), giving a total of 200 F-D curves per GelMA hydrogel for the analysis. On each GelMA hydrogel, this measurement protocol was repeated for the different antibodies that were introduced during the F-D curves for blocking experiments, which are described further below.

4.2.8 Integrin Blocking Experiment

Anti-integrins α5β1, β1 and αv blocking antibody (Merck/Millipore) were separately aliquoted (2 µl) into 2 ml tubes and stored at -80 °C prior to use. After pipetting out 1 ml of the cell suspension (80,000 cells/ml), 1 ml of cell suspension was injected into the aliquoted 2 µl of antibody. One ml of the cell suspension with the anti-integrin α5β1, β1 or αv antibody was then transferred to a 15 ml tube with 1 ml of cell suspension, followed by addition of 4 ml of fresh CO_2-independent medium. The 5 ml cell suspension with 2 µl antibody was kept at 37 °C in an incubator for 30 minutes, followed by centrifugation for 12 min at 190 g and washed with 1 ml fresh CO_2-independent media. Finally, cells were injected into 3-electrode electrochemical cell of the AFM for the SCFS experiments.

4.2.9 Force Curve Analysis

Analysis of F-D curves

Analysis of the F-D curves was performed using the JPK Data Processing software (Version spm-5.1.11), which enabled the quantification of adhesion force, adhesion energy, detachment length, and determination of unbinding event such as ruptures and plateaus. Raw curves were converted into F-D curves using the measured detection sensitivity and spring constant into force [162]. Box-Whisker plots were plotted using OriginPro (2015) b9.2.272 and presented as means ± standard error of the mean. Non-parametric tests such as Mann-Whitney test were performed using the statistical package of OriginPro (2015) b9.2.272. Confidence for all data analyses was set at 95% ($p \leq 0.05$).

Analysis of loading rates

To investigate the loading rate on cell adhesion, the effective spring constant of the cell-cantilever system, k_{eff}, was measured, as described previously by Taubenberger et al. (2007) [190]. Briefly, the slope of a straight line was fitted through the final third of a rupture event for calculation of k_{eff} [190]. With a known k_{eff}, the loading rate, r, was then calculated according to $r = k_{eff} * v$, where v is the retraction speed of the cantilever (20 µm/sec) [270].

4.3 Results/Discussion

4.3.1 Effect of Modulus on Hydrogel–Cell Interaction

SCFS measurements were initially performed using two different cell types, L929 fibroblast cells (L929) and hNSCs. F-D curves for both cell types showed typical rupture events, for example, saw-tooth and plateau interactions; which are commonly observed in SCFS [271, 272] and indicate de-adhesion interactions with the GelMA hydrogel (**Figure 35A-F**). For both cell types, the GelMA modulus was

observed to have a significant effect on the de-adhesion profile in F-D curves. For GelMA modulus of 160 Pa (**Figure 35A-B**, red trace), the F-D curve consisted of an initial, large non-linear peak(s) (**Figure 35A-B**, **i**) that showed long-range interactions of ~ 10-20 µm and was typically followed by smaller peaks (**Figure 35A-B**, **ii**), usually referred to as rupture events or jumps in SCFS [48, 197]. Similarly, for the GelMA modulus of 450 Pa (**Figure 35C-D**, blue trace), an initial, non-linear peak (**Figure 35C-D**, **i**) followed by small ruptures (**Figure 35C-D**, **ii**) were also observed. In contrast, GelMA modulus of 900 Pa (**Figure 35E-F**, green trace) showed F-D curves that lacked an initial, large non-linear peak but typically consisted of only smaller ruptures (**Figure 35E-F**, **ii**). In addition, the force magnitude of the rupture peaks for the 900 Pa GelMA clearly showed a significant decrease in comparison to the other two lower GelMA moduli, i.e. the rear curves for 900 Pa GelMA are on the same scale while the front curves represent a magnified region. Differences in the F-D curves were also revealed in analysis of maximum detachment length (**Figure 35G**), which signifies the distance reached until the cell finally detaches from the surface. For both cell types, the average maximum detachment length for 160 Pa GelMA gave values of 25.6 ± 15.6 µm (L929) and 20.7 ± 8.2 µm (hNSCs) (**Figure 35G**). For 450 Pa GelMA, values of 26.9 ± 18.5 µm (L929) and 24 ± 13.1 µm (hNSC) were obtained (**Figure 35G**). Due to the initial, non-linear peak exhibiting significantly longer interaction lengths for these two lower moduli GelMA, their detachment lengths were significantly greater than those of the 900 Pa GelMA, which had values of 10.6 ± 4.1 µm (L929) and 16.2 ± 5.6 µm (hNSC) (**Figure 35G**). Together, these results suggest that the initial, non-linear peak originates from de-adhesion interactions with less cross-linked GelMA (160 Pa and 450 Pa samples), while smaller ruptures can occur on all GelMA samples.

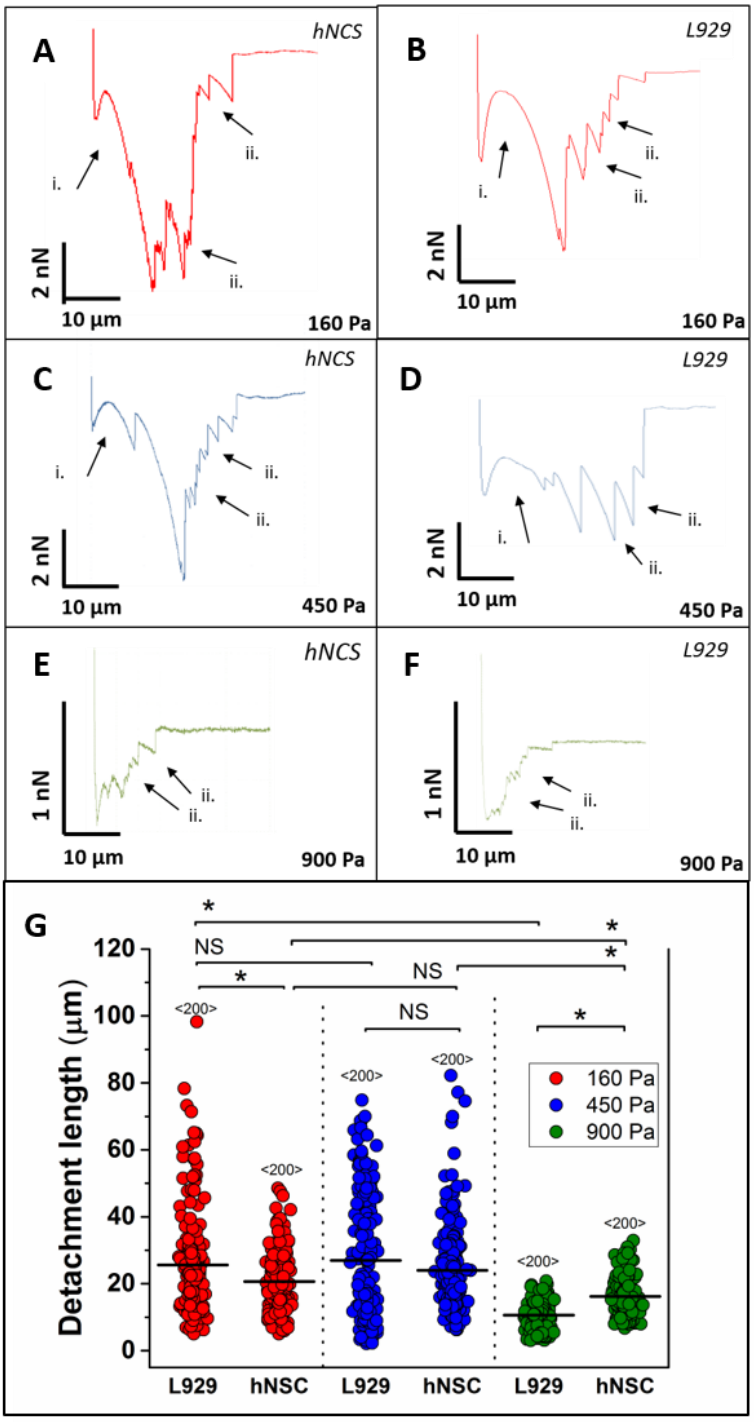

Figure 35: F-D curves on GelMA by AFM-based SCFS. (**A-F**) F-D curves on GelMA of L929 cell lines and hNSCs measured by SCFS. The GelMA hydrogels differ in their Young's modulus (900 Pa, 450 Pa and 160 Pa) and showing a significant effect on de-adhesion profiles in F-D curves. (**G**) Detachment length of L929 cell lines and hNSCs measured by SCFS. Comparisons of three different GelMA hydrogels are plotted as column scatters. A dwell time of 1 sec was applied. The number of analysed F-D curves is given above column scatters (<n>). Asterisks indicate statistical significance *p≤0.05, (NS) not significant (Mann-Whitney test).

4.3.2 Effect of Modulus on Cell De-Adhesion Force and Energy

Statistical analysis of the maximum de-adhesion force and energy from F-D curves is shown in **Figure 35**. Similar to qualitative observations of F-D curves in **Figure 36A**, the SCFS measurements revealed a significant decrease in the de-adhesion force (**Figure 36A**) and energy (**Figure 36B**) with an increase in GelMA modulus. Specifically, for hNSCs, the de-adhesion force decreased with values of 4.2 ± 2.7 nN, followed by 3.5 ± 3.2 nN and 0.5 ± 0.2 nN for GelMA moduli of 160 Pa, 450 Pa and 900 Pa, respectively (Fig. 2A). Similarly, a decrease in de-adhesion energy of 3.1 ± $2.3e^{-14}$ J followed by 2.9 ± $4.0e^{-14}$ J and 3.3 ± $2.0e^{-15}$ J was observed for the increasing moduli, respectively (**Figure 36B**). For L929 cells, significantly decreasing de-adhesion forces of 4.2 ± 4.0 nN, 1.9 ± 1.0 nN and 0.8 ± 0.4 nN (**Figure 36A**), in addition to decreasing energy values of 3.7 ± $3.9e^{-14}$ J, 1.9 ± $2.4e^{-14}$ J and 3.5 ± $2.1e^{-15}$ J (**Figure 36B**), were also observed for the increasing GelMA moduli. Both cell types showed a similar range of de-adhesion values, with all differences between the different GelMA moduli showing statistical significance ($p \leq 0.05$, Mann-Whitney test) (**Figure 36A-B**). Lastly, the statistical variation (standard error of the mean) of the de-adhesion force and energy showed a significant decrease with increasing modulus (**Figure 36A-B**), particularly evident when comparing the 160 Pa and 450 Pa GelMA with the 900 Pa GelMA for both cell types.

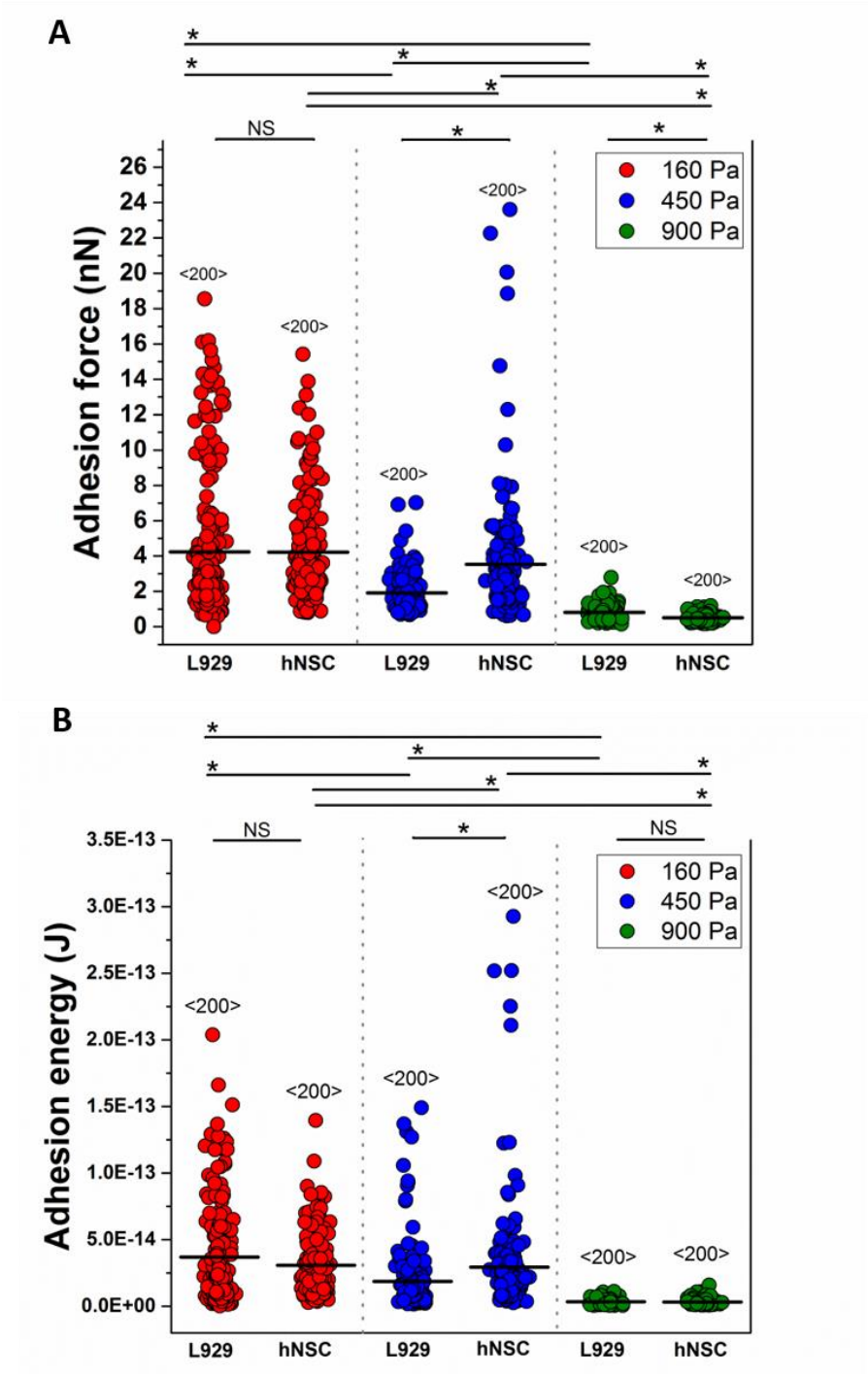

Figure 36: Quantifying hNSC adhesion to various GelMA samples by SCFS. (**A**) Adhesion force of L929 cell lines and hNSCs measured by SCFS. Comparisons of three different GelMA hydrogels are plotted as column scatters. The GelMA hydrogels differ in their Young's modulus (900 Pa, 450 Pa and 160 Pa). (**B**) Adhesion energy of L929 cell lines and hNSCs measured by SCFS. A dwell time of 1 sec was applied. The number of analysed F-D curves is given above column scatters (<n>). Asterisks indicate statistical significance *p≤0.05, (NS) not significant (Mann-Whitney test).

4.3.3 Physical Mechanisms of Single Cell De-Adhesion

The effect of modulus on cell de-adhesion can be interpreted from differences in the F-D profiles. Specifically, for the 160 Pa and 450 Pa GelMA, the initial non-linear peak is qualitatively similar to long-range interactions previously observed in fluid, soft colloid and microbial cell interactions with surfaces. For example, such profiles have been observed in liquid droplet [273] and resin lipid colloids [274], relating to adhesion and subsequent 'neck' thinning of the fluid. Similar responses have been measured by AFM on fungal spores [275] and other microbial organisms, e.g. diatoms [276], due to stretching of polymeric substances on their cell surfaces. AFM stretching of isolated single polysaccharide chains shows characteristic non-linear extension, with forces up to several nanonewtons [277]. For the lower moduli GelMA, we suggest the involvement of multiple gelatin chains that undergo binding to the cell and their subsequent extension due to a lower degree of cross-linking, enabling the chains to freely extend from the surface. Importantly, because multiple gelatin chains can interact in parallel, both the magnitude of de-adhesion and energy effectively scales (increases) according to the number of GelMA polymer chains, as described by entropic chain models [278]. For this situation, a greater statistical variation in the values is interpreted as being due to the increase in probability of binding a varying number of GelMA polymer chains. Eventually the elastic restoring force of the GelMA polymer chains overcomes the GelMA-single cell adhesion, causing their detachment followed by unbinding of remaining, fewer chains, e.g. smaller ruptures, until the cell completely detaches from the surface. In contrast, the more cross-linked chains of the 900 Pa GelMA provide less of a contribution from elastic restoring forces, i.e. the initial non-linear peak is lacking, and instead the observed smaller ruptures of ~ < 100 pN are indicative of mainly unbinding adhesion complexes formed between the peptide groups of gelatin methacylate chains and cell surface receptors. The absence of a larger, non-linear peak on the 900 Pa GelMA also excludes any significant elastic contributions from the single cell during the SCFS measurements. **Figure 35B** supports the above observations whereby the softer 160 Pa and 450 Pa GelMA have significantly longer detachment lengths compared to the 900 Pa GelMA. The degree of cross-linking may also affect the number of cell

peptides (e.g. RGD) available for binding. Ostensibly, a lower-crosslinked hydrogel may expose more peptide groups on gelatin methacylate chains whereas highly cross-linked chains may alternatively impede access to peptides. These findings are contrary to the general observation of greater cell spreading and adhesion on stiffer material surfaces when cells are allowed to establish longer-term adhesion in conventional cell culture studies [279]. In one other SCFS study, Jalali et al. (2015) investigated endothelial cell adhesion on PAAm hydrogels with different moduli and found an increase in de-adhesion with increasing modulus. On a 1 kPa PAAm hydrogel they measured an adhesion force of ~2 nN, which decreased to 0.28 nN on a 65 Pa PAAm hydrogel with contact time of 10 sec [207]. Evidently, they observed an opposite effect of modulus, which may be due to several reasons, including differences in the cell type and/or presence of a collagen layer that was separately deposited onto the PAAm surfaces as opposed to interactions via inherent cell binding peptide sequences of the hydrogel polymer chain.

4.3.4 Effect of Modulus on Integrin-Mediated Interactions

Blocking experiments were performed whereby antibodies were introduced to hNSCs to investigate the involvement of α5β1 integrin and both β1- and αv-integrin subunits in the GelMA-cell interaction. All F-D curves for the different antibodies and GelMA samples qualitatively showed very similar profiles comprising multiple ruptures (**Figure 35**) but lacked the characteristic differences observed for the different GelMA moduli in **Figure 37**. Despite the similarity in their F-D profiles, there was a clear decrease in the de-adhesion force with blocking for both 160 Pa (red curve) and 450 Pa GelMA (blue curve) (**Figure 35A** and **Figure 37**A-I), i.e. comparable force scales are given in **Figure 35A** and **Figure 37**A-I. Unexpectedly, an opposing increase in the de-adhesion force was observed for the 900 Pa GelMA (**Figure 37**A-I). Statistical analysis of de-adhesion force and energy confirmed these observations, clearly showing a decrease in the maximum de-adhesion force when all three α5β1 integrins, αv- and β1-subunit classes were applied to the 160 Pa and 450 Pa GelMA (**Figure 38A-B**), with statistically significant difference ($p \leq 0.05$) observed between

each antibody (**Figure 38A-B**). The 160 Pa GelMA with blocking by α5β1 integrin, β1- and αv-subunits had significantly decreased de-adhesion forces by 55%, 61.7% and 66.1%, respectively, compared to the control sample without blocking ($p \leq 0.05$, Mann-Whitney test, larger asterisks). The same trend was observed for 450 Pa GelMA with significant decreases in de-adhesion force by 34%, 78% and 70%, respectively, for the same antibodies. Blocking experiments on the 160 Pa GelMA also resulted in significant decreases in de-adhesion energy by 81% ($5.91 \pm 6.26e^{-15}$ J), 71% ($8.84 \pm 1.04e^{-15}$ J) and 81% ($5.79 \pm 4.21e^{-15}$) for the α5β1, β1 and αv, respectively, compared to the control (**Figure 38B**). Suppression of cell adhesion by antibodies during SCFS is typically used to specify the involvement of receptors [190], in this case integrins which are known to be predominately expressed by hNSC's [280]. It is generally expected that binding of antibodies will reduce the capacity for cells to adhere, as confirmed for the 160 and 450 Pa GelMA in **Figure 38**. Hence, this indicates specific involvement of α5β1 integrin and β1- and αv-subunits of which the latter subunits inevitably cover a wider-range of different integrin receptors. Despite confirming the specificity of α5β1 integrin and β1- and αv-subunit interactions with GelMA, the de-adhesion is not completely blocked, indicating remaining contributions from either those integrins that have not been blocked and/or non-specific interactions such as those conceivably due to interactions with the cell surface glycocalyx or non-RGD, charged sites within GelMA polymer network [281].

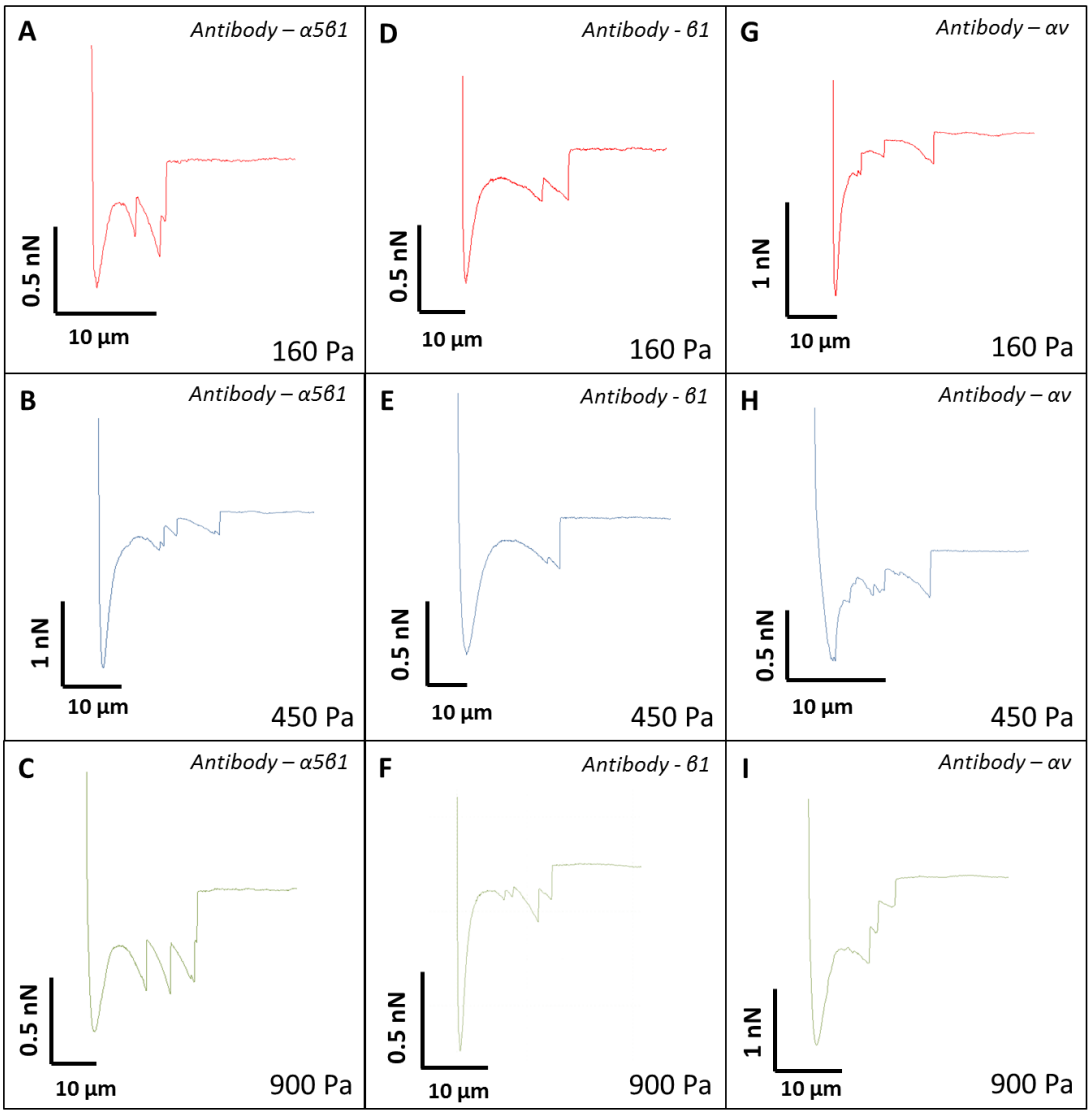

Figure 37: F-D curve profiles measured for three GelMA moduli with applied integrin blocking antibodies. Performed F-D curves on 160 Pa GelMA modulus (red), on 450 Pa GelMA hydrogel modulus (blue) and on 900 Pa GelMA hydrogel modulus (green) with a single live hNSC.

As mentioned, blocking had an opposite effect for the 900 Pa GelMA. Maximum de-adhesion forces were a significantly increased by 141%, 265% and 171% with blocking by α5β1 integrin, αv- and β1-subunit classes, respectively, in comparison to the control sample (**Figure 38A**). Consistent with the de-adhesion force, energy was significantly increased with blocking, with measures of 9.43 ± 6.65e^{-15} J (α5β1), 6.68 ± 7.98e^{-15} (β1) and 9.63 ± 0.11e^{-15} J (αv) (**Figure 38B**). The 900 Pa GelMA also showed an increase in statistical variation for all three antibodies (**Figure 38A-B**). Unexpected

increases in cell de-adhesion during SCFS blocking experiments using α5β1, αv and β3 antibodies have previously been observed for pre-osteoblast cells on glass substrates coated with collagen and explained by integrin crosstalk whereby blocking of integrin induced activation of other collagen-binding integrins [197]. Similar crosstalk between αv-subunit and α5β1 integrins has recently been reported in SCFS experiments using mouse embryonic fibroblast cells [199] and described earlier by others as a kinase C dependent mechanism [282]. Furthermore, the αvβ1 integrin is specifically shown to work in concert with α5β1 integrins to promote spreading of cells on fibronectin [283]. While further studies are necessary to determine the specific mechanism, a significant finding in this study is that the increase in de-adhesion was induced by a small change in modulus within a narrow range, i.e. < 1 kPa, suggesting coupling effects between substrate modulus and proposed crosstalk mechanisms.

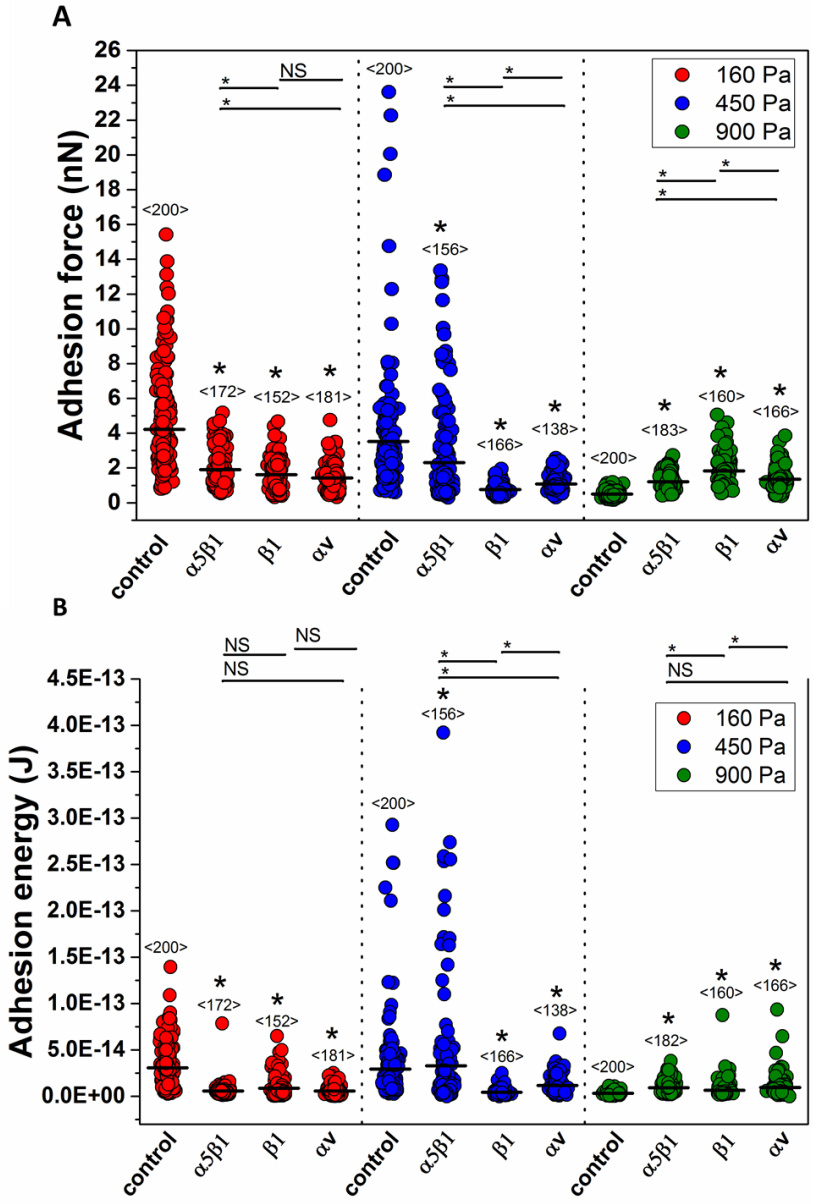

Figure 38: Quantifying the effect of integrin blocking on hNSC adhesion to various GelMA moduli by SCFS. (**A**) Adhesion forces of hNSC on three different GelMA hydrogel moduli (160 Pa = red, 450 Pa = blue and 900 Pa = green) with different blocking antibodies. (**B**) Adhesion Energy of hNSC on three different GelMA hydrogel moduli (160 Pa = red, 450 Pa = blue and 900 Pa = green) with different integrin blocking antibodies. The number of analysed F-D curves is given above column scatters (<n>). Asterisks indicate statistical significance *p≤0.05, (NS) not significant (Mann-Whitney test). Larger asterisks show the statistical significance of control versus blocking antibody.

Lastly, two other observations in **Figure 38A-B** include a decrease in the variation (error) of de-adhesion force and energy when cell adhesion was supressed by blocking on 160 Pa and 450 Pa GelMA but an opposite effect observed for the 900 Pa GelMA. Secondly, blocking with β1- and αv antibodies on 160 Pa and 450 Pa GelMA was associated with the greatest reduction in de-adhesion compared to α5β1 antibody. More specifically, anti-α5β1 integrin antibodies had a minimal effect on the 450 Pa GelMA. Integrin α5β1 binds to fibronectin and osteopontin and belongs to the ligand group for RGD receptors. In contrast, all αv-subunits bind to RGD tripeptide active sites [284] whereas β1-subunits bind to the complete range of integrin subunit interaction groups, such as RGD-, collagen-, leukocyte and laminin receptors [285]. Significant blocking by αv- and β1 antibodies is perhaps expected given they cover a wider range of integrins, and further supported by a decrease in the number of rupture peaks (discussed further below in **Figure 39E**).

4.3.5 Effect of Modulus and Integrin Blocking on Individual Ruptures

In addition to the maximum de-adhesion force, analysis of individual ruptures was undertaken to provide further details on the GelMA- hNSC de-adhesion. In particular, SCFS experiments are typically designed to have low applied forces in combination with short contact times (< 1 sec) to increase the probability of detecting only single receptor complexes with unbinding forces of ~ < 100 pN. **Figure 39A** shows that the individual ruptures have significantly high forces of 1000.2 ± 1371.7 pN and 641.9 ± 551.2 pN for 450 Pa and 160 Pa GelMA, respectively, which clearly indicated that interactions are with multiple integrin complexes and associated GelMA polymer chains. In contrast, ruptures forces of 65.2 ± 72.5 pN for 900 Pa GelMA (**Figure 39A**) are in the range for unbinding of single integrin complexes [190, 192]. These differences in rupture forces are seen in F-D curves in **Figure 35** and support mechanisms ascribed to interactions either involving integrin-RGD complexes with associated elastic contributions of gelatin methacrylate chains (160 Pa and 450 Pa

GelMA) versus predominately the discrete unbinding of integrin-RGD complexes on the 900 Pa GelMA, i.e. without the same degree of elastic contributions from more crosslinked chains. By introducing the three antibodies, the individual rupture forces decreased for 160 Pa and 450 Pa GelMA (**Figure 39C-D**), with the exception of the α5β1 antibody, which correlated to de-adhesion forces in **Figure 38A**. In particular, the α5β1 antibody showed the highest rupture forces on the 450 Pa GelMA, supporting the reduced blocking capacity of this antibody. An opposite effect showing increased rupture forces on the 900 Pa GelMA was again consistent with the blocking effect on de-adhesion forces for this GelMA sample. Further analysis of number of rupture peaks per F-D curve for blocking versus without blocking is shown in **Figure 39E**. For all antibodies, a decrease in the number of ruptures by ~ 3-4 fold was observed on 160 Pa and 450 Pa GelMA, indicating that these rupture events are primarily associated with integrin complexes and emphasized a blocking effect on these GelMA hydrogels. However, a decrease in the number of ruptures was also observed for the 900 Pa GelMA, indicating a 'blocking effect' despite the increase in de-adhesion forces and energy on these stiffer GelMA samples.

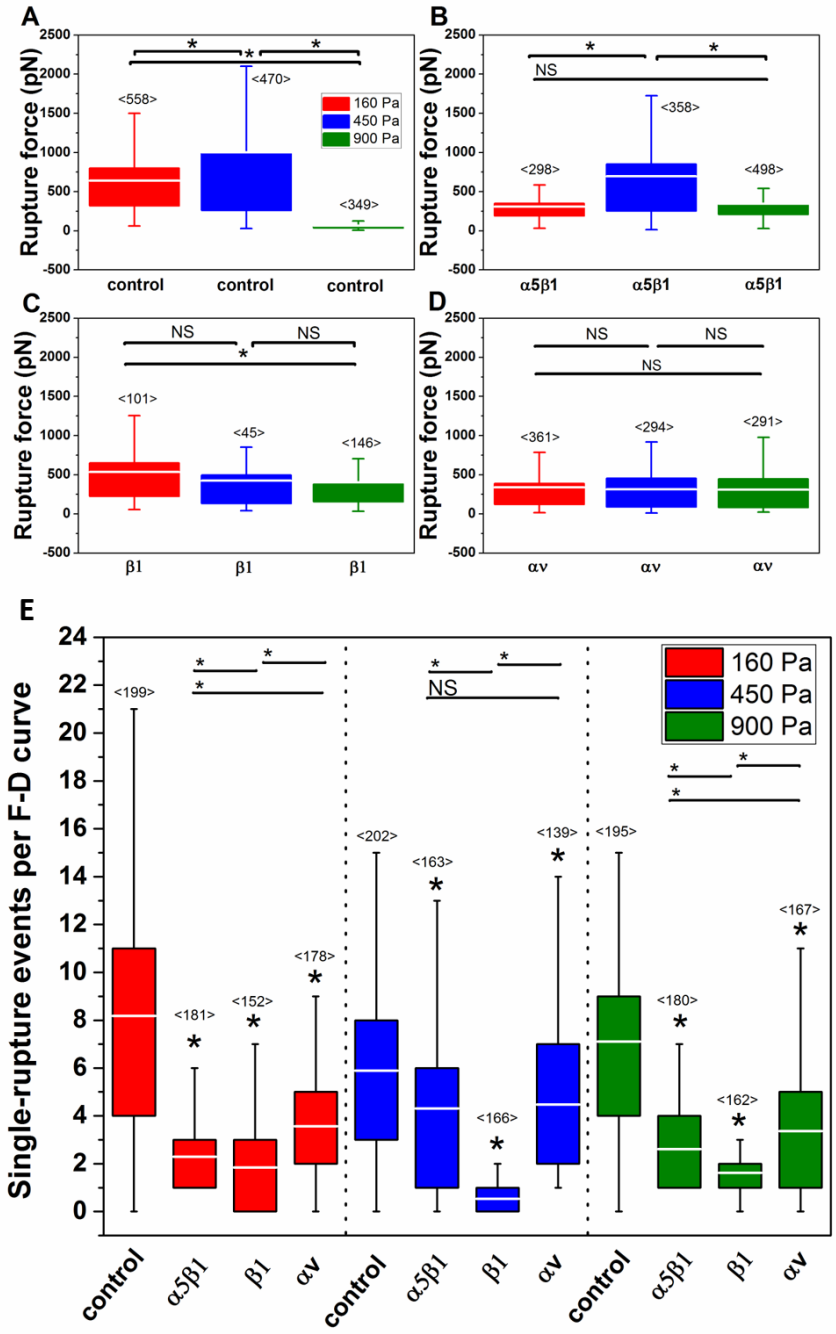

Figure 39: Box-Whisker plots of bond rupture forces and single rupture events on each GelMA modulus. (**A**) Rupture forces of hNSCs on GelMA hydrogel without applied antibody. (**B**) Rupture forces of hNSCs on GelMA hydrogel with applied blocking antibody α5β1. (**C**) Rupture forces of hNSCs on GelMA hydrogel with applied blocking antibody β1. (**D**) Rupture forces of hNSCs on GelMA hydrogel with applied blocking antibody αv. Red =160 Pa, blue=450 Pa and green=900 Pa. (**E**) quantification of single rupture events per F-D curve of hNSCs on three different GelMA moduli with different blocking integrin antibodies. The number of analysed F-D curves is given above Box-Whisker plot (<n>). Asterisks indicate statistical significance *p≤0.05, (NS) not significant (Mann-Whitney test). Larger asterisks show the statistical significance of control versus blocking antibody.

4.3.6 Loading Rate and Dynamic Force Regimes

The adhesion force is effectively a 'static' value and does not consider the dynamic nature of the cell interactions, particularly with respect to the rate in which the de-adhesion force is applied to the hydrogel-cell system over a given time. The latter is referred to as loading rate and can be estimated from F-D curves using various methods [286]. Investigating effects of loading rate in AFM single molecule [287-289] and cell measurements [192, 290], referred to as 'dynamic force microscopy' [291], has been extensively studied over the past decade yet the role of soft, compliant substrates has only recently been explored in SCFS [192]. Previous models describing filopodia traction dynamics [292], motor-clutch transmission [293], and integrin rigidity sensing [294] on compliant substrates have proposed that substrate elasticity influences the loading rate on integrins, thus affecting bond kinetic properties [192]. In SCFS, the elasticity of the hydrogel substrate is expected to affect the loading rate of integrin−ligand bonds via its impact on the effective spring constant system, k_{eff}, of the system. Recent SCFS of bone marrow mesenchymal stem cell adhesion on collagen I binding peptide, DGEA, coated onto PAAm gels revealed higher unbinding forces of single DGEA-α2β1 complexes on stiffer (130 pN) versus softer (94 pN) substrates [192]. Using the DFS approach, both the soft and stiff PAAm gels showed two dynamic force regimes, with the stiffer gel inducing much longer DGEA-α2β1 complex lifetimes and hence a lower probability of bond disassociation compared with the soft substrate. Importantly, for an equivalent pulling speed (> 10 μm/sec), a greater % of adhesion events occurred in the long lifetime region on stiff substrates. However, at low pulling speeds of 1 μm/sec none of the adhesive events occurred in the long lifetime region, suggesting that when the pulling speed on the integrin α2β1−DGEA complex is low, the bond did not respond to substrate elasticity.

For analysis of loading rate we applied previous methods by Taubenberger et al. (2007) [190]. For a single pulling speed of 10 μm/sec, no significant difference in loading rate was observed for the 160 Pa (12052.21 ± 13848.18 pN/s) and 450 Pa (10358.24 ± 11292.1 pN/s) GelMA (**Figure 40A**). However, a significant decrease in loading rate to 740.7 ± 749.7 pN/s occurred for the 900 Pa (**Figure 40A**). In particular,

there was a clear difference in the variation of loading rate, with 160 Pa and 450 Pa GelMA showing a significantly greater spread of values compared to 900 Pa GelMA (**Figure 40A**). Without antibody blocking, plots of the corresponding rupture force versus loading rate interestingly showed the presence of a non-linear, or dual slopes, for 160 Pa and 450 Pa GelMA, with the higher slope onset occurring at loading rates of ~ 10,000 pN/sec (**Figure 40B**). The 900 Pa GelMA however, only showed a single slope at < 4000 pN/sec) (**Figure 40B**). Introduction of all integrin blocking antibodies (**Figure 41**, 8 and 9) on both the 160 Pa (**Figure 41**) and 450 Pa (**Figure 42**) GelMA appeared to suppress the higher loading rates (higher force regime) by shifting to loading rates (lower force regime) when compared to having no antibodies. In contrast, the 900 Pa GelMA showed a distinct opposite effect whereby introduction of all antibodies induced an additional higher loading rate region corresponding to a higher force regime (**Figure 43**).

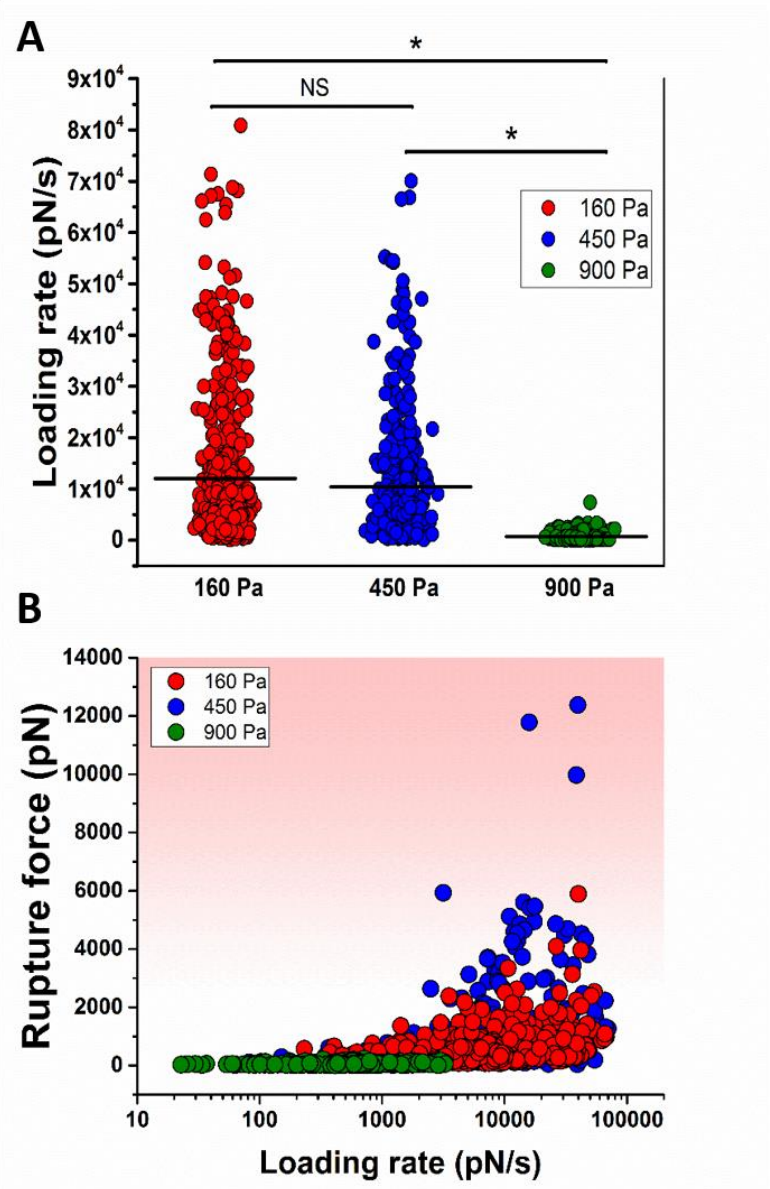

Figure 40: Loading rates as function of GelMA moduli by SCFS. (**A**) Loading rates of hNSCs on GelMA hydrogel moduli were calculated with a retraction speed of 20 µm/s. (**B**) Overlay of scatter plots of loading rates vs rupture forces on 160 Pa, 450 Pa and 900 Pa GelMA. Number of events <n> for 160 Pa = <557>, for 450 Pa = <369> and for 900 Pa = <337>.

The above findings are contrary to previous SCFS studies showing greater cell adhesion [207], as well as increased loading rates and associated longer lifetime regions [192], on stiffer PAAm gels. We note, however, that we have not attempted to apply a typical DFS analysis such as those based on Bell's Model and modified

versions thereof to describe the kinetics [193], namely as this is mainly applicable to analysis of single bonds, which is clearly not the case for the GelMA – hNSC interaction. Here, we only provide empirical observation of the loading rate under the experimental conditions of the SCFS (applied force: 500 pN, contact time: 3 sec, pulling speed: 10 µm/sec) and without attempting to isolate single molecule events. Furthermore, the GelMA hydrogel – hNSC interaction is complex, involving multiple gelatin methacrylate chains and integrin complexes. Despite expecting a decrease in the effective spring constant, k_{eff}, for softer 160 and 450 Pa GelMA, we interpret that their adhesion involving multiple GelMA polymer chains acting in parallel, increases the effective stiffness of the interaction, e.g. deviations to low persistence length. Recent DFS models by Friddle et al. (2012) have introduced an alternative multiple-bond theory, which may be more appropriate for the non-linear slope (dual slope) in rupture force versus loading rate for the 160 and 450 Pa GelMA (**Figure 41A** and **Figure 42A**) [295]. On the other hand, for the 900 GelMA, restriction of the GelMA polymer chain extension due to higher crosslinking density results in greater probability of observing discrete unbinding of integrin-RGD complexes. This is supported by significantly lower rupture forces of 65 pN (**Figure 39**), which is close to unbinding forces of single molecule integrins [185, 286]. Thus, it is possible that the single slope in rupture force versus loading rate for 900 Pa GelMA is more representative of single barrier kinetics of unbinding pathways, as described by conventional DFS theory [192]. In the presence of antibodies, we suggest that the suppression of a non-linear slope for 160 Pa and 450 Pa GelMA is due to blocking of integrin receptors, thus reducing the ability of multiple gelatin methacrylate chains to interact via their RGD groups. However, the reverse effect seen for 900 Pa GelMA where an additional higher force regime, e.g. longer-lived lifetime, is surprising and not clear at this stage, though again could relate to activation of other integrin receptors via crosstalk, as discussed above.

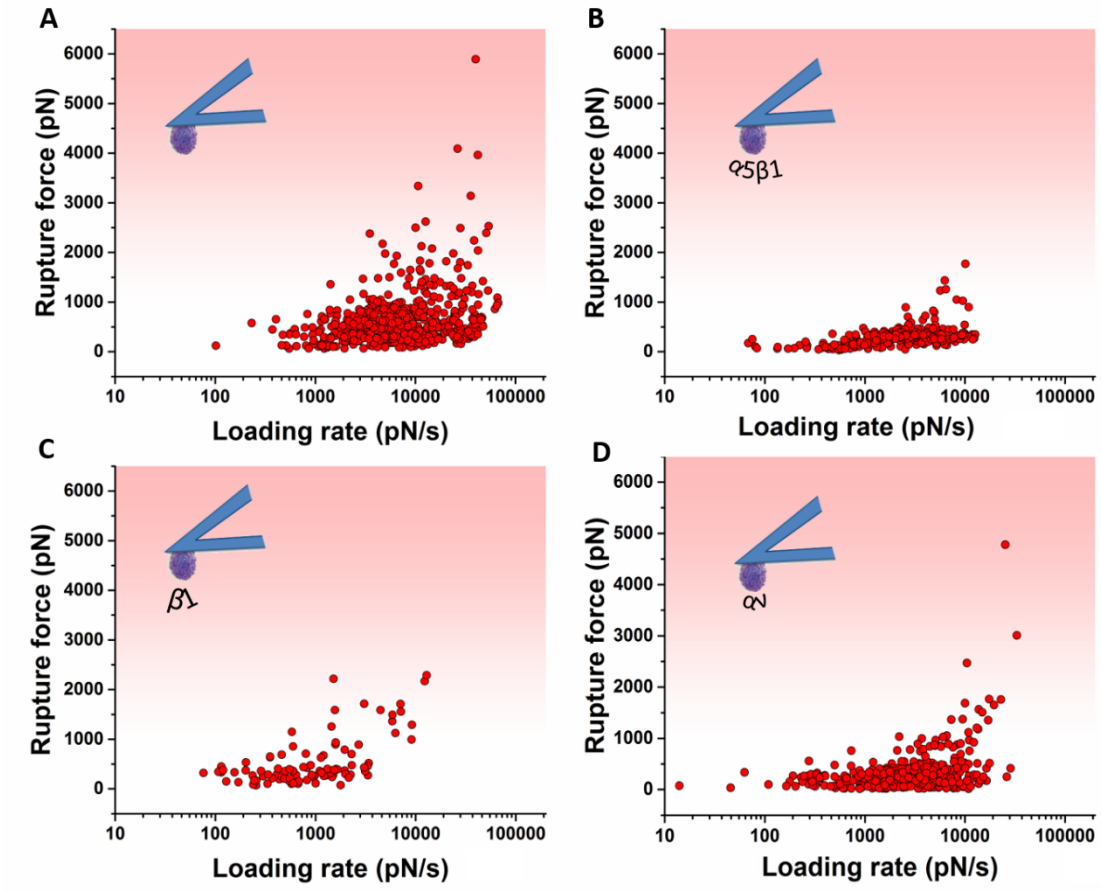

Figure 41: Scatter plot of loading rates vs. bond rupture forces on 160 Pa GelMA. Analysis of loading rate interaction forces between 160 Pa GelMA hydrogel and hNSCs at varying applied integrin blocking antibodies and a constant retraction speed of 20 µm/s. (**A**) No intergrin blocking antibody, (**B**) integrin blocking antibody α5β1, (**C**) integrin blocking antibody β1, (**D**) integrin blocking antibody αv. Number of events <n> for no integrin blocking antibody = <558>, for integrin blocking antibody α5β1 = <298>, for integrin blocking antibody β1 = <95> and for integrin blocking antibody αv = <361>.

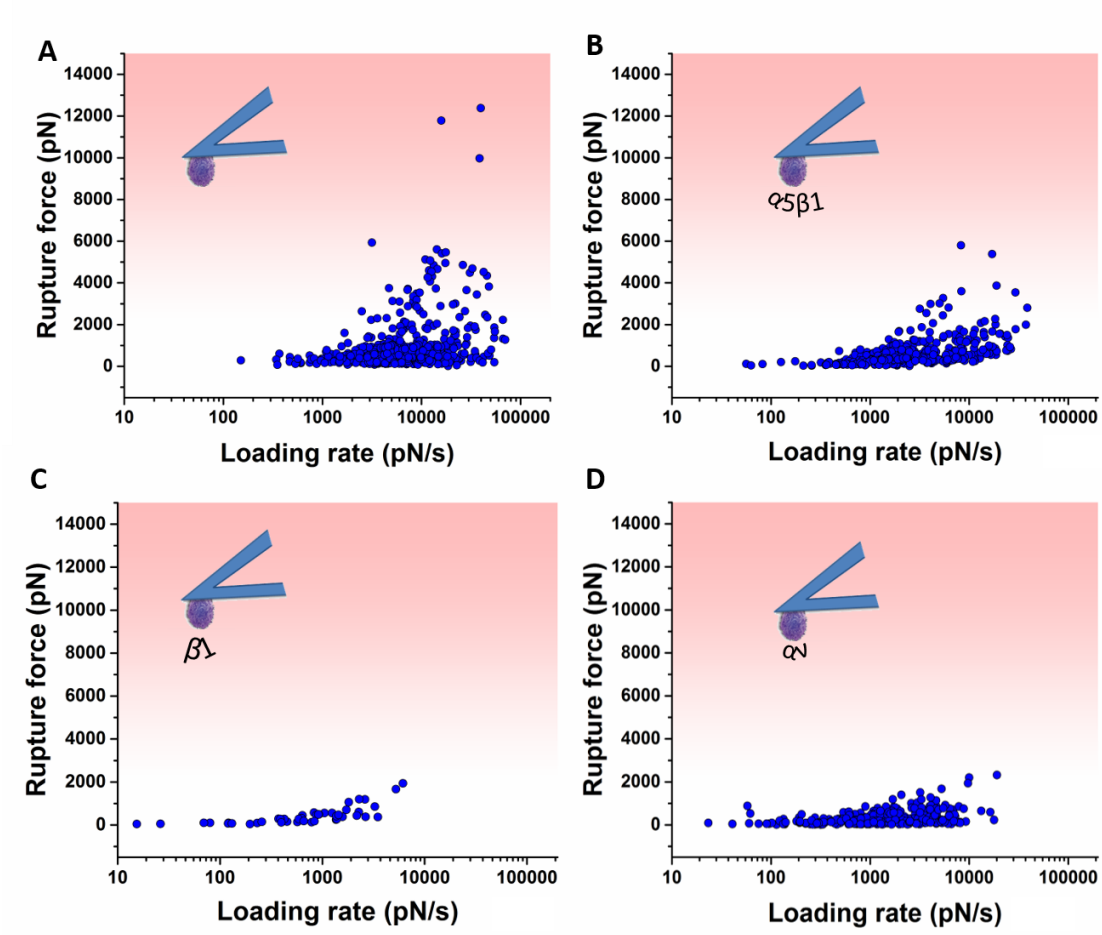

Figure 42: Scatter plot of loading rates vs. bond rupture forces on 450 Pa GelMA. Analysis of loading rate interaction forces between 450 Pa GelMA hydrogel and hNSCs at varying applied integrin blocking antibodies and a constant retraction speed of 20 µm/s. (**A**) No integrin blocking antibody, (**B**) Integrin blocking antibody α5β1, (**C**) Integrin blocking antibody β1, (**D**) Integrin blocking antibody αv. Number of events <n> for no integrin blocking antibody = <460>, for integrin blocking antibody α5β1 = <358>, for integrin blocking antibody β1 = <45> and for integrin blocking antibody αv = <293>.

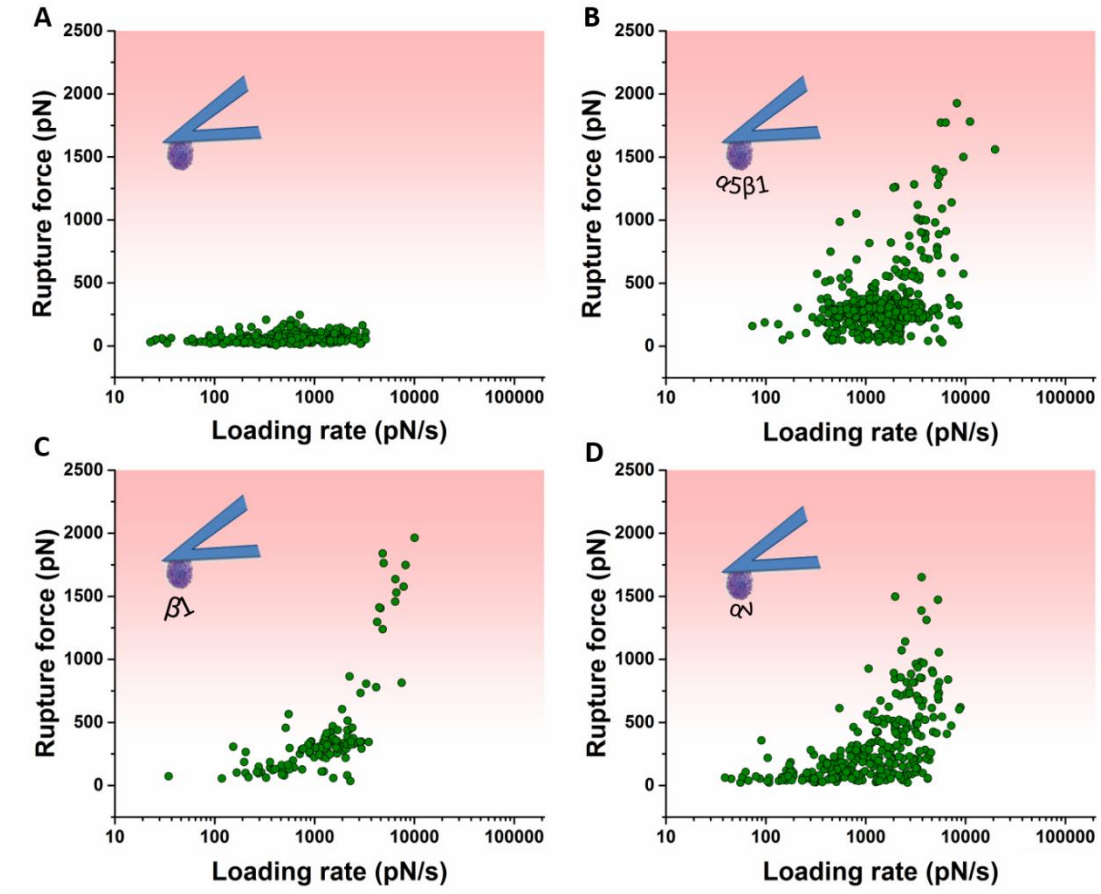

Figure 43: Scatter plot of loading rates vs. bond rupture forces on 900 Pa GelMA. Analysis of loading rate interaction forces between 450 Pa GelMA hydrogel and hNSCs at varying applied integrin blocking antibodies and a constant retraction speed of 20 µm/s. (**A**) No integrin blocking antibody, (**B**) Integrin blocking antibody α5β1, (**C**) Integrin blocking antibody β1, (**D**) Integrin blocking antibody αv. Number of events <n> for no integrin blocking antibody = <349>, for integrin blocking antibody α5β1 = <417>, for integrin blocking antibody β1 = <120> and for integrin blocking antibody αv = <291>.

4.4 Conclusion

Understanding the physical interactions between cells and the hydrogel polymer network, especially the mechanisms by which cells sense modulus and viscoelastic material properties to enable integration of force-feedback over time [255], is critical in development of functional biomaterials and tissue engineering [79, 296]. Here, we reveal that even a small change in modulus within a narrow range (equivalent to modulus of brain tissue [27]) gives rise to significant effects on the physical, molecular interactions between the GelMA polymer network and hNSCs. Lower modulus, or less cross-linked GelMA, enables greater extension of individual GelMA polymer chains during cell de-adhesion, giving rise to elastic restoring forces of GelMA polymer chains and hence greater de-adhesion forces and energy. More crosslinked GelMA chains, however, participate whereby the cell de-adhesion is governed predominately by discrete unbinding forces between their RGD groups and cell surface (integrin) receptors, with significantly less elastic contributions. Importantly, the GelMA polymer chain interactions lead to unexpectedly higher loading rates, in particular the presence of a dual low and high force regimes. In contrast, the discrete unbinding of integrin-RGD complexes (on 900 GelMA) gives only a single low force regime that we suggest is more representative of typical single activation barriers in DFS [287, 297]. When antibodies are introduced to bind various integrin receptors, we reveal a decrease in de-adhesion forces and energy for lower moduli GelMA, presumably due to blocking of receptors and associated decrease in number of interacting GelMA polymer chains. A key finding is that the effect of antibody binding is shown to be modulus-dependent, as in the case for 900 Pa GelMA that increases the cell-deadhesion, specifically by activating a high force regime.

In conclusion, this work emphasizes the modulus-dependent, dynamic nature of the hydrogel-hNSC interactions, originating from differences in the GelMA polymer chain interactions, and evident by the presence of dual low and force regimes in **Figure 41-43**. It also highlights the possibility of presenting differential elastic or viscoelastic properties through single GelMA polymer chains, e.g. tethered to a surface or controlled polymer network, in combination with ligand headgroups,

e.g. comprising antibodies, growth factors, and cytokines, to explore their coupling effects exerted on cell interactions. Further insight on molecular-level, physical, cell interactions occurring at hydrogel surfaces will shed light on molecular properties such as molecular weight, chain length, cross-linking density, and degree of branching, which govern the cell interactions yet are not necessarily described by the bulk properties.

Chapter 5:

Effect of Electrical Stimulation on Cell De-Adhesion between Human Neural Stem Cells and Gelatin Methacrylate (GelMA) Hydrogels as Revealed by Single Cell Force Spectroscopy

5.1 Introduction

The integration of implantable electronic devices and human tissue, commonly referred to as 'bionics' or neural prosthetics, is used to achieve applications [9] such as electrical stimulation to treat neural disorders [3], restore hearing (i.e. cochlear implant) [298], or depression (i.e. DBS) [299]. Conventional neural prosthetics are typically based on electrical stimulation to induce action potentials via gated ion channels for neuromodulation of brain electrical activity [300]. Alternatively, direct electrical stimulation can be applied to cells and tissues to activate intracellular signalling pathways to trigger the synthesis of proteins and DNA involved in cell proliferation, differentiation and growth [301, 302]. There is also an emerging area of electroceuticals whereby implantable electrodes are used to stimulate nerves (e.g. vagus nerve) innervating tissues and organs, resulting in activation of cytokines and anti-inflammatories to address a range of diseases such as arthritis [303], multiple sclerosis [304] or urinary urge incontinence [305]. Lastly, electrical stimulation has been explored to generate ionic current gradients in tissues, which have shown to be important for tissue development [306].

For efficacy and safety in electrical stimulation, the implantable electrodes must be capable of injecting high-intensity electrical charge, have high flexibility and mechanical fixation, and importantly not cause potentially harmful irreversible, electrochemical reactions or inflammatory responses [9, 10]. At present,

conventional implantable electrodes are made of inert metals and their alloys like stainless steel, titanium, platinum or platinum/iridium, which provide good charge transfer, biocompatibility (i.e. inertness) [307] and long-term stability of material properties [308]. However, there are critical challenges in using such metals, particularly the poor recipient tissue immune response due to a mechanical mismatch between hard metals and soft biological tissue. Here, the mechanical compliance of the electrode with neural tissue is important for preventing long-term inflammatory response of tissue associated with neuronal cell depletion and glial scar formation, which is also responsible for decreasing electrical performance of the electrode [309-311]. Once implanted, metal electrodes continuously result in encapsulation and sub-optimal integration at the soft tissue interface [312]. In addition, their other limitations include corrosion due to the wet environment, as well as delamination and degradation of thin metal electrodes that drastically decreases their efficacy [313, 314].

Softer, organic conductive materials such as OCPs have been developed to improve mechanical compliance. Yet, despite being significantly softer than metals, the OCPs still have significantly higher Young's modulus (up to 1000 MPa [33]) compared to human tissue, for example, brain tissue with a modulus in the range of 500 - 1000 Pa [27]. Therefore, research on further bridging the electrode interface with biological tissues using even softer materials such as hydrogels and their use in the development of composite hydrogel-conducting polymer electrodes, or the concept of 'living' hydrogel-based electrodes, has been ongoing [60, 61, 74]. Composite hydrogel-OCP electrodes were first studied by Gilmore et al. (1994) and based on PPy directly electropolymerised onto a preformed polyacrylamide hydrogel [74]. Kim et al. (2010) has shown that coating a PEDOT electrode with alginate improved the long-term performance of the electrode and increased the efficiency of signal transmission [60]. Similarly, Green et al. (2013) showed that a bioactive degradable hydrogel based on PVA cast onto a PEDOT layer improved the electrical response of the coated electrode and supported the survival and differentiation of PC12 cells during electrical stimulation [61].

During electrical stimulation, the hydrogel in the composite electrodes is subject to injection of charge and therefore significant effects are exerted on the hydrogel properties. This is particularly evident in earlier studies on electrical field-induced hydrogel responses, such as bending and actuation, as well as other underlying mechanisms responsible for changes in hydrogel properties [91, 242]. Hydrogels are especially sensitive to electrical fields, resulting in significant swelling and contraction [86, 242] and suited to application in mechanical components like valves and artificial limbs (e.g. soft robotics). Electrically-induced de-swelling that affects the movement of solutes out of the hydrogel is especially attractive for drug release [87]. In Chapter 3, electrical stimulation via the underlying OCP electrode was observed to have significant effects on the modulus and actuation of a top layer (GelMA) hydrogel [134]. Furthermore, Chapter 4 subsequently revealed that single fibroblast and hNSC de-adhesion was strongly dependent on hydrogel modulus, specifically due to cross-linking dependent elastic contributions from interactions of GelMA polymer chains. In combination with antibodies, these physical mechanisms of the GelMA polymer chain interactions activated integrin binding through very small changes in modulus (~ 100 Pa) within a range equivalent to brain tissue (< 1 KPa). Given that hydrogel modulus is known for playing a critical role in cell growth, development and differentiation [111], the use of electrical stimulation to impart multiple effects on cell interactions through modification of the hydrogel physical properties or directly by charge injection is a focus of this chapter.

Therefore, we aimed to investigate the combined effects of both modulus and electrical stimulation delivered through a hydrogel coating with an underlying conducting polymer electrode. We specifically quantify the strength of hNSC adhesion on GelMA of different moduli as a coating on PPy-DBSA electrodes while simultaneously electrochemically switching the oxidized and reduced state of the conducting polymer. GelMA is a hydrogel of increasing interest in tissue engineering, particularly as a common reagent in bioprinting and three-dimensional (3D) cell culture [221]. It is a photopolymerizable hydrogel composed of modified natural ECM components such as decellularized collagen derivatives (e.g. RGD peptide) [120] and

currently used in several applications, including wound healing and 3D printed scaffolds for tissue regeneration [121, 126, 132, 222].

To directly measure the single cell adhesion, this chapter again applied the technique electrochemical-single cell force spectroscopy (EC-SCFS), which combines SCFS and EC-AFM. EC-SCFS is capable of repeatable measurements of single cell de-adhesion on electrically switchable surfaces with force resolution on order of tens of piconewtons on millisecond to minute timescales. SCFS has made a significant impact by elucidating molecular mechanisms of integrin-extracellular matrix adhesion (e.g. collagen) [197], including early stages of adhesion [267], receptor cross-talk [180] and effect of culturing agents [199]. Furthermore, the ability to repeatedly probe molecular interactions of a cell on a material surface is important for gaining access to temporal and dynamic effects of switchable surfaces. Related to this thesis, EC-SCFS has been used to measure cell adhesion of fibroblast cells on conducting polymers as they are electrochemically switched from an oxidized to reduced state [48]. Here, we follow up on the previous Chapter 4 by using EC-SCFS to provide new insights into the cell interactions on GelMA/PPy-DBSA electrodes with varying modulus and as a function of electrical stimulation.

5.2 Materials and methods

5.2.1 Reagents

The pyrrole (Py) monomer was obtained from Sigma Aldrich and distilled prior to use. Dodecylbenzenesulfonate (DBSA) was used as the dopant and obtained from Sigma Aldrich. GelMA monomer was synthesized following the protocol described by O'Connell et al. (2016) and stored as a freeze-dried material with methacrylate degree of 72% [229]. GelMA solutions were prepared using PBS and a photoinitiator, Irgacure 2959 in 100% ethanol, which were both obtained from Sigma Aldrich.

5.2.2 Preparation of PPy-DBSA Films

The Polypyrrole (PPy) film doped with DBSA (PPy-DBSA film) was grown by electrodeposition at constant current on gold coated Mylar (gold-mylar) electrode. The gold-mylar was firstly prepared by cutting it into 2.2 cm x 2.2 cm area and cleaned with Milli-Q water (18.2 MΩ*cm) and UV exposure. An aqueous solution of 0.2 M Py and 6 mM of the counter-ion dopant DBSA was degassed for 2 min prior to polymerization of the monomer. The PPy-DBSA film was electrodeposited on gold-mylar with a current density of 0.25 mA/cm² for 10 min using an eDAQ EA161 potentiostat in a JPK Electrochemical Cell (ECCell^{TM}) to have PPy-films compatible to the JPK AFM-setup. The gold-mylar was used as working electrode, a platinum mesh as counter electrode and a Ag/AgCl NaCl 3M as the reference electrode (DRIREF-2SH, World Precision Instruments). Afterwards, the films were washed with Milli-Q water, gently dried with N2 gas and stored in a petri dish until use [53].

5.2.3 Preparation of GelMA/PPy-DBSA electrodes

GelMA hydrogel coatings on PPy-DBSA films were prepared according to our previous study [134]. Phosphate Buffer Solution (PBS) was prepared at pH 7.4 in Milli-Q water (18.2 MΩ*cm). Freeze dried GelMA (1 g) was dissolved in 5 ml PBS in a water bath at 37 °C. Aliquots of 500 µl GelMA solution were prepared in Eppendorf tubes, each sealed with parafilm and stored at 4 °C until use. GelMA/PPy-DBSA electrodes were prepared by warming the GelMA solution in a water bath at 37 °C for 5 min, followed by dissolution in PBS to 10% GelMA with 0.5 % Irgacure 2959. The mixture was then cast onto the PPy-DBSA film within a 0.5 cm x 1.0 cm acrylic frame with a height of 1 mm that was fabricated using laser cutting with a PLS6MW laser engraver from Universal Laser Systems (ULS). More specifically, the PPy-DBSA film was held within the acrylic frame using a clamp and then the GelMA solution cast to completely cover the film and fill the entire volume of frame area, giving a GelMA thickness of ~ 1 mm. The GelMA hydrogel was crosslinked using a UV Curing Spot Light Device “Blue Wave 50” from DYMAX (USA) by UV-light exposure with a wavelength of 365 nm. Different

intensities and exposure times (**Table 5**) were applied for the crosslinking of GelMA hydrogel to prepare samples with different moduli and porosity, as characterized in our previous study [134]. **Table 5** shows three GelMA/PPy-DBSA electrodes of different modulus that were used in experiments. After curing the GelMA hydrogel on top of the PPy-DBSA film, the GelMA/PPy-DBSA electrode was immersed in a small petri dish filled with PBS and stored at 4 °C overnight to ensure a fully hydrated hydrogel. Afterwards, it was sterilized in 70% ethanol for 15 min, washed 3 times in PBS and stored at 4 °C until use.

Table 5: Crosslinking conditions and nanomechanical properties of GelMA. Asterix * values measured from previous study [134].

Sample	GelMA (w/v %)	I2959 (w/v %)	Intensity (mW/cm^2)	Curing time (min)	Energy (J/cm^2)	Young's modulus* (Pa)	Pore size* (µm)
Soft	10	0.5	3	1	0.18	160	8.54
Medium	10	0.5	12.6	10	7.56	450	3.39
Stiff	10	0.5	89	1	5.34	900	1.16

5.2.4 Cell culture

ReNcell VM hNSC (SCC008, Millipore; approved for use by the University of Wollongong's Human Research Ethics Committee; HE14/049) culture was performed and cells were provided by co-supervisor Dr. Eva Tomaskovic-Crook for subsequent SCFS experiments according to previous methods [268]. Briefly, cells were retained in 6-well culture plates (Corning, Mulgrave, Australia) coated with 10 µg/ml laminin (Invitrogen). Cells were initially seeded at a density of 96 x 10^3 cells in 2 ml Complete NeuroCult Proliferation Medium (human); STEMCELL Technologies) and maintained in a humidified incubator at 37 °C with 5% CO_2. Cells were monitored daily and a half-volume media change performed every 3-4 days. Cell passaging was performed every 7 days by digesting in 0.5 ml pre-warmed TrypLE (Gibco BRL) for 3 min at 37 °C. Following digestion, TrypLE was neutralized by adding 1 ml Complete NeuroCult

Proliferation Medium and cells were gently resuspended in solution followed by centrifugation at 190 x g for 3 min. After removal of supernatant, cells were resuspended in fresh pre-warmed Complete NeuroCult Proliferation Medium and reseeded as described above for further subculture and/or experimentation. One ml of CO_2-independent medium containing cells with a concentration of approximately 80,000 cells/ml was then transferred into a 5 ml centrifuge tube and 300 µl injected into the electrochemical cell for single cell attachment onto AFM probes described in section 5.2.6 below.

5.2.5 AFM Probe functionalization

AFM probe functionalization to enable attachment of live single cells was done based on previous work [184] and following our recent studies [48, 204]. Firstly, tipless probes (NP-O10) obtained from Bruker were calibrated for their spring constant (~0.06 N/m) using the thermal noise method [269] (nb: the subsequent chemical functionalization did not affect the spring constant values). The probes were incubated at 37 °C in 0.5 mg/ml biotin-BSA (Sigma A6043) solution obtained from Sigma overnight, followed by washing in PBS three times. The probes were then incubated in 0.5 mg/ml streptavidin (Sigma S4762) solution for 30 min at room temperature, followed by further rinsing with PBS three times. Finally, the probes were incubated in 0.4 mg/ml Concanavalin-A-biotin (Sigma C2272) solution for 30 min at room temperature and washed with PBS three times. The probes were stored up to one week immersed in PBS at 4 °C. After usage the cantilevers were cleaned in sulfuric acid for 2 hrs and rinsed with Milli-Q water. Cleaned cantilevers could be reused and were calibrated again prior to each functionalization.

5.2.6 Electrochemical-Single Cell Force Spectroscopy (EC-SCFS)

Cyclic Voltammetry

Prior to each EC-SCFS experiment cyclic voltammetry of the GelMA/PPy-DBSA electrodes were performed using an eDAQ EA161 potentiostat in a JPK Electrochemical Cell (ECCell^{TM}) to have PPy-films compatible to the JPK AFM-setup. The gold-mylar was used as working electrode, a platinum mesh as counter electrode and a Ag/AgCl NaCl 3M as the reference electrode (DRIREF-2SH, World Precision Instruments). The JPK Electrochemical Cell (ECCell^{TM}) was used as BioCell to ensure complete oxidation and reduction of the GelMA-PPy/DBSA electrode and full uptake of electrolyte. Sweeping electrochemical voltage was cycled between 0 mV to -1000 mV, at a scan rate of 50 mV/s for 15 cycles in CO_2-Independent medium as the electrolyte in 37 °C.

Preparation of Single Cell AFM Probes

SCFS was performed using a JPK Biowizard II Atomic Force Microscope (JPK, Germany) mounted on a fully automated Nikon inverted optical microscope. The AFM-inverted optical microscope was fully enclosed in a cell incubation system for temperature and humidity control. The GelMA-PPy film was placed in a JPK 3-electrode electrochemical cell of the AFM and 600 µl of CO_2-independent medium was injected into the electrochemical cell. The Concanavalin functionalized tipless cantilever was then brought into contact with the GelMA/PPy-DBSA electrode and subsequently retracted by approximately 50 µm from the GelMA/PPy-DBSA electrode surface while heating was applied to enable the CO_2-independent media to reach thermal equilibration at 37 °C. A further 300 µl of CO_2-independent medium containing cells with a concentration of approximately 80,000/ml cells was then injected into the electrochemical cell and the cells allowed to settle onto the hydrogel surface for a period of 10 min. Rounded up cells that were yet to adhere to the surface were located with the optical microscope and the functionalized AFM probe

was positioned over a single cell. The cell was attached manually to the apex of the cantilever with the stepper motor in 1 µm steps and an applied force of 0.5 nN. After attaching the cell, the cantilever was retracted 50 µm and the optical microscope was used to confirm that the cell was positioned correctly at the end of the cantilever. Afterwards the single cell was allowed to adhere for 10-15 min to ensure the strength of cell attachment to the cantilever was greater than to the hydrogel surface during the SCFS. This procedure combined with only short cell contact times (e.g. seconds) is previously described as an important procedure for ensuring that cell adhesion to the cantilever is greater than adhesion to the opposing surface [315].

SCFS Measurements

The live single cell probe was then repositioned over a cell-free region of the hydrogel surface and F-D curves were performed with a loading force of 500 pN, contact-time of 1 sec and retraction speed of 20 µm/s for all experiments. For this SCFS experiment an z-extended travel stage (100 µm) was used due to the occurrence of longer-range interactions (in the z-length) of the F-D curves. 10 different cells were measured on each GelMA/PPy-DBSA electrode with different modulus (**Table *5***) and up to 20 F-D curves were collected for each cell (at 4 different positions on the sample), giving a total of 200 F-D curves per GelMA/PPy-DBSA electrode for the analysis.

Electrical Stimulation during the SCFS

Prior to the SCFS measurements, CV were run between 0 mV to -1000 mV, at a scan rate of 50 mV/s for 15 cycles in the CO_2-Independent medium as the electrolyte in 37 °C to ensure complete oxidation and reduction of the GelMA-PPy/DBSA electrode and full uptake of electrolyte. Using the F-D parameters described above, the SCFS curves were then setup to run continuously with a loading force of 500 Pa, a contact time of one second and a retraction speed of 20 µm/s. After each performed F-D curve a waiting period of 10 sec was given before the next F-D curve was

automatically triggered. The first F-D curve was manually triggered to run simultaneously with cyclic voltammetry applied in a potential range from 0 mV to -1000 mV with scan rate of 100 mV/s for approximately 300 s which conforms 13 full cycles (**Figure 45**). Importantly, the continuous SCFS was triggered at the same point on the CV in each single cell measurement and begun approximately 30 sec after the CV had commenced. As a result of the F-D and CV parameters, each individual SCFS curve was completed in 16 sec while a single CV cycle took 20 sec. The time to complete a SCFS curve relative to a CV cycle was done such that the retraction part of the SCFS curve (i.e. after the cell was kept in contact with GelMA surface for 1 sec) occurred at five different voltage-ranges over the different CV cycles and allowed for continuous sampling in both the reduced and oxidized states. Due to manual triggering and differences in the CV response of the different GelMA-PPy/DBSA electrodes, the specific voltage-ranges over which the force curves were collected slightly varied within a range of ± 30 mV between the different samples though were constant within the one type of sample.

5.2.7 Force Curve Analysis

Analysis of F-D curves

Analysis of the F-D curves was performed using the JPK Data Processing software (Version spm-5.1.11), which enabled the quantification of adhesion force, adhesion energy, detachment length, and determination of unbinding event such as ruptures and plateaus. Raw curves were converted into F-D curves using the measured detection sensitivity and spring constant into force [162]. Box-Whisker plots were plotted using OriginPro (2015) b9.2.272 and presented as means ± standard error of the mean. Non-parametric tests such as Mann-Whitney test were performed using the statistical package of OriginPro (2015) b9.2.272. Confidence for all data analyses was set at 95% ($p \leq 0.05$).

Analysis of loading rates

To investigate the loading rate on cell adhesion, the effective spring constant of the cell-cantilever system, k_{eff}, was measured, as described previously by Taubenberger et al. (2007) [190]. Briefly, the slope of a straight line was fitted through the final third of a rupture event for calculation of k_{eff} [190]. With a known k_{eff}, the loading rate, r, was then calculated according to $r = k_{eff} * v$, where v is the retraction speed of the cantilever (20 µm/sec) [270].

5.3 Results/Discussion

5.3.1 Cyclic Voltammetry of GelMA/PPy-DBSA electrodes

Cyclic voltammetry of the GelMA/PPy-DBSA electrodes with different moduli was performed in the same *in-situ* JPK 3-electrode electrochemical cell used for SCFS measurements under the AFM (**Figure 45**). The CV measurements were undertaken in CO_2-Independent media at 37 °C and showed clear oxidation and reduction peaks for all three GelMA/PPy-DBSA electrodes (**Figure 44**). For the PPy-DBSA film without the GelMA (solid black line), oxidation and reduction peaks were observed at -0.38 V and -0.63 V, respectively. The CV profiles for the different GelMA/PPy-DBSA electrodes did not significantly differ with the exception of a slight shift in the reduction potential towards lower values and overall small decrease in the redox current (**Figure 44**). In particular, the largest decrease in the current signal, primarily during reduction, was observed for the 160 Pa GelMA/PPy-DBSA electrode (-1.78 mA/cm^2) followed by the 450 Pa GelMA/PPy-DBSA electrode (-2.05 mA/cm^2) and then 900 Pa GelMA/PPy-DBSA electrode (-2.21 mA/cm^2) in comparison to the PPy-DBSA only (-2.34 mA/cm^2). The electrochemical response of the different GelMA/PPy-DBSA electrodes is in agreement with our previous study [134], indicating that the presence of the ~ 1 mm thick GelMA layer on top of the PPy-DBSA slightly increased the resistance though the overall electroactivity of the film is not

greatly affected as ions can freely diffuse through the porous GelMA/PPy-DBSA electrode.

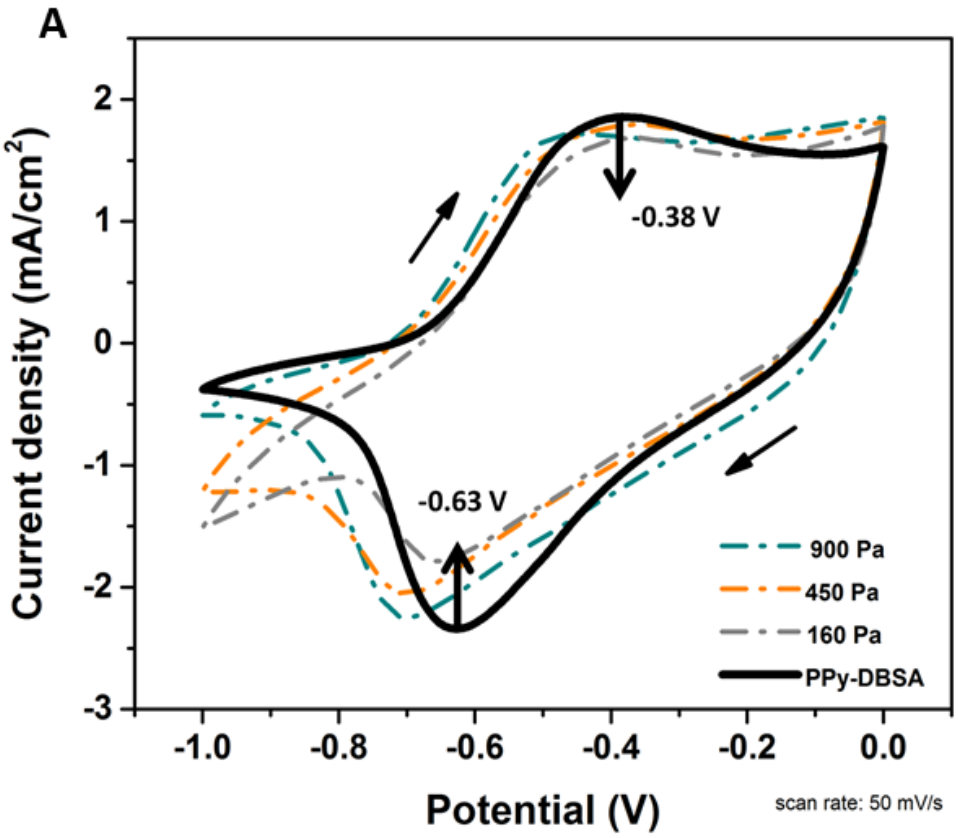

Figure 44: Cyclic Voltammograms during EC-SCFS. Cyclic voltammograms of the plain PPY-DBSA film (black line) and three GelMA/PPy-DBSA electrodes (900 Pa, 450 Pa and 160 Pa) in CO_2-independent media at 37 °C.

5.3.2 Electrical Stimulation Scheme for SCFS

Figure 45A shows representative, continuous F-D curves taken while simultaneously applying CV on the 900 Pa GelMA/PPy-DBSA electrode in CO_2-Independent media at 37 °C. The F-D curves are plotted as a function of time (black trace) with the overlaid corresponding CV voltage (orange trace) and current (green trace) signals (**Figure**

45A). Based on the CV measurements in **Figure 44**, a potential window between 0 mV and -1000 mV with a scan rate of 50 mV/s was applied to ensure full oxidation and reduction of the underlying PPy-DBSA. Whilst running the CV, triggering of continuous F-D curves whereby the first F-D curve started at ~190 secs and finished at ~205 secs resulted in the acquisition of individual F-D curves that repeatedly traversed five different voltage ranges (**Figure 45A**). These voltage ranges are labelled by numbers 1-5 (between the vertical dashed lines) and also correspond to the duration for acquiring a single F-D curve. It is noted that during the total time of 16 secs to acquire a single F-D curve, there are a series of different interactions between the hNSC and GelMA/PPy-DBSA electrode surface. For example, **Figure 45B** shows a zoomed in region from **Figure 45A** of a single F-D curve with overlaid applied voltage and current signals plotted as a function of time. During the CV, the F-D curve consists of an approaching region until the cell makes contact and continues to deform the GelMA/PPy-DBSA electrode surface. During this period, the cell may also undergo deformation. Following this, once the maximum applied force of 500 pN is reached, the cell is then held in contact with the GelMA/PPy-DBSA electrodes surface for 1 sec, which corresponds to the dwell contact time. Subsequently, the cell is retracted from the surface, resulting in de-adhesion interactions with the GelMA/PPy-DBSA electrode surface, until the cell completely detaches and is further retracted to a distance of 50 µm above the surface. Finally, the cell was held above the surface for 10 sec before the next F-D curve was performed. Therefore, the cell actually spends > 1 sec in various types of contact with the GelMA/PPy-DBSA electrode surface due to the indentation, dwell-contact, and adhesive interaction regions within a single F-D curve. In addition, given that the CV and F-D curve are also run continuously for a single cell measurement, the cell is also potentially subject to electrical stimulation even when not in contact with the surface, i.e. when retracted 50 µm above, during the waiting period of 10 secs before commencement of the next F-D curve. To further depict the acquisition of F-D curves in relation to the CV, **Figure 45C** shows a CV curve with the different voltage ranges only during the dwell contact time of 1 sec (orange highlighted sections) of a single F-D curve. In this case, the dwell-contact time of the F-D curve repeatedly occurred at different regions in the

CV scan, including in the fully reduced (1), reduction sweep (2), fully oxidized (3), oxidation potential (4), and oxidation sweep (5) of which the order was not governed by the CV scan direction but by the timing of the F-D curves (Fig. 2C). More specifically, the potential ranges for regions 1-5 were -0.72 V to -0.82 V (reduction), -0.27 V to -0.37 V (reduction sweep), -0.01 V to -0.02 V (fully oxidation), -0.49 V to -0.39 V (oxidation) and -0.74 V to -0.64 V (oxidation sweep), respectively.

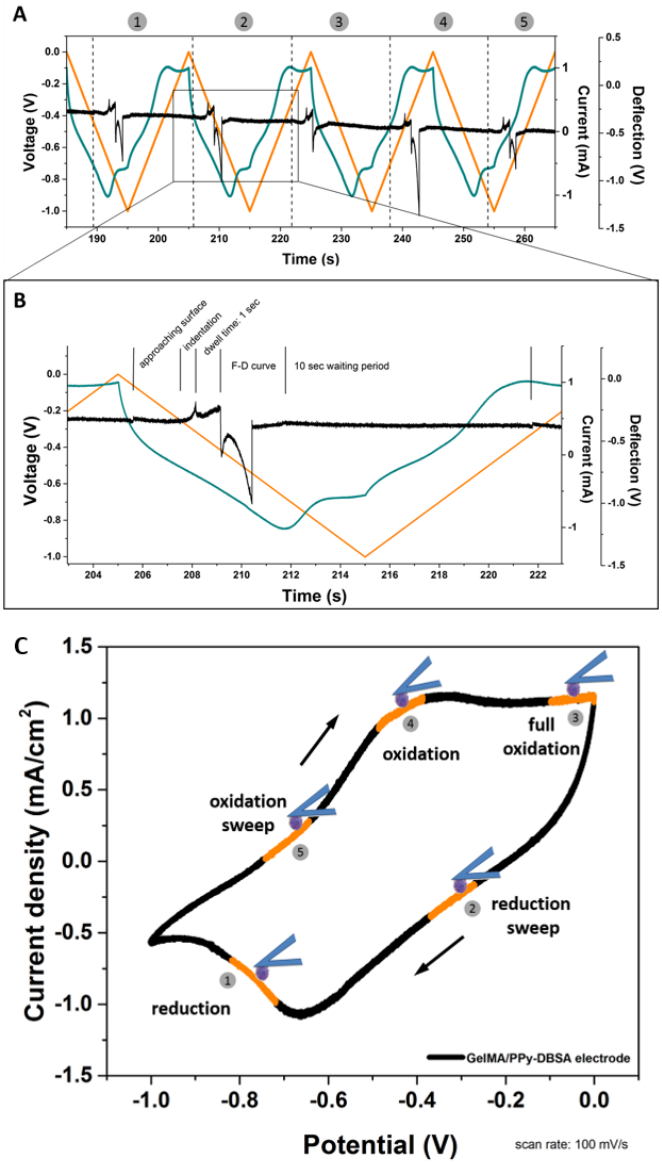

Figure 45: ES-SCFS as function of a triangle waveform stimulation. (**A**) Example data plot for 900 Pa GelMA/PPy-DBSA electrode obtained during ES-SCFS as a function of a triangle waveform stimulation and five continuous F-D curves at five different potential range (1-5). (**B**) Detailed explanation for the F-D curve at potential range (2). A complete F-D curve takes 16 sec; the cantilever with the attached cell approaches the surface until it makes contact and indentates into the surface of the GelMA/PPy-DBSA electrode. The surface contact will be hold for 1 sec, afterwards the cantilever pulls the cell from the GelMA/PPy-DBSA electrode surface with a retraction speed of 20 µm/s. A 10 sec waiting period is allowed to let the cell readjust and the cantilever starts to approach the GelMA/PPy-DBSA electrode surface again. Redox states (1) and (3) are reduced and fully oxidized states. (**C**) Cyclic voltammogram of 900 Pa GelMA/PPy-DBSA electrode in CO_2-Independent media at 37 °C marked with the areas (orange) when the single cell is hold in contact with the GelMA/PPy-DBSA electrode surface for one sec (dwell time) at the five potential ranges.

5.3.3 Effect of Electrical Stimulation on Hydrogel-Cell Interaction

Representative F-D curves for the interaction between hNSC and GelMA/PPy-DBSA electrode with GelMA of different moduli as a function of electrical stimulation are shown in **Figure 46**. F-D curves are only shown for two potential ranges, corresponding to the reduced (1) and oxidized (3) regions described in **Figure 45C**. Representative F-D curves for all potential ranges (1-5) are given in **Figure 47**. No qualitative differences were observed in F-D curves profiles between the reduced and oxidized potentials for GelMA/PPy-DBSA electrodes of different moduli (**Figure 46**), with the F-D curves showing similar rupture peaks and force magnitude. In contrast, irrespective of reduction or oxidation, significant differences were observed in the F-D profiles between the different GelMA moduli of 160 Pa, 450 Pa and 900 Pa. For the 160 Pa GelMA/PPy-DBSA electrode, the F-D curve showed an initial detachment of the cell from the surface followed by a series of smaller rupture peaks, i.e. the "saw-tooth" profile, and plateaus (**Figure 46**, **i**) that are commonly observed in SCFS experiments [48, 303]. In the case of 450 Pa GelMA/PPy-DBSA electrode, the F-D profiles also consisted of rupture peaks that were qualitatively similar to the 160 Pa though generally were fewer in number and had larger force magnitude (**Figure 46**, **ii**). In contrast, the F-D curves on 900 Pa GelMA/PPy-DBSA electrode showed an initial detachment peak followed by a larger non-linear curve forming additional peaks, typically 2-3 peaks, with forces that were significantly greater than those of the 160 Pa and 450 Pa /PPy-DBSA electrodes (**Figure 46**, **iii**).

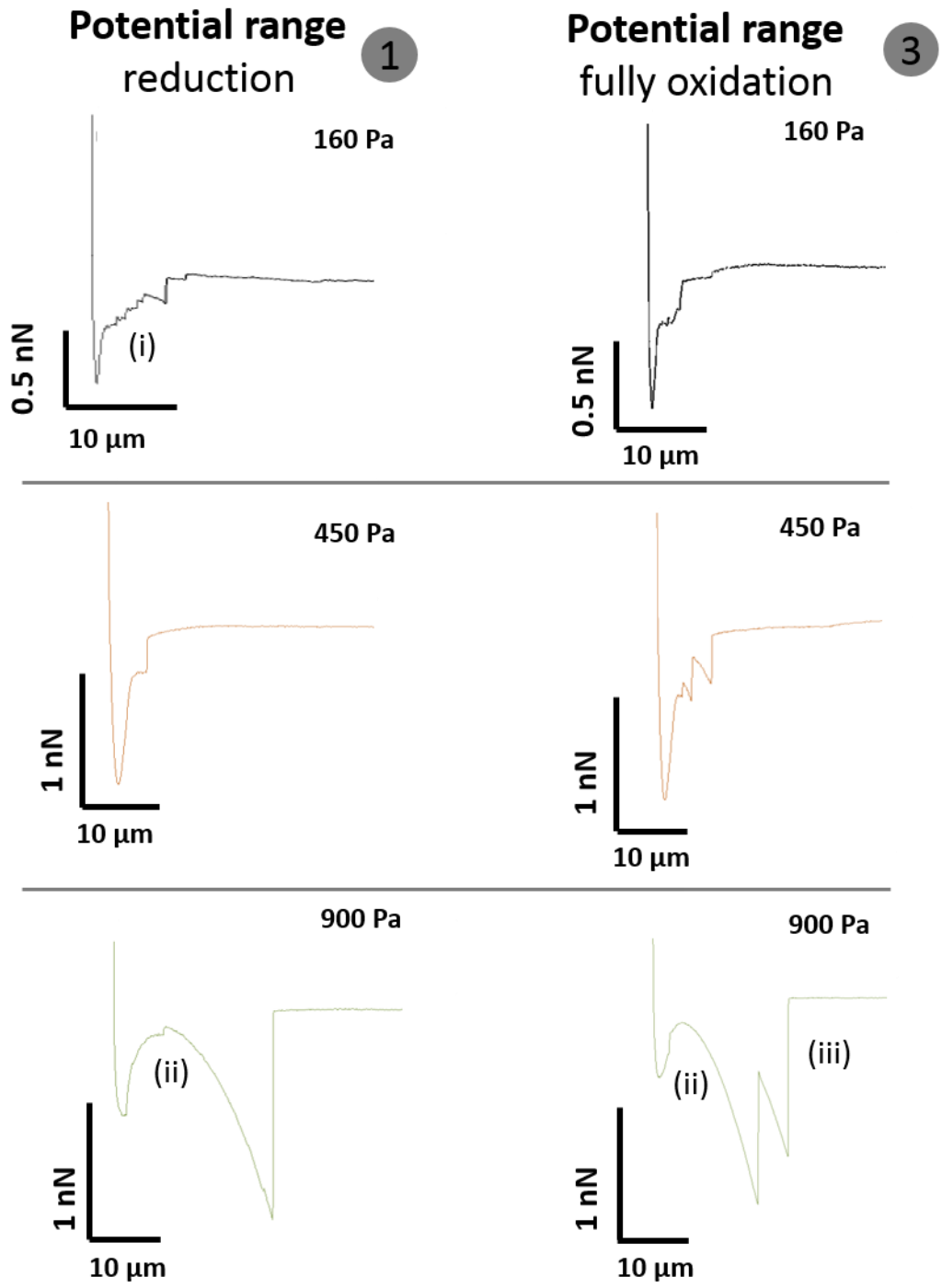

Figure 46: F-D curve profiles of three GelMA/PPy-DBSA electrodes at potential ranges one and three. F-D curves profiles of 160 Pa GelMA/PPY-DBSA electrode (grey), 450 Pa GelMA/PPY-DBSA electrode (orange) and 900 Pa GelMA/PPY-DBSA electrode (green). F-D curve profiles from different GelMA/PPy-DBSA electrodes show different properties such as typical rupture events (i), (ii) non-linear curve and (iii) large rupture forces.

Similar types of F-D curve profile characteristics were observed in the previous Chapter 4 on GelMA hydrogel of different moduli without electrical stimulation, however in **Figure 35**, they showed a completely opposite dependence on the modulus. For example, in Chapter 4, the non-linear peak with large de-adhesion force originated only from adhesive interactions with the softer GelMA hydrogels of 160 Pa and 450 Pa, whereas a greater number of smaller ruptures occurred on the stiffest 900 Pa GelMA hydrogel. The difference in these types of interaction profiles was interpreted as being due to elastic contributions from multiple, interacting GelMA polymer chains extending from the lower modulus, less cross-linked GelMA hydrogel versus the discrete unbinding of integrin –peptide complexes, i.e. smaller ruptures, without significant elastic contributions from GelMA polymer chains of the stiffer polymer (see Chapter 3). Therefore, **Figure 47** indicates that the electrical stimulation significantly alters these physical interactions of the GelMA-hNSC de-adhesion observed in Chapter 4, remarkably causing a reverse effect of the modulus.

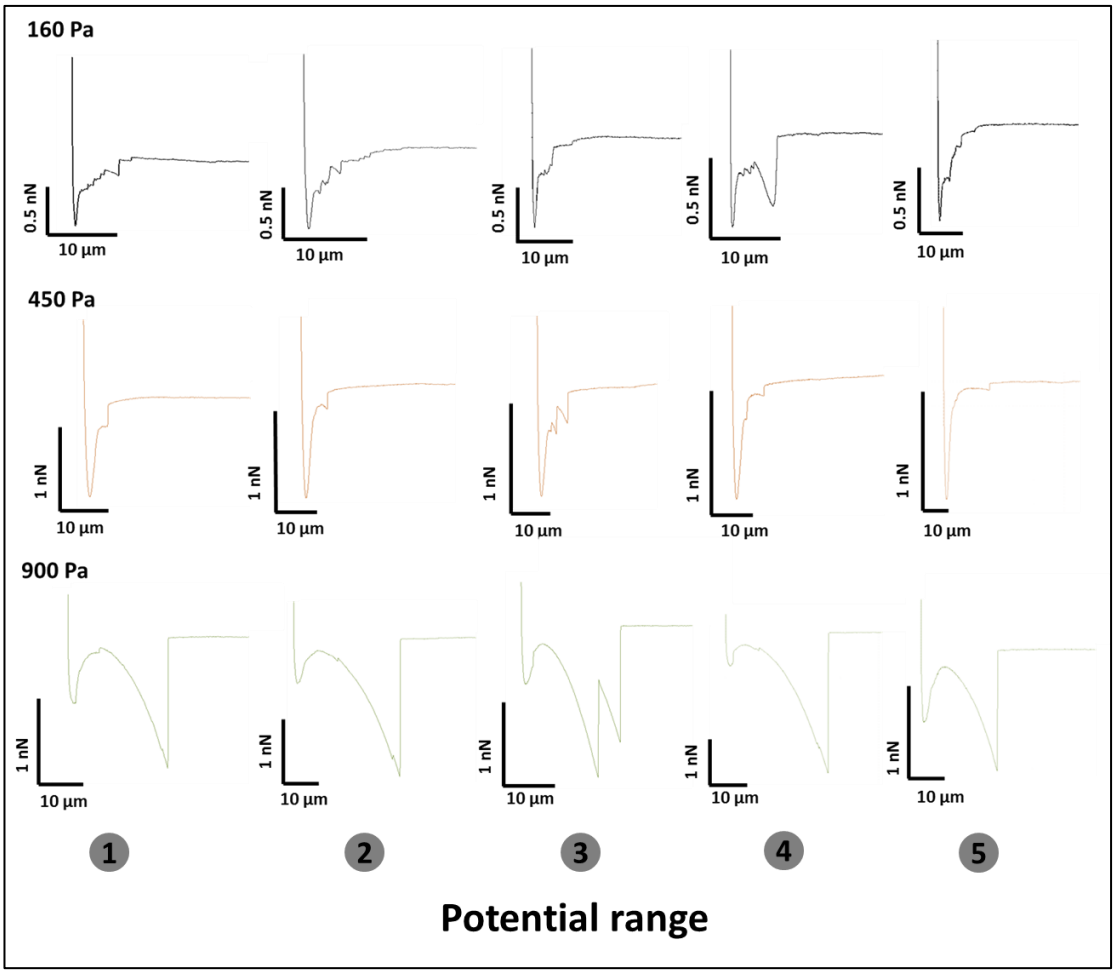

Figure 47: Representatives F-D curves profiles of five potential ranges. F-D curves profiles of each potential range within the three GelMA/PPy-DBSA electrodes (160 Pa, 450 Pa and 900 Pa). Potential range (1) = reduction, (2) = oxidation sweep, (3) fully oxidation, (4) oxidation, (5) reduction sweep.

5.3.4 Effect of Electrical Stimulation on Cell De-Adhesion Force and Energy

To confirm the qualitative differences in F-D curves, statistical analysis of the maximum cell de-adhesion force and energy from all F-D curves is shown in **Figure 48**. Compared to without electrical stimulation (control), both the softer 160 Pa and 450 Pa GelMA/PPy-DBSA electrodes showed significant decreases in the de-adhesion force (**Figure 48A**) and energy (**Figure 48B**) during electrical stimulation, involving either reduction or oxidation of the underlying PPy-DBSA. Specifically, the de-adhesion force of the control samples (4.2 ± 2.6 nN) decreased by 81% to values of

0.8 ± 0.4 nN and 0.8 ± 0.6 nN, respectively, for electrical stimulation of the 160 GelMA/PPy-DBSA electrode. De-adhesion forces of control samples of the 450 Pa (3.5 ± 3.1 nN) showed similar decreases to values of 0.8 ± 0.5 nN and 0.7 ± 0.4 nN during electrical stimulation. In contrast, the 900 Pa GelMA/PPy-DBSA electrode showed an opposing significant increase in the de-adhesion force during electrical stimulation for both reduction and oxidation (**Figure 48A**), however, no significant difference was observed for de-adhesion energy (**Figure 48B**). Lastly, no significant differences in the de-adhesion force and energy between the reduction and oxidation potentials was observed for any GelMA/PPy-DBSA electrodes (**Figure 48**), confirming the qualitative comparison of their F-D curves in **Figure 46**.

The statistical variation in the de-adhesion force and energy values showed a significant increase with increasing modulus, which was particularly evident when comparing both the 160 Pa and 450 Pa with the 900 Pa GelMA hydrogels without electrical stimulation (**Figure 48A-B**, control samples). In Chapter 4, a greater statistical variation (standard error of the mean) was attributed to higher probability of interactions occurring with varying number of less cross-linked GelMA polymer chains of the softer GelMA hydrogels. Additional effects on the statistical variation were observed when hNSC de-adhesion was supressed during blocking of integrin receptors by antibodies, specifically causing a decrease in statistical variation for the 160 Pa and 450 Pa GelMA hydrogels (see Chapter 4). For the 900 Pa GelMA hydrogel, however, the antibody blocking increased cell de-adhesion but also had the effect of increasing the statistical variation. In **Figure 48A-B**, the electrical stimulation had similar effects, namely causing a decrease in statistical variation for both the 160 Pa and 450 Pa GelMA/PPy-DBSA electrodes, while an opposing increase was observed for the 900 Pa GelMA/PPy-DBSA electrode (**Figure 48A-B**).

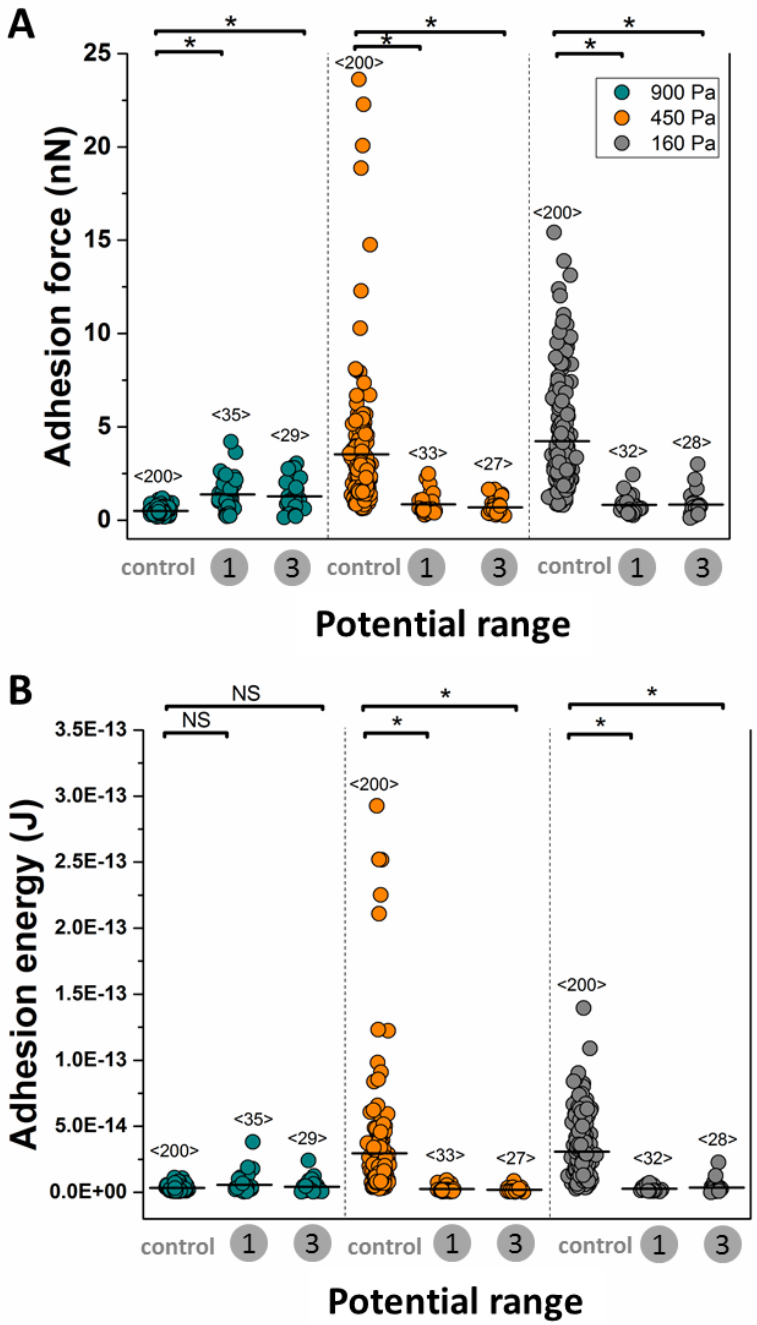

Figure 48: Quantifying cell adhesion at two potential ranges by EC-SCFS. (A) Adhesion forces between a hNSC and three GelMA/PPy-DBSA electrodes at potential range reduction and fully oxidation compared to non-stimulation (control) shown as scatter plots. (**B**) Adhesion energy between a hNSC and three GelMA/PPy-DBSA electrodes at potential range reduction and fully oxidation compared to non-stimulation (control) shown as scatter plots. (1) = reduction; (3) = fully oxidation. The number of analysed F-D curves is given above column scatters (<n>). Asterisks indicate statistical significance *p≤0.05, (NS) not significant (Mann-Whitney test).

In addition to analysis of de-adhesion force and energy, the number of ruptures and their detachment length provide further insight into the GelMA – hNSC interaction. **Figure 49A** shows that the number of single rupture events decreased during electrical stimulation for all GelMA/PPy-DBSA electrode samples, with statistical significance observed between the control and all electrically stimulated GelMA samples. **Figure 49B** shows that the electrical stimulation, including both reduction and oxidation potentials, also caused a significant decrease in detachment length compared to the control. For the 900 Pa GelMA/PPy-DBSA electrode, the control values were 17.2 ± 7.0 µm, which decreased to 12.0 ± 8.8 µm (reduction) and 9.0 ± 5.9 µm (oxidization) (**Figure 49B**). Similarly, the 450 Pa GelMA/PPy-DBSA electrode had control values of 20.9 ± 12.4 µm, which decreased to 9.0 ± 8.4 µm (reduction) and 6.6 ± 6.6 µm (oxidation) (**Figure 49B**). The 160 Pa control sample showed similar detachment length of 20.8 ± 8.9 µm, which decreased to 13.5 ± 10.2 µm (reduction) and 12.3 ± 8.1 µm (oxidation) (**Figure 49B**). When comparing the different potentials, the detachment length was greater for the oxidized compared to the reduced potential for all GelMA moduli, however, no statistically significant difference was observed between the values (**Figure 49B**).

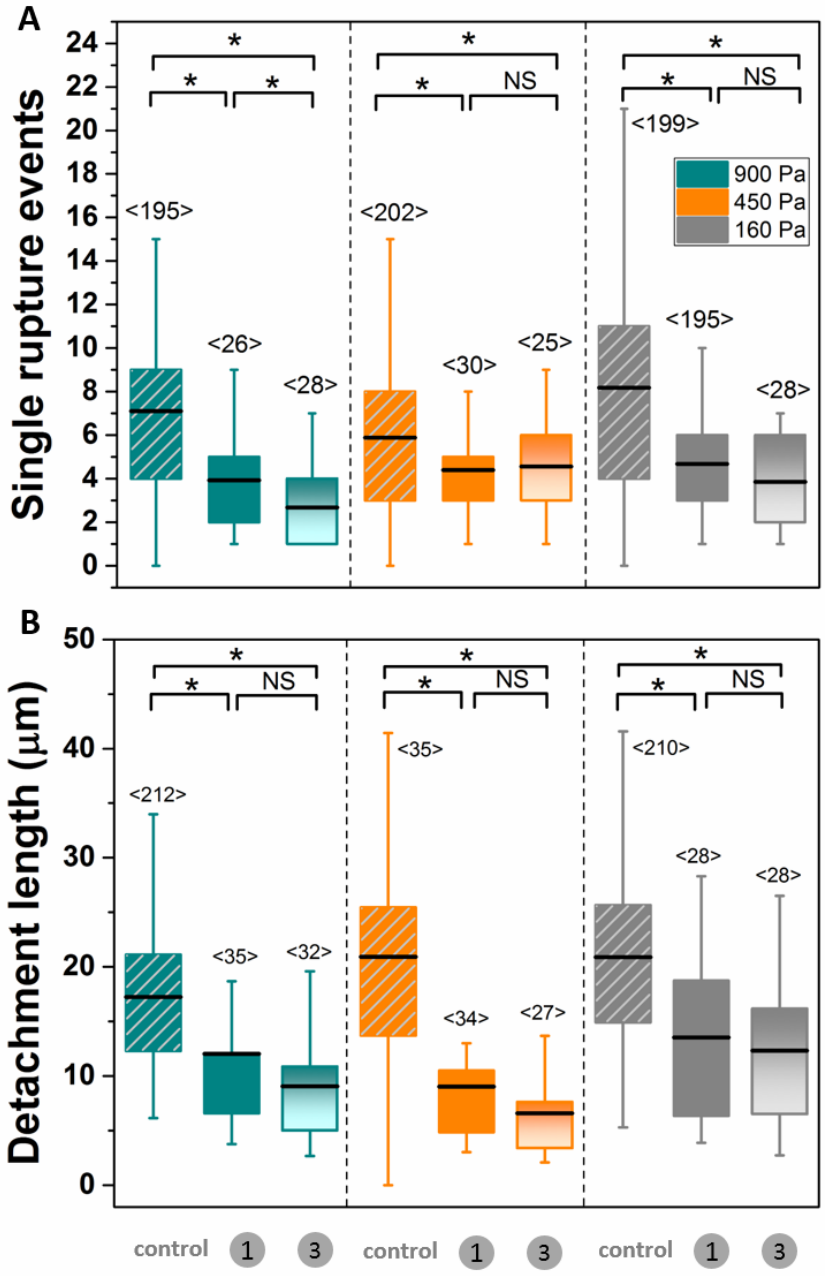

Figure 49: Analysis of single rupture events and detachment length. A. Box-Whisker plots of detachment length per F-D curve. Detachment length of non-stimulated (control) and electrical stimulated 900 Pa (green), 450 Pa (orange) and 160 Pa (grey) GelMA/PPy-DBSA electrodes. (1) = reduction; (3) = fully oxidation. B. Quantification of single rupture events per force curve of hNSCs on three different GelMA/PPy-DBSA electrodes at five different potential ranges shown as Box-Whisker plots. The number of analysed events is given above Box-Whisker plots (<n>). Asterisks indicate statistical significance *p≤0.05, (NS) not significant (Mann-Whitney test).

The effect of electrical stimulation on cell de-adhesion force and energy across all potential ranges is shown in **Figure 50**. Firstly, as above for reduced (1) and oxidized (3) potential ranges, we found no significant difference in both the de-adhesion force (**Figure 50A**) and energy (**Figure 50B**) between potential ranges 1-5 for all GelMA/PPy-DBSA electrodes, indicating that oxidation and reduction of the underlying PPy-DBSA had the same effect on the GelMA-hNSC interaction despite their different electrochemical redox processes. Electrical stimulation across all potential ranges showed that the 900 Pa GelMa/PPy-DBSA electrode had the greatest de-adhesion forces ranging from 1.54 ± 1.04 nN to 1.25 ± 0.86 nN compared to the 450 Pa and 160 Pa GelMA/PPy-DBSA electrodes with values ranging from 0.85 ± 0.54 nN to 0.67 ± 0.38 nN (**Figure 50A**). Statistically significant differences were observed between the 900 Pa and other two GelMA samples in potential ranges 1 and 2, with other statistical comparisons given in **Figure 50**. A similar trend was observed for the de-adhesion energy (**Figure 50B**).

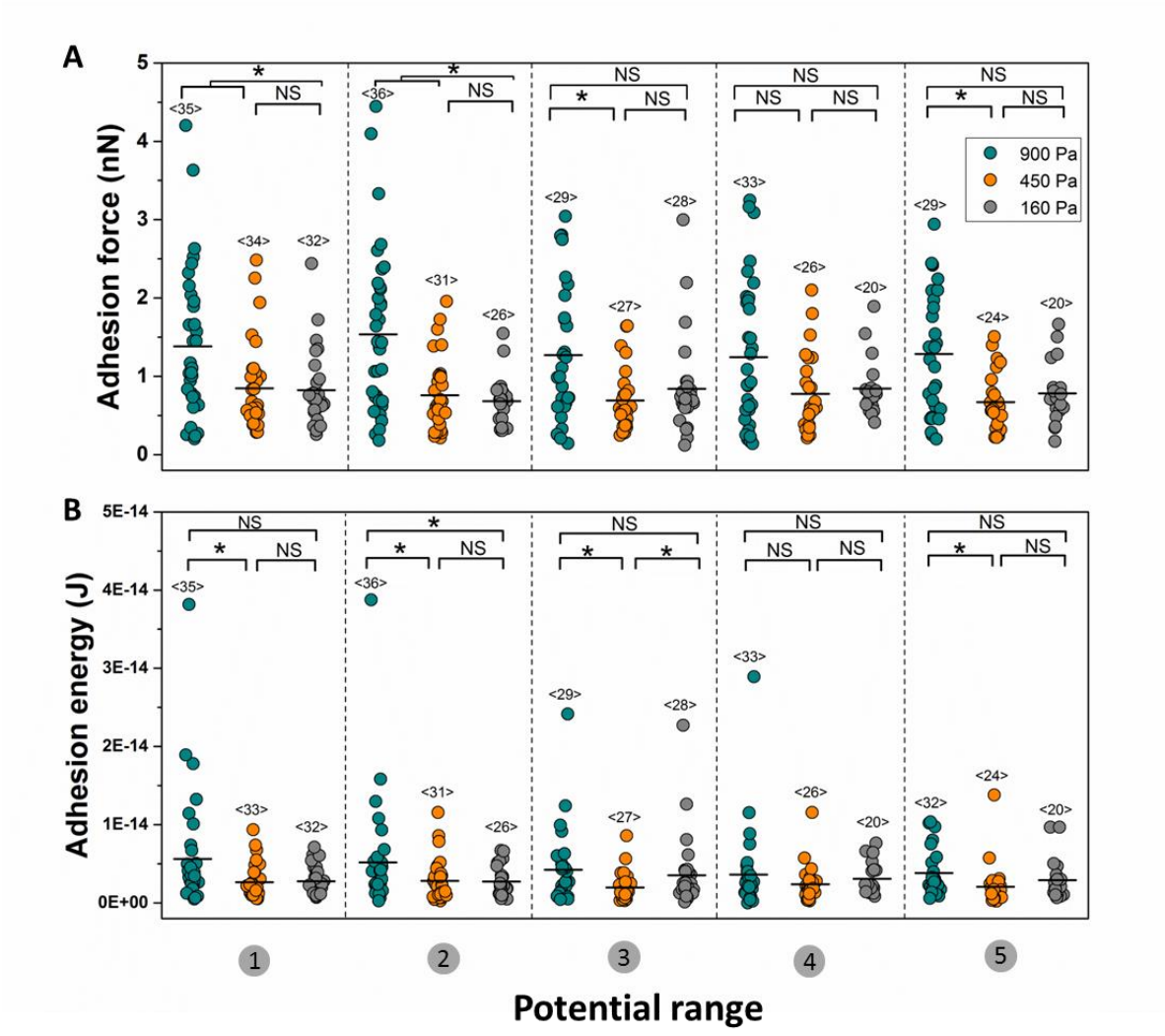

Figure 50: Quantifying cell adhesion at five potential ranges of GelMA by EC-SCFS. (**A**) Adhesion forces between a hNSC and three GelMA/PPy-DBSA electrodes shown as scatter plot at five different redox states (1-5). (**B**) Adhesion energy between a hNSC and three GelMA/PPy-DBSA electrodes shown as scatter plot at five different potential ranges. 900 Pa GelMA/PPy-DBSA electrode (green), 450 Pa GelMA/PPy-DBSA electrode (orange) and 160 Pa GelMA/PPy-DBSA electrodes (grey). The number of analysed F-D curves is given above column scatters (<n>). Asterisks indicate statistical significance *p≤0.05, (NS) not significant (Mann-Whitney test).

5.3.5 Effect of Electrical Stimulation and Modulus on Individual Ruptures

For all GelMA samples, statistically significant differences were observed between the control (non-stimulation) and electrically stimulated samples for analysis of individual rupture forces (**Figure 51**). Single rupture peaks for 900 Pa gave values of 70.0 ± 9.0 pN, which are reflective of those forces typically required for unbinding of single receptor complexes [197] (**Figure 51A**). During electrical stimulation, these piconewton forces significantly increased to 0.55 ± 0.59 nN and 0.55 ± 0.66 nN for reduction and oxidation, respectively (**Figure 51A**), possibly indicating the involvement of multiple receptor interactions. Control samples of both 450 Pa (**Figure 51B**) and 160 Pa (**Figure 51C**) without electrical stimulation had significantly higher rupture forces of 0.97 ± 1.43 nN and 0.81 ± 0.85 nN, respectively, due to the greater number of interacting GelMA polymer chains, as demonstrated in the previous Chapter 4. Both softer GelMA/PPy-DBSA electrodes, however, showed a significant reduction in the rupture forces during electrical stimulation (**Figure 51B-C**). More specifically, the reduction potential gave rupture forces of 0.18 ± 0.27 nN and 0.4 ± 0.95 nN for 160 Pa and 450 Pa GelMA/PPy-DBSA electrodes, respectively (**Figure 51B-C**). At the oxidation potential, similar rupture forces of 0.22 ± 0.41 nN (160 Pa) and 0.33 ± 0.66 nN (450 Pa) were obtained. Thus, changes in single rupture forces for all GelMA/PPy-DBSA electrode moduli were concomitant with the effects of electrical stimulation on the maximum de-adhesion forces in **Figure 48A**. Lastly, comparison of the rupture length between the control and electrically-stimulated samples showed a less clear trend compared to the rupture force (**Figure 51D-F**).

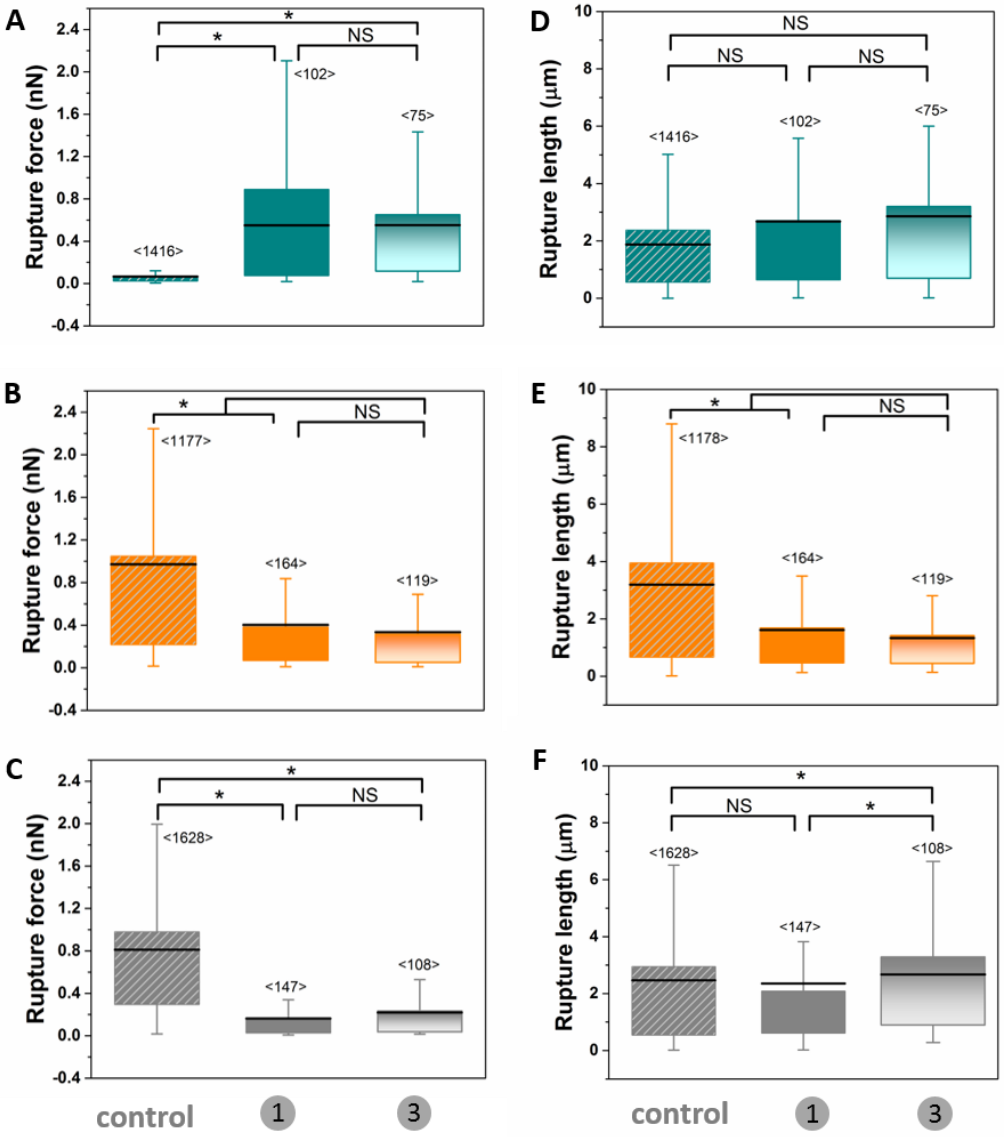

Figure 51: Analysis of rupture force and rupture length during ES-SCFS. Box-Whisker plots of molecular level interactions between a hNSC and GelMA/PPy-DBSA electrodes. (**A**) Rupture force of non-stimulated (control) and electrical stimulated 900 Pa GelMA/PPy-DBSA electrodes (green). (**B**) Rupture length of non-stimulated (control) and electrical stimulated 900 Pa GelMA/PPy-DBSA electrodes (green). (**C**) Rupture force of non-stimulated (control) and electrical stimulated 450 Pa GelMA/PPy-DBSA electrodes (orange). (**D**) Rupture length of non-stimulated (control) and electrical stimulated 450 Pa GelMA/PPy-DBSA electrodes (orange). (**E**) Rupture force of non-stimulated (control) and electrical stimulated 160 Pa GelMA/PPy-DBSA electrodes (grey). (**F**) Rupture length of non-stimulated (control) and electrical stimulated 160 Pa GelMA/PPy-DBSA electrodes (grey). (1) = reduction; (3) = fully oxidation. The number of analysed events is given above Box-Whisker plots (<n>). Asterisks indicate statistical significance *p≤0.05, (NS) not significant (Mann-Whitney test).

5.3.6 Loading Rate and Dynamic Force Regimes

Loading rate refers to the dynamic nature of the cell interactions, particularly with respect to the rate in which the force applied over a given time, and can be estimated from the F-D curves using various methods [316]. Investigating effects of loading rate in AFM single molecule [287-289] and cell measurements [192, 316] is referred to as 'dynamic force microscopy' [291] and extensively studied over the past decade yet the role of soft, compliant substrates has only recently been explored in SCFS [192]. In SCFS, the elasticity of the hydrogel substrate is expected to affect the loading rate of integrin−ligand bonds via its impact on the effective spring constant system, k_{eff}, of the system, i.e. loading rate increases with increasing k_{eff}, as demonstrated in previous SCFS studies [192]. In Chapter 4, we revealed that the loading rate unexpectedly increased for lower GelMA modulus, proposed by the cell de-adhesion involving interactions of multiple chains in parallel that effectively increases the k_{eff}. Interestingly, the rupture force versus loading rate for the two softer GelMA hydrogels (160 and 450 Pa) showed a non-linear relationship, or dual slope regimes (i.e. both low and high loading rate regimes) whereas the stiffer 900 Pa GelMA hydrogel only showed a single linear slope. Furthermore, the binding of anti-integrin antibodies to main integrin subunits reversed the relationship between the dynamic force regimes and modulus, i.e. the high force was deactivated for 160 and 450 Pa GelMA hydrogels and oppositely activated for the 900 Pa GelMA hydrogel (see Chapter 4). Importantly, Chapter 4 highlighted the complexity of interactions involving cross-linked and multiple GelMA polymer chains within a hydrogel polymer network, which are not well described by classical DFS analysis (e.g. Bells model) [186] and whose bulk modulus cannot be assumed to directly determine the loading rate. More recent extensions of DFS models that consider multiple bonds [295] have potential to be applied to hydrogel systems, with a review on this topic for complex polyelectrolytes given by [317].

Using previous methods to determine loading rate from F-D curves [190], **Figure 52** showed that the electrical stimulation similarly induced a reverse effect on the dynamic force regimes in rupture force versus loading rate curves. In particular,

the electrical stimulation activated an additional higher force regime, presenting a dual slope for the 900 Pa GelMA/PPy-DBSA electrode (**Figure 52A-B**, green). In contrast, the two softer GelMA/PPy-DBSA electrodes showed a significant reduction, or complete absence of the higher force regime, and reverted to only a single slope, or low force regime during electrical stimulation (**Figure 52C-F**). In addition, no significant difference in the dynamic force regimes between the reduced and oxidized potentials was observed (**Figure 52**). We suggest that the effects of electrical stimulation on the dynamic force regimes and their dependence on the modulus are again related to changes in the physical interactions of GelMA polymer chains, which is summarized below.

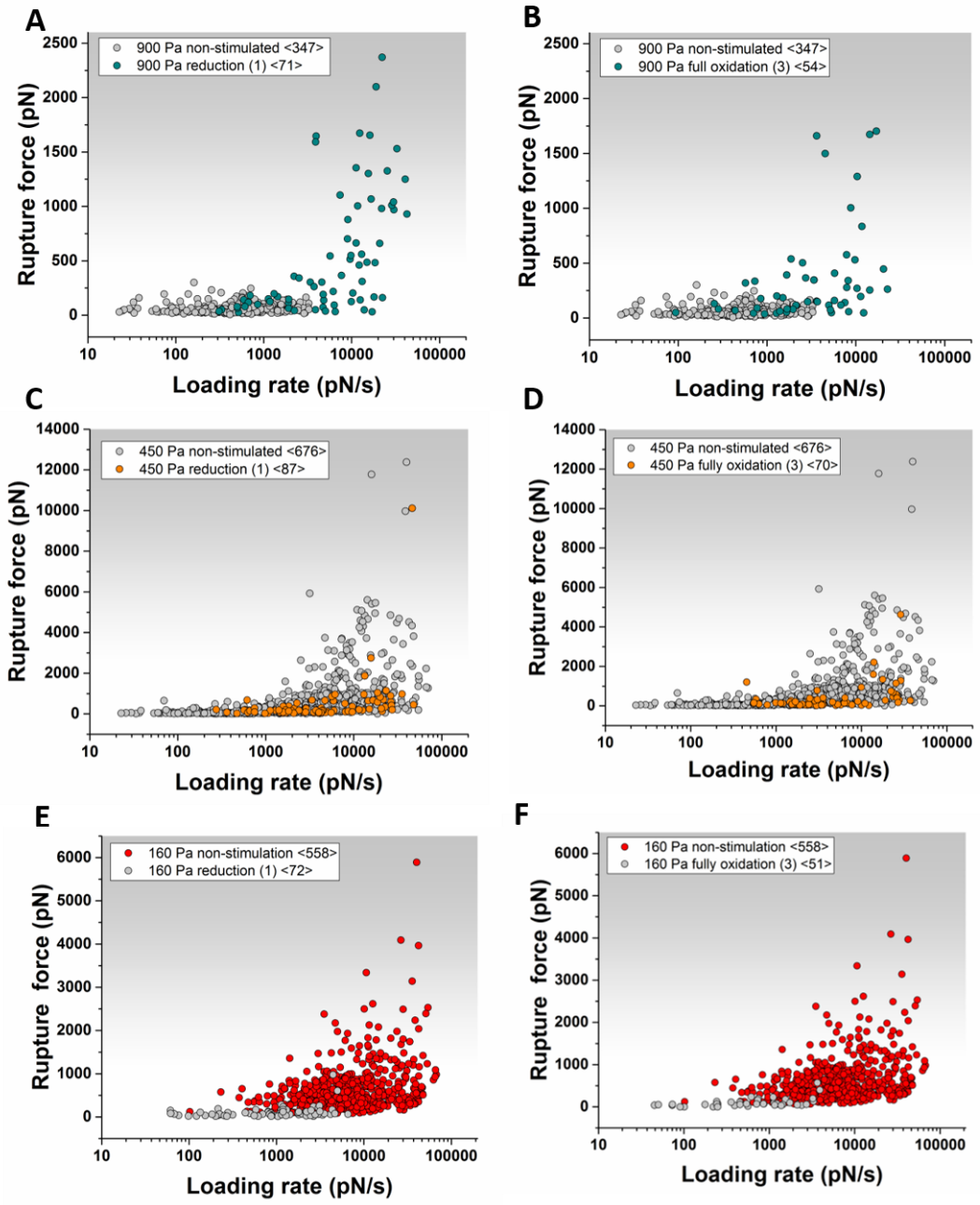

Figure 52: Scatter plots of loading rates vs bond rupture forces. Quantified between hNSC and GelMA/PPy-DBSA electrodes non-stimulated (control) and as function of electrical stimulation at potential ranges reduction (1) and fully oxidation (3). (**A**) 900 Pa GelMA/PPy-DBSA electrode at potential range reduction (1) (green) and non-stimulation (grey). (**B**) 900 Pa GelMA/PPy-DBSA electrode at potential range fully oxidation (3) (green) and non-stimulation (grey). (**C**) 450 Pa GelMA/PPy-DBSA electrode at potential range reduction (1) (orange) and non-stimulation (grey). (**D**) 450 Pa GelMA/PPy-DBSA electrode at potential range fully oxidation (3) (orange) and non-stimulation (grey). (**E**) 160 Pa GelMA/PPy-DBSA electrode at potential range reduction (1) (grey) and non-stimulation (red). (**F**) 160 Pa GelMA/PPy-DBSA electrode at potential range fully oxidation (3) (grey) and non-stimulation (red). Number of events <n> beside legend.

5.3.7 Electrical Stimulation Mechanism Involved in Cell Adhesion

To interpret the above effects of electrical stimulation on the cell de-adhesion, including the influence of the modulus, we firstly explain the redox processes the underlying PPy-DBSA electrode that provide the driving force for changes in the GelMA hydrogel properties. In the oxidized PPy-DBSA, immobile DBSA- balances positive charges of the PPy+ chain, while during reduction the PPy° becomes neutral, causing excess negative charge due to immobile DBSA- in the polymer [239]. The latter is charged compensated by the influx of cations and associated solvent from the electrolyte. This cation-driven actuation process is reversible, and contraction of the polymer is then caused by ejection of ions during oxidation [239, 240]. When correlating this process with the changes in the GelMA/PPy-DBSA electrodes it was confirmed that expansion of the GelMA hydrogel occurs during reduction, or when ions move into the GelMA hydrogel and towards the PPy-DBSA film, and contraction occurs during the ejection of the cations from the GelMA hydrogel. Furthermore, the reduction potential correlated with an increase in the Young's modulus and explained by a likely increase in volume change and osmotic pressure produced by counterions as the GelMA hydrogel expands. Evidently, this electrochemical process is reversible and therefore a decrease in the modulus occurs upon oxidation, as the ions move out of the gel. The magnitude of this effect was dependent on modulus, with the 900 Pa GelMA/PPy-DBSA electrode showing up to 33.7% change in modulus compared to 16.1% for the 160 Pa, when the PPy-DBSA was electrochemically switched between oxidized and reduced states.

Since no difference in the GelMA-hNSC interaction was observed for oxidation and reduction, we suggest that general mechanisms of electrical field induced volume changes, including the main forces (i.e. osmotic pressure) of phase transitions in hydrogels play an important role. For example, as described in Chapter 1 (section 1.3.2), osmotic pressure can be separated into discrete parts, including negative pressure due to polymer-polymer chain affinity, elasticity of the polymer chains, and the counterion pressure [94, 95]. The electrical field can also directly

exert a net force on charged groups of the polymers, or alternatively cause depletion (accumulation) of ions at the hydrogel-solution interface, causing a shift in local ionic strength that has been shown to induce bending [91]. Electro-osmosis involving migration of counterions has potential to generate hydrodynamic shear forces acting on the polymer network. Therefore, through any of these mechanisms, we suggest that phase transitions may constrain the motion or flexibility of individual GelMA polymer chains despite the reversible changes in the osmotic pressure. We emphasize that it is not the absolute change in modulus per se, i.e. changes in GelMA/PPy-DBSA electrode modulus during electrochemical switching, but the discrete forces impeding on individual GelMA polymer chains. For the 160 and 450 Pa GelMA/PPy-DBSA electrodes, this may have the effect of reducing the number of chain interactions and their elastic contributions, evidently leading to a significant decrease in the cell de-adhesion. Similar electrically induced osmotic forces acting on the 900 Pa GelMA/PPy-DBSA electrode, unexpectedly causes an opposite effect by increasing the cell de-adhesion. F-D curve profiles show larger non-linear peaks (**Figure 46**), with fewer numbers of individual ruptures (**Figure 51A**), suggesting that multiple chain interactions are induced. Whilst not completely clear at this stage, we suggest that the GelMA polymer chains, having greater restricted chain mobility, within the more cross-linked 900 Pa GelMA/PPy-DBSA electrode may alternatively undergo structural or conformation changes due to osmotic forces. Such changes then have potential to either increase integrin access to peptide groups or strengthen binding of integrin complexes along the gelatin chain, promoting a greater number of chain interactions during the cell de-adhesion.

Despite the above effects attributed to changes in hydrogel properties, the single cells are also subject to electrical stimulation, i.e. electrical field and charge injection, even when not in contact with the GelMA electrode surface. For example, studies on electrophoresis by Poo et al. (1977), Jaffe et al. (1979), and McLaughlin et al. (1981) discuss that an electro-osmotic flow of fluid parallel to a cell membrane exerts a hydrodynamic force on mobile macromolecules, causing negatively charged macromolecules to accumulate to the negative side of a cell [318-320]. Moreover, it is assumed that the cell surface has a net negative charge and causes mobile

counterions to accumulate in an “aqueous diffuse double layer”. This fluid movement exerts a force on macromolecules that protrude from the lipid bilayer of the membrane [320]. McLaughlin et al. (1981) predicted that mobile, negatively charged macromolecules will move to the positive side of the cell depending on each of their zeta potentials [320]. For example, ConA receptors can be electric field-induced to reverse their normal direction of movement and accumulate at the positive side of embryonic muscle cells. Therefore, it is conceivable that electrical field generated through the GelMA could have direct effects on the cell surface molecules in combination with changes in the hydrogel properties though this requires further investigation.

5.4 Conclusion

In conclusion, the use of electrical stimulation, irrespective of either oxidation or reduction potentials, caused a significant decrease in cell de-adhesion on 160 and 450 Pa GelMA but an increase for the 900 Pa. These changes in cell de-adhesion force were also in agreement with associated changes in force magnitude of individual rupture peaks. Analyses of the rupture force versus loading rate showed that the electrical stimulation activated an additional higher force regime, presenting a dual slope for the 900 Pa GelMA. In contrast, the two softer GelMA/PPy-DBSA electrodes, which initially showed two dynamic force regimes, reverted to only a single, low force regime during electrical stimulation. These findings are analogous to those in Chapter 4 where the anti-integrin antibodies increased both the de-adhesion forces and rupture forces, as well as activated higher force regimes for 900 Pa GelMA, while the opposite effect occurred for both the 160 and 450 Pa GelMA. In this case, the anti-integrins have a direct effect by binding to the cell receptors, for which their subsequent activation and nature of their interaction, is dependent on the hydrogel modulus. On the other hand, for electrical stimulation, clearly there are direct effects on the hydrogel properties, i.e. 20 - 50% changes in modulus, as demonstrated in

Chapter 3 though the cells are also exposed to charge injection from the electrode during the SCFS experiments. In summary, a key finding in the thesis is that the effects of stimuli such as antibody binding to integrins or electrical stimulation on the cell interactions are coupled to a modulus-dependence mechanism. Therefore, investigating the effects of the polymer network properties, e.g. crosslinking, elasticity, viscoelasticity, coupled with the presentation of ligands, e.g. antibodies, or external stimuli (electrical, optical, magnetic) presents novel approaches in the development of surfaces and materials to control stem cell interactions.

Chapter 6:
Future Work

To conclude this thesis, a brief description of ideas for future research based on SCFS and other key findings arising from the work are given below.

6.1 Single Molecule Interactions of GelMA Peptides

In the thesis, it was found that the interaction between the living cell and GelMA strongly depends on the GelMA polymer chains. In Chapter 4, the lower modulus, or less cross-linked GelMA, enables greater extension of individual GelMA polymer chains during cell de-adhesion, giving rise to their collective elastic restoring forces and hence greater de-adhesion forces and energy. This effect ultimately depends also on the crosslinking conditions and properties of GelMA, as detailed in Chapter 3. Currently, it is unknown how the RGD peptide groups along polymer chains of the GelMA (see Chapter 1, **Figure 10**) are affected by the UV crosslinking process. For example, studies show that the proteins such as collagen I and fibronectin attached to a gel network have different underlying mechanical properties that affect the cell interaction [321]. In future work, AFM could be used to elucidate the binding properties and distribution of cell binding peptides, e.g. RGD, within polymer chain networks, particularly looking at the effect of crosslinking and other sample preparation conditions of the GelMA. For this type of study, an AFM cantilever functionalized with an antibody (e.g. RGD or collagen) can be brought into contact with the hydrogel surface to initiate binding between ligands on the tip and hydrogel peptide groups (**Figure 53**). The measurement of the binding forces could shed light on the peptide distribution, orientation or effect of polymer chain stiffness on the

single molecule interactions. Furthermore, regarding to the main findings from Chapter 4, where the combined effect of modulus (chain elasticity) with antibody binding – which induced a significant change in the interaction, force, dynamic regimes, i.e. receptor crosstalk is presented, these types of AFM measurements could be done on model polymer surfaces with end ligand functionalized polymer chains. Various combinations of single chain stiffness (length of polymer chain) with ligands (antibodies, growth factors, ECM proteins) could be investigated by using single molecule of cell force spectroscopy. Subsequently, this work could be continued by testing a wide range of different combination of the stiffness/ligands in *in vitro* cell culture for NCS differentiation.

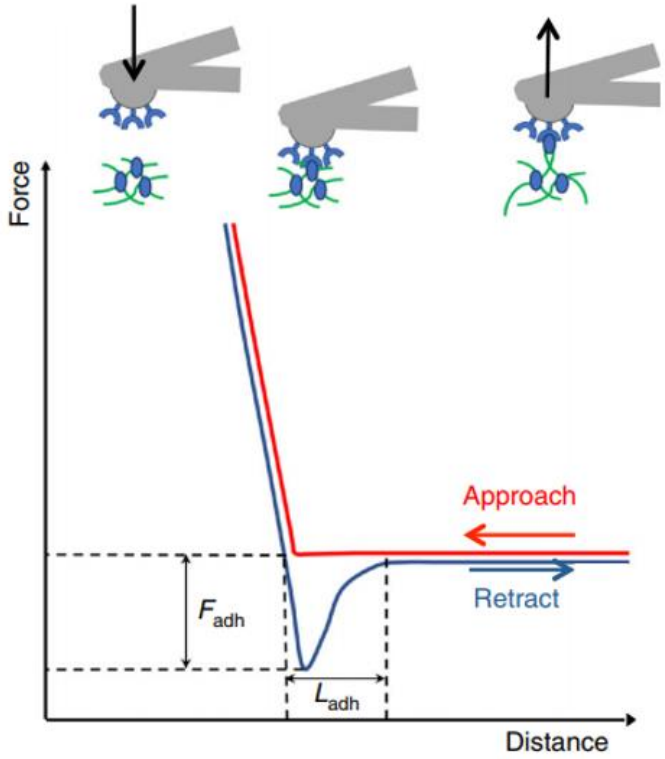

Figure 53: Characterization of protein crosslinking to the surface of the gel. Principle of the measurement. The AFM tip is brought close to the gel until contact is made between the anti-antibody on the tip and the protein at the surface of the gel (red curve). Then the tip is retracted (blue curve) until the contact breaks at the values noted as $\mathbf{L}_{adh}$ and $\mathbf{F}_{adh}$ [321].

6.2 Combined Optical- SCFS Measurements

In the thesis, the GelMA-cell interaction is evident from only the F-D curves though future work would benefit from combining the force data with direct visual observation of the cell, which is possible as the AFM is mounted on an optical microscope. For example, a setup currently available in combination with SCFS is an optical side-view path and camera that can be used to observe the cell-substrate interaction while simultaneously performing an SCFS measurement (**Figure 54**). This has previously been used to study the role of cell mechanics and adhesion forces involved in cell membrane blebbing (**Figure 54**) [322]. Applying this technique would reveal the spontaneous formation of GelMA-cell adhesive structures, e.g. membrane tethers, during retraction of the cantilever and whilst recording the F-D curve. In addition, visual differences in the elastic or viscoelastic properties of the GelMA polymer chains could be revealed and correlated to the force data such as the initial, large non-linear peaks observed in chapter 4 (**Figure 35**).

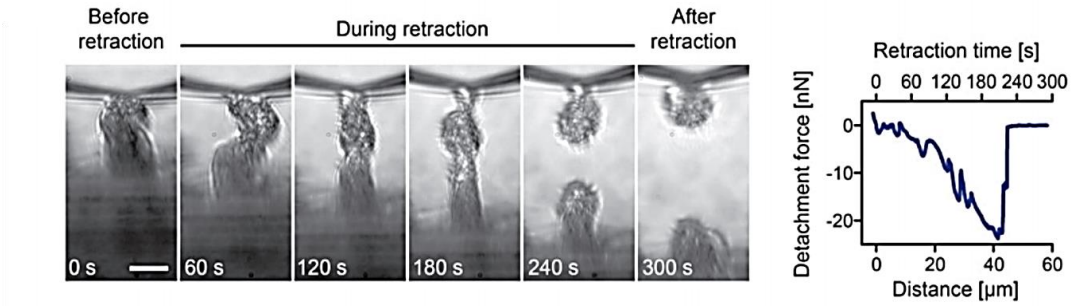

Figure 54: Cell-Cell separation using SCFS. Sideview time lapse image series of two cells separating at a 0.2 mm/s retraction speed (left side) and the corresponding F-D curve (right side) [322].

References

1. Penfield, W. and E. Boldrey, *SOMATIC MOTOR AND SENSORY REPRESENTATION IN THE CEREBRAL CORTEX OF MAN AS STUDIED BY ELECTRICAL STIMULATION.* Brain, 1937. **60**(4): p. 389-443.
2. Hassler, R., et al., *Physiological observations in stereotaxic operations in extrapyramidal motor disturbances.* Brain, 1960. **83**: p. 337-50.
3. Sem-Jacobsen, C.W., *Depth-electrographic observations related to Parkinson's disease. Recording and electrical stimulation in the area around the third ventricle.* J Neurosurg, 1966. **24**(1): p. Suppl:388-402.
4. Hosobuchi, Y., J.E. Adams, and B. Rutkin, *Chronic thalamic stimulation for the control of facial anesthesia dolorosa.* Arch Neurol, 1973. **29**(3): p. 158-61.
5. Cooper, I.S., *Effect of chronic stimulation of anterior cerebellum on neurological disease.* Lancet, 1973. **1**(7796): p. 206.
6. Benabid, A.L., et al., *Long-term suppression of tremor by chronic stimulation of the ventral intermediate thalamic nucleus.* Lancet, 1991. **337**(8738): p. 403-6.
7. Benabid, A.L., et al., *Chronic electrical stimulation of the ventralis intermedius nucleus of the thalamus as a treatment of movement disorders.* J Neurosurg, 1996. **84**(2): p. 203-14.
8. Chen, X.L., et al., *Deep Brain Stimulation.* Interventional Neurology, 2012. **1**(3-4): p. 200-212.
9. Wallace, G.G., Moulton S. E., Kapsa R. M. I. & Higgins M. J. , *Organic Bionics.* Wiley-VCH Verlag GmbH & Co. KGaA, 2012.
10. Wallace, G. and G. Spinks, *Conducting polymers - bridging the bionic interface.* Soft Matter, 2007. **3**(6): p. 665-671.
11. Polikov, V.S., P.A. Tresco, and W.M. Reichert, *Response of brain tissue to chronically implanted neural electrodes.* J Neurosci Methods, 2005. **148**(1): p. 1-18.
12. Marin, C. and E. Fernandez, *Biocompatibility of intracortical microelectrodes: current status and future prospects.* Frontiers in Neuroengineering, 2010. **3**(8).
13. Howlader, M.M.R., et al., *Materials analyses and electrochemical impedance of implantable metal electrodes.* Physical Chemistry Chemical Physics, 2015. **17**(15): p. 10135-10145.
14. Green, J.D., *A simple microelectrode for recording from the central nervous system.* Nature, 1958. **182**(4640): p. 962.
15. Eisenberg, L.S., J.R. Nelson, and W.F. House, *Effects of the single-electrode cochlear implant on the vestibular system of the profoundly deaf adult.* Ann Otol Rhinol Laryngol Suppl, 1982. **91**(2 Pt 3): p. 47-54.
16. Clark, G.M., et al., *A multiple electrode cochlear implant.* J Laryngol Otol, 1977. **91**(11): p. 935-45.
17. Strumwasser, F., *Long-term recording' from single neurons in brain of unrestrained mammals.* Science, 1958. **127**(3296): p. 469-70.
18. Wark, H.A.C., et al., *A new high-density (25 electrodes/mm 2) penetrating microelectrode array for recording and stimulating sub-millimeter neuroanatomical structures.* Journal of Neural Engineering, 2013. **10**(4): p. 045003.
19. Clark, G.M., et al., *A multiple-electrode hearing prosthesis for cochlear implantation in deaf patients.* Medical Progress through Technology, 1977. **5**(3): p. 127-140.

20. Ong, J.M. and L. da Cruz, *The bionic eye: a review.* Clin Exp Ophthalmol, 2012. **40**(1): p. 6-17.
21. Walton, C., S. Gergely, and A.P. Economides, *Platinum Pacemaker Electrodes: Origins and Effects of the Electrode-Tissue Interface Impedance.* Pacing and Clinical Electrophysiology, 1987. **10**(1): p. 87-99.
22. Butson, C.R. and C.C. McIntyre, *Tissue and electrode capacitance reduce neural activation volumes during deep brain stimulation.* Clin Neurophysiol, 2005. **116**(10): p. 2490-500.
23. Luo, X. and X.T. Cui, *Electrochemical deposition of conducting polymer coatings on magnesium surfaces in ionic liquid.* Acta Biomaterialia, 2011. **7**(1): p. 441-446.
24. Shih, C.-C., Lin, S.-J., Chen, Y.-L., Su, Y.-Y., Lai, S.-T., Wu, G. J., Kwok, C.-F. and Chung, K.-H, *The cytotoxicity of corrosion products of nitinol stent wire on cultured smooth muscle cells.* J. Biomed. Mater. Res., 2000. **52**: p. 395–403.
25. Geddes, L.A. and R. Roeder, *Criteria for the Selection of Materials for Implanted Electrodes.* Annals of Biomedical Engineering, 2003. **31**(7): p. 879-890.
26. Ward, M.P., et al., *Toward a comparison of microelectrodes for acute and chronic recordings.* Brain Res, 2009. **1282**: p. 183-200.
27. Leipzig, N.D. and M.S. Shoichet, *The effect of substrate stiffness on adult neural stem cell behavior.* Biomaterials, 2009. **30**(36): p. 6867-6878.
28. Salvadori, M.C., et al., *Measurement of the elastic modulus of nanostructured gold and platinum thin films.* Physical Review B, 2003. **67**(15): p. 153404.
29. Williams, J.C., R.L. Rennaker, and D.R. Kipke, *Long-term neural recording characteristics of wire microelectrode arrays implanted in cerebral cortex.* Brain Res Brain Res Protoc, 1999. **4**(3): p. 303-13.
30. Xindong, L., et al., *Stability of the interface between neural tissue and chronically implanted intracortical microelectrodes.* IEEE Transactions on Rehabilitation Engineering, 1999. **7**(3): p. 315-326.
31. Service, R.F., *CHEMISTRY NOBEL: Getting a Charge Out of Plastics.* (0036-8075 (Print)).
32. Valentová, H. and J. Stejskal, *Mechanical properties of polyaniline.* Synthetic Metals, 2010. **160**(7): p. 832-834.
33. Gelmi, A., M.J. Higgins, and G.G. Wallace, *Physical surface and electromechanical properties of doped polypyrrole biomaterials.* Biomaterials, 2010. **31**(8): p. 1974-1983.
34. Janmanee, R., et al., *Functional Conducting Polymers in the Application of SPR Biosensors.* Journal of Nanotechnology, 2012. **2012**: p. 7.
35. Svirskis, D., et al., *Electrochemically controlled drug delivery based on intrinsically conducting polymers.* J Control Release, 2010. **146**(1): p. 6-15.
36. Berdichevsky, Y. and Y.H. Lo, *Polypyrrole Nanowire Actuators.* Advanced Materials, 2006. **18**(1): p. 122-125.
37. Reichert, W.M., *Indwelling Neural Implants: Strategies for Contending with the In Vivo Environment*, in *Indwelling Neural Implants: Strategies for Contending with the In Vivo Environment*. 2008, CRC Press/ Taylor & Francis Group, LLC.: Boca Raton (FL).
38. Kim, D.-H., M. Abidian, and D.C. Martin, *Conducting polymers grown in hydrogel scaffolds coated on neural prosthetic devices.* Journal of Biomedical Materials Research Part A, 2004. **71A**(4): p. 577-585.
39. Gerard, M., A. Chaubey, and B.D. Malhotra, *Application of conducting polymers to biosensors.* Biosens Bioelectron, 2002. **17**(5): p. 345-59.
40. George, P.M., et al., *Fabrication and biocompatibility of polypyrrole implants suitable for neural prosthetics.* Biomaterials, 2005. **26**(17): p. 3511-9.

41. Wang, X., et al., *Evaluation of biocompatibility of polypyrrole in vitro and in vivo.* J Biomed Mater Res A, 2004. **68**(3): p. 411-22.
42. Lee, J.Y., et al., *Polypyrrole-coated electrospun PLGA nanofibers for neural tissue applications.* Biomaterials, 2009. **30**(26): p. 4325-4335.
43. Li, Y., et al., *Porous and electrically conductive polypyrrole-poly(vinyl alcohol) composite and its applications as a biomaterial.* Langmuir, 2005. **21**(23): p. 10702-9.
44. Ateh, D.D., P. Navsaria Ha Fau - Vadgama, and P. Vadgama, *Polypyrrole-based conducting polymers and interactions with biological tissues.* (1742-5689 (Print)).
45. Armes, S.P., *Optimum reaction conditions for the polymerization of pyrrole by iron(III) chloride in aqueous solution.* Synthetic Metals, 1987. **20**(3): p. 365-371.
46. MacDiarmid, A.G., et al., *The Concept of `Doping' of Conducting Polymers: The Role of Reduction Potentials [and Discussion].* Philosophical Transactions of the Royal Society of London A: Mathematical, Physical and Engineering Sciences, 1985. **314**(1528): p. 3-15.
47. Kumar, D. and R.C. Sharma, *Advances in conductive polymers.* European Polymer Journal, 1998. **34**(8): p. 1053-1060.
48. Zhang, H., et al., *Quantifying Molecular-Level Cell Adhesion on Electroactive Conducting Polymers using Electrochemical-Single Cell Force Spectroscopy.* Scientific Reports, 2015. **5**: p. 13334.
49. Higgins, M.J. and G.G. Wallace, *Surface and Biomolecular Forces of Conducting Polymers.* Polymer Reviews, 2013. **53**(3): p. 506-526.
50. Lundin, V., et al., *Control of neural stem cell survival by electroactive polymer substrates.* PLoS One, 2011. **6**(4): p. e18624.
51. Wong, J.Y., R. Langer, and D.E. Ingber, *Electrically conducting polymers can noninvasively control the shape and growth of mammalian cells.* Proceedings of the National Academy of Sciences, 1994. **91**(8): p. 3201-3204.
52. Schmidt, C.E., et al., *Stimulation of neurite outgrowth using an electrically conducting polymer.* Proceedings of the National Academy of Sciences, 1997. **94**(17): p. 8948-8953.
53. Stewart, E., et al., *Electrical stimulation using conductive polymer polypyrrole promotes differentiation of human neural stem cells: a biocompatible platform for translational neural tissue engineering.* Tissue Eng Part C Methods, 2015. **21**(4): p. 385-93.
54. Puckert, C., et al., *Optimisation of conductive polymer biomaterials for cardiac progenitor cells.* RSC Advances, 2016. **6**(67): p. 62270-62277.
55. Sisken, B.F., J. Walker, and M. Orgel, *Prospects on clinical applications of electrical stimulation for nerve regeneration.* J Cell Biochem, 1993. **51**(4): p. 404-9.
56. Green, R.A., et al., *Conducting polymers for neural interfaces: challenges in developing an effective long-term implant.* Biomaterials, 2008. **29**(24-25): p. 3393-9.
57. Kip, A.L., et al., *Chronic neural recordings using silicon microelectrode arrays electrochemically deposited with a poly(3,4-ethylenedioxythiophene) (PEDOT) film.* Journal of Neural Engineering, 2006. **3**(1): p. 59.
58. Cui, X., et al., *In vivo studies of polypyrrole/peptide coated neural probes.* Biomaterials, 2003. **24**(5): p. 777-787.
59. Bai, H., et al., *Graphene oxide/conducting polymer composite hydrogels.* Journal of Materials Chemistry, 2011. **21**(46): p. 18653-18658.
60. Kim, D.-H., et al., *Conducting polymers on hydrogel-coated neural electrode provide sensitive neural recordings in auditory cortex.* Acta Biomaterialia, 2010. **6**(1): p. 57-62.
61. Green, R.A., et al., *Living electrodes: tissue engineering the neural interface.* Conf Proc IEEE Eng Med Biol Soc, 2013. **2013**: p. 6957-60.

62. Heilmann, S., et al., *A thermosensitive morphine-containing hydrogel for the treatment of large-scale skin wounds.* Int J Pharm, 2013. **444**(1-2): p. 96-102.
63. Murakami, K., et al., *Hydrogel blends of chitin/chitosan, fucoidan and alginate as healing-impaired wound dressings.* Biomaterials, 2010. **31**(1): p. 83-90.
64. El-Sherbiny, I.M. and M.H. Yacoub, *Hydrogel scaffolds for tissue engineering: Progress and challenges.* Global Cardiology Science & Practice, 2013. **2013**(3): p. 316-342.
65. Lee, K.Y. and D.J. Mooney, *Hydrogels for tissue engineering.* Chem Rev, 2001. **101**(7): p. 1869-79.
66. Zhu, J. and R.E. Marchant, *Design properties of hydrogel tissue-engineering scaffolds.* Expert Rev Med Devices, 2011. **8**(5): p. 607-26.
67. Kloxin, A.M., et al., *Photodegradable hydrogels for dynamic tuning of physical and chemical properties.* (1095-9203 (Electronic)).
68. Aurand, E.R., K.J. Lampe, and K.B. Bjugstad, *Defining and designing polymers and hydrogels for neural tissue engineering.* Neuroscience Research, 2012. **72**(3): p. 199-213.
69. Gnanaprakasam Thankam, F. and J. Muthu, *Alginate based hybrid copolymer hydrogels—Influence of pore morphology on cell–material interaction.* Carbohydrate Polymers, 2014. **112**(0): p. 235-244.
70. Eddington, D.T. and D.J. Beebe, *Flow control with hydrogels.* Advanced Drug Delivery Reviews, 2004. **56**(2): p. 199-210.
71. Hoffman, A.S., *Hydrogels for biomedical applications.* Advanced Drug Delivery Reviews, 2002. **54**(1): p. 3-12.
72. Kopeček, J., *Hydrogel biomaterials: A smart future?* Biomaterials, 2007. **28**(34): p. 5185-5192.
73. Lutolf, M.P., *Biomaterials: Spotlight on hydrogels.* Nat Mater, 2009. **8**(6): p. 451-453.
74. Gilmore, K., et al., *Preparation of hydrogel/conducting polymer composites.* Polymer Gels and Networks, 1994. **2**(2): p. 135-143.
75. Sasaki, M., et al., *Highly Conductive Stretchable and Biocompatible Electrode–Hydrogel Hybrids for Advanced Tissue Engineering.* Advanced Healthcare Materials, 2014. **3**(11): p. 1919-1927.
76. Pardo-Yissar, V., et al., *Gold Nanoparticle/Hydrogel Composites with Solvent-Switchable Electronic Properties.* Advanced Materials, 2001. **13**(17): p. 1320-1323.
77. Thoniyot, P., et al., *Nanoparticle–Hydrogel Composites: Concept, Design, and Applications of These Promising, Multi-Functional Materials.* Advanced Science, 2015. **2**(1-2): p. 1400010.
78. Spencer, A.R., et al., *Electroconductive Gelatin Methacryloyl-PEDOT:PSS Composite Hydrogels: Design, Synthesis, and Properties.* ACS Biomaterials Science & Engineering, 2018. **4**(5): p. 1558-1567.
79. Banerjee, A., et al., *The influence of hydrogel modulus on the proliferation and differentiation of encapsulated neural stem cells.* Biomaterials, 2009. **30**(27): p. 4695-4699.
80. Lee, K.Y., et al., *Controlling Mechanical and Swelling Properties of Alginate Hydrogels Independently by Cross-Linker Type and Cross-Linking Density.* Macromolecules, 2000. **33**(11): p. 4291-4294.
81. Guo, H., et al., *Self-crosslinked polyaniline hydrogel electrodes for electrochemical energy storage.* Carbon, 2015. **92**: p. 133-141.
82. Xu, B., et al., *Directed neural stem cell differentiation on polyaniline-coated high strength hydrogels.* Materials Today Chemistry, 2016. **1-2**: p. 15-22.
83. Liu, G. and X. Zhao, *Electromechanochemical Behavior of Gelatin Hydrogel Under Electric Field.* Journal of Macromolecular Science, Part A, 2005. **42**(1): p. 51-59.

84. Haider, S., S.-Y. Park, and S.-H. Lee, *Preparation, swelling and electro-mechano-chemical behaviors of a gelatin-chitosan blend membrane.* Soft Matter, 2008. **4**(3): p. 485-492.
85. Kuhn, W., et al., *Reversible Dilation and Contraction by Changing the State of Ionization of High-Polymer Acid Networks.* Nature, 1950. **165**: p. 514.
86. Ikeda, T., J.-i. Mamiya, and Y. Yu, *Photomechanics of Liquid-Crystalline Elastomers and Other Polymers.* Angewandte Chemie International Edition, 2007. **46**(4): p. 506-528.
87. Murdan, S., *Electro-responsive drug delivery from hydrogels.* Journal of Controlled Release, 2003. **92**(1): p. 1-17.
88. Ma, J.T., et al., *Bending behavior of gelatin/poly(hydroxyethyl methacrylate) IPN hydrogel under electric stimulus.* Journal of Applied Polymer Science, 1995. **56**(1): p. 73-77.
89. Osada, Y. and J.-P. Gong, *Soft and Wet Materials: Polymer Gels.* Advanced Materials, 1999. **10**(11): p. 827-837.
90. Shiga, T. and T. Kurauchi, *Deformation of polyelectrolyte gels under the influence of electric field.* Journal of Applied Polymer Science, 1990. **39**(11-12): p. 2305-2320.
91. Glazer, P.J., et al., *Role of pH gradients in the actuation of electro-responsive polyelectrolyte gels.* Soft Matter, 2012. **8**(16): p. 4421-4426.
92. Bassil, M., J. Davenas, and M. El Tahchi, *Electrochemical properties and actuation mechanisms of polyacrylamide hydrogel for artificial muscle application.* Sensors and Actuators B: Chemical, 2008. **134**(2): p. 496-501.
93. Sun, S. and A.F.T. Mak, *The dynamical response of a hydrogel fiber to electrochemical stimulation.* Journal of Polymer Science Part B: Polymer Physics, 2001. **39**(2): p. 236-246.
94. Kim, S.Y., et al., *Properties of electroresponsive poly(vinyl alcohol)/poly(acrylic acid) IPN hydrogels under an electric stimulus.* Journal of Applied Polymer Science, 1999. **73**(9): p. 1675-1683.
95. TANAKA, T., et al., *Collapse of Gels in an Electric Field.* Science, 1982. **218**(4571): p. 467-469.
96. Flory, P.J., *Principle of Polymer Chemistry.* Cornell Univ. Press, Ithaca, NY, 1953.
97. Temple, S., *The development of neural stem cells.* Nature, 2001. **414**: p. 112.
98. Morrison, S.J. and A.C. Spradling, *Stem Cells and Niches: Mechanisms That Promote Stem Cell Maintenance throughout Life.* Cell, 2008. **132**(4): p. 598-611.
99. Li, L. and T. Xie, *STEM CELL NICHE: Structure and Function.* Annual Review of Cell and Developmental Biology, 2005. **21**(1): p. 605-631.
100. Baumann, K., *Holding tight onto the niche.* Nature Reviews Molecular Cell Biology, 2012. **13**: p. 278.
101. Marthiens, V., et al., *Adhesion molecules in the stem cell niche – more than just staying in shape?* Journal of Cell Science, 2010. **123**(10): p. 1613.
102. Kazanis, I., et al., *Quiescence and Activation of Stem and Precursor Cell Populations in the Subependymal Zone of the Mammalian Brain Are Associated with Distinct Cellular and Extracellular Matrix Signals.* The Journal of Neuroscience, 2010. **30**(29): p. 9771.
103. Kazanis, I. and C. ffrench-Constant, *Extracellular matrix and the neural stem cell niche.* Developmental Neurobiology, 2011. **71**(11): p. 1006-1017.
104. Niola, F., et al., *Id proteins synchronize stemness and anchorage to the niche of neural stem cells.* Nature Cell Biology, 2012. **14**: p. 477.
105. Ayala, R., et al., *Engineering the cell-material interface for controlling stem cell adhesion, migration, and differentiation.* (1878-5905 (Electronic)).

106. DuFort, C.C., M.J. Paszek, and V.M. Weaver, *Balancing forces: architectural control of mechanotransduction.* Nat Rev Mol Cell Biol, 2011. **12**(5): p. 308-19.
107. Mammoto, T. and D.E. Ingber, *Mechanical control of tissue and organ development.* Development, 2010. **137**(9): p. 1407-20.
108. Seidlits, S.K., et al., *The effects of hyaluronic acid hydrogels with tunable mechanical properties on neural progenitor cell differentiation.* Biomaterials, 2010. **31**(14): p. 3930-3940.
109. Seliktar, D., *Designing Cell-Compatible Hydrogels for Biomedical Applications.* Science, 2012. **336**(6085): p. 1124.
110. Banerjee, A., et al., *The influence of hydrogel modulus on the proliferation and differentiation of encapsulated neural stem cells.* Biomaterials, 2009. **30**(27): p. 4695-9.
111. Saha, K., et al., *Substrate Modulus Directs Neural Stem Cell Behavior.* Biophysical Journal, 2008. **95**(9): p. 4426-4438.
112. Gu, Q., et al., *Functional 3D Neural Mini-Tissues from Printed Gel-Based Bioink and Human Neural Stem Cells.* Advanced Healthcare Materials, 2016. **5**(12): p. 1429-1438.
113. Gu, Q., et al., *3D Bioprinting Human Induced Pluripotent Stem Cell Constructs for In Situ Cell Proliferation and Successive Multilineage Differentiation.* Advanced Healthcare Materials, 2017. **6**(17): p. 1700175.
114. Park, K.I., Y.D. Teng, and E.Y. Snyder, *The injured brain interacts reciprocally with neural stem cells supported by scaffolds to reconstitute lost tissue.* Nature Biotechnology, 2002. **20**: p. 1111.
115. Prang, P., et al., *The promotion of oriented axonal regrowth in the injured spinal cord by alginate-based anisotropic capillary hydrogels.* Biomaterials, 2006. **27**(19): p. 3560-3569.
116. Cheng, T.-Y., et al., *Neural stem cells encapsulated in a functionalized self-assembling peptide hydrogel for brain tissue engineering.* Biomaterials, 2013. **34**(8): p. 2005-2016.
117. Mothe, A.J., et al., *Repair of the injured spinal cord by transplantation of neural stem cells in a hyaluronan-based hydrogel.* Biomaterials, 2013. **34**(15): p. 3775-3783.
118. Lim, H.L., et al., *Dynamic Electromechanical Hydrogel Matrices for Stem Cell Culture.* Advanced Functional Materials, 2010. **21**(1): p. 55-63.
119. Sun, S., I. Titushkin, and M. Cho, *Regulation of mesenchymal stem cell adhesion and orientation in 3D collagen scaffold by electrical stimulus.* Bioelectrochemistry, 2006. **69**(2): p. 133-141.
120. Van Den Bulcke, A.I., et al., *Structural and rheological properties of methacrylamide modified gelatin hydrogels.* Biomacromolecules, 2000. **1**(1): p. 31-8.
121. Nichol, J.W., et al., *Cell-laden microengineered gelatin methacrylate hydrogels.* Biomaterials, 2010. **31**(21): p. 5536-5544.
122. Cha, C., et al., *Microfluidics-Assisted Fabrication of Gelatin-Silica Core–Shell Microgels for Injectable Tissue Constructs.* Biomacromolecules, 2014. **15**(1): p. 283-290.
123. Zhao, X., et al., *Photocrosslinkable Gelatin Hydrogel for Epidermal Tissue Engineering.* Adv Healthc Mater, 2015.
124. Jung, J. and J. Oh, *INFLUENCE OF PHOTO-INITIATOR CONCENTRATION ON THE VIABILITY OF CELLS ENCAPSULATED IN PHOTO-CROSSLINKED MICROGELS FABRICATED BY MICROFLUIDICS.* Digest Journal of Nanomaterials & Biostructures (DJNB), 2014. **9(2)**: p. 503-509.

125. Ramon-Azcon, J., et al., *Gelatin methacrylate as a promising hydrogel for 3D microscale organization and proliferation of dielectrophoretically patterned cells.* Lab Chip, 2012. **12**(16): p. 2959-69.
126. Schuurman, W., et al., *Gelatin-Methacrylamide Hydrogels as Potential Biomaterials for Fabrication of Tissue-Engineered Cartilage Constructs.* Macromolecular Bioscience, 2013. **13**(5): p. 551-561.
127. Wang, Z., et al., *An ultrafast hydrogel photocrosslinking method for direct laser bioprinting.* RSC Advances, 2016. **6**(25): p. 21099-21104.
128. Ferreira, P., et al., *Photocrosslinkable polymers for biomedical applications*. 2011: INTECH Open Access Publisher.
129. Bartnikowski, M., et al., *Protective effects of reactive functional groups on chondrocytes in photocrosslinkable hydrogel systems.* Acta Biomaterialia, 2015. **27**: p. 66-76.
130. Allen, N.S., et al., *Photochemistry and photoinduced chemical crosslinking activity of type I & II co-reactive photoinitiators in acrylated prepolymers.* Journal of Photochemistry and Photobiology A: Chemistry, 1999. **126**(1–3): p. 135-149.
131. Williams, C.G., et al., *Variable cytocompatibility of six cell lines with photoinitiators used for polymerizing hydrogels and cell encapsulation.* Biomaterials, 2005. **26**(11): p. 1211-1218.
132. Chen, Y.C., et al., *Functional Human Vascular Network Generated in Photocrosslinkable Gelatin Methacrylate Hydrogels.* Adv Funct Mater, 2012. **22**(10): p. 2027-2039.
133. Schuurman, W., et al., *Gelatin-methacrylamide hydrogels as potential biomaterials for fabrication of tissue-engineered cartilage constructs.* Macromol Biosci, 2013. **13**(5): p. 551-61.
134. Puckert, C., et al., *Electro-mechano responsive properties of gelatin methacrylate (GelMA) hydrogel on conducting polymer electrodes quantified using atomic force microscopy.* Soft Matter, 2017. **13**(27): p. 4761-4772.
135. Benton, J.A., et al., *Photocrosslinking of gelatin macromers to synthesize porous hydrogels that promote valvular interstitial cell function.* Tissue Eng Part A, 2009. **15**(11): p. 3221-30.
136. Yue, K., et al., *Synthesis, properties, and biomedical applications of gelatin methacryloyl (GelMA) hydrogels.* Biomaterials, 2015. **73**: p. 254-271.
137. Aubin, H., et al., *Directed 3D cell alignment and elongation in microengineered hydrogels.* Biomaterials, 2010. **31**(27): p. 6941-6951.
138. Grogan, S.P., et al., *Digital micromirror device projection printing system for meniscus tissue engineering.* Acta Biomaterialia, 2013. **9**(7): p. 7218-7226.
139. Benton, J.A., et al., *Photocrosslinking of Gelatin Macromers to Synthesize Porous Hydrogels That Promote Valvular Interstitial Cell Function.* Tissue Engineering Part A, 2009. **15**(11): p. 3221-3230.
140. Nikkhah, M., et al., *Directed endothelial cell morphogenesis in micropatterned gelatin methacrylate hydrogels.* Biomaterials, 2012. **33**(35): p. 9009-9018.
141. Cha, C., et al., *Controlling Mechanical Properties of Cell-Laden Hydrogels by Covalent Incorporation of Graphene Oxide.* Small, 2013. **10**(3): p. 514-523.
142. Jaiswal, M.K., et al., *Mechanically Stiff Nanocomposite Hydrogels at Ultralow Nanoparticle Content.* ACS Nano, 2016. **10**(1): p. 246-256.
143. Kaemmerer, E., et al., *Gelatine methacrylamide-based hydrogels: An alternative three-dimensional cancer cell culture system.* Acta Biomaterialia, 2014. **10**(6): p. 2551-2562.
144. KjÆR, M., *Role of Extracellular Matrix in Adaptation of Tendon and Skeletal Muscle to Mechanical Loading.* Physiological Reviews, 2004. **84**(2): p. 649-698.

145. Marshall, B.T., et al., *Direct observation of catch bonds involving cell-adhesion molecules.* Nature, 2003. **423**: p. 190.
146. Thomas, W.E., V. Vogel, and E. Sokurenko, *Biophysics of catch bonds.* Annu Rev Biophys, 2008. **37**: p. 399-416.
147. Engler, A.J., et al., *Matrix elasticity directs stem cell lineage specification.* Cell, 2006. **126**(4): p. 677-89.
148. Klebe, R.J., *Isolation of a collagen-dependent cell attachment factor.* Nature, 1974. **250**(5463): p. 248-251.
149. Garcia, A.J., P. Ducheyne, and D. Boettiger, *Quantification of cell adhesion using a spinning disc device and application to surface-reactive materials.* Biomaterials, 1997. **18**(16): p. 1091-8.
150. Kaplanski, G., et al., *Granulocyte-endothelium initial adhesion. Analysis of transient binding events mediated by E-selectin in a laminar shear flow.* Biophys J, 1993. **64**(6): p. 1922-33.
151. Helenius, J., et al., *Single-cell force spectroscopy.* Journal of Cell Science, 2008. **121**(11): p. 1785-1791.
152. Griffin, M.A., et al., *Patterning, Prestress, and Peeling Dynamics of Myocytes.* Biophysical Journal, 2004. **86**(2): p. 1209-1222.
153. Andersson, M., et al., *Using optical tweezers for measuring the interaction forces between human bone cells and implant surfaces: System design and force calibration.* Review of Scientific Instruments, 2007. **78**(7): p. 074302.
154. Muller, D.J., et al., *Force probing surfaces of living cells to molecular resolution.* Nat Chem Biol, 2009. **5**(6): p. 383-390.
155. Andrea, A. and F. Paolo, *AFM: a versatile tool in biophysics.* Measurement Science and Technology, 2005. **16**(6): p. R65.
156. Binnig, G. and H. Rohrer, *Scanning tunneling microscopy.* Physica B+C, 1984. **127**(1): p. 37-45.
157. Bustamante, C., C. Rivetti, and D.J. Keller, *Scanning force microscopy under aqueous solutions.* Curr Opin Struct Biol, 1997. **7**(5): p. 709-16.
158. Drake, B., et al., *Imaging crystals, polymers, and processes in water with the atomic force microscope.* Science, 1989. **243**(4898): p. 1586-9.
159. Ando, T., T. Uchihashi, and T. Fukuma, *High-speed atomic force microscopy for nano-visualization of dynamic biomolecular processes.* Progress in Surface Science, 2008. **83**(7): p. 337-437.
160. Jalili, N. and K. Laxminarayana, *A review of atomic force microscopy imaging systems: application to molecular metrology and biological sciences.* Mechatronics, 2004. **14**(8): p. 907-945.
161. Butt, H.J. and M. Jaschke, *Calculation of thermal noise in atomic force microscopy.* Nanotechnology, 1995. **6**(1): p. 1.
162. Puckert, C. and M.J. Higgins, *Force Spectroscopy*, in *Compendium of Surface and Interface Analysis*, J. The Surface Science Society of, Editor. 2018, Springer Singapore: Singapore. p. 193-200.
163. Sader, J.E., J.W.M. Chon, and P. Mulvaney, *Calibration of rectangular atomic force microscope cantilevers.* Review of Scientific Instruments, 1999. **70**(10): p. 3967-3969.
164. Hutter, J.L. and J. Bechhoefer, *Calibration of atomic-force microscope tips.* Review of Scientific Instruments, 1993. **64**(7): p. 1868-1873.
165. Butt, H.-J., B. Cappella, and M. Kappl, *Force measurements with the atomic force microscope: Technique, interpretation and applications.* Surface Science Reports, 2005. **59**(1): p. 1-152.
166. Johnson K. L. and L.J. K., *Contact Mechanics.* Cambridge University Press 1987.

167. Johnson, K.L., K. Kendall, and A.D. Roberts, *Surface Energy and the Contact of Elastic Solids.* Proceedings of the Royal Society of London A: Mathematical, Physical and Engineering Sciences, 1971. **324**(1558): p. 301-313.
168. Charles, A.C. and M.P. Seah, *Modelling of nanomechanical nanoindentation measurements using an AFM or nanoindenter for compliant layers on stiffer substrates.* Nanotechnology, 2006. **17**(21): p. 5283.
169. N., S.I., *The relation between load and penetration in the axisymmetric boussinesq problem for a punch of arbitrary profile.* Int. J. Engng., 1965. **3**: p. 47-57.
170. Domke, J. and M. Radmacher, *Measuring the Elastic Properties of Thin Polymer Films with the Atomic Force Microscope.* Langmuir, 1998. **14**(12): p. 3320-3325.
171. Martin, S., et al., *Polymer hydrogel particles as biocompatible AFM probes to study CD44/hyaluronic acid interactions on cells.* Polymer, 2016.
172. Kashef, J. and C.M. Franz, *Quantitative methods for analyzing cell-cell adhesion in development.* Dev Biol, 2015. **401**(1): p. 165-74.
173. Taubenberger, A.V., D.W. Hutmacher, and D.J. Muller, *Single-cell force spectroscopy, an emerging tool to quantify cell adhesion to biomaterials.* Tissue Eng Part B Rev, 2014. **20**(1): p. 40-55.
174. Gelmi, A., M.J. Higgins, and G.G. Wallace, *Physical surface and electromechanical properties of doped polypyrrole biomaterials.* Biomaterials, 2010. **31**(8): p. 1974-83.
175. Wojcikiewicz, E.P., et al., *Contributions of molecular binding events and cellular compliance to the modulation of leukocyte adhesion.* J Cell Sci, 2003. **116**(Pt 12): p. 2531-9.
176. Panorchan, P., et al., *Single-molecule analysis of cadherin-mediated cell-cell adhesion.* Journal of Cell Science, 2005. **119**(1): p. 66-74.
177. Thie, M., et al., *Interactions between trophoblast and uterine epithelium: monitoring of adhesive forces.* Hum Reprod, 1998. **13**(11): p. 3211-9.
178. Hsiao, S.C., et al., *DNA-coated AFM cantilevers for the investigation of cell adhesion and the patterning of live cells.* Angew Chem Int Ed Engl, 2008. **47**(44): p. 8473-7.
179. Potthoff, E., et al., *Rapid and Serial Quantification of Adhesion Forces of Yeast and Mammalian Cells.* PLoS ONE, 2012. **7**(12): p. e52712.
180. Friedrichs, J., J. Helenius, and D.J. Muller, *Quantifying cellular adhesion to extracellular matrix components by single-cell force spectroscopy.* Nat Protoc, 2010. **5**(7): p. 1353-61.
181. Meister, A., et al., *FluidFM: Combining Atomic Force Microscopy and Nanofluidics in a Universal Liquid Delivery System for Single Cell Applications and Beyond.* Nano Letters, 2009. **9**(6): p. 2501-2507.
182. Dorobantu, L.S., G.G. Goss, and R.E. Burrell, *Atomic force microscopy: a nanoscopic view of microbial cell surfaces.* Micron, 2012. **43**(12): p. 1312-22.
183. Krieg, M., et al., *A Bond for a Lifetime: Employing Membrane Nanotubes from Living Cells to Determine Receptor–Ligand Kinetics.* Angewandte Chemie, 2008. **120**(50): p. 9921-9923.
184. Friedrichs, J., et al., *A practical guide to quantify cell adhesion using single-cell force spectroscopy.* Methods, 2013. **60**(2): p. 169-78.
185. Evans, E.A. and D.A. Calderwood, *Forces and Bond Dynamics in Cell Adhesion.* Science, 2007. **316**(5828): p. 1148-1153.
186. Evans, E. and K. Ritchie, *Dynamic strength of molecular adhesion bonds.* Biophysical Journal, 1997. **72**(4): p. 1541-1555.
187. Li, F., et al., *Force Measurements of the α5β1 Integrin–Fibronectin Interaction.* Biophysical Journal, 2003. **84**(2): p. 1252-1262.

188. Elter, P., et al., *The influence of topographic microstructures on the initial adhesion of L929 fibroblasts studied by single-cell force spectroscopy.* Eur Biophys J, 2011. **40**(3): p. 317-27.
189. Cohen, M., et al., *Spatial and temporal sequence of events in cell adhesion: from molecular recognition to focal adhesion assembly.* Chembiochem, 2004. **5**(10): p. 1393-9.
190. Taubenberger, A., et al., *Revealing early steps of alpha2beta1 integrin-mediated adhesion to collagen type I by using single-cell force spectroscopy.* Mol Biol Cell, 2007. **18**(5): p. 1634-44.
191. Gallant, N.D. and A.J. García, *Model of integrin-mediated cell adhesion strengthening.* Journal of Biomechanics, 2007. **40**(6): p. 1301-1309.
192. Jiang, L., et al., *Cells Sensing Mechanical Cues: Stiffness Influences the Lifetime of Cell-Extracellular Matrix Interactions by Affecting the Loading Rate.* ACS Nano, 2016. **10**(1): p. 207-17.
193. Bell, G.I., *Models for the specific adhesion of cells to cells.* Science, 1978. **200**(4342): p. 618-27.
194. Kuznetsova, T.G., et al., *Atomic force microscopy probing of cell elasticity.* Micron, 2007. **38**(8): p. 824-833.
195. Weder, G., et al., *Use of force spectroscopy to investigate the adhesion of living adherent cells.* Langmuir, 2010. **26**(11): p. 8180-6.
196. Friedrichs, J., et al., *Galectin-3 Regulates Integrin α2β1-mediated Adhesion to Collagen-I and -IV.* Journal of Biological Chemistry, 2008. **283**(47): p. 32264-32272.
197. Taubenberger, A.V., et al., *The effect of unlocking RGD-motifs in collagen I on pre-osteoblast adhesion and differentiation.* Biomaterials, 2010. **31**(10): p. 2827-35.
198. Dao, L., C. Gonnermann, and C.M. Franz, *Investigating differential cell-matrix adhesion by directly comparative single-cell force spectroscopy.* Journal of Molecular Recognition, 2013. **26**(11): p. 578-589.
199. Bharadwaj, M., et al., *αV-class integrins exert dual roles on α5β1 integrins to strengthen adhesion to fibronectin.* 2017. **8**: p. 14348.
200. Friedrichs, J., J. Helenius, and D.J. Muller, *Stimulated single-cell force spectroscopy to quantify cell adhesion receptor crosstalk.* Proteomics, 2010. **10**(7): p. 1455-62.
201. Beaussart, A., et al., *Single-cell force spectroscopy of probiotic bacteria.* Biophys J, 2013. **104**(9): p. 1886-92.
202. Thewes, N., et al., *Hydrophobic interaction governs unspecific adhesion of staphylococci: a single cell force spectroscopy study.* Beilstein Journal of Nanotechnology, 2014. **5**: p. 1501-1512.
203. Rodriguez-Emmenegger, C., et al., *Quantifying bacterial adhesion on antifouling polymer brushes via single-cell force spectroscopy.* Polymer Chemistry, 2015. **6**(31): p. 5740-5751.
204. Zhang, H., et al., *Effect of electrochemical oxidation and reduction on cell de-adhesion at the conducting polymer–live cell interface as revealed by single cell force spectroscopy.* Biointerphases, 2018. **13**(4): p. 041004.
205. Martin, S., et al., *Polymer hydrogel particles as biocompatible AFM probes to study CD44/hyaluronic acid interactions on cells.* Polymer, 2016. **102**: p. 342-349.
206. Yu, M., et al., *Increasing throughput of AFM-based single cell adhesion measurements through multisubstrate surfaces.* Beilstein Journal of Nanotechnology, 2015. **6**: p. 157-166.
207. Jalali, S., et al., *Regulation of Endothelial Cell Adherence and Elastic Modulus by Substrate Stiffness.* Cell Communication & Adhesion, 2015. **22**(2-6): p. 79-89.

208. Polikov, V.S., P.A. Tresco, and W.M. Reichert, *Response of brain tissue to chronically implanted neural electrodes.* Journal of Neuroscience Methods, 2005. **148**(1): p. 1-18.
209. Taylor, Z. and K. Miller, *Reassessment of brain elasticity for analysis of biomechanisms of hydrocephalus.* Journal of Biomechanics, 2004. **37**(8): p. 1263-1269.
210. Gefen, A. and S.S. Margulies, *Are in vivo and in situ brain tissues mechanically similar?* Journal of Biomechanics, 2004. **37**(9): p. 1339-1352.
211. Cui, X., et al., *In vivo studies of polypyrrole/peptide coated neural probes.* Biomaterials, 2003. **24**(5): p. 777-87.
212. Balint, R., N.J. Cassidy, and S.H. Cartmell, *Conductive polymers: Towards a smart biomaterial for tissue engineering.* Acta Biomaterialia, 2014. **10**(6): p. 2341-2353.
213. Wallace, G.G., M. Smyth, and H. Zhao, *Conducting electroactive polymer-based biosensors.* TrAC Trends in Analytical Chemistry, 1999. **18**(4): p. 245-251.
214. Bidez, P.R., et al., *Polyaniline, an electroactive polymer, supports adhesion and proliferation of cardiac myoblasts.* Journal of Biomaterials Science, Polymer Edition, 2006. **17**(1-2): p. 199-212.
215. Wallace G. G., Moulton S. E., and C.G. M., *Electrode-cellular interface.* Science, 2009. **324**: p. 185-186.
216. Wallace G. G., et al., *Organic Conducting Polymers, in Organic Bionics.* Wiley-VCH Verlag GmbH & Co. KGaA, 2012: p. 81 - 112.
217. Collinsworth, A.M., et al., *Apparent elastic modulus and hysteresis of skeletal muscle cells throughout differentiation.* Am J Physiol Cell Physiol, 2002. **283**(4): p. C1219-27.
218. Green, R.A., et al., *Conducting polymers for neural interfaces: Challenges in developing an effective long-term implant.* Biomaterials, 2008. **29**(24–25): p. 3393-3399.
219. Small, C.J., C.O. Too, and G.G. Wallace, *Responsive conducting polymer-hydrogel composites.* Polymer Gels and Networks, 1997. **5**(3): p. 251-265.
220. Brahim, S. and A. Guiseppi-Elie, *Electroconductive Hydrogels: Electrical and Electrochemical Properties of Polypyrrole-Poly(HEMA) Composites.* Electroanalysis, 2005. **17**(7): p. 556-570.
221. Shi, W., R. He, and Y. Liu, *3D printing scaffolds with hydrogel materials for biomedical applications.* 2015, 2015. **1**(3): p. 6.
222. Zhao, X., et al., *Photocrosslinkable Gelatin Hydrogel for Epidermal Tissue Engineering.* Advanced Healthcare Materials, 2016. **5**(1): p. 108-118.
223. Chen, Y.-C., et al., *Functional Human Vascular Network Generated in Photocrosslinkable Gelatin Methacrylate Hydrogels.* Advanced Functional Materials, 2012. **22**(10): p. 2027-2039.
224. Cha, C., et al., *Microfluidics-assisted fabrication of gelatin-silica core-shell microgels for injectable tissue constructs.* Biomacromolecules, 2014. **15**(1): p. 283-90.
225. Xing, Q., et al., *Increasing Mechanical Strength of Gelatin Hydrogels by Divalent Metal Ion Removal.* Scientific Reports, 2014. **4**: p. 4706.
226. Fukushima, T., et al., *Fully plastic actuator through layer-by-layer casting with ionic-liquid-based bucky gel.* Angew Chem Int Ed Engl, 2005. **44**(16): p. 2410-3.
227. Doi, M., M. Matsumoto, and Y. Hirose, *Deformation of ionic polymer gels by electric fields.* Macromolecules, 1992. **25**(20): p. 5504-5511.
228. Servant, A., et al., *Graphene-based electroresponsive scaffolds as polymeric implants for on-demand drug delivery.* Adv Healthc Mater, 2014. **3**(8): p. 1334-43.
229. O'Connell, C.D., et al., *Development of the Biopen: a handheld device for surgical printing of adipose stem cells at a chondral wound site.* Biofabrication, 2016. **8**(1): p. 015019.

230. Boudou, T., et al., *An extended relationship for the characterization of Young's modulus and Poisson's ratio of tunable polyacrylamide gels.* Biorheology, 2006. **43**(6): p. 721-8.
231. Cesa, C.M., et al., *Micropatterned silicone elastomer substrates for high resolution analysis of cellular force patterns.* Rev Sci Instrum, 2007. **78**(3): p. 034301.
232. Ashley, D.S., et al., *Calibration of atomic force microscope cantilevers using standard and inverted static methods assisted by FIB-milled spatial markers.* Nanotechnology, 2013. **24**(1): p. 015710.
233. Greaves, G.N., et al., *Poisson's ratio and modern materials.* Nature Materials, 2011. **10**: p. 823–837.
234. Ashley, D.S., et al., *Spring constant calibration techniques for next-generation fast-scanning atomic force microscope cantilevers.* Nanotechnology, 2014. **25**(33): p. 335705.
235. Topkaya, S.N., *Gelatin methacrylate (GelMA) mediated electrochemical DNA biosensor for DNA hybridization.* Biosensors and Bioelectronics, 2015. **64**: p. 456-461.
236. Higgins, M.J., S.T. McGovern, and G.G. Wallace, *Visualizing dynamic actuation of ultrathin polypyrrole films.* Langmuir, 2009. **25**(6): p. 3627-33.
237. Smela, E. and N. Gadegaard, *Volume Change in Polypyrrole Studied by Atomic Force Microscopy.* The Journal of Physical Chemistry B, 2001. **105**(39): p. 9395-9405.
238. Wu, Y., et al., *Soft Mechanical Sensors Through Reverse Actuation in Polypyrrole.* Advanced Functional Materials, 2007. **17**(16): p. 3216-3222.
239. Valero, L., et al., *Characterization of the movement of polypyrrole–dodecylbenzenesulfonate–perchlorate/tape artificial muscles. Faradaic control of reactive artificial molecular motors and muscles.* Electrochimica Acta, 2011. **56**(10): p. 3721-3726.
240. Martinez, J.G., T.F. Otero, and E.W.H. Jager, *Effect of the Electrolyte Concentration and Substrate on Conducting Polymer Actuators.* Langmuir, 2014. **30**(13): p. 3894-3904.
241. Otero, T.F., *Soft, wet, and reactive polymers. Sensing artificial muscles and conformational energy.* Journal of Materials Chemistry, 2009. **19**: p. 681-689.
242. T. Tanaka, D.J.F., *Kinetics of swelling gels.* J. Chem. Phys., 1979. **70**: p. 1214-1218.
243. Brandl, F., F. Sommer, and A. Goepferich, *Rational design of hydrogels for tissue engineering: Impact of physical factors on cell behavior.* Biomaterials, 2007. **28**(2): p. 134-146.
244. Lee, C.H., A. Singla, and Y. Lee, *Biomedical applications of collagen.* Int J Pharm, 2001. **221**(1-2): p. 1-22.
245. Hoffman, A.S., *Hydrogels for biomedical applications.* Advanced Drug Delivery Reviews, 2012. **64, Supplement**: p. 18-23.
246. Gupta, P., K. Vermani, and S. Garg, *Hydrogels: from controlled release to pH-responsive drug delivery.* Drug Discovery Today, 2002. **7**(10): p. 569-579.
247. Dong, L.-c. and A.S. Hoffman, *A novel approach for preparation of pH-sensitive hydrogels for enteric drug delivery.* Journal of Controlled Release, 1991. **15**(2): p. 141-152.
248. Hyon, S.-H., et al., *Poly(vinyl alcohol) hydrogels as soft contact lens material.* Journal of Biomaterials Science, Polymer Edition, 1994. **5**(5): p. 397-406.
249. Guvendiren, M. and J.A. Burdick, *The control of stem cell morphology and differentiation by hydrogel surface wrinkles.* Biomaterials, 2010. **31**(25): p. 6511-6518.
250. Liu, J.C. and D.A. Tirrell, *Cell Response to RGD Density in Cross-Linked Artificial Extracellular Matrix Protein Films.* Biomacromolecules, 2008. **9**(11): p. 2984-2988.

251. Sakamoto, H., et al., *Cell-type Specific Recognition of RGD- and Non-RGD-containing Cell Binding Domains in Fibrillin-1.* Journal of Biological Chemistry, 1996. **271**(9): p. 4916-4922.
252. Li, P., et al., *Enhanced cell adhesion on a bio-inspired hierarchically structured polyester modified with gelatin-methacrylate.* Biomaterials Science, 2018. **6**(4): p. 785-792.
253. Li, X., et al., *3D Culture of Chondrocytes in Gelatin Hydrogels with Different Stiffness.* Polymers, 2016. **8**(8): p. 269.
254. Hersel, U., C. Dahmen, and H. Kessler, *RGD modified polymers: biomaterials for stimulated cell adhesion and beyond.* Biomaterials, 2003. **24**(24): p. 4385-4415.
255. Discher, D.E., P. Janmey, and Y.-l. Wang, *Tissue Cells Feel and Respond to the Stiffness of Their Substrate.* Science, 2005. **310**(5751): p. 1139.
256. Nemir, S., H.N. Hayenga, and J.L. West, *PEGDA hydrogels with patterned elasticity: Novel tools for the study of cell response to substrate rigidity.* Biotechnology and Bioengineering, 2010. **105**(3): p. 636-644.
257. Takemasa, M., et al., *Bridging the Gap Between Single-Molecule Unbinding Properties and Macromolecular Rheology*, in *Rheology of Biological Soft Matter: Fundamentals and Applications*, I. Kaneda, Editor. 2017, Springer Japan: Tokyo. p. 3-37.
258. Vats, K., et al., *Nanoscale physicochemical properties of chain- and step-growth polymerized PEG hydrogels affect cell-material interactions.* Journal of Biomedical Materials Research Part A, 2017. **105**(4): p. 1112-1122.
259. Megone, W., N. Roohpour, and J.E. Gautrot, *Impact of surface adhesion and sample heterogeneity on the multiscale mechanical characterisation of soft biomaterials.* Scientific Reports, 2018. **8**(1): p. 6780.
260. Chen, J., K.E. Wright, and M.A. Birch, *Nanoscale viscoelastic properties and adhesion of polydimethylsiloxane for tissue engineering.* Acta Mechanica Sinica, 2014. **30**(1): p. 2-6.
261. Burdick, J.A. and W.L. Murphy, *Moving from static to dynamic complexity in hydrogel design.* Nature Communications, 2012. **3**: p. 1269.
262. Malo de Molina, P., S. Lad, and M.E. Helgeson, *Heterogeneity and its Influence on the Properties of Difunctional Poly(ethylene glycol) Hydrogels: Structure and Mechanics.* Macromolecules, 2015. **48**(15): p. 5402-5411.
263. Kloxin, A.M., et al., *Mechanical Properties of Cellularly Responsive Hydrogels and Their Experimental Determination.* Advanced Materials, 2010. **22**(31): p. 3484-3494.
264. Puech, P.-H., et al., *A new technical approach to quantify cell–cell adhesion forces by AFM.* Ultramicroscopy, 2006. **106**(8): p. 637-644.
265. Sankaran, S., et al., *Cell Adhesion on Dynamic Supramolecular Surfaces Probed by Fluid Force Microscopy-Based Single-Cell Force Spectroscopy.* ACS Nano, 2017. **11**(4): p. 3867-3874.
266. Zhang, H., et al., *Effect of electrochemical oxidation and reduction on cell de-adhesion at the conducting polymer–live cell interface as revealed by single cell force spectroscopy.* Biointerphases, 2018. **13**(4): p. 041004.
267. Strohmeyer, N., et al., *Fibronectin-bound α5β1 integrins sense load and signal to reinforce adhesion in less than a second.* Nature Materials, 2017. **16**: p. 1262.
268. Crook, J.M. and E. Tomaskovic-Crook, *Culturing and Cryobanking Human Neural Stem Cells*, in *Stem Cell Banking: Concepts and Protocols*, J.M. Crook and T.E. Ludwig, Editors. 2017, Springer New York: New York, NY. p. 199-206.
269. Hutter, J. and J. Bechhoefer, *Calibration of atomic-force microscope tips.* Review of Scientific Instruments, 1993. **64**(7): p. 1868-1873.

270. Zhang, X., E. Wojcikiewicz, and V.T. Moy, *Force spectroscopy of the leukocyte function-associated antigen-1/intercellular adhesion molecule-1 interaction.* Biophys J, 2002. **83**(4): p. 2270-9.
271. Rief, M., et al., *Reversible Unfolding of Individual Titin Immunoglobulin Domains by AFM.* Science, 1997. **276**(5315): p. 1109.
272. Aguayo, S., et al., *Influence of biomaterial nanotopography on the adhesive and elastic properties of Staphylococcus aureus cells.* RSC Advances, 2016. **6**(92): p. 89347-89355.
273. O'Connell, C.D., et al., *Liquid Ink Deposition from an Atomic Force Microscope Tip: Deposition Monitoring and Control of Feature Size.* Langmuir, 2014. **30**(10): p. 2712-2721.
274. Tham, Y.Y., et al., *Development of in situ soft colloidal probe atomic force microscopy for probing the adhesion between wood extractives and model surfaces.* Colloids and Surfaces A: Physicochemical and Engineering Aspects, 2016. **500**: p. 203-213.
275. van der Aa, B.C., et al., *Stretching Cell Surface Macromolecules by Atomic Force Microscopy.* Langmuir, 2001. **17**(11): p. 3116-3119.
276. Higgins, M.J.C., Simon A; Mulvaney, Paul; Wetherbee, Richard., *Characterization of the adhesive mucliages secreted by live diatom cells using atomic force microscopy.* Protist, 2002. **Vol. 153**(1): p. 25-38.
277. Hugel, T., et al., *Elasticity of Single Polyelectrolyte Chains and Their Desorption from Solid Supports Studied by AFM Based Single Molecule Force Spectroscopy.* Macromolecules, 2001. **34**(4): p. 1039-1047.
278. Bemis, J.E., B.B. Akhremitchev, and G.C. Walker, *Single Polymer Chain Elongation by Atomic Force Microscopy.* Langmuir, 1999. **15**(8): p. 2799-2805.
279. Yeung, T., et al., *Effects of substrate stiffness on cell morphology, cytoskeletal structure, and adhesion.* Cell Motility, 2005. **60**(1): p. 24-34.
280. Hall, P.E., et al., *Integrins are markers of human neural stem cells.* Stem Cells, 2006. **24**(9): p. 2078-84.
281. Holland, N.B., et al., *Biomimetic engineering of non-adhesive glycocalyx-like surfaces using oligosaccharide surfactant polymers.* Nature, 1998. **392**: p. 799.
282. Pacifici, R., et al., *Ligand binding to monocyte alpha 5 beta 1 integrin activates the alpha 2 beta 1 receptor via the alpha 5 subunit cytoplasmic domain and protein kinase C.* The Journal of Immunology, 1994. **153**(5): p. 2222.
283. Cha, C., et al., *Tuning the dependency between stiffness and permeability of a cell encapsulating hydrogel with hydrophilic pendant chains.* Acta Biomater, 2011. **7**(10): p. 3719-28.
284. Humphries, J.D., A. Byron, and M.J. Humphries, *Integrin ligands at a glance.* Journal of Cell Science, 2006. **119**(19): p. 3901.
285. Barczyk, M., S. Carracedo, and D. Gullberg, *Integrins.* Cell Tissue Res, 2010. **339**(1): p. 269-80.
286. Franz, C., et al., *Studying Integrin-Mediated Cell Adhesion at the Single-Molecule Level Using AFM Force Spectroscopy*. Vol. 2007. 2007. pl5.
287. Strunz, T., et al., *Dynamic force spectroscopy of single DNA molecules.* Proceedings of the National Academy of Sciences, 1999. **96**(20): p. 11277.
288. Hinterdorfer, P. and Y.F. Dufrêne, *Detection and localization of single molecular recognition events using atomic force microscopy.* Nature Methods, 2006. **3**: p. 347.
289. Schwesinger, F., et al., *Unbinding forces of single antibody-antigen complexes correlate with their thermal dissociation rates.* Proceedings of the National Academy of Sciences, 2000. **97**(18): p. 9972.
290. Franz, C.M., et al., *Studying integrin-mediated cell adhesion at the single-molecule level using AFM force spectroscopy.* Sci STKE, 2007. **2007**(406): p. pl5.

291. Evans E. and W. P., *Dynamic Force Spectroscopy. Physics of bio-molecules and cells.* Springer, 2002. **75**.
292. Chan, C.E. and D.J. Odde, *Traction dynamics of filopodia on compliant substrates.* Science, 2008. **322**(5908): p. 1687-91.
293. Bangasser, Benjamin L., Steven S. Rosenfeld, and David J. Odde, *Determinants of Maximal Force Transmission in a Motor-Clutch Model of Cell Traction in a Compliant Microenvironment.* Biophysical Journal, 2013. **105**(3): p. 581-592.
294. Elosegui-Artola, A., et al., *Rigidity sensing and adaptation through regulation of integrin types.* Nature Materials, 2014. **13**: p. 631.
295. Friddle, R.W., A. Noy, and J.J. De Yoreo, *Interpreting the widespread nonlinear force spectra of intermolecular bonds.* Proceedings of the National Academy of Sciences, 2012. **109**(34): p. 13573-13578.
296. Trappmann, B. and C.S. Chen, *How cells sense extracellular matrix stiffness: a material's perspective.* Current Opinion in Biotechnology, 2013. **24**(5): p. 948-953.
297. Evans, E., *Probing the Relation Between Force—Lifetime—and Chemistry in Single Molecular Bonds.* Annual Review of Biophysics and Biomolecular Structure, 2001. **30**(1): p. 105-128.
298. Hillman, T., et al., *Cochlear nerve stimulation with a 3-dimensional penetrating electrode array.* Otol Neurotol, 2003. **24**(5): p. 764-8.
299. Kwon, K.Y., et al., *Integrated slanted microneedle-LED array for optogenetics.* Conf Proc IEEE Eng Med Biol Soc, 2013. **2013**: p. 249-52.
300. Rise, M.T., *Instrumentation for Neuromodulation.* Archives of Medical Research, 2000. **31**(3): p. 237-247.
301. Stephen, J.B., et al., *Nanosecond pulsed electric fields modulate cell function through intracellular signal transduction mechanisms.* Physiological Measurement, 2004. **25**(4): p. 1077.
302. Beebe, S.J., et al., *Diverse effects of nanosecond pulsed electric fields on cells and tissues.* DNA Cell Biol, 2003. **22**(12): p. 785-96.
303. Fichtner, D., et al., *Covalent and Density-Controlled Surface Immobilization of E-Cadherin for Adhesion Force Spectroscopy*. Vol. 9. 2014. e93123.
304. Marrosu, F., et al., *Vagal nerve stimulation improves cerebellar tremor and dysphagia in multiple sclerosis.* Multiple Sclerosis Journal, 2007. **13**(9): p. 1200-1202.
305. Siegel, S.W., et al., *Long-term results of a multicenter study on sacral nerve stimulation for treatment of urinary urge incontinence, urgency-frequency, and retention.* Urology, 2000. **56**(6, Supplement 1): p. 87-91.
306. McCaig, C.D., B. Song, and A.M. Rajnicek, *Electrical dimensions in cell science.* Journal of Cell Science, 2009. **122**(23): p. 4267.
307. Ereifej, E.S., et al., *Comparative assessment of iridium oxide and platinum alloy wires using an in vitro glial scar assay.* Biomed Microdevices, 2013. **15**(6): p. 917-24.
308. Weremfo, A., et al., *Investigating the Interfacial Properties of Electrochemically Roughened Platinum Electrodes for Neural Stimulation.* Langmuir, 2015. **31**(8): p. 2593-2599.
309. Turner, J.N., et al., *Cerebral Astrocyte Response to Micromachined Silicon Implants.* Experimental Neurology, 1999. **156**(1): p. 33-49.
310. Edell, D.J., et al., *Factors influencing the biocompatibility of insertable silicon microshafts in cerebral cortex.* IEEE Trans Biomed Eng, 1992. **39**(6): p. 635-43.
311. Schmidt, S., K. Horch, and R. Normann, *Biocompatibility of silicon-based electrode arrays implanted in feline cortical tissue.* J Biomed Mater Res, 1993. **27**(11): p. 1393-9.
312. Groothuis, J., et al., *Physiological Challenges for Intracortical Electrodes.* Brain Stimulation, 2014. **7**(1): p. 1-6.

313. Cogan, S.F., et al., *Over-pulsing degrades activated iridium oxide films used for intracortical neural stimulation.* Journal of Neuroscience Methods, 2004. **137**(2): p. 141-150.
314. Harnack, D., et al., *The effects of electrode material, charge density and stimulation duration on the safety of high-frequency stimulation of the subthalamic nucleus in rats.* J Neurosci Methods, 2004. **138**(1-2): p. 207-16.
315. Wojcikiewicz, E.P., X. Zhang, and V.T. Moy, *Force and Compliance Measurements on Living Cells Using Atomic Force Microscopy (AFM).* Biological Procedures Online, 2004. **6**: p. 1-9.
316. Franz, C.M., et al., *Studying Integrin-Mediated Cell Adhesion at the Single-Molecule Level Using AFM Force Spectroscopy.* Science's STKE, 2007. **2007**(406): p. pl5.
317. Minko, S. and Y. Roiter, *AFM single molecule studies of adsorbed polyelectrolytes.* Current Opinion in Colloid & Interface Science, 2005. **10**(1): p. 9-15.
318. Jaffe, L.F., *Control of development by ionic currents.* Society of General Physiologists series, 1979. **33**: p. 199-231.
319. Poo, M.-m. and K.R. Robinson, *Electrophoresis of concanavalin A receptors along embryonic muscle cell membrane.* Nature, 1977. **265**: p. 602.
320. McLaughlin, S. and M.M. Poo, *The role of electro-osmosis in the electric-field-induced movement of charged macromolecules on the surfaces of cells.* Biophysical Journal, 1981. **34**(1): p. 85-93.
321. Charrier, E.E., et al., *Control of cell morphology and differentiation by substrates with independently tunable elasticity and viscous dissipation.* Nature Communications, 2018. **9**(1): p. 449.
322. Gonnermann, C., et al., *Quantitating membrane bleb stiffness using AFM force spectroscopy and an optical sideview setup.* Integrative Biology, 2015. **7**(3): p. 356-363.